e-ISSN: 2602-277X

International Journal of Chemistry and Technology

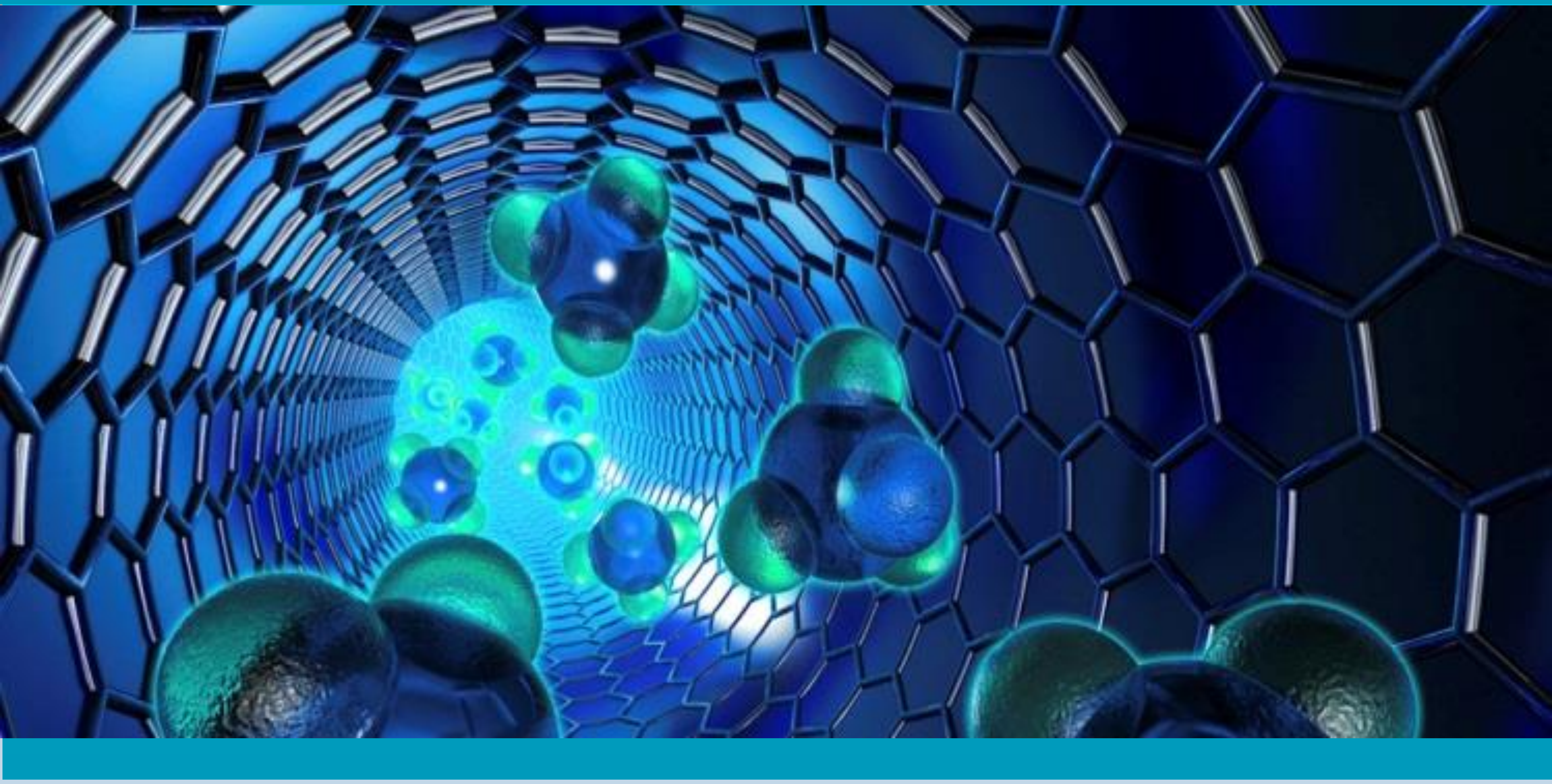

Volume: 4, Issue: 1 30 June 2020

E - Journal http://dergipark.org.tr/ijct

e-ISSN: 2602-277X

International Journal of Chemistry and Technology

JOURNAL INFO

Journal Name	International Journal of Chemistry and Technology
Journal Initial	IJCT
Journal Abbreviation	Int. J. Chem. Technol.
ISSN (Online)	2602-277X
Year of Launching	2017, August
Editor-in-Chief and Managing Editor	Prof. Dr. Bilal Acemioğlu
Manager of Publication	Assist. Prof. Mehmet Akyüz
Scope and Focus	Chemistry, Material Science, Technology
Review Type	Peer Review Double-Blinded
Ethical Rules	Plagiarism check, copyright agreement form, conflict of interest, ethics committee report
Access Type	Open Access
Publication Fee	Free
Article Language	English
Frequency of Publication	Biannualy
Publication Issue	June, December
Publisher	Prof. Dr. Bilal ACEMİOĞLU
Web Page	http://dergipark.org.tr/ijct
Contact E-mail address	ijctsubmission@gmail.com, ijctsubmission@yahoo.com
Contact Address and Executive address	Kilis 7 Aralik University, Faculty of Science and Arts, Department of Chemistry, 79000, Kilis
Contact Telephone	90 5535983054 (Editor-in-Chief), 90 530 3645222 (Manager of Publication), 90 532 233 17 38 (Secretary)
Publication Date	28/12/2018
Technical Editor	Assist. Prof. Dr. Evrim BARAN AYDIN
Spelling Editor	Dr. Oğuzhan Koçer, MSc. Rabia Acemioğlu
Language (Grammar) Editor	Assist. Prof. Dr. Muhammet KARAMAN, Assist. Prof. Dr. Muhittin KULAK, Dr. Lawali YABO DAMBAGI
Secretary	Dr. Oğuzhan KOÇER, MSc. Rabia ACEMIOĞLU

All detailed information including instructions for authors, aim and scopes, ethical rules, manuscript evaluation, indexing info, and manuscript template etc. can be found on the main web page of IJCT (http://dergipark.gov.tr/ijct).

e-ISSN: 2602-277X

International Journal of Chemistry and Technology

Volume: 4, Issue: 1, 30 Tuesday 2020

e-ISSN: 2602-277X

International Journal of Chemistry and Technology

Advisory Editorial Board

Prof. Dr. Harun PARLAR
(Technical University of Munich, München, Germany)

Prof. Dr. Ana Beatriz Rodriguez MORATINOS
(Univesity of Exramadura, Badajoz, Spain)

Prof. Dr. Rashid AHMAD
(University of Malakand, Chakdara, Pakistan)

Prof. Dr. Jaine H. Hortolan LUIZ
(Federal University of Alfenas, Unıfal-MG, Brazil)

Prof. Dr. Vagıf ABBASOV
(Nef-Kimya Prosesleri Institutu, Baku, Azerbaijan)

Prof. Dr. Mika SILLANPAA
(LUT Lappeenranta University of Technology, Lappeenranta, Finland)

Prof. Dr. Gilbert Kapche DECCAUX
(University of Yaounde I, Yaounde, Cameroon)

Prof. Dr. Ahmet ÇAKIR
(Kilis 7 Aralik University, Kilis, Turkey)

Prof. Dr. Nurullah SARAÇOĞLU
(Atatürk University, Erzurum, Turkey)

Prof. Dr. Ahmet Baysar
(Inonu University, Malatya, Turkey)

Prof. Dr. Ö. İrfan KÜFREVIOĞLU
(Atatürk University, Erzurum, Turkey)

Prof. Dr. Anatoli DIMOGLU
(Düzce University, Düzce, Turkey

Prof. Dr. Şükrü BEYDEMIR
(Anadolu University, Eskişehir, Turkey)

Prof. Dr. Mahfuz ELMASTAŞ
(Health Sciences University, İstanbul, Turkey)

Prof. Dr. Giray TOPAL
(Dicle University, Diyarbakır, Turkey)

Prof. Dr. Shaobin WANG
(Curtin University, Perth, Australia)

Prof. Dr. Jon-Bae KIM
(College of Health Sciences, South Korea)

Prof. Dr. Guang-Jie ZHAO
(Beijing Forestry University, Beijing, China)

Prof. Dr. Papita DAS
(Jadavpur University, Jadavpur, India)

Prof. Dr. Atiqur RAHMAN
(Islamic University, Kushita, Bangladesh)

Prof. Dr. Salah AKKAL
(University of Mentouri Consatntine, Consatntine, Algeria)

Prof. Dr. Gelu BOURCEANU
(Alexandru Ioan Cuza University, Romania)

Prof. Dr. M. SALIH AĞIRTAŞ
(Yüzünücü Yıl University, Van, Turkey)

Prof. Dr. Rahmi KASIMOĞULLARI
(Dumlupınar University, Kütahya, Turkey)

Prof. Dr. Hamdi TEMEL
(Dicle University, Diyarbakır, Turkey)

Prof. Dr. Ömer ŞAHIN
(Siirt University, Siirt, Turkey)

Prof. Dr. Mehmet UĞURLU
(Sıtkı Kocman University, Muğla, Turkey)

Prof. Dr. Ramazan SOLMAZ
(Bingol University, Bingöl, Turkey)

Prof. Dr. Mehmet DOĞAN
(Balıkesir University, Balıkesir, Turkey)

Prof. Dr. Birgül YAZICI
(Cukurova University, Adana, Turkey)

e-ISSN: 2602-277X

International Journal of Chemistry and Technology

Advisory Editorial Board

Prof. Dr. Barbaros NALBANTOĞLU
(Yıldız Technical University, İstanbul, Turkey)

Prof. Dr. T. Abdulkadir ÇOBAN
(Erzincan Binali Yıldırım University, Erzincan, Turkey)

Prof. Dr. Serhan URUŞ
(Sütçü İmam University, K.Maraş, Turkey)

Prof. Dr. Halim AVCI
(Kilis 7 Aralik University, Kilis, Turkey)

Prof. Dr. Duygu EKINCI
(Atatürk University, Erzurum, Turkey)

Prof. Dr. Ali KARA
(Uludağ University, Bursa, Turkey)

Prof. Dr. Murat SADIKOĞLU
(Gaziosman Paşa University, Tokat, Turkey)

Assoc. Prof. Dr. Şenay ŞIMŞEK
(North Dakota State Unıversıty, Fargo, USA)

Assoc. Prof. Dr. Muhammet KÖSE
(Sütçü İmam University, K.Maraş, Turkey)

Assoc. Prof. Niyaz M. MAHMOODI
(Institute for Color Science and Technology, Tehran, Iran)

Assoc. Prof. Dr. Metin AÇIKYILDIZ
(Kilis 7 Aralik University, Kilis, Turkey)

Assist. Prof. Dr. Mutasem Z. BANI-FWAZ
(King Khalid University, Asir-Abha, Saudi Arabia

Dr. Zineb TRİBAK
(Sidi Mohamed Ben Abdellah University, Fez Morocco)

Dr. Ramadan E. ASHERY
(Damanhour University, Egypt)

Prof. Dr. Murat ALANYALIOĞLU
(Atatürk University, Erzurum, Turkey)

Prof. Dr. İsmet KAYA
(18 Mart University, Çanakklae, Turkey)

Prof. Dr. Ömer IŞILDAK
(Gaziosmanpaşa University, Tokat, Turkey)

Prof. Dr. Ahmet TUTAR
(Sakarya University, Sakarya, Turkey)

Prof. Dr. Metin BÜLBÜL
(Dumlupınar University, Kütahya, Turkey)

Prof. Dr. Murat SARAÇOĞLU
(Erciyes University, Kayseri, Turkey)

Prof. Dr. Mustafa KARATAŞ
(Aksaray University, Aksaray, Turkey

Assoc. Prof. Dr. Mahjoub JABLI
(University of Monastir, Monastir, Tunisia)

Assoc. Prof. Chin-Hung LAI (Chung Shan Medical University, Taiwan)

Assoc. Prof. Dr. Mustafa ÖZDEMIR
(Süleyman Demirel University, Isparta, Turkey)

Assist. Prof. Masood Ayoub KALOO
(Govt. Degree College Shopian, J **&**K, India)

Assist. Prof. Dr. Bakhtiyor RASULEV
(North Dakota State Unıversıty, Fargo, USA)

Dr. Sameer Ahmed AWAD
(University of Anbar, Ramadi, Iraq)

e-ISSN: 2602-277X

International Journal of Chemistry and Technology

Reviewers for June 2020, Vol: 4, Issue: 1

Prof. Dr. Atiqur RAHMAN
(Islamic University, Bangladesh)

Prof. Dr. Şerife YALÇIN
(Harran University, Şanlıurfa, Turkey)

Prof. Dr. Şükrü ÖZĞAN
(Sütçü İmam University, K. Maraş, Turkey)

Prof. Dr. Esvet AKBAŞ
(Yüzüncü Yıl University, Van, Turkey)

Prof. Dr. Burhan ATEŞ
(İnönü University, Malatya, Turkey)

Assoc Prof. Dr. Ayşe DINÇER
(Manisa Celal Bayar University, Manisa, Turkey)

Assoc. Prof. Dr. Güven TURGUT
(Erzurum Teknik University, Erzurum,Turkey)

Assoc. Prof. Dr. Ali ŞAMIL
(Sütçü İmam University, K. Maraş, Turkey)

Assoc. Prof. Dr. Nihan GÖNÜLOL (Ondokuz
Mayıs University, Samsun, Turkey)

Assoc Prof. Dr. Mustafa ÖZDEMIR (Süleyman
Demirel University, Isparta, Turkey)

Assoc Prof. Dr. Mustafa ÖZDURAN
(Kırşehir Ahi Evran University, Kırşehir, Turkey)

Assist Prof. Dr. Güler Bengisu TEZEL
TANRISEVER
(Texas AM University, USA)

Prof. Dr. Yahya CAN
(Pamukkale University, Denizli, Turkey)

Prof. Dr. Ramazan ERENLER
(Gazi Osanpaşa University, Tokat, Turkey)

Prof. Dr. Burhan ATEŞ
(İnönü University, Malatya, Turkey)

Prof. Dr. Veysel ÖZCEYHAN
(Erciyes University, Kayseri, Turkey)

Assoc. Prof. Dr. Esen TAŞĞIN
(Atatürk University, Erzurum, Turkey)

Assoc. Prof. Dr. Hüseyin ERTAP
(Kakas University, Kars, Turkey)

Assoc. Prof. Dr. Orhan BAYTAR
(Siirt University, Siirt, Turkey)

Assoc Prof. Dr. Ali ARSLANTAŞ
(Karabük University, Karabük, Turkey)

Assoc. Prof. Dr. Aydın KESKINRÜZGAR
(Adıyaman University, Adıyaman, Turkey)

Assist Prof. Dr. Mehmet AKYÜZ
(Kilis 7 Aralik University, Kilis, Turkey)

Assist Prof. Dr. Fazlıhan YILMAZ
(Atatürk University, Erzurum, Turkey)

Assist Prof. Dr. Lalehan AKYÜZ
(Aksaray University, Aksaray, Turkey)

e-ISSN: 2602-277X

International Journal of Chemistry and Technology

TABLE OF CONTENTS

Research Articles **Pages**

DOI: http://dx.doi.org/10.32571/ijct.669762 **E-ISSN:2602-277X**

International Journal of Chemistry and Technology

http://dergipark.org.tr/ijct

Research Article

Effect of bleaching treatment on element content of enamel

Derya SÜRMELİOĞLU[1], Zeyneb Merve ÖZDEMİR[1,*], Sevim ATILAN YAVUZ[1], Halime KOLSUZ ÖZÇETİN[1]

ID on the last page

[1]*Department of Restorative Dentistry, Dentistry Faculty, Gaziantep University, 27310, Gaziantep, Turkey*

Received: 3 January 2020; Revised: 21 January 2020; Accepted: 27 January 2020

*****Corresponding author e-mail: zeyneb_merve@yahoo.com

Citation: Sürmelioğlu, D.; Özdemir, Z. M.; Atılan Yavuz, S.; Kolsuz Özçetin, H. *Int. J. Chem. Technol.* **2020**, 4 (1), 1-7.

ABSTRACT

The aim of study was to evaluate the mineral changes caused by enamel bleaching treatments at different application times by scanning electron microscope- energy dispersive X-Ray (SEM-EDX). In this study, 36 teeth were divided into 3 groups after mineral measurements (Flour, Silicon, Aluminum, Strontium) with SEM-EDX ($n = 12$). 40% hydrogen peroxide gel was used for bleaching in all groups. Bleaching was performed 20 min for Group 1, 40 min for Group 2, 60 min for Group 3. Mineral measurements were performed with SEM-EDX after treatment. In the intra-group comparison, although there was no significant difference between Flour (F) and Silicon (Si) values ($p > 0.05$), there was statistically significant difference in Aluminum (Al) and Strontium (Sr) values ($p < 0.05$). After the bleaching process for different application times, mineral change was observed in time-depending comparison. The best results were obtained for Group 2, appling according to manufacturer's instructions.

Keywords: Bleaching, mineral content, SEM-EDX.

Beyazlatma uygulamasının minenin mineral içeriği üzerine etkisi

ÖZ

Çalışmanın amacı, taramalı elektron mikroskobu-enerji dağıtıcılı X-Ray (SEM-EDX) cihazı ile farklı uygulama zamanlarında minedeki beyazlatma işlemleri sonrası meydana gelen mineral değişikliklerini değerlendirmektir. Bu çalışmada, 36 adet diş SEM-EDX ($n = 12$) ile mineral (Flor, Silisyum, Alüminyum, Stronsiyum) ölçümlerinden sonra üç gruba ayrıldı. Tüm gruplarda beyazlatma işlemi için % 40 hidrojen peroksit jel kullanıldı. Beyazlatma uygulaması, Grup 1 için 20 dakika, Grup 2 için 40 dakika, Grup 3 için 60 dakika olarak uygulandı. Mineral ölçümleri, işlemden sonra SEM-EDX cihazı ile gerçekleştirildi. Grup içi karşılaştırmada Flor (F) ve Silisyum (Si) değerleri arasında anlamlı bir fark olmamasına rağmen ($p > 0.05$), Alüminyum (Al) ve Stronsiyum (Sr) değerleri arasında istatistiksel olarak anlamlı fark vardı ($p < 0.05$). Farklı uygulama süreleri için beyazlatma işleminden sonra, zamana bağlı karşılaştırmada mineral değişikliği gözlendi. En iyi sonuçlar, üretici talimatlarına göre Grup 2 için elde edildi.

Anahtar Kelimeler: Beyazlatma, mineral içeriği, SEM-EDX.

1. INTRODUCTION

In recent years, the increasing interest in aesthetic applications has made dental aesthetic applications popular. A person's smile is the most important factor that emphasizes the importance of outward appearance. Bleaching treatment is a non-invasive and easily applied method that is often preferred for tooth discoloration. Nowadays, there are three types of bleaching techniques: office bleaching (professional application), home bleaching (individual application) and a combination of both methods.[1] Although the chosen technique varies according to the expectations and treatment needs of the patients, both techniques have advantages and disadvantages. The known major disadvantage of home bleaching is that it requires a long

DOI: http://dx.doi.org/10.32571/ijct.669762 **E-ISSN:2602-277X**

preparation process and is not easily controlled by the patient during application. In office bleaching, the main advantages are that the application of the gel under the control of the clinician can be prevented from contacting the soft tissue and the desired results can be achieved in one session.[2]

Hydrogen peroxide (HP) and carbamide peroxide (CP) gels are the most commonly used bleaching agents in discoloration.[1] HP-containing gels have been used in modern dentistry for more than 70 years.[3] The free radicals produced by HP can oxidize the conjugated chain of organic compounds and chromophores. Bleaching treatment is the brightening of tooth color by chemical agents applied to teeth oxidizing organic pigments in enamel and dentin tissue.[4] In the bleaching process, free radicals destructing double carbon bonds leads to a single carbon bond, while light and low molecular weight compounds are obtained from dark and large molecular weight compounds.

Some studies in the literature have shown that bleaching treatment disrupts the surface integrity of enamel,[5] increases the roughness,[6-7] changes the inorganic composition,[8] reduces microhardness and mineral content[7,9-10] and causes morphological changes. Therefore, the widespread use of high concentrations of peroxides is controversial.

Studies on the changes caused by HP-containing products in enamel are insufficient. Some researchers have reported negative effects such as microhardness reduction,[11-12] elastic modulus change or mineral loss,[13-17] on the other hand, other investigators also stated that these negative effects are clinically insignificant due to the remineralization power of saliva.[18-21] In the study of Goßtz and co-workers,[16] Although it has been reported that there is no significant change in enamel structure, other researchers have suggested that bleaching caused microstructural changes[22-23] in enamel at different depths and longer application times.[24]

There are few studies in the literature about fluoride (F), aluminum (Al), silicon (Si) and strontium (Sr) content of dental hard tissues after bleaching treatment.[25-28] However, no previous study evaluated the correlation of application time and the level of mineral content increase/decrease. The aim of this study was to evaluate the mineral changes in enamel after bleaching treatment for different periods by using Scanning Electron Microscopy-Energy Dispersion X-Ray Analysis (SEM-EDX) method.

2. MATERIALS AND METHODS

This study was approved by Gaziantep University Faculty of Dentistry Ethics Committee with the decision no 2019 / 468 and it was conducted in accordance with the Helsinki Declaration Principles. Each patient who participated in the study read and signed the informed consent form.

2.1. Preparation of Samples

In this study, 36 maxillary incisor teeth with no cracks or caries extracted for periodontal reasons were used. The teeth were divided into three groups as 12 teeth in each group and kept in artificial saliva during treatment.

The content of artificial saliva is; 1.1 g K_2HPO_4, 0.87 g NaCl, 0.62 g KCl, 0.3g KH_2PO_4, 0.17g $CaCl_2$ per 1000 ml and pH was 7. This chemical composition was obtained from Gaziantep University Biochemistry Department. Artificial saliva was maintained until from beginning to end of treatment and the solution was changed regularly every day. Mineral measurements with SEM-EDX were performed both before treatment and on the 14th day of treatment. The teeth were embedded in the *Si* impression material with the crown parts exposed, and their enamel surfaces were smoothed with a sanding device (Mecapol P 230 Press, Grenoble, France) using 600, 800 and 1000 grain silicon carbide water sanders.

2.2. Definition of groups and bleaching treatment

Opalescence Boost PF (Ultradent Products, Inc., SJ, USA) bleaching agent containing 40% HP was used according to the manufacturer's instructions. The samples were divided into three groups ($n = 12$):

Group 1: Application of the bleaching agent at the minimum time recommended by the manufacturer (20 min).

Group 2: Application of the bleaching agent to the ideal time recommended by the manufacturer (40 min).

Group 3: Application of the bleaching agent within the maximum time recommended by the manufacturer (60 min).

2.3. Mineral content analysis with SEM-EDX device

The SEM-EDX (JSM-6390LV, Jeol Inc., MA, USA) device provides information about the chemical composition of the material by allowing X-rays to be emitted from the ions and atoms on the sample surface.[29] Prepared samples were stored in an oven at 100˚C for 12 hours to isolate from the available moisture before SEM-EDX analysis. Each tooth was analyzed under 100 magnifications for elemental distribution from 3 standardized points on the crown. Al, F, Si and Sr minerals obtained from SEM-EDX analysis were investigated.

DOI: http://dx.doi.org/10.32571/ijct.669762 **E-ISSN:2602-277X**

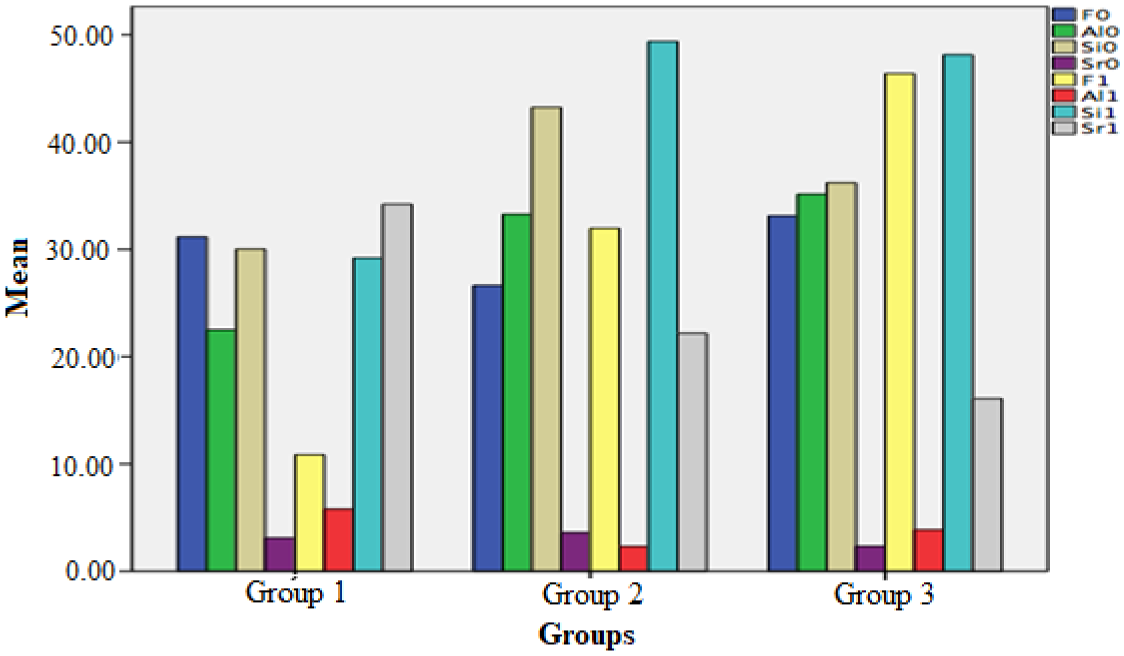

2.4. Statistical analysis

Compliance of normal distribution of numerical variables was tested by the Kolmogorov-Smirnov test. ANOVA, Bonferroni, pair *t* tests were used to compare the normally distributed variables in three independent groups; Kruskal Wallis and Wilcoxen tests were used to compare the variables that were not normally distributed in three independent groups. SPSS 22.0 Windows package program was used in the analysis and $p < 0.05$ was considered meaningful.

3. RESULTS AND DISCUSSION

3.1. Findings of fluorine content

Table 1 shows the results of F obtained from SEM-EDX analysis. Both intergroup and intragroup F value differences were evaluated in percent by weight. Although there was no statistically significant difference between the groups in terms of mineral changes before bleaching treatment (F_0) ($p > 0.05$), a significant difference was found in measurements on the 14th day of bleaching treatment (F_1) ($p = 0.002$). This significant difference is present only between Groups 1-3. No significant difference was found in F values of each group before and after treatment ($p > 0.05$).

3.2. Findings of aluminum content

Findings of Al values are shown in Table 2. Both intergroup and intragroup Al was evaluated in percent by weight. No significant difference was found between the groups in the measurements performed before (Al_0) and on the 14th day of bleaching treatment (Al_1) ($p > 0.05$). A significant difference was found in Al values of each group before and after treatment ($p < 0.05$).

3.3. Findings of silicon content

The values of Si obtained by SEM-EDX analysis are shown in Table 3. Both intergroup and intragroup Si values were evaluated in percent by weight. No statistically significant difference was found between the groups in the measurements performed before bleaching treatment (Si_0) ($p > 0.05$), however there was a significant difference in the values obtained on the 14th day of bleaching treatment (Si_1) ($p = 0.026$). Post-treatment evaluation was significantly lower in Group 1 than in Groups 2 and 3. No significant difference was found in Si values of each group before and after treatment ($p > 0.05$).

3.4. Findings of strontium content

The data related to Sr are shown in Table 4. Both inter-group and intra-group data were used to evaluate Sr in percent by weight. Although there was no statistically significant difference between the groups in terms of Sr_0 changes before the bleaching treatment ($p > 0.05$), there was a significant difference in the measurements made on the 14th day following the bleaching treatment (Sr_1) ($p = 0.010$). This significant difference was found between Groups 1and 2 and Groups 1 and 3. There was a statistically significant difference between before and 14 days following the bleaching treatment ($p = 0.005$).

All the mineral changes obtained from the study before treatment and on the 14th day of treatment are shown in Figure 1.

Table 1. Fluorine values (mean ± standard deviation)

	Group 1	Group 2	Group 3	*p*
F_0	31.16 ± 26^{aA}	$26.63 \pm 25{,}51^{aA}$	$33.12 \pm 37{,}41^{aA}$	0.879
F_1	10.85 ± 20.13^{aA}	$31.96 \pm 16{,}44^{bA}$	$46.38 \pm 15{,}51^{bA}$	0.002*
p	0.093	0.445	0.241	

*Different letters within columns and lines indicate statistically significant differences. Lowercases represent linear differences while uppercases represent columnar differences.

Table 2. Aluminum values (mean ± standard deviation)

	Group 1	Group 2	Group 3	***p***
Al_0	22.51 ± 13.21^{aA}	33.26 ± 33.74^{aA}	35.14 ± 22.41^{aA}	0.547
Al_1	5.78 ± 5.51^{aB}	2.30 ± 2.02^{aB}	3.85 ± 2.91^{aB}	0.154
p	0.005*	0.007*	0.005*	

*The same is as in Table 1.

Table 3. Silicon values (mean ± standard deviation)

	Group 1	Group 2	Group 3	*p*
Si_0	30.03 ± 30.06^{aA}	43.24 ± 24.40^{aA}	36.21 ± 21.90^{aA}	0.348
Si_1	29.18 ± 17.39^{aA}	49.37 ± 16.21^{bA}	48.14 ± 19.85^{aA}	0.026*
p	0.959	0.333	0.203	

*The same is as in Table 1.

Table 4. Strontium values (mean ± standard deviation)

	Group 1	Group 2	Group 3	*p*
Sr_0	3.09 ± 4.69^{aA}	3.59 ± 1.96^{aA}	2.32 ± 4.38^{aA}	0.052
Sr_1	34.21 ± 17.95^{aB}	22.19 ± 8.21^{bB}	16.09 ± 8.84^{bB}	0.010*
p	0.005*	0.005*	0.005*	

*The same is as in Table 1.

.

DOI: http://dx.doi.org/10.32571/ijct.669762 **E-ISSN:2602-277X**

Bleaching treatment is a widely preferred method for discoloration of teeth, however the results are still controversial. It has been reported that it causes morphological changes such as erosion and porosity in enamel structure.[30-31] In this study, mineral changes in the enamel structure were evaluated with SEM-EDX device.

Oxidation-reduction reactions caused by bleaching treatment cause degradation of organic and inorganic matrix structure.[32] However, the remineralizing effect of saliva can reverse the structural changes caused by bleaching agents. In conclusion, the clinical significance of mineral loss caused by bleaching agents may be limited.[33] Therefore, in order to utilize from the remineralization effect of saliva, samples were stored in artificial saliva solution.

Hydroxyapatite crystals, whose main inorganic component is calcium (Ca) and phosphorus (P), constitute the majority of the enamel structure.[34] There are various anions and cations in enamel structure in different ratios. The most important known cations are: sodium (Na), Sr, magnesium (Mg); anions are F, Si and *Al.*[35] These changes in mineral ratios results in differences in the organic / inorganic structure of the enamel and subsequently lead to morphological changes such as surface roughness and microhardness.[36-38]

SEM-EDX is a device that determines the mineral content in dental hard tissues in a percentage by weight and provides accurate and non-destructive analysis of samples.[39-40] This method was used to evaluate changes in enamel mineral content in our study. In the study of Kutuk and co-workers,[25] it has been shown that F containing desensitizing agents used after bleaching or in addition to bleaching gels increase the F levels in enamel. The possible explanation for this increase may be the use of F-containing bleaching agent to prevent sensitivity or demineralization during the bleaching process. However, there are controversial conclusions that there is no evidence to support the effect of F-containing bleaching gels on demineralization.

In the study of Saffarpour and co-workers,[26] a Sr-based agent was applied to all samples and bleaching treatment was applied to only one group. According to the obtained data, it was reported that the amount of Sr increased significantly in the group treated with bleaching treatment. In our study, Sr values were significantly increased. We assume that the reason for this increase is the use of artificial saliva in the study.

There was an increase in *Si* measurements before and on 14th day of the bleaching treatment. The increase of Si in percentage by weight can be explained by the basic mapping of Si and its consistent distribution with beehive-like structures. In accordance with these findings, it is known that *Si* precipitates on the uneven enamel surface by reacting with free oxygen radicals produced by HP contained by bleaching agents. These values are consistent with the results obtained in a study done by Tsujimoto and co-workers.[27]

Although Olcay and co-workers[28] have showed an increase in mineral changes in Al, our results are contradictory. There are no other studies regarding the change in the percentage of Al due to bleaching treatment in the literature. Since there is no study about Al mineral in the literature, its mechanism has not been clarified, therefore more studies are needed.

One of the limitations of our study is that in-vitro conditions do not fully mimic the in-vivo environment. We assume that the morphological and chemical changes in dental hard tissues are the most important side effect of the bleaching agents. These undesired effects may be reduced with the aid of both the buffering capacity of saliva and the administration of remineralization agents when applied in vivo. Assessing the long-term impacts of bleaching agents on dental tissues should be further investigated.

4. CONCLUSIONS

When the Opalescence Boost PF 40% HP used in the study was applied in three different periods, mineral change was observed in each group. However; the best results were obtained in Group 2, which was applied in the ideal time according to the manufacturer's instructions. Although there are few studies in the relevant literature, different studies are needed to better understand the effects of bleaching.

ACKNOWLEDGEMENTS

The study was self-funded by the authors. The authors would like to thank to Assoc. Prof. Dr. Uğur AYDIN for checking the text in English and its final version.

Conflict of interests

Authors declare that there is no a conflict of interest with any person, institute, company, etc.

DOI: http://dx.doi.org/10.32571/ijct.669762 **E-ISSN:2602-277X**

REFERENCES

1. Sulieman, A. M. *Periodontol. 2000.* **2008,** 48 (1), 148-169.

2. De Geus, J.; Wambier, L.; Kossatz, S.; Loguercio, A.; Reis, A. *Oper. Dent.* **2016,** 41 (4), 341-356.

3. Marshall, M. V.; Cancro, L. P.; Fischman, S. L. *J. Periodontol.* **1995,** 66 (9), 786-796.

4. Oktay, E. K. *Farklı vital beyazlatma sistemlerinin diş rengi üzerine etkilerinin klinik olarak karşılaştırılması*, Ankara, Türkiye, 2006 (in Turkish).

5. Oltu, Ü.; Gürgan, S. *J. Oral Rehabil.* **2000,** 27 (4), 332-340.

6. Cavalli, V.; Arrais, C.; Giannini, M.; Ambrosano, G. *J. Oral Rehabil.* **2004,** 31 (2), 155-159.

7. Pinto, C. F.; Oliveira, R. d.; Cavalli, V.; Giannini, M. *Braz. Oral Res.* **2004,** 18 (4), 306-311.

8. Tezel, H.; Ertaş, Ö. S.; Özata, F.; Dalgar, H.; Korkut, Z. O. *Quintessence Int.* **2007,** 38 (4), 339-347.

9. Cesar, I. C. R.; Redigolo, M. L.; Liporoni, P. C. S.; Munin, E. *Am. J. Dent.* **2005,** 18, 219-222.

10. Al-Salehi, S.; Wood, D.; Hatton, P. *J. Dent.* **2007,** 35 (11), 845-850.

11. Attin, T.; Vollmer, D.; Wiegand, A.; Attin, R.; Betke, H. *Am. J. Dent.* **2005,** 18 (1), 8-12.

12. Magalhães, J. G.; Marimoto, Â. R.; Torres, C. R.; Pagani, C.; Teixeira, S. C.; Barcellos, D. C. *Acta Odontol. Scand.* **2012,** 70 (2), 122-126.

13. Soares, D. G.; Ribeiro, A. P. D.; Sacono, N. T.; Loguércio, A. D.; Hebling, J.; Costa, C. A. D. S. *Braz. Dent. J.* **2013,** 24 (5), 517-521.

14. Abouassi, T.; Wolkewitz, M.; Hahn, P. *Clin. Oral Invest.* **2011,** 15 (5), 673-680.

15. Smidt, A.; Feuerstein, O.; Topel, M. *Quintessence Int.* **2011,** 42 (5), 407-412.

16. Götz, H.; Duschner, H.; White, D. J.; Klukowska, M. A. *J. Dent.* **2007,** 35 (6), 457-466.

17. Götz, H.; Klukowska, M. A.; Duschner, H.; White, D. J. *J. Clin. Dent.* **2007,** *18* (4), 112-119.

18. de Abreu, D. R.; Sasaki, R. T.; Amaral, F. L. B.; Florio, F. M.; Basting, R. T. *J. Esthet. Restor. Dent.* **2011,** 23 (3), 158-168.

19. Lopes, G. C.; Bonissoni, L.; Baratieri, L. N.; Vieira, L. C. C.; Monteiro Jr, S. *J. Esthet. Restor. Dent.* **2002,** 14 (1), 24-30.

20. Lewinstein, I.; Fuhrer, N.; Churaru, N.; Cardash, H. *J. Prosthet. Dent.* **2004,** 92 (4), 337-342.

21. Teixeira, E.; Ritter, A. V.; Thompson, J. Y.; Leonard, J. R.; Swift, J. E. *Am. J. Dent.* **2004,** 17 (6), 433-436.

22. Efeoglu, N.; Wood, D.; Efeoglu, C. *J. Dent.* **2005,** 33 (7), 561-567.

23. Joiner, A. *J. Dent.* **2006,** 34 (7), 412-419.

24. Goldberg, M.; Grootveld, M.; Lynch, E. *Clin. Oral Invest.* **2010,** 14 (1), 1-10.

25. Kutuk, Z. B.; Ergin, E.; Cakir, F. Y.; Gurgan, S. *J. Appl. Oral Sci.* **2019,** 27:e20180233.

26. Saffarpour, M.; Asgartooran, B.; Reza Tahriri, M.; Savadroudbari, M. M.; Khabazkhoob, M. *Braz. J. Oral Sci.* **2019,** 18, e191424-e191424.

27. Tsujimoto, M.; Ookubo, A.; Wada, Y.; Matsunaga, T.; Tsujimoto, Y.; Hayashi, Y. *J. Endodont.* **2011,** 37 (2), 231-234.

28. Olcay, K.; Ataoğlu, H.; Belli, S. *Selcuk Dent. J.* 2016, 3 (3), 107-119 (in Turkish).

29. Barbour, M.; Rees, J. *J. Dent.* **2004,** 32 (8), 591-602.

30. Josey, A.; Meyers, I.; Romaniuk, K.; Symons, A. *J. Oral Rehabil.* **1996,** 23 (4), 244-250.

31. McCracken, M. S.; Haywood, V. B. *J. Dent.* **1996,** 24 (6), 395-398.

32. Soldani, P.; Amaral, C. M.; Rodrigues, J. A. *Int. J. Periodont. Rest. Dent.* **2010,** 30 (2), 203-211.

33. Metz, M. J.; Cochran, M. A.; Matis, B. A.; Gonzalez, C.; Platt, J.; Lund, M. R. *Oper. Dent.* **2007,** 32 (5), 427-436.

34. Ari, H.; Erdemir, A. *J. Endodont.* **2005,** 31 (3), 187-189.

DOI: http://dx.doi.org/10.32571/ijct.669762 **E-ISSN:2602-277X**

35. Kang, D.; Amarasiriwardena, D.; Goodman, A. H. *Anal. Bioanal. Chem.* **2004,** 378 (6), 1608-1615.

36. Timpawat, S.; Harnirattisai, C.; Senawongs, P. *J. Endodont.* **2001,** 27 (3), 168-171.

37. De-Deus, G.; Paciornik, S.; Mauricio, M. *Int. Endodont. J.* **2006,** 39 (5), 401-407.

38. Mello, I.; Coil, J.; Antoniazzi, J. H. *Oral Surg. Oral Med. Oral Pathol. Oral Radiol. Endodont.* **2009,** 107 (4), e47-e51.

39. Llena, C.; Esteve, I.; Forner, L. *An. Anat.* **2018,** 217, 97-102.

40. Cakir, F.; Korkmaz, Y.; Firat, E.; Oztas, S.; Gurgan, S. *Oper. Dent.* **2011,** 36 (5), 529-536.

ORCID

iD https://orcid.org/0000-0002-6034-3131 (D. Sürmelioğlu)

iD https://orcid.org/0000-0002-3290-9871 (Z. M. Özdemir)

iD https://orcid.org/0000-0002-6192-4931 (S. Atılan Yavuz)

iD https://orcid.org/0000-0001-5068-5720 (H. Kolsuz Özçetin)

DOI: http://dx.doi.org/10.32571/ijct.687373 **E-ISSN:2602-277X**

International Journal of Chemistry and Technology

http://dergipark.org.tr/ijct

Research Article

Photovoltaic, thermal, fluorescence and aggregation properties of non-peripherally metallophthalocyanines bearing four 3,4-dimethoxyphenethoxy substituents

Derya GÜNGÖRDÜ SOLĞUN[1], Mehmet Salih AĞIRTAŞ[1,*], Sabit HOROZ[2]

ID on the last page

[1]*Department of Chemistry, Faculty of Science, Van Yuzuncu Yıl University, 65080, Van, Turkey*

[2]*Faculty of Engineering and Architecture Department of Electrical and Electronic Engineering, Siirt University, Siirt, Turkey*

Received: 10 February 2020; Revised: 26 February 2020; Accepted: 27 February 2020

*****Corresponding author e-mail: salihagirtas@hotmail.com

Citation: Güngördü Solğun, D.; Ağırtaş, M. S.; Horoz, S. *Int. J. Chem. Technol.* **2020**, 4 (1), 8-15.

ABSTRACT

In this study, a non-peripheral phthalonitrile compound was prepared as a starting material. Then this 3,4-dimethoxymethoxy substituted non-peripheral phthalonitrile compound was reacted with Co, Zn and Cu salts. Non-peripheral phthalocyanine compounds were prepared using an easy and practical method. The fluorescence spectra of the zinc phthalocyanine compound were measured in tetrahydrofuran. Aggregation studies showed the compliance with the lambert-beer law in the concentration range studied for non-peripheral phthalocyanine compounds. Thermogravimetric (TG) analyses showed that the compounds were stable. The photovoltaic performance of these phthalocyanine compounds was measured as current density-voltage (J-V). The calculated power conversion effects showed that these compounds had the potential to be used for dye-sensitized solar cell (DSSC) structures.

Keywords: Photovoltaic, phthalocyanine, thermal, non-peripheral, fluorescence.

3,4-dimetoksifentoksi sübstitüenti taşıyan periferik olmayan metaloftalosiyaninlerin fotovoltaik, termal, floresans ve agregasyon özellikleri

ÖZ

Bu çalışmada, başlangıç materyali olarak non periferik bir ftalonitril bileşiği hazırlanmıştır. Daha sonra bu 3,4-dimetoksifentoksi sübstitüentli non periferal ftalonitril bileşiği, Co, Zn ve Cu tuzları ile reaksiyona sokuldu. Kolay ve pratik bir metot kullanılarak non periferal ftalosiyanin bileşikleri hazırlandı. Çinko ftalosiyanin bileşiğinin floresan spektrumları tetrahidrofuran içinde ölçüldü. Agregasyon çalışmaları, non periferal ftalosiyanin bileşikleri için incelenen konsantrasyon aralığında lambert-beer yasasına uyum göstermiştir. Termogravimetrik (TG) analizler bileşiklerin kararlı olduğunu gösterdi. Bu ftalosiyanin bileşiklerinin fotovoltaik performansı akım yoğunluk voltajı (J-V) olarak ölçüldü. Hesaplanan güç dönüşüm etkileri, bu bileşiklerin, boyaya duyarlı güneş pili (DSSC) yapıları için kullanılma potansiyeline sahip olduğunu göstermiştir.

Anahtar Kelimeler: Fotovoltaik, ftalosiyanin, termal, periferik olmayan, floresan.

1. INTRODUCTION

Phthalocyanines are a class of macrocyclic compounds of organic origin paying attention for researchers. Phthalocyanines are compounds with green and blue colors. The most important applications are dyes, dye sensitized solar cells (DSSCs)[1], pigments[2], liquid crystals[3], semiconductors[4], solar cells[5], optics[6], catalysts[7] and sensors.[8] Nanotechnology and photodynamic therapy (PDT) are being extensively investigated for their applications.[9,10] Phthalocyanine compounds have also been a subject of research for therapeutic medicine and antioxidant potentials.[11]

DOI: http://dx.doi.org/10.32571/ijct.687373 **E-ISSN:2602-277X**

One of the obstacles in front of the mentioned applications is the low solubility of these compounds.[12] To solve this problem, solubility can be increased by attaching appropriate peripheral or non-peripheral groups to the core of phthalocyanine.[13-14] Synthesis of soluble phthalocyanines contributes to potential application areas (PDT etc.). This allows the compounds to be used in new technological areas. It contributes to setting new targets for research. Another important issue is the effort to find alternative energy sources for rapidly depleted fossil fuels. One of the best alternatives is research on dye sensitized solar cells (DSSCs). DSSCs are of great interest because they are cheap and environmentally friendly for photovoltaic cells.[15] It provides a possibility to form different DSSCs with exchangeable substituents on the phthalocyanine compounds.[16] Due to their photoelectron properties, ruthenium and silicon compounds which have the applications for DSSCs are known to have commercially high costs. Phthalocyanine complexes are extensively researched for use in applications such as electronics, optics, DSSC with lower cost and economic value.[17-18] Herein, non-peripheral 3,4-dimethoxyphenethoxy substituted cobalt(II), zinc(II) and copper(II) phthalocyanine compounds were selected as dyes for DSSCs. These phthalocyanine compounds that are low cost and practically ready provide the needed alternatives for photovoltaic applications.

2. EXPERIMENTAL

2.1. General

$Co(CH_3COOH)_2$, $Zn(CH_3COO)_2$, $CuCl_2$, K_2CO_3, Ethanol, methanol, hexane, ether, THF, DMF, DMSO, CH_2Cl_2, $CHCl_3$, acetonitrile, acetone, DBU were purchased from Merck and Sigma. It has benefited from the literature for some solvents requiring purification.[19] The devices used in structure analysis and measurements can be listed as follows: Absorption measurements were performed by a Hitachi U-2900 Spectrophotometer. Fluorescence measurements were done using a Shımadzu RF-6000 spectrofluorophotometer. Thermo Scientific FT-IR spectrum was used for functional vibrations. Proton and carbon spectra were determined by an Agilent 400 MHz spectrometer. A SETARAM TG / DTA / DSC-16 was used for thermal stability. A PCE-S20 instrument was used to plot current density (J) versus voltage (V) data.

2.2. 3-(3,4-dimethoxyphenethoxy)phthalonitrile (3)

A mixture of 2-(3,4-dimethoxyphenyl)ethanol **2** (0.527 g, 2.89 mmol) and 3-nitrophthalonitrile **1** (0.500 g, 2.89 mmol) in 25 ml dimethylsulfoxide (DMSO) was stirred under nitrogen atmosphere and at room temperature. After stirring for 15 min, K_2CO_3 (2.2 g, 15.94 mmol) was added into the mixture over a period of 2 h. The temperature was raised to 50°C and stirred for 48 hours. The resulting mixture was transferred into ice water (150 ml). The precipitated substance was washed with distilled water and filtered until neutral. The product was then washed with hexane and diethyl ether and dried. The compound is easily dissolved in solvents such as dichloroethane, acetonitrile, acetone, chloroform, dichloromethane, THF, DMF and DMSO. Yield; 0.63 g (71%). Mp: 143°C. ^1H NMR (400 MHz, DMSO-d_6) δ ppm: 7.84, 7.81, 7.79, 7.63, 7.61, 6.94, 6.91, 6.85, 6.81, 4.37, 3.74, 3.70, 3.39, 3.00, 2.48, 2.07, 1.07. ^{13}C NMR (400 MHz, DMSO-d_6) δ ppm: 161.58, 148.85, 147.79, 136.19, 130.54, 125.77, 120.99, 118.72, 115.90, 115.35, 113.95, 113.08, 111.98, 102.98, 70.70, 55.81, 40.60, 39.45, 34.42. FT-IR spectrum (cm^{-1}): 3078, 3005, 2939, 2916, 2881, 2839, 2233, 1585, 1519, 1458, 1423, 1354, 1288, 1265, 1238, 1195, 1157, 1138, 1045, 1022, 864, 794, 763. Anal calculated for $C_{18}H_{16}N_2O_3$: (308.33 g mol^{-1}) C 70.12; H 5.23; N 9.09 %. Found C 70.19; H 5.18; N 9.06 %.

2.3. 2,10,16,24–tetrakis (3,4-dimethoxyphenethoxy phthalocyaninato) Cobalt (II) (4)

The substances 3- (3,4-dimethoxyphentoxy) phthalonitrile **3** (0.050 g, 0.16 mmol) and $Co(CH_3COOH)_2$ (0.021 g) were powdered in a quartz crucible. It was heated in a glass tube for 5 minutes under nitrogen at 280 ºC and in the presence of DBU. After cooling, the product was washed with cold and hot water, ethanol, methanol, hexane and diethylether. The product soluble in THF was collected and the solvent was removed to obtain a green solid. This compound is soluble in acetone, dichloromethane, $CHCl_3$, THF, DMF, DMSO. Yield: 0.020 g (38.69%). Anal calculated for $C_{72}H_{64}CoN_8O_{12}$: (1292.26 g mol^{-1}) C 66.92; H, 4.99; N, 8.67%. Found: C, 71.05; H, 5.02; N, 8.64 %. UV-Vis (THF) λmax (log ε): 696 (5.07), 630 (4.60). IR spectrum (cm^{-1}): 2958, 2912, 2870, 1600, 1516, 1489, 1465, 1365, 1234, 1141, 1068, 860. MS (MALDI-TOF) m/z: 1292.8$[M]^+$.

2.4. 2,10,16, 24–tetrakis (3,4-dimethoxyphenethoxy phthalocyaninato) zinc (II) (5)

Preparation of compound **5** was prepared under the same conditions as compound **4**, except for metal salt and temperature ($Zn(CH_3COO)_2$). Yield: 0.033 g (63.52%). Anal calculated for $C_{72}H_{64}N_8O_{12}Zn$ (1298.70 g mol^{-1}) C 66.59; H 4.97; N 8.63 %. Found C, 66.54; H, 4.93; N, 8.59%. UV-Vis (THF) λmax (log ε): 698 (5.14), 630 (4.47), 314 (4.73). ^1H NMR (400 MHz, DMSO-d_6) δ ppm: 8.02, 7.73, 7.58, 7.25, 7.03, 6.91, 6.85, 6.78, 6.56, 4.87, 3.76, 3.64, 3.30, 2.47, 2.05, 1.34. IR spectrum (cm^{-1}): 3066 (Ar-H), 2931, 2870 (aliphatic), 1589, 1516 (C=C), 1489, 1465, 1265, 1234, 1203, 1141, 1026, 806, 748 cm^{-1}. MS (MALDI-TOF) m/z: 1299.8 $[M+1]^+$.

DOI: http://dx.doi.org/10.32571/ijct.687373 **E-ISSN:2602-277X**

2.5. 2,10,16,24–tetrakis(3,4-dimethoxyphenethoxy phthalocyaninato) Copper (II) (6)

Preparation of compound **6** was prepared under the same conditions as compound **4**, except for metal salt ($Zn(CH_3COO)_2$,). Yield: 0.015 g (28.95%). Anal calculated for $C_{72}H_{64}CuN_8O_{12}$: (1296.87 g mol^{-1}) C 66.68; H 4.97; N, 8.64. % Found C, 66.71; H, 4.91; N, 8.61%; UV-Vis (THF) λmax (log ε): 706 (5.06), 636(4.57). IR spectrum (cm^{-1}): 2947, 1597, 1512(C=C), 1462, 1265, 1161, 1049, 798, 744. MS (MALDI-TOF) m/z: 1297.6[M +1]$^+$.

2.6. The current density (J) – voltage (V)

Fluorine doped tin oxide (FTO) coated conductive glasses were used as photoelectrodes in DSSC structures. The doctor blade method was used to coat TiO_2 on these substrates. The prepared TiO_2/FTO substrates were sintered at 450°C for 45 minutes. A certain amount of compound **4**, **5** and **6** solutions were dropped on TiO_2/FTO substrates. The prepared metal complex/TiO_2/FTO structures were dried with N_2 gas. Cu_2S counter electrodes containing polysulfide electrolytes were used to secure the DSSC structures.

3. RESULTS AND DISCUSSION

3.1. Synthesis and characterization

Similar to our previous method[20], 3-(3,4-dimethoxyphenitoxy) phthalonitrile (**3**) was synthesized as the starting material of non-peripheral phthalocyanines. The temperature and reaction time were slightly altered to give the desired phthalonitrile derivative. Non-peripheral metallophthalocyanines (**4-6**) were also obtained from the appropriate reaction of the metal salts with this starting material. The reaction route of all these newly synthesized substances is given in Scheme 1. An important feature of these compounds is that the absorption range is more suited to the phototherapeutic window. Elemental analysis, mass spectra, FTIR, ^{1}H NMR, ^{13}C NMR and UV-spectrum spectra were used for the characterization of chemical structures. The data obtained with the expected structure was found to be in good agreement. In the ^{1}H NMR spectrum of compound **3** in DMSO-d_6, aromatic protons appear at 7.84, 7.81, 7.79, 7.63, 7.61, 6.94, 6.91, 6.85,6.81 (Ar-H) and aliphatic protons appear at 4.37, 3.74, 3.00, 2.07, 1.07. In ^{13}C NMR spectrum of compound **3** (400 MHz, DMSO-d_6) δ ppm: 161.58, 148.85, 147.79, 136.19, 130.54, 125.77, 120.99, 118.72, 115.90, 115.35, 113.95, 113.08, 111.98, 102.98, 70.70, 55.81, 40.60, 39.45, 34.42. In the ^{1}H NMR spectrum of compound **5** within DMSO-d_6, aromatic protons appear at 8.02, 7.73, 7.58, 7.25, 7.03, 6.91, 6.85, 6.78, 6.56, and aliphatic protons appear at 4.87, 3.76, 3.64, 2.05,1.34 ppm. ^{1}H NMR spectra for compounds **4** and **6** were not deemed necessary due to the magnetic state of their electronic structure. The practical method used in this study gives the same data as the spectral data of the functional groups in the previous studies, but provides the advantage of an easier and more economical preparation.[20,21]

When the IR spectral data for the evaluation of functional groups are examined, the intermediate peaks are observed at 3078 cm^{-1} (Ar-CH), nitrile 2233 cm^{-1} (CN), carbon carbon peak 1585-1519 cm^{-1} (C = C), aromatic oxygen peak 1265 cm^{-1} (Ar-O-Ar). These peaks confirm the phthalonitrile structure. The most significant change in the IR peaks of phthalonitrile derivatives and phthalocyanine compounds is the change in the nitrile peak. It is the complete disappearance of the sharp nitrile peak in the phthalonitrile derivative. IR vibrations of the resulting phthalocyanine compounds resemble the phthalonitrile peaks with minor shifts, except for nitrile peaks. The IR spectra of compound **4** displayed vibration peaks at 2958, 2912, 2870 cm^{-1} (aliphatic), 1600, 1516 C=C cm^{-1}, and Ar-O-Ar peaks at 1234 cm^{-1}. Vibration peaks compound **5** appeared at 3066 cm^{-1} (Ar-H), 2931, 2870 cm^{-1} (aliphatic), 1589, 1516 cm^{-1} C=C cm^{-1}, and Ar-O-Ar peaks at 1234 cm^{-1}. For compound **6**, the vibration peaks were also observed at 2947, 1597-1512 C=C cm^{-1}, and Ar-O-Ar peaks at 1265 cm^{-1}. This data confirms the expected structures.

One of the techniques used to characterize new compounds is the mass spectrum. It makes an important contribution to supporting the structure. The mass spectral study by the MALDI-TOF technique on the new compounds (**4-6**) gave the following results, *m/z*: 1292.8 [M]$^+$for **4**, *m/z*: 1299.8 [M +1]$^+$for **5**, *m/z*: 1297.6 [M +1]$^+$ for **6**.

The characteristic Q and B bands in THF were observed due to **4**, **5** and **6** phthalocyanine compounds in the UV-Vis spectra. The Q band of the phthalocyanine compounds is due to the transitions of $\pi\rightarrow\pi^*$ from the highest occupied molecular orbital (HOMO) to the lowest unoccupied molecular orbital (LUMO) of the phthalocyanine ring. Non-peripheral electron donor groups are known to cause bathochromic shift in the Q band.[22] It can be said that in the UV-Vis spectra of compounds **4** and **5**, the Q bands are observed at 696 and 698 nm due to the non-peripheral shift. The compound **6** give the Q band at 706 nm as expected. These spectral data confirm the bathochromic shift. The Q bands of non-peripheral substituted cobalt (II) phthalocyanines (**4**) were approximately 36 nm red-shifted according to the related peripheral substituted

DOI: http://dx.doi.org/10.32571/ijct.687373 **E-ISSN:2602-277X**

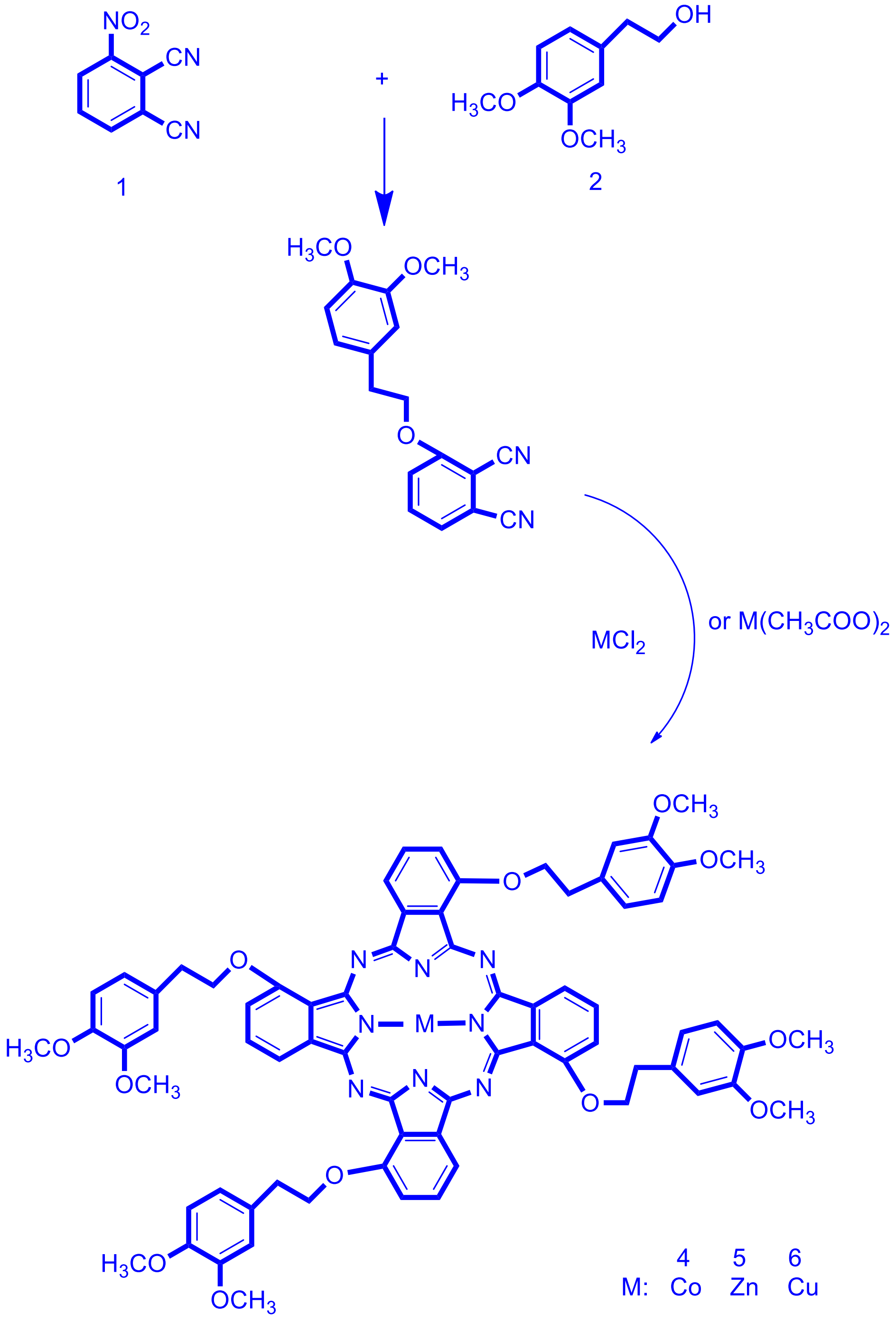

Scheme 1. Representation of compounds prepared for DSSC with formula.

counterparts. The Q bands of non-peripheral substituted Zn (II) and Cu (II) phthalocyanines shifted to about 22 and 30 nm red, respectively, relative to their respective peripheral substituted analogs.[20] The substitution group which is non-peripherally bound to phthalocyanines is more affected as it is closer to the phthalocyanine ring conjugation. As a result, it more incapacitates HOMO orbitals and cause bathochromic shifts.[23] The changes in absorbance versus the varying concentration of complex **5** compound is given in Figure 1.

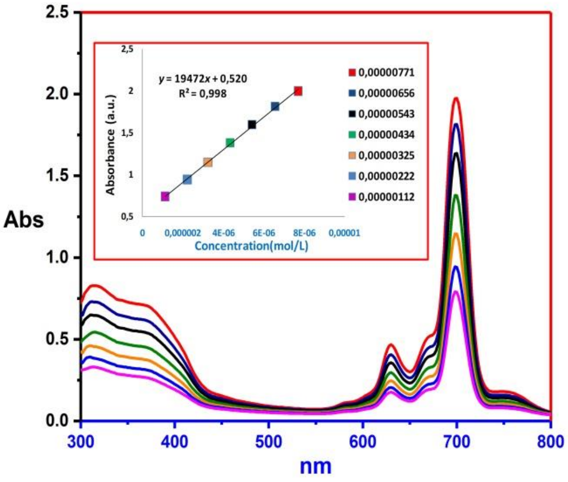

Figure 1. The change of absorption of compound **5** against concentration.

The fluorescence emission, absorption and excitation spectra of zinc phthalocyanine were recorded in THF at 1x10^{-5} M and the spectra obtained were given in Figure 2. In this study, the emission and extinction measurements and stokes shift value of diamagnetic zinc phthalocyanine compound were determined. The difference between emission (704 nm) and extinction (698) is given by the Stokes shift value. The stokes shift value of this compound was found to be 6 nm. This value is close to the values in the literature.[24]

The synthesized phthalocyanine compounds are soluble in polar organic solvents such as acetone, dichloromethane, $CHCl_3$, THF, DMF, DMSO. Resolution is required for many application areas. The absorption spectra of compound (**5**) in different solvents are given in Figures 3. The choice of solvent for photodynamic therapy and the determination of fluorescence efficacy have become necessary for applications. In addition to the best possible singlet oxygen production, some parameters such as solubility, low dark toxicity, strong absorption in phototherapeutic window should be considered when a photosensitizer is designed for biomedical applications.[25]

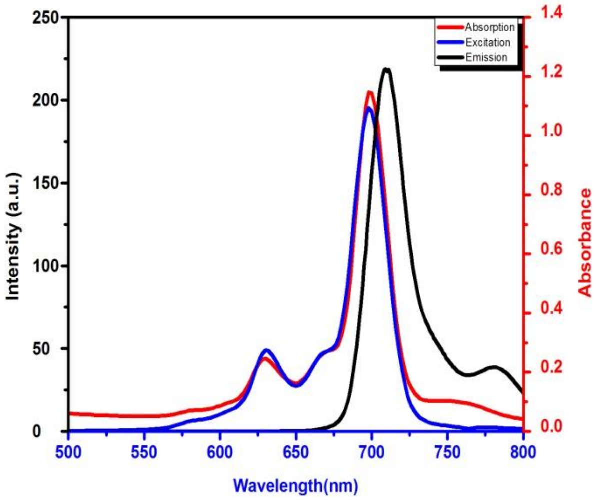

Figure 2. Emission, excitation, and absorption spectra of zinc phthalocyanine.

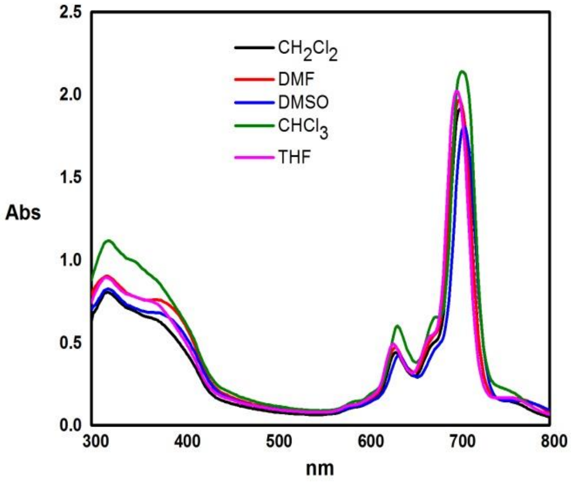

Figure 3. Absorption of complex **5** in different solvents.

Thermogravimetric (TG) analyses of 3-(3,4-dimethoxyphenethoxy) phthalonitrile **3** and phthalocyanine complexes **4-6** were carried out in air and nitrogen atmosphere. After initial loss of moisture, the substance is decomposed in a single step at a temperature ranges of 250°C and 370°C, and the loss of weight at major decomposition temperature was 91% for compound **3** (Figure 4). The thermal decomposition of zinc phthalocyanine **4** in nitrogen atmosphere was observed to be at temperature ranges of 220°C and 800°C, and the loss of weight at major decomposition temperature was 61%. At the same conditions, the weight losses of the compounds **5** and **6** were estimated

DOI: http://dx.doi.org/10.32571/ijct.687373 **E-ISSN:2602-277X**

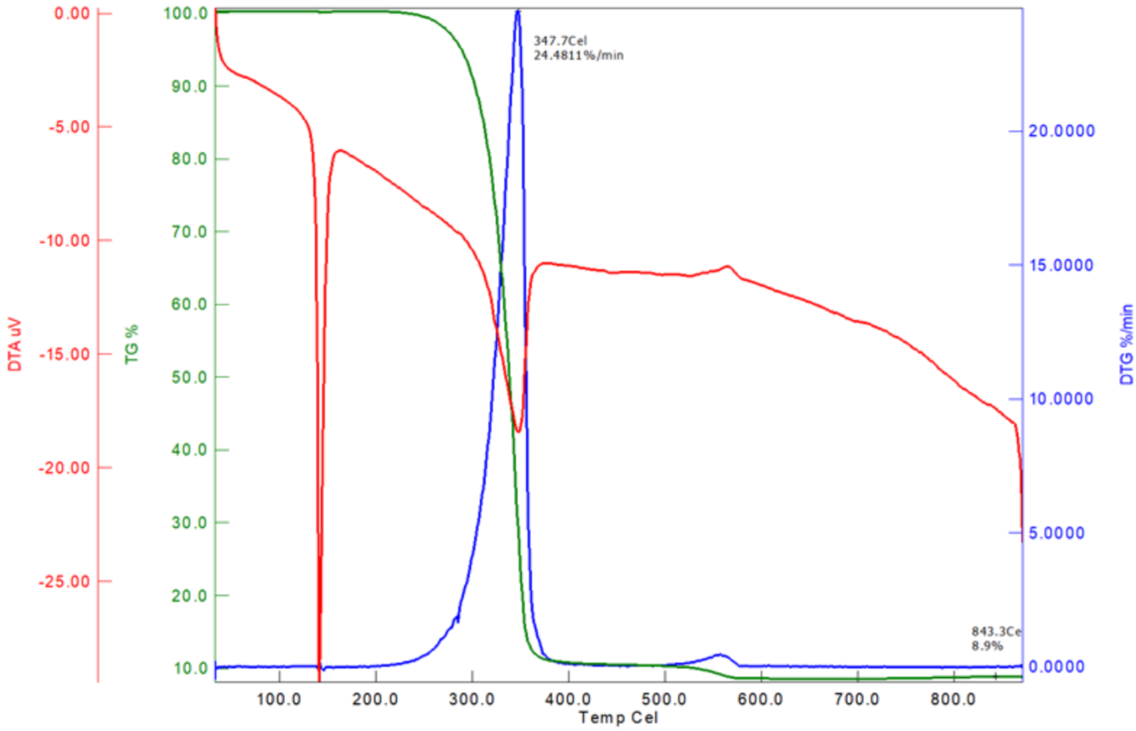

Figure 4. TG/DTG curves of compound **3**.

to be 54% and 53%, respectively. When 3-(3,4-dimethoxyphenethoxy)phthalonitrile is organic, it is decomposed 90% at low temperature while phthalocyanine compounds give lower weight loss at higher temperatures. This provides an adequate contribution to the literature.[26] The results of TG and DTA show that the compounds of phthalocyanine are thermochemically stable.

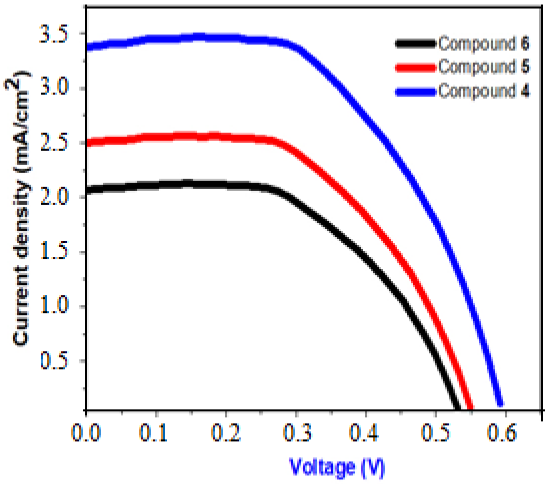

Figure 5. J-V curves of DSSCs based on phthalocyanines complexes (**4-6**).

Figure 5 shows current density–voltage (J–V) characteristics of devices based on the three metal complexes (**4-6**). The corresponding open-circuit voltage (V_{oc}), short-circuit current density (J_{sc}), fill factor (FF) and power conversion efficiency (PCE) for different three samples are listed in Table 1. It can be seen that all V_{oc}, J_{sc}, FF, and PCE arel increased from compound **6** to compound **4**. The J_{sc} based on compound **4** reached 3.38 mA/cm^2, which is nearly 1.6 times of that of the device based on compound **6** (2.07 mA/cm^2); the power conversion efficiency (PCE) based on compound **4** reached 1.15%, which is more than two times of that of the device based on compound **6** (0.56%). The lower J_{sc} of compounds **5** and **6** might be ascribed to the poor charge separation and transportation.

Table 1. The photovoltaic parameters for DSSCs.

Samples	**J_{SC} (mA/cm^2)**	**V_{OC} (V)**	**FF**	**PCE (%)**
Compound **6**	2.07	0.53	0.51	0.56
Compound **5**	2.50	0.55	0.55	0.76
Compound **4**	3.38	0.59	0.58	1.16

DOI: http://dx.doi.org/10.32571/ijct.687373 **E-ISSN:2602-277X**

It suggests that the compound **4** could make better electric contact than the complexes of compounds **5** and compound **6**. Poor adsorption to the TiO_2 surface and recombination losses due to short alkyl in the thiophene ring are two main factors limiting the effectiveness of DSSCs. More works are being researched to optimize device performance. Phthalocyanines are able to overcome the disadvantages of porphyrins with their remarkable light gathering capabilities and thermal stability in the distant and near IR spectral region and show themselves among the dyes accepted in photovoltaic technologies. In particular, Phthalocyanines have an effective role in improving the technology of dye-sensitized solar cells (DSSCs). Therefore they are good candidates for inclusion in such trial programs.[27] Phthalocyanine compounds synthesized in this study show that they are soluble in many different solvents, can be prepared easily and can be used in different applications with their photovoltaic performances. Phthalocyanine compounds are also commercially important with high thermal stability in dye chemistry. Recently, DSSCs have been receiving intense interest as a solution to increasing energy demands. Phthalocyanine dyes are promising for DSSCs.[27] The power conversion effects offer the option of being interchangeable depending on the bound substituent group. Among the renewable energy sources, solar energy is the cleanest and greenest. Investigations for this purpose focus on phthalocyanine compounds with p-type organic semiconductor for DSSCs. The Photovoltaic conversion effect can be significantly enhanced by both composite material and varying substituents.[28] The advantages of metal phthalocyanines are not limited to the rich metal variety, the conjugated system, the organic solar cell, the organic semiconductor material for hybrid solar cells, but also the potential of electronic and optical device application as xerographic application.[29]

4. CONCLUSIONS

The major advantage of these compounds is that they are soluble in organic solvents and non-aggregation in the concentration range studied. Zinc phthalocyanine compound shows fluorescence property. This property indicates that the compounds can potentially be used in medical applications such as PDT. The studied phthalocyanines have thermal stability. Photovoltaic measurement results show that cobalt, zinc and copper phthalocyanine compounds can potentially be used in dye-sensitive solar cell (DSSC) technology. The measurements show that compound **4** provide the best electrical contact.

ACKNOWLEDGEMENTS

We thanks to Van YYU Office of Scientific Research Projects (Project number: FDK-2019-8105).

Conflict of interests

Authors declare that there is no a conflict of interest with any person, institute, company, etc.

REFERENCES

1. Martín-Gomis, L.; Parejo, C.; Álvarez, J. C.; Fernández-Lázaro, F.; Sastre-Santos, Á. *Inorg. Chim. Acta* **2017**, 468, 327-333.

2. Haroun, A.A.; Diab, H.A.; Hakeim, O.A. *Carbohydr. Polym.* **2016,** 146, 102-108.

3. Xiao, Y.; Zhang, M. R.; Li, J. J.; Pan, G.B. *Chem. Phys. Lett.* **2017,** 687, 317-321.

4. Ağırtaş, M. S.; Güven, M. E.; Gümüş, S.; Özdemir, S.; Dündar, A. *Synthetic Met.* **2014,** 195, 177-184.

5. Torabi, N.; Rahnamanic, A.; Amrollahi, H.; Mirjalili, F.; Sadeghzade, M. A.; Behjat, A. *Org. Electron.* **2017**, 48, 211-216.

6. Zhao, P.; Wang, Z.; Chen, J.; Zhou, Y.; Zhang, F.; *Opt. Mater.* **2017**, 66, 98-105.

7. Huang, W.; Ahlfield, J. M.; Kohl, P. A.; Zhang, X. *Electrochim. Acta.* **2017**,257, 224-232.

8. Klyamera, D. D.; Sukhikha, A. S.; Krasnov, P. O.; Gromilov, S. A.; Morozova, N. B.; Basova, T. V. *Appl. Surf. Sci.* **2016**, 372, 79-86.

9. Fujishiro, R.; Sonoyama, H.; Ide, Y.; Fujimura, T.; Sasai, R.; Nagai, A.; Mori, S.; Kaufman, N. E.M.; Zhou, Z.; Vicente, M. G. H.; Ikeue, T. *J. Inorg. Biochem.* **2019**, 192, 7-16.

10. Yang, H.; Pan, S.; Ma, D.; He, D.; Wang, Y.; Xie, S.; Peng, Y. *J. Lumin.* **2016**, 179, 588-594.

11. Ağırtaş, M. S.; Karatas, C.; Gümüş, S.; Okumuş, V. *Z. Anorg. Allg. Chem*. **2015**, 641, 442-447.

12. Ağırtaş, M. S. *Dyes Pigments* **2008**, 79, 247-251.

13. Sodeifian, G.; Ardestani, N.S.; Sajadian, S. A. *Fluid Phase Equilibr.* **2019**, 494, 61-73.

14. Fukuda, T.; Ishikawa, N. *Dyes Pigments* **2014**, 109, 151-154.

15. Vittal, R.; Ho, K.C. *Renew. Sust. Energ. Rev*. **2017**, 70, 920-935.

16. Güngördü Solğun, D.; Horoz, S.; Ağırtas, M. S. *Inorg. Nano-Metal Chem*. **2019**, 48 (10), 508-514.

DOI: http://dx.doi.org/10.32571/ijct.687373 E-ISSN:2602-277X

17. Huang, H.; Cao, Z.; Li, X.; Zhang, L.; Liu, X.; Zhao, H.; Tan, S. *Synthetic Met.* **2012**, 162, 2316-2321.

18. Osifeko, O.; Nyokong, T. *Dyes Pigments* **2016**, 131, 186-200.

19. Armarego, W. L. F.; Chai, C. L. L. Purification of laboratory chemicals, 7nd ed., Butterwordh Heinemann, Oxford, 2013.

20. Ağırtaş, M. S.; Güngördü Solğun, D.; Özdemir, S.; İzgi, M. S. *Chem. Select* **2018**, 3, 3523-3528.

21. Güzel, E.; Günsel, A.; Tüzün, B.; Yaşa Atmaca, G.; Bilgiçli, A.T.; Erdoğmus, A.; Yarasir, M.N. *Polyhedron* **2019**, 158, 316-324.

22. Yanik, H.; Aydin, D.; Durmuş, M.; Ahsen, V. *J. Photochem. Photobiol. A.* **2009**, 206 (1), 18-26.

23. Erdoğmuş, A.; Durmuş, M.; Uğur, A. L.; Avciata, O.; Avciata, U.; Nyokong, T. *Synthetic Met.* **2010**, 160, 1868-1876.

24. Cabir, B.; Yildiko, U.; Agirtas, M. S. *J. Coord. Chem*. **2019**, 72 (17), 2997-3011.

25. Gui, L.; Zhang, Q.; Wang, Y.; Fang, K.; Wang, A.; You, X.; Zhou, L.; Zhou, J.; Wei, S. *Inorg. Chem. Commun.* **2017**, 75, 1-4.

26. Ağırtaş, M. S.; Gümüs, İ.; Okumus, V.; Dundar. A. *Z. Anorg. Allg. Chem*. **2012**, 638 (11), 1868-1872.

27. Urbani, M.; Ragoussi, M. E.; Nazeeruddin, M. K.; Torres, T. *Coordin Chem. Rev*. **2019**, 381, 1-64.

28. Sun, Z.; Fang, S.; Li, F.; Xu, L.; Hu, Y.; Ren, J. *J. Photochem. Photobioli. A.* **2013**, 252, 25-30.

29. Suzuki, A.; Okumura, H.; Yamasaki, Y.; Oku, T. *Appl. Surf. Sci*. **2019**, 488, 586-592.

ORCID

ID https://orcid.org/0000-0001-9492-5669 (D. Güngördü Solğun)

ID https://orcid.org/0000-0003-1296-2066 (M. S. Ağırtaş)

ID https://orcid.org/0000-0002-3238-8789 (S. Horoz)

DOI: http://dx.doi.org/10.32571/ijct.679553 **E-ISSN:2602-277X**

International Journal of Chemistry and Technology

http://dergipark.org.tr/ijct

Research Article

The synthesizing of different hydrogel nanocarriers for oral ınsulin delivery

Pelin PEKER, Burcu OKUTUCU*

ID on the last page

Biochemistry Department, Faculty of Science, Ege University, 35100-Bornova, Izmir, Turkey

Received: 24 January 2020; Revised: 11 March 2020; Accepted: 13 March 2020

***Corresponding author e-mail: burcu.okutucu@ege.edu.tr

Citation: Peker, P.; Okutucu, B. *Int. J. Chem. Technol.* **2020**, 4 (1), 16-21.

ABSTRACT

Diabetes is seen as the global health problem of the world due to the high risk of complications and the increasing prevalence of death. The routine diagnosis of diabetes is the injection of insulin. This treatment has a lot of side effects known to the patient (infection at injection sites, irritation, etc.). In order to overcome such conditions in the treatment of diabetes and provide faster recovery, many different delivery systems for insulin are being studied. Hydrogels are interesting polymers with hydrophobic structure that can be designed in 3D networks for oral insulin delivery. In this study, we studied the synthesis of biodegradable, biocompatible, low-toxicity therapeutic hydrogels. Acrylamide (ACR):carboxymethyl cellulose (CMC) (ACR/CMC), Acrylamide (ACR): Chitosan (Chi) and Chitosan:glutaraldehyde hydrogels were prepared. The CMC was used in acrylamide-based hydrogels for both comonomer and biocompatibility. The swelling capacity of hydrogels and the in vitro release of insulin from hydrogels were studied at different pH. Insulin release studies have shown that ACR/CMC hydrogels are a good and new alternative as an oral insulin carrier.

Keywords: Hydrogel, insulin, delivery systems, diabetes, acrylamide.

Oral insulin taşınımı için farklı hidrojel nanotaşıyıcıların sentezlenmesi

ÖZ

Diyabet, yüksek komplikasyon riski ve buna bağlı olarak artan ölüm prevalansından dolayı dünyanın global sağlık problemi olarak görülmektedir. Diyabetin rutin tedavisi insulin enjeksiyonudur. Bu tedavinin hasta da bilinen oldukça fazla yan etkisi mevcuttur (enjeksiyon bölgesinde enfeksiyon, iritasyon, vb.). Diyabetin tedavisindeki bu tip durumları bertaraf etmek ve daha hızlı iyileşme sağlamak için, insülinin birçok farklı taşınım sistemleri çalışılmaktadır. Hidrojeller, oral insülin taşınımı için 3D ağlarda tasarlanabilen hidrofobik yapılı ilgi çeken polimerlerdir. Bu çalışmada biz, biyo parçalanır, biyo uyumlu, düşük toksiteli teropötik hidrojellerin sentezini çalıştık. Akrilamid (ACR): karboksimetil selüloz (CMC) (ACR/CMC), Akrilamid (ACR): Kitosan (Chi) ve Kitosan:glutaraldehid hidrojelleri hazırlandı. CMC hem komonomer hem de biyouyumluluk için akrilamid tabanlı hidrojellerde kullanıldı. Hidrojellerin şişme kapasitesi ve hidrojellerden İnsulinin in vitro salınımı farklı pH'larda çalışıldı. İnsulin salınım çalışmaları, ACR/ CMC hidrojellerinin oral insülin taşıyıcı olarak iyi ve yeni bir alternatif olduğunu göstermiştir.

Anahtar Kelimeler: Hidrojel, insulin, taşınım sistemleri, diyabet, akrilamid.

1. INTRODUCTION

Diabetes is the most important health problem all over the world. The classification of diabetes is complex but there are three main types of diabetes; type I diabetes (T1DM), type II diabetes (T2DM) and gestational diabetes. The most diabetes patients have commonly Type II diabetes, and they include nearly 90% of diabetic persons. T2DM is a complex disease associated with pancreatic β- cell dysfunction and varying degrees of insulin resistance. Moreover, the control of insulin level and traditional treatments are unsatisfactory. Because macro (stroke, cardiovascular disease, coronary artery disease, cerebrovascular disease, diabetic foot)

DOI: http://dx.doi.org/10.32571/ijct.679553 **E-ISSN:2602-277X**

and micro (retionapathy, cataract, nephropathy, neuropathy) vascular complications of T2DM patients can vary from person to person and may reduce the qualities of the lifes of the patients and their families. The common anti-diabetic drugs are metformin, sulfonylureas, glinides, α-glucosidase inhibitors, GLP-1 agonists, thiazolidinediones, DDP-4 inhibitors and insulin. To control blood glucose level, exogenous insulin must be taken by who are suffering insulin deficiency. Insulin is a polypeptide hormone that consists of 51 amino acids in two chains (A chain, 21 amino acids; B chain, 30 amino acid), joined together by two disulfide bonds that helps in regulating the uptake and storage of glucose in the liver and muscles. It is produced by ß-cells of pancreas and released into the blood via exocytosis process. There are three major sources of insulin preparations based on different diagnosis strategies; rapid-acting insulin (to manage meal time blood glucose), long-acting (to manage daily basal insulin needs) and pre-mixed insulin. A standard treatment of T2DM patients who are suffering with insulin deficiency is repeated subcutaneous injections of insulin. Multiple insulin injections cause bad shortcomings; local skin irritation, fat deposits at injection points, stress, so on. All of these disadvantages lead that the researchers research new alternative routes for delivery of insulin and other peptide drugs. Oral, pulmonary and nasal delivery of insulin are other alternative routes. The most promising challenge is oral delivery of insülin.[1-3] The problems of oral delivery insulin systems are the physical instability of insulin at different conditions (acidic pH, elevated temperature, solvent, buffer media), the enzymatic degradation at gastrointestinal track (the protein structure of insulin) and rapid systemic clearance (concentration). Many techniques have been developed to overcome these problems. To overcome the mentioned problems above, some modifications can be done. Just like that, to overcome digestive destruction, the surface of nano carriers are biotinylated or PEGylated. For the solution of transformation and enhancing adsorption, cell-penetrating peptides, muco- adhensive polymeric systems, oral micro particle delivery systems are used. And the last way is to use the natural and synthetic polymers (liposomes, inorganic particles, nano-emulsions and hydrogels).[4] Natural polymers are studied more than others because they exhibit higher biocompatibility, biodegradability, safety, low toxicity and better physiological stability.[5-7] The known disadvantages of nanocarrier systems are their particle size, coating, modification, inherent characteristics of nanoparticles, and the biological degradation. One of the most attractive polymers for oral delivery systems is hydrogels. Hydrogels are considered as super absorbent because they are able to absorb large quantities of water or the mixed environmental solvents. 2D and 3D compositions of hydrogels change with the composition of polymerization mixture (cross linker, monomers, comonomers, solvent). An injectable hydrogel can undergo sol-gel transformation in the body and be utilized for the controlled release of therapeutics, thus reducing the dosing frequency and side effects.[8-16]

The aim of our study is to synthesis promising and improvable different insulin oral delivery nanocarriers. To obtain biocompatible, low toxicity and biodegradable acrylic based hydrogels, it was studied with carboxyl methylcellulose (CMC) and chitosan. To contribute the results, the conventional chitosan insulin nanocarrier is also studied. PH stability, swelling properties (water, buffers) and in vitro insulin release in glucose medium were performed to analyze the ability of nanocarriers to be used as oral insulin delivery. *In vivo* analysis is planned for further experiments.

2. MATERIALS AND METHODS

2.1. Materials

The acrylamide (ACR), N, N- Methylenebisacrylamide (N,N-MBA), chitosan (Chi) (low molecular weight; 75-85% deacetylated) , carboxylmethyl cellulose (CMC) (0.60-0.95 substitution**),** glutaraldehyde, Tetramethylethylenediamine (TEMED), ammonium persulfate (APS) were purchased from Sigma (USA). All the other chemicals were analytical grade.

2.2. Hydrogel synthesis

Different hydrogel compositions and different ratio of ACR/CMC, ACR/Chi and Chi/glutaraldehyde were studied.

2.2.1. Acrylamide based hydrogels

For biodegradability and biocompatibility, CMC was used as comonomer.[17-20] The different ratios of ACR/CMC [1:0.01; 0.1:0.01; 1:0.02] were dissolved in distillated water and mixed with appreciate weight of N, N-MBA (crosslinker) (10 mg). To start radical polymerization, TEMED/APS was added. After 30 min at 37°C, the hydrogel samples were ready to use. All samples were washed in excess water to remove unreacted components. In this study, all of the samples were gelated 100% and no extractable monomers were observed. To change hydrophilic character and the strength of acrylamide-based hydrogels, chitosan is used as comonomer. The toxicity of hydrogels is minimized by using chitosan. The different ratios of ACR/Chi [1.5:0.02; 1:0.02; 0.1:0.02] were dissolved in distillated water and mixed with appreciate weight of N,N-MBA (10 mg) (crosslinker). To start radical polymerization, TEMED/APS was added. After 15 min at 37°C, the hydrogel samples were ready to use. Some gellating problems were occurred since hydrogel synthesis from. While preparing ACR/Chi hydrogels, different amount

DOI: http://dx.doi.org/10.32571/ijct.679553 **E-ISSN:2602-277X**

ACR/Chi. The hydrogels did not gellated completely of N,N-MBA was studied but the best result was obtained for only ACR/Chi (1.5:0.02) and 10 mg N,N-MBA. All samples were washed in excess water to remove unreacted components.

2.2.2.Chitosan based hydrogels

The chitosan hydrogels were crosslinked with glutaraldehyde. The constant amount of chitosan (3%, 0.5 ml) and different ratio of glutaraldehyde [2; 2.5; 5; 7.5; 10] was mixed and polymerized at 40°C for 90 min. After that time the hydrogel samples were ready to use. All samples were washed in excess water to remove unreacted components. In this study, all of the samples were gelated 100% and no extractable monomers were observed.

2.3. Swelling properties

For testing pH dependent of hydrogels, all hydrogel samples were equilibrated in 2 ml 0.1 M buffer solutions [acetate pH 4.5; P_i (phosphate) pH 7- 7.5], 0.1 M HCl and 0.1 M NaOH solutions at 37°C. The time intervals are 5 min - 10 min - 30 min - 1 h - all day. The gravimetric method was used to determine the swelling ratio of hydrogels. The swelling ratio was calculated according to Eq. (1).

$$SR\ \% = [(w_S - w_D) / w_D]*100 \qquad (1)$$

Where w_D and w_S are dry and wet weights of hydrogels, respectively. All experiments were repeated triplicate, and the calculated swelling ratios were the average of these three experiments.

2.4. Insulin loading and release experiments of hydrogels

In this study pre-mixed insulin solution was used (purchased from pharmacy). The pH of this insulin was adjusted pH 7 by adding P_i buffer. Before the insulin loading, the dried acrylamide-based hydrogels (ACR/CMC and ACR/Chi) and Chi/glutaraldehyde hydrogel were pulverized. The dried particles were equilibrated in insulin solution (20 mg 5 ml^{-1}) (which was adjusted to pH 7 with Pi buffer) for 30 min at 37°C. Also, the same procedure was repeated for Chi/glutaraldehyde hydrogel for insulin loading (only the best hydrogel composition).

The hydrogels were washed with water to remove excess insulin. The amount of insulin released was measured spectrophotometrically at a wavelength of 276 nm. All of the insulin loaded hydrogels were stand up 5 mM glucose solution. The glucose solutions were prepared in stimulated gastric fluid (pH 1.2) and intestinal fluid (pH 7.2). The changing of glucose was determined by DNS method. DNS method was done according to Miller.[21] Briefly; an aliquot of the glucose solution (0.5 ml) and 0.5 ml of the DNS reagent was added to the test tube and the mixture was incubated in a boiling water bath for 5 min. After cooling to room temperature, the absorbance of the supernatant was measured at 540 nm.

3. RESULTS AND DISCUSSION

Nowadays, the oral insulin therapeutic hydrogels are very attractive and good alternative for diagnosis of diabetes. 3D crosslinked polymer structures as known hydrogels can be the best alternatives. They absorb large amounts of water that is the most important property for oral delivery therapeutics. It means that the polymer can swell and the therapeutics can be released into fluid. Many factors can affect the structure and their swelling such as charge, concentration, hydrophobic/ hydrophilic balance, cross-link density. One of the examples of the charge effect is acidic solutions of Chi. Acidic solutions of Chi when exposed to alkaline pH result in a decrease of the apparent charge density of the polymer, and thereby in the formation of physical gels due to hydrogen bonding and hydrophobic interactions. To obtain CS-based homogeneous hydrogels or porous materials with chemical stability at pH < 5.5, CS has been cross-linked by glutaraldehyde (GA), epichlorohydrin (ECH), and so on.[19,20] In this study, we aimed to modulate the mechanical properties, the water content of hydrogels, the response to an external stimulus, and also to design chelating performances, composite hydrogels.

3.1. Acrylamide based hydrogels

The different requirements for oral hydrogels for using clinical approach are existed, and these are biocompability/nontoxicity, mechanical properties, viscosity, stability and biodegradability.

As known, if acrylamide is used large amount or alone, it can be cancerogenic. Herein, to overcome this problem, the hydrogels were prepared with biocompatible and semi-natural comonomers (CMC and chitosan). CMC which is derivative of cellulose is widely used in pharmaceutical industry as emulsifier, viscosity modifier and stabilizer to develop different pharmaceutical dosage form. CMC is semi-natural polymer and has excellent water absorbing and swelling capacities. It is physiologically non-toxic and compatible with mucous membrane, bone and skin.[18] The ACR based hydrogels were formed by chemical crosslinking for better mechanical properties and long term stability in different medium conditions. The usage of toxic crosslinkers can be dangerous while preparing hydrogels, but all of the washing solutions and the stability tests show that any excess component is not

DOI: http://dx.doi.org/10.32571/ijct.679553 **E-ISSN:2602-277X**

exist. The swelling test (especially 24 h) results of hydrogels can be seen in Figure 1. These results showed that hydrogel was not dissolved totally and could not accumulated in the body as stated in the papers.[18-20]

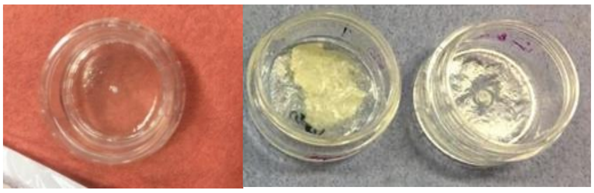

Figure 1. Photos of hydrogels: a) Dried hydrogel, b) Swelled insulin-loaded hydrogels.

CMC is used to prevent postoperative adherences and epidural scarring. CMC is also degraded by cellulolytic enzymes which is found intestinal fluid. There are some different models for *in vivo* analysis. Cell culture models are suitable to study acute, delayed and repeated toxicity. Also, parallel artificial membrane permeability assay (PAMPA) and CaCo-2 cell systems can be studied. While PAMPA is used to evaluate passive permeability, the CaCo-2 cell systems are used to measure passive and active permeability. CaCo-2 cells allow to simultaneously evaluate efficacy and safety of delivery systems, investigating their action mode. We will planning to study cell culture assays of our hydrogels the future, but in this study, our only aim is to make the best promising hydrogel as insulin nanocarrier.

3.2. Chitosan based hydrogels

In most of the oral delivery system, chitosan is used because of its biodegradability, low toxicity, modifying with different chemicals. By this way, many different alternative gels can be prepared effectively.[17,23] The main problem is synthesized chitosan hydrogels which have poor mechanical strength and stability. To overcome this problem, glutaraldehyde is used as crosslinker but it can be accumulated in the body if used excess amount.[18] In our study, the 2.5 (v/v) % glutaraldehyde was chosen.

3.3. pH responsive and swelling characteristics of hydrogels

The pH sensitivity of hydrogels usually depends to acidic and basic groups in the structure. The charge and ionization state of the groups can be changed according to the pH of the medium. As seen in Table 1, ACR/CMC and ACR/Chi hydrogels can be stable at all acidic pHs (HCl pH 1 and acetate buffer pH 4.5). Chi/Glutaraldehyde hydrogels were affected after 10 min in all acidic solutions. As known, chitosan hydrogels swell at acidic pHs and the structure of chitosan hydrogels can be deformed in basic solutions. This may be due to the reactive groups at the surface of chitosan hydrogels. The deprotonation structure on the surface of chitosan increased, ionic interactions in the medium changed and this situation may lead to the decrease of the crosslinking followed by increased swelling.

P_i buffer studies of all hydrogels are very important. These results are the clues of the behavior of hydrogels for insulin delivery system in body fluids. ACR/CMC and Chi/glutaraldehyde hydrogels started to swell after 30 min. This could be a good result and showed that they could be alternative materials for delivery of insulin. However, ACR/Chi hydrogels were very stable and rigid and it is a big problem for releasing of insulin.

Insulin has to be released in small intestine at 0-30 min range. After that time, insulin releasing can be resulted by hypoglycemia. The composition of ACR/CMC hydrogels can change the results. Because, CMC has excellent water adsorption and can swell at different ratios according to medium conditions. The mechanical strength is more than many other biopolymers used in pharmaceutical field. The less amount of CMC can be a problem for swelling.

The swelling characteristics of hydrogels mostly depend on the hydrophilic network. The water or buffer solutions migrate into the network and can change the hydrogel structure. The swelling ratio of ACR/CMC hydrogels was 80 % after 1 h, the reason of these result is due to the carboxyl groups of CMCs ionized at pH 4.5 and above. But these ionic changes did not affect the hydrogels structure too much. ACR/Chi hydrogels swell 400% and this shows that it can be a good alternative only in short time period (0-10 min).

3.4. *In vitro* release study of insulin

The insulin was loaded on all of the hydrogels. ACR/CMC hydrogel (1:0.01) showed best results. The particles were loaded in the range of 45-65%. Insulin molecules tend to polar groups and can make hydrogen bonds. More acidic or carboxyl groups provides more hydrogen bonds at low pH (acetate buffer). The release of insulin is nearly 45%. At pH 1 (HCl solution), the effective pore size of the hydrogel decreased and the insulin entrapped inside hydrogel. At pH 7, ACR/CMC hydrogels released 65% of insülin.[25]

In vitro release of insulin depends on many factors. An initial release of the hydrogels was more than expected. Because some of the insulin molecules could be adsorbed toward the structure of the hydrogel and this caused rapid releasing. At pH 7, 65% of insulin was released from ACR/CMC hydrogels within 30 min and remaining insulin was released up within 1 h. At pH 4.5, most of the carboxylic groups of the hydrogel were ionized so that 60% of insulin released within 10 min and remaining insulin released up within 30 min. The reason may be that the swelling rate of the hydrogel at pH 4.5 is more than pH 7. These results show that the ACR/CMC hydrogel structure, reactive groups of the hydrogel and swelling properties are pH sensitive.

ACR/Chi and Chi/ glutaraldehyde hydrogels released 85% of insulin within 5-10 min and released the remaining within 30 min. The reason of this rapid releasing can be the amount of insulin which is too high for these hydrogels (the pore structure can be small) and there is not also ionized groups for hydrogen bonding with insülin.[26]

Table 1. The swelling behavior of hydrogels in buffer and solutions (NaOH, HCl)

Hydrogel	Buffer/ Solution (0.1M)	5 min.	10 min.	30 min.	1 h.	24 h
ACR/ CMC	Acetate (pH 4.5)	+++	+++	+++	+++	++
	P_i (pH 7)	+++	+++	+++	+++	+++
	P_i (pH 7.5)	+++	+++	++	++	++
	NaOH	+++	+++	+++	++	++
	HCl	+++	+++	+++	++	++
ACR/ Chi	Acetate (pH 4.5)	+++	++	++	-	-
	P_i (pH 7)	+++	++	++	-	-
	P_i (pH 7.5)	+++	++	++	-	-
	NaOH	+++	++	++	-	-
	HCl	+++	+++	++	-	-
Chi/glutaraldehyde	Acetate (pH 4.5)	+++	++	++	+	+
	P_i (pH 7)	+++	++	++	+	+
	P_i (pH 7.5)	+++	++	++	+	+
	NaOH	+++	++	++	+	--
	HCl	+++	++	++	--	--

+++ : stabile, ++ : partially swelled, + : swelled, - : not gellated

As a result, it can be said that the ACR/CMC hydrogels can be good, low toxicity, biocompatible alternative for insulin deliver

4. CONCLUSIONS

The ACR/CMC and ACR/Chi hydrogels were synthesized by free radical polymerization. This may leads to the mechanical strengths of these hydrogels. ACR/CMC, ACR/Chi and Chi/glutaraldehyde hydrogels showed pH sensitivite properties. The pH behavior and the insulin releasing results showed that ACR/CMC hydrogels could be used in biomedical approaches especially biomolecule delivery systems. In our study, the hydrogel was prepared with CMC as a comonomer and also for biocompability. This is the first time for therapeutic hydrogel preparing with ACR/CMC. The results of insulin releasing showed that ACR/CMC hydrogels could be a good and new alternative for delivery at small intestine. This study is a preliminary work for the therapeutic hydrogels with ACR/CMC for biomolecule delivery.

ACKNOWLEDGEMENTS

This study was financially supported by Ege University Scientific Research Foundation (Project No: 17 FEN 008).

Conflict of interests

Authors declare that there is no a conflict of interest with any person, institute, company, etc.

REFERENCES

1. Hu, C.; Weiping, J. *Adv. Drug Deliver Rev*. **2019**, 139, 3-15.

2. Khursheed, R.; Singh, K. S.; Wadhwa, S.; Kapoor, B.; Gulati, M.; Kumar, R.; Ramanunny, A. K.; Awasthi, A.; Dua, K. *Eur. J. Pharmacol*. **2019**, 862, 172625-172662.

3. Tan, S. Y.; Wong, J. L. M.; Sim, Y. J.; Wong, S. S.; Elhassan, S. A. M.; Tan, S. H.; Lim, G. P. L.; Tay, N. W. R.; Annan, N. C.; Bhattamisra, S. K.; Candasamy, M. *Diabetes Metab. Syndr*. **2019,** 13, 364-372.

4. Vega-Villa, K. R.; Takemoto, J. K.; Yáñez, J. A.; Remsberg, C. M.; Forrest, M. L.; Davies Neal, M. *Adv. Drug Deliver Rev*. **2008**, 60, 929-938.

5. Ciappellano, S. G.; Tedesco, E.; Venturini, M.; Benetti F. *Adv. Drug Deliver Rev*. **2016**, 106, 381-401

6. Chaturvedi, K.; Ganguly, K.; Nadagouda, M. N.; Aminabhavi, T.M. *J. Control. Release* **2013,** 165, 129-138.

7. Nur, M.; Vasiljevic, T**.** *Int. J. Biol. Macromol*. **2017**, 103, 889-901.

8**.** Kumar, A.; Lahiri, S. S.; Singh, H. *Int. J. Pharmacol*. **2006**, 323, 117-124.

9. Taleb, M. F. A. *Int. J. Biol. Macromol*. **2013,** 62, 341-347.

10. Wonga, C. Y.; Al-Salamia, H.; Dassa C.R. *Int. J. Pharmacol.* **2018**, 537**,** 223-244.

11. Pande, P. P. *IJMS*. **2017**, 12, 11-14.

12. Mahinroosta, M.; Farsangi, Z. J.; Allahverdi, A.; Shakoori, Z. *Mater. Today Chem*. **2018**, 8, 42-55.

13. Kabiri, K.; Zohuriaan-Mehr, M. J. *Iran. Polym. J.* **2008**, 17, 451-477.

14. Li, X.; Fu, M.; Wu, J.; Zhang, C.; Deng, X.; Dhinakar, A.; Huang, W.; Qian, H.; Ge, L. *Acta Biomater*. **2017**, 51, 294-303.

15. Li, Y.; Huang, G.; Zhang, X.; Li, B.; Chen, Y.; Lu, T.; Lu, T. J.; Xu, F. *Adv. Funct. Mater*. **2012**, 23, 660-672.

16. Zhao, W.; Jin, X.; Cong, Y.; Liu, Y.; Fu, J. *J. Chem. Technol. Biot*. **2013**, 88, 327-339.

17. Sharpe, L. A.; Daily, A. M.; Horava, S. D.; Peppas, N. A. *Expert. Opin. Drug Del.* **2014,** 11, 901-915.

18. Basu, P.; Narendrakumar, U.; Arunachalam, R.; Devi, S.; Manjubala, I. *ACS Omega*. **2018,** 3 (10), 12622-12632.

19. Barbucci, R.; Magnani, A.; Consumi, M. *Macromolecules* **2000,** 33, 7475-7480

20. Ng, S. F.; Jumaat, N. *Eur. J. Pharm Sci*. **2014,** 51, 173-179.

21. Miller, G. L. *Anal. Chem.* **1959,** 31, 426-428.

22. Nizam, El-Din, H.M.; Abd Alla, S. G.; El-Naggar, A. W .M. *Radiat. Phys. Chem*. **2010,** 79, 725-730.

23. Varaprasad, K.; Narayana Reddy, N.; Mithil Kumar, N.; Vimala, K.; Ravindra, S.; Mohana Raju, K. *Int. J. Polym. Mater. Po*. **2010,** 59 (12), 981-993.

24. Mirzaei, E. B.; Ramazani, S. A. A.; Shafiee, M.; Danaei, M. *Int. J. Polym. Mater. Po*. **2013**, 62, 605-611.

25. Nur Raihan, M.; Nadras, O.; Zulkifl, A.; Fauzi, R. *Adv. Mater. Res*. **2013,** 812, 20-29.

26. Chavda, H. V.; Patel, C. N. *Int. J. Pharm. Investig*. **2011**, 1 (1), 17-21.

ORCID

ID https://orcid.org/0000-0002-1064-8789 (P. Peker)

ID https://orcid.org/0000-0002-0907-4175 (B. Ökutucu)

DOI: http://dx.doi.org/10.32571/ijct.697728 **E-ISSN:2602-277X**

International Journal of Chemistry and Technology

http://dergipark.org.tr/ijct

Research Article

A numerical study of mixed convection heat transfer in a lid-driven cavity using Al_2O_3-water nanofluid

Neşe KEKLİKCİOĞLU ÇAKMAK[1,*], Hasan H. DURMAZUÇAR[1], Kerim YAPICI[2]

on the last page

[1]*Department of Chemical Engineering, Faculty of Engineering, Sivas Cumhuriyet University, Sivas, Turkey,*

[2]*Department of Chemical Engineering, Faculty of Engineering, Süleyman Demirel University, Isparta, Turkey*

Received: 03 March 2020; Revised: 15 March 2020; Accepted: 16 March 2020

*****Corresponding author e-mail: nkeklikcioglu@cumhuriyet.edu.tr

Citation: Keklikcioglu Cakmak, N.; Durmazuçar, H. H.; Yapıcı, K. *Int. J. Chem. Technol.* **2020**, 4 (1), 22-37.

ABSTRACT

This study aims a numerical investigation of steady, laminar mixed convection heat transfer in a two-dimensional cavity by employing a finite volume method with a fourth-order approximation of convective terms, when nanoparticles are present. With the aim of solving two-dimensional momentum and energy conservation equations, a finite volume method on a non-uniform staggered grid is utilized. Second-order central differences are utilized to approximate diffusion terms in momentum and energy equations, while the development of a non-uniform four-point fourth-order interpolation (FPFOI) scheme is performed for the convective terms. Continuity and momentum equations are solved using the SIMPLE (Semi-Implicit Method for Pressure-Linked Equation) algorithm. In order to evaluate heat transfer enhancement, various viscosity and thermal conductivity models were employed. Numerical solution results were obtained in different models in cases where Gr number is between 10^3 and 10^5, Re number is 10-100-1000 and nanoparticle volumetric fraction is 0-5%.

Keywords: Nanofluid, finite volume method, fourth-order linear scheme, lid-driven cavity, mixed convection.

Al_2O_3-su nanoakışkan kullanılarak kapak tahrikli düzgün dörtgen boşluk içerisinde karışık konveksiyon ısı aktarımın sayısal olarak incelenmesi

ÖZ

Bu çalışma nanoparçacıklar varlığında konvektif terimlerin dördüncü dereceden doğruluğa sahip sonlu hacimler yöntemi kullanılarak iki boyutlu sistemlerde yatışkın, laminer karışık konveksiyon ısı aktarımının sayısal olarak incelenmesini amaçlamaktadır. İki-boyutlu momentum ve enerji tasarrufu eşitliklerini çözme amacı ile düzgün dağılımlı olmayan yapısal kaydırılmış ızgara yapısında sonlu hacimler yöntemi kullanılmıştır. Konvektif terimler için düzgün dağılımlı olmayan ağ yapılarında dördüncü dereceden doğruluğa sahip (FPFOI) şemanın geliştirilmesi gerçekleştirilirken ikinci dereceden merkezi farklar, momentum ve enerji eşitlikleri içerisindeki yaklaşık difüzyon terimleri için kullanılmıştır. Süreklilik ve momentum denklemleri basit (Basınca Bağlı denklem için yarı örtük yöntem) algoritma kullanılarak çözülmüştür. Isı aktarım artışını değerlendirmek için çeşitli viskozite ve ısıl iletkenlik modelleri kullanılmıştır. Gr sayısı 10^3 ve 10^5 aralığında, Re sayısı 10-100-1000 ve nanoparçacık hacimsel fraksiyonu % 0-5 olduğu durumlarda farklı modellerde sayısal çözüm sonuçları elde edilmiştir.

Anahtar Kelimeler: Nanoakışkan, sonlu hacimler yöntemi, dördüncü dereceden doğrusal şema, kapak tahrikli düzgün dörtgen boşluk, karışık konveksiyon.

1. INTRODUCTION

Because of the quick advancements experienced in computer technology and computational sciences, computational fluid dynamics (CFD) has turned into a significant instrument in industrial and scientific research activities. It is possible to indicate the comparatively significant costs and considerable

DOI: http://dx.doi.org/10.32571/ijct.697728 **E-ISSN:2602-277X**

time requirements of experimental research and occasionally unpractical conditions of experiments among the primary causes promoting numerical CFD research. Natural and mixed convection heat transfer is involved in various engineering applications, including the cooling of electronic devices, solar collectors, building insulation, etc. Since there are numerous applications of natural and mixed convection heat transfer in engineering, there is a lot of numerical and experimental research on the mentioned transport processes in the scientific literature.[1] Tiwari and Das[2] published the first research on the mixed convection of nanofluids in enclosures. The researchers conducted the numerical investigation of the heat transfer improvement in a two-sided lid-driven square cavity utilizing nanofluids. They employed a finite volume approach by utilizing the SIMPLE (Semi-Implicit Method for Pressure-Linked Equation) algorithm. They presented a summary of a number of significant observations in the following way. The average Nusselt number changes nonlinearly with the solid volume fraction, nanoparticles can alter the fluid's flow pattern from natural convection to the forced convection regime, and the highest Nusselt number improvement is approximately 100%. Talebi and co-workers[3] investigated the mixed convection of nanofluids in a laminar flow with the volume fraction of $\varphi = 0 - 0.05$ in an enclosure. The Patel and Brinkman models have been employed for the estimation of the thermal conductivity and effective dynamic viscosity of nanofluids, respectively. It has been understood that enhancement will occur in the flow function with the increased Reynolds number at every nanoparticle concentration, particularly at higher Rayleigh numbers. Furthermore, it has been determined that a decrease occurs in the impact of nanoparticle concentration with the increased Reynolds number, particularly at lower Rayleigh numbers.

Arefmanesh and Mahmoodi[4] examined the impact of non-effective dynamic viscosity with nanoparticle volume fractions of $\varphi = 0; 0:1; 0:06; 0:03$ in laminar flow mixed convection and heat transfer in a square enclosure. The finite volume method and SIMPLE algorithm have been employed for the numerical solution of the governing equations, and two various models suggested by Brinkman[5] and Maiga and co-workers[6] have been utilized for nanofluid effective dynamic viscosity. Forced convection in an enclosure has been acquired as a result of moving the enclosure's lower wall, whereas natural convection has been occurred in case of a higher temperature of the enclosure's lower wall in comparison with its other walls. There is a strong dependence of the uncertainty impacts in the viscosity formula for water-Al_2O_3 nanofluid on the Richardson number and nanoparticle volume fraction. Chamkha and co-workers[7] have carried out the numerical investigation of the impacts of partial slip on the generation of entropy magnetohydrodynamics (MHD) combined convection in a square lid-driven porous enclosure that was saturated with Cu–water nanofluids. The result they have obtained demonstrates that an augmentation in the heat generation/absorption parameter causes a decrease in the Nusselt number. Moreover, with the increased volume fraction, a decrease in the Nusselt number and entropy generation takes place. In a recent numerical study carried out by Kapil and co-workers[8] has been investigated mixed convection heat transfer of the Al_2O_3 - water nanofluid in a lid driven cavity with heated square obstacle at the center. They have used the upwind scheme to solve the set of equations. Three different *Re* (1, 10 and 100) numbers in the fixed Gr (10^4) number has also been studied, and in addition to the these, it has been not specified taht what correlation equation of Al_2O_3-water nanofluid viscosity has been modeled. They have concluded that while Nusselt number increases with increasing *Re* numbers, it decreases at low *Re* numbers. The current study primarily aims to examine the mixed convection heat transfer in a lid-driven cavity using nanofluids. Al_2O_3-water nanofluids and three variable viscosity and thermal conductivity models have been utilized for the purpose of investigating the impact of nanoparticles on the mixed convection flow and temperature fields, and comprehensive research has been conducted on the used model of the nanofluid together with other parameters that determines the flow pattern. In our study, to approximate the diffusion terms in the governing equations, the second-order central differencing scheme is used. The non-uniform form of the four-point fourth-order interpolation (FPFOI) scheme is used to approximate the convective terms. In this respect, our study is different from the studies mentioned above, and no similar studies has been found in the literature in terms of different Re and Gr number, viscosity and thermal conductivity models and equations used.

2. PROBLEM STATEMENT AND MATHEMATICAL FORMULATION

Figure 1 presents the mentioned physical models, along with the corresponding boundary conditions and geometric dimensions. This figure clearly demonstrates the boundary conditions used for velocity and temperature and the flow geometry, in which the upper wall moves at a certain constant velocity, the other walls are motionless, the lower wall is heated, the upper wall is cooled, and the other walls are insulated. In this study, the results with fourth-order accuracy are given at different Grashof (*Gr*) and Reynolds (*Re*) numbers. The thermophysical parameters of Al_2O_3 nanoparticles and water are given in Table 1.[9, 10.]

DOI: http://dx.doi.org/10.32571/ijct.697728 **E-ISSN:2602-277X**

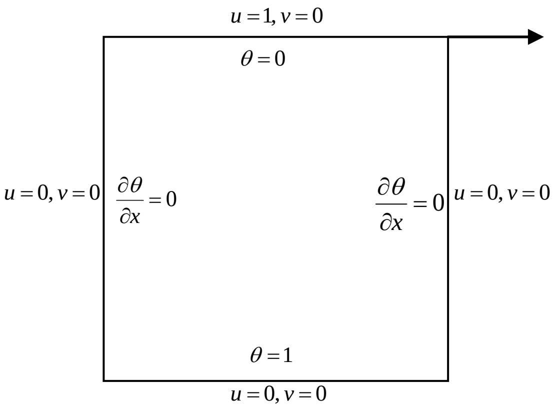

Figure 1. Both natural and forced convection heat transfer flow geometry and dimensionless velocity and temperature boundary conditions.

Table 1. Thermophysical parameters of Al_2O_3 nanoparticles and water

	ρ (kg m^{-3})	**C_p (Jkg^{1}K^{-1})**	**k (W m^{-1}K^{-1})**	**μ (kgm^{-1}s^{-1})**	**β (K^{-1})**
Al_2O_3	3970	765	40	-	0.85×10^{-5}
Water	997-1	4170	0.613	0.001	21×10^{-5}

Furthermore, the solution of natural and mixed convection problems is performed with Al_2O_3-water nanofluid as a working fluid. In order to solve the Al_2O_3-water nanofluid, the homogeneous single-phase approach is accepted, and thus, the Al_2O_3-water nanofluid takes the place of the physical characteristics of the Newtonian fluid mentioned above.

$$\frac{\partial u}{\partial x}+\frac{\partial v}{\partial y}=0 \tag{1}$$

$$u\frac{\partial u}{\partial x}+v\frac{\partial v}{\partial y}=-\frac{1}{\rho_{nf}}\frac{\partial p}{\partial x}+\nu_{nf}\left(\frac{\partial^2 u}{\partial x^2}+\frac{\partial^2 u}{\partial y^2}\right) \tag{2}$$

$$u\frac{\partial v}{\partial x}+v\frac{\partial v}{\partial y}=-\frac{1}{\rho_{nf}}\frac{\partial p}{\partial y}+\nu_{nf}\left(\frac{\partial^2 v}{\partial x^2}+\frac{\partial^2 v}{\partial y^2}\right)+g\beta_{nf}\left(T-T_c\right) \tag{3}$$

$$u\frac{\partial T}{\partial x}+v\frac{\partial T}{\partial y}=\alpha_{nf}\left(\frac{\partial^2 T}{\partial x^2}+\frac{\partial^2 T}{\partial y^2}\right) \tag{4}$$

It is possible to write the non-dimensional governing equations in the following way, where the subscript *nf* denotes the characteristics of the Al_2O_3-water nanofluid, and the subscript *f* refers to the features of the base fluid (water):

$$x' = \frac{x}{H}, \quad y' = \frac{y}{H}, \quad u' = \frac{uH}{\alpha_f}, \quad v' = \frac{vH}{\alpha_f}, \quad p' = \frac{pH^2}{\rho_{nf}{\alpha_f}^2}, \quad \theta = \frac{T - T_C}{T_H - T_C} \tag{5}$$

$$\frac{\partial u'}{\partial x'} + \frac{\partial v'}{\partial y'} = 0 \tag{6}$$

$$u'\frac{\partial u'}{\partial x'} + v'\frac{\partial v'}{\partial y'} = -\frac{\partial p'}{\partial x'} + \frac{1}{\mathrm{Re}}\left(\frac{\partial^2 u'}{\partial x'^2} + \frac{\partial^2 u'}{\partial y'^2}\right) \tag{7}$$

$$u'\frac{\partial v'}{\partial x'} + v'\frac{\partial v'}{\partial y'} = -\frac{\partial p'}{\partial y} + \frac{1}{\mathrm{Re}}\left(\frac{\partial^2 v'}{\partial x'^2} + \frac{\partial^2 v'}{\partial y'^2}\right) + Ri\theta \tag{8}$$

$$u'\frac{\partial \theta}{\partial x'} + v'\frac{\partial \theta}{\partial y'} = \frac{1}{\mathrm{Re}\,\mathrm{Pr}}\left(\frac{\partial^2 \theta}{\partial x'^2} + \frac{\partial^2 \theta}{\partial y'^2}\right) \tag{9}$$

The governing equations presented above are acquired by utilizing the following non-dimensional quantities: The dimensionless Reynolds (*Re*), Prandtl (*Pr*), Richardson (*Ri*) and Grashof (*Gr*) numbers are presented in Eq. (10).

$$Re = \frac{\rho u_{lid} H}{\mu} \qquad \mathrm{Pr} = \frac{C_p \mu}{k} \qquad Ri = \frac{Gr}{\mathrm{Re}^2} \qquad Gr = \frac{g\beta(T_H - T_C)H^3}{\nu^2} \tag{10}$$

The finite volume method is employed for the discretization of the governing flow equations. approximate the diffusion terms in the governing equations, the second-order central differencing scheme is used. At the same time, the non-uniform form of FPFOI scheme suggested by Yapici and Obut[11] is used to approximate the convective terms. In the literature, there are different relations introduced for the physical characteristics of the Al_2O_3-water nanofluid. In the current paper, an investigation of three various viscosity and thermal conductivity correlation model equations given in Table 2 was carried out.

Table 2. Thermal conductivity and viscosity models utilized in numerical analysis

Model	**Researcher**	**Viscosity**	**Thermal conductivity**
I	(Einstein)[12]	$\frac{\mu_{nf}}{\mu_f} = (1 + 2.5\phi)$	$\frac{k_{nf}}{k_f} = \frac{(k_p + 2k_f) - 2\phi(k_f - k_p)}{(k_p + 2k_f) - \phi(k_f - k_p)}$ (Maxwell)[13]
II	(Chandrasekar and co-workers)[14]	b = 5300, n = 2.8 $\frac{\mu_{nf}}{\mu_f} = \left(1 + b\left(\frac{\phi}{1-\phi}\right)^n\right)$	
III	This study (Experimentally)	$\frac{\mu_{nf}}{\mu_f} = (1 + 2.5\phi + 107.2\phi^2)$	

DOI: http://dx.doi.org/10.32571/ijct.697728 **E-ISSN:2602-277X**

where ϕ refers to the volume fraction of Al_2O_3 nanoparticles in water, the base fluid. The mixing rule is used to evaluate the density (ρ_{nf}), heat capacity (C_{pnf}), thermal expansion coefficient (β_{nf}), and molecular weight (M_{nf}) of the Al_2O_3-water nanofluid:[13]

$$\rho_{nf} = (1-\phi)\rho_f + \phi\rho_p \tag{11}$$

$$C_{p\,nf} = \frac{(1-\phi)Cp_f\rho_f + \phi Cp_p\rho_p}{\rho_{nf}} \tag{12}$$

$$\beta_{nf} = \frac{(1-\phi)\beta_f\rho_f + \phi\beta_p\rho_p}{\rho_{nf}} \tag{13}$$

$$M_{nf} = (1-\phi)M_f + \phi\, M_p \tag{14}$$

The second viscosity model presented in Table 2 was acquired experimentally for the nanofluid that was obtained at nanoparticle volumetric fractions varying in the range from 0.33% to 5% with 43 nm Al_2O_3 nanoparticles and the water based fluid. A Brookfield cone and plate viscometer was utilized. Whereas an increase occurred in the nanofluid viscosity along with the nanoparticle volumetric fraction in case of the highest nanoparticle volumetric fraction of 2%, a nonlinear correlation was demonstrated between the increased nanofluid viscosity and nanoparticle volumetric fraction in case of the nanoparticle volumetric faction higher than 2%. The cause of the mentioned situation above may be due to more considerable hydrodynamic interaction between particles in case of the nanoparticle volumetric fraction above 2%. The third viscosity model in Table 2 represents the correlation equation acquired for the nanofluid at various nanoparticle volumetric fractions (1-5%), established experimentally in the current research with 80 nm Al_2O_3 nanoparticles and the water based fluid. Moreover, the model employed as the thermal conductivity model represents the effective thermal conductivity model suggested by Maxwell in theoretical terms.

3. RESULTS AND DISCUSSION

In this study, contour plots of stream function and dimensionless temperature isotherms of Al_2O_3-water nanofluid at various nanoparticle volumetric fractions and different *Re* and *Gr* numbers were studied in a square cavity geometry. Stream function and temperature contour values were obtained for nanoparticle volumetric fractions of 0%, 3%, and 5% with Model 1, Model 2, and Model 3. In Figure 2, the cases when the *Re* number was 100 and the *Gr* number was 10^3, 10^4, and 10^5 at different nanoparticle volumetric fractions were examined for Model 1. In case when the *Gr* number is 10^3, a flow occurs in the square cavity geometry due to the movement of the upper plate, and the primary vortex (eddy) is formed in the center of the geometry. In case when the *Gr* number is 10^4, the secondary vortex occurs in the lower right corner at the constant nanoparticle volumetric fraction. The reason for the formation of the secondary vortex is stagnation pressure and friction losses. The primary vortex occurs in the center of the square cavity geometry, while the secondary vortexes occur in the corners resulting from the movement of upper plate and in the direction in which the plate moves. Another smaller vortex occurs when the *Gr* number is 10^5 in the lower left corner of the geometry. The reason for the formation of the tertiary vortex is the formation of a negative pressure gradient. At the constant nanoparticle volumetric fraction and constant *Re* number, the number *Ri* increases with the increased *Gr* number. With the increase in the *Re* number at the constant *Gr* number, the *Ri* number will decrease, and forced convection heat transfer will become more dominant. Contrary to this situation, with the increase in the *Gr* number at the constant *Re* number, the *Ri* number will also increase, and natural convection heat transfer will become more dominant. In Figure 2, when the *Gr* number was 10^5, the primary vortex formed in the center shrank, and the secondary vortex formed in the lower right corner grew. In this case, natural convection heat transfer became more dominant. In the case when the nanoparticle volumetric fraction was 3% and the *Gr* number was10^3, only a large vortex was observed in the center, and when the *Gr* number increased to 10^5, a large vortex occurred in the lower right corner, and a tertiary vortex wasformed in the lower left corner.

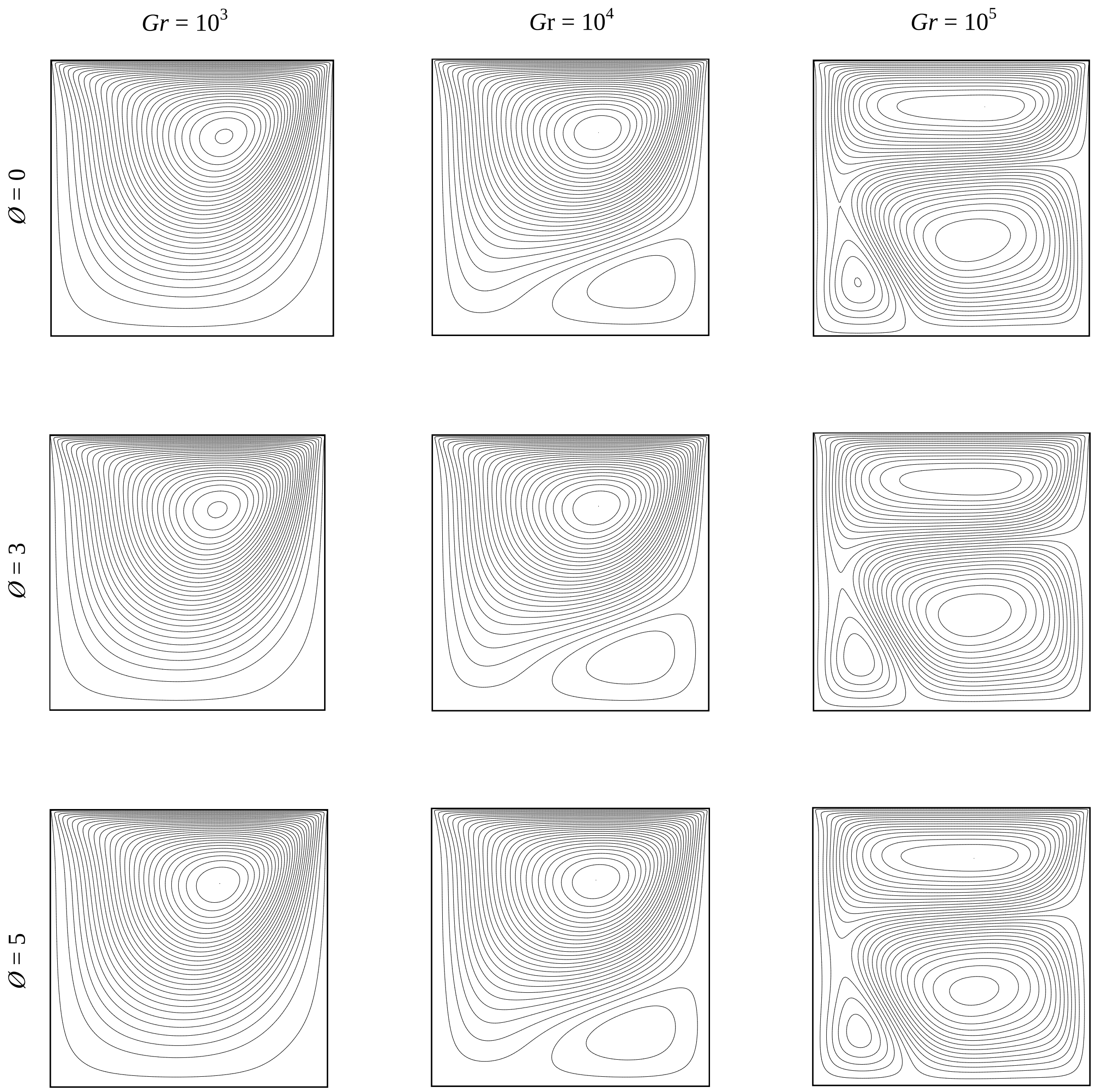

Figure 2. Plots of stream function contours obtained at the *Re* number of 100 and the *Gr* numbers of 10^3, 10^4, and 10^5 from Model 1 at different nanoparticle volumetric fractions.

It is thought that the secondary vortex occurs because of heat transfer, and the effect of natural convection increases with the formation of the secondary vortex. No change is observed in the primary and secondary vortexes with the increased nanoparticle volumetric fraction at the constant *Gr* number. According to the conclusions drawn in Figure 2, it is understood that the heat transfer at low *Ri* numbers occurs with forced convection and the increase in the nanoparticle volumetric fraction does not have an impact on the stream function contours, and the increase in the nanoparticle volumetric fraction does not have a significant impact on the flow when natural convection heat transfer occurred. In Figure 3, dimensionless temperature isotherms are observed at different *Gr* numbers and different nanoparticle volumetric fractions at the constant *Re* number for Model 1. In Figure 3, as the *Gr* number increases at the constant nanoparticle volumetric fraction in dimensionless temperature isotherms of the Al_2O_3-water nanofluid in the square cavity geometry, the thermal boundary layer thickens and becomes frequent since the secondary vortex will also increases, and heat transfer occurs by natural convection, as can be clearly observed when the *Gr* number becomes 10^5. In case when the *Gr* number is 10^3, the thermal boundary layer gets very close to the

DOI: http://dx.doi.org/10.32571/ijct.697728 **E-ISSN:2602-277X**

walls of the square cavity geometry, and this is an indication of forced convection heat transfer, and the medium in the main region of the geometry is almost isothermal.

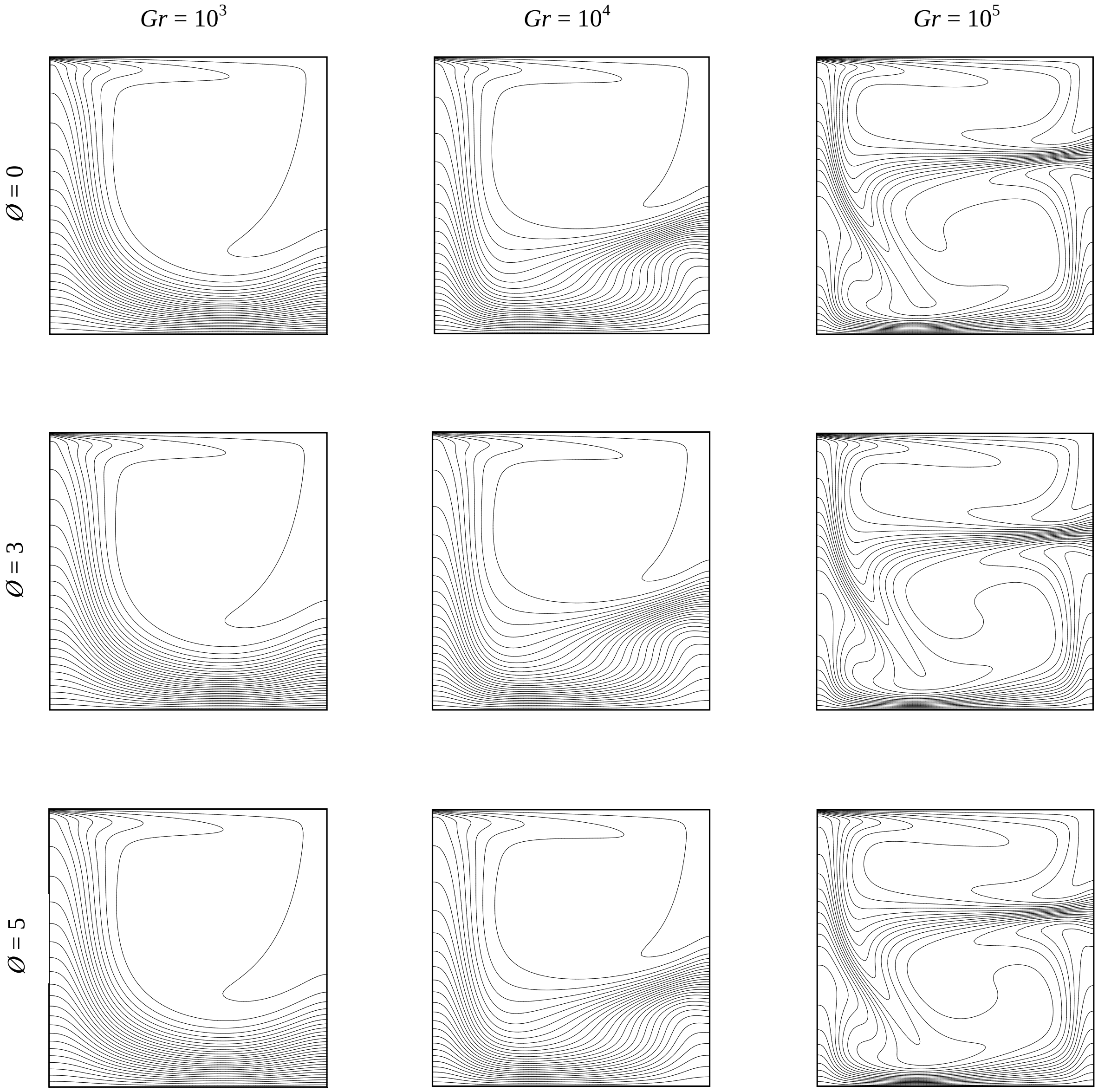

Figure 3. Plots of isotherms obtained at the *Re* number of 100 and *Gr* numbers of 10^3, 10^4, and 10^5 from Model 1 at different nanoparticle volumetric fractions.

In Figure 4, the cases when the *Re* number was 100 and the *Gr* number was 10^3, 10^4, and 10^5 at different nanoparticle volumetric fractions for Model 2 were examined. When the *Gr* number was 10^3, the primary vortex (eddy) occurred in the center of the geometry. In this case, the primary vortex was not affected much by the increase in the nanoparticle volumetric fraction, and a very small amount of decrease in the size of the vortex was observed. Since there is movement here, in other words, there is forced convection heat transfer, the primary vortex did not show much change with the increased nanoparticle volumetric fraction because the movement of the nanofluid is more dominant. The secondary vortex that is heat-induced is not affectebecause the primary vortex, which is movement-induced, is much more dominant. When the *Re* number was 100 and the *Gr* number was 10^4, the size and width of the secondary vortex were observed to decrease slightly with the increased nanoparticle volumetric fraction. The secondary vortex decreases with the nanoparticle volumetric fraction that increases with the increasing *Gr* number. Because the viscosity of the

DOI: http://dx.doi.org/10.32571/ijct.697728 **E-ISSN:2602-277X**

nanofluid will increase here, the movement is restricted, and the heat transfer due to natural convection decreases. A similar situation arises when the *Re* number is 100 and the *Gr* number is 10^5. Here, the size and width of the tertiary vortex also decrease with the increasing nanoparticle volumetric fraction.

Unlike Model 2, any change was not observed in stream function values with the increasing nanoparticle volumetric fraction in Model 1. Model 1 is the model created by the combination of the models of Einstein as a viscosity model and Maxwell as a thermal conductivity model and is a traditionally common model in the literature. In case when Model 1 was used in natural convection heat transfer, no alteration in the heat transfer rate was observed with the increased nanoparticle volumetric fraction.

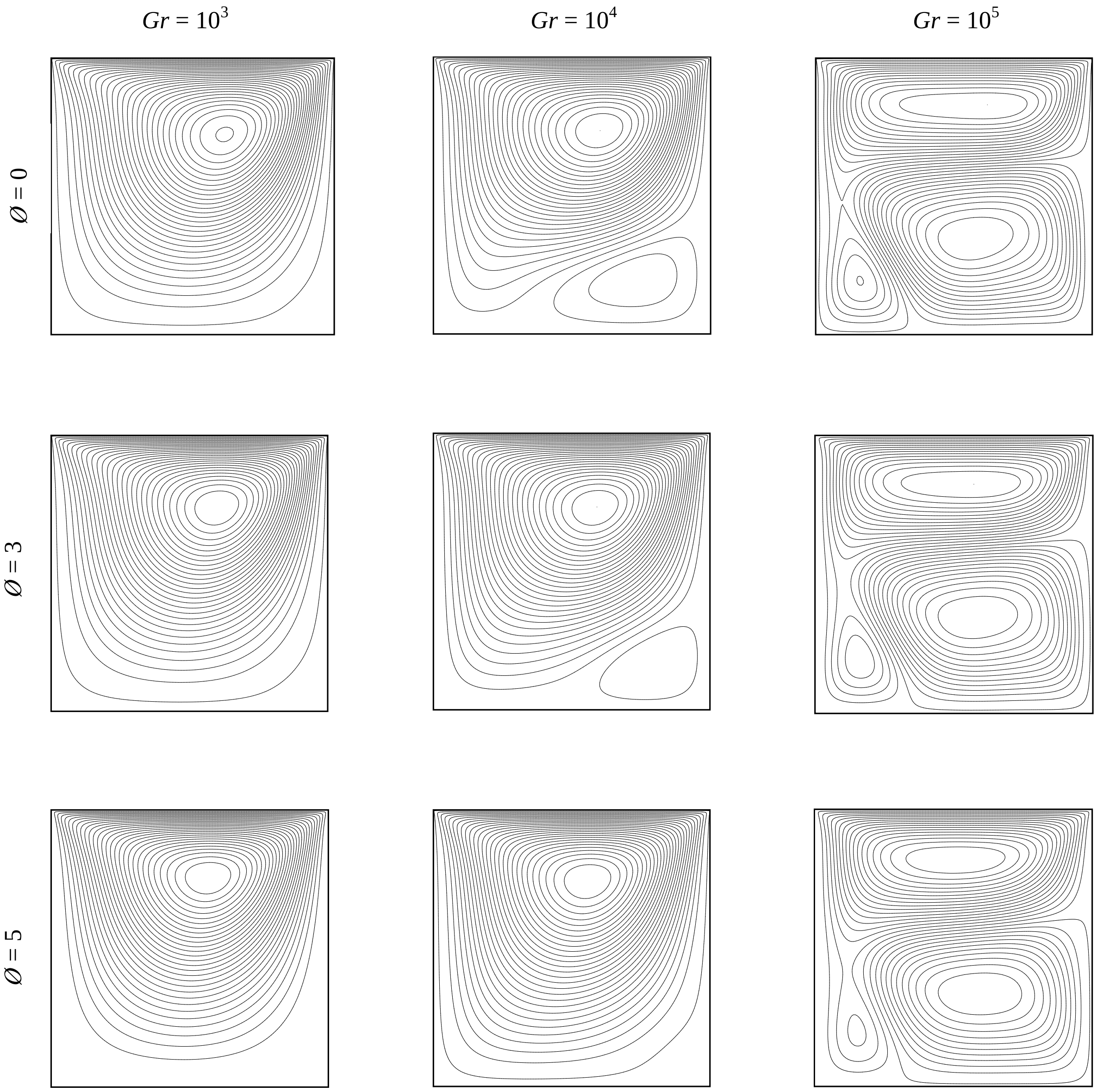

Figure 4. Plots of stream function contours obtained at the *Re* number of 100 and the *Gr* numbers of 10^3, 10^4, and 10^5 from Model 2 at different nanoparticle volumetric fractions.

In Figure 5, dimensionless temperature isotherms are observed at different *Gr* numbers and different nanoparticle volumetric fractions at the constant *Re* number for Model 2. In Figure 5, as the Gr number increases at the constant nanoparticle volumetric fraction in the dimensionless temperature isotherms of the Al_2O_3-water nanofluid in the square cavity geometry, the thermal boundary layer thickens and becomes frequent since the secondary vortex will also increase, and heat transfer occurs by natural convection, as can be clearly observed when the *Gr* number is 10^5. In case when the *Gr* number is 10^3, the thermal boundary layer gets very close to the walls of the square cavity geometry, and this is an indication of forced convection heat transfer, and the medium in the main region of the geometry is almost isothermal. In case when the *Gr* number is 10^4, it was revealed that the isothermal image formed in the center disappeared with the increased nanoparticle volumetric fraction, and the impact of natural convection heat transfer was observed.

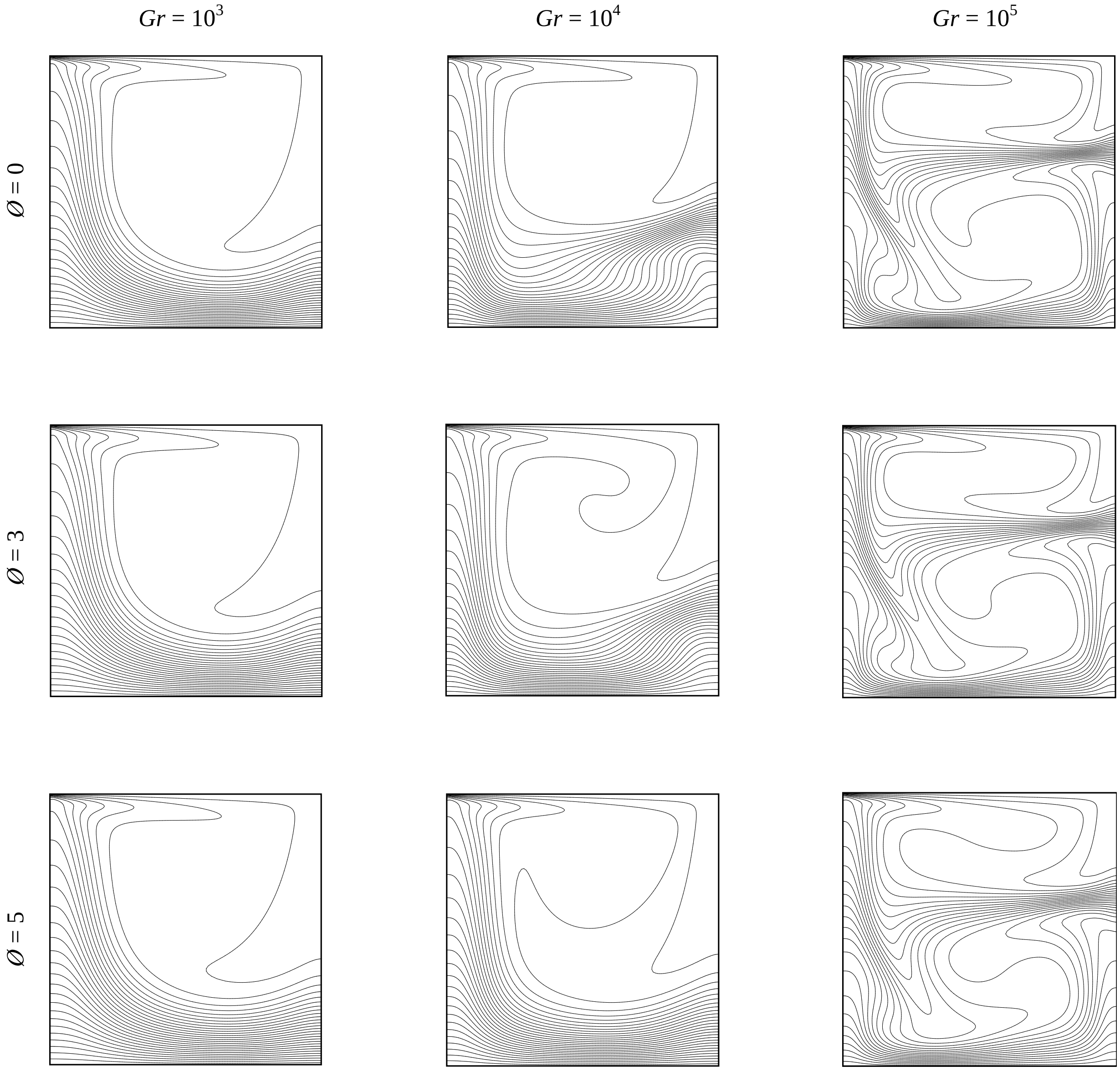

Figure 5. Plots of isotherms obtained at the *Re* number of 100 and the *Gr* numbers of 10^3, 10^4, and 10^5 from Model 2 at different nanoparticle volumetric fractions.

In Figure 6, the cases when the *Re* number was constant and 100 and the *Gr* number was 10^3, 10^4, and 10^5 at different nanoparticle volumetric fractions for Model 3 were examined. In case when the *Gr* number is 10^3, a flow occurs in the square cavity geometry due to the movement of the upper plate, and a primary vortex occurs in the center of the geometry. While heat transfer is realized by the forced convection mechanism at a low *Gr* number at the constant *Re* number and constant nanoparticle volumetric fraction, it is clearly observed to be realized by natural convection mechanism at high *Gr* numbers at the constant *Re* number and constant nanoparticle volumetric fraction. The primary vortex was almost unaffected by the increase in the nanoparticle volumetric fraction in case when the *Re* number was constant and the *Gr* number was 10^3. This is an expected situation because, although the viscosity of the nanofluid would increase with the increase in the presence of nanoparticles in the medium, the movement of the nanoparticle was not influenced since the forced convection heat transfer here was more dominant than natural convection heat transfer, and no change was observed in the size and width of the stream function values. In the second case, it was observed that the size and width of the secondary vortex formed in the lower right corner decreased slightly with the increased nanoparticle volumetric fraction in case when the *Re* number was constant and the *Gr* number was 10^4. The secondary vortex decreases with the nanoparticle volumetric fraction increasing with an increase in the *Gr* number because, since the viscosity of the nanofluid will increase here, the movement will be restricted, and natural convection heat transfer will be decreased. A similar situation arises when the *Re* number is 100 and the *Gr* number is 10^5. Here, the size and width of the tertiary vortex also decrease with increasing nanoparticle volumetric fraction.

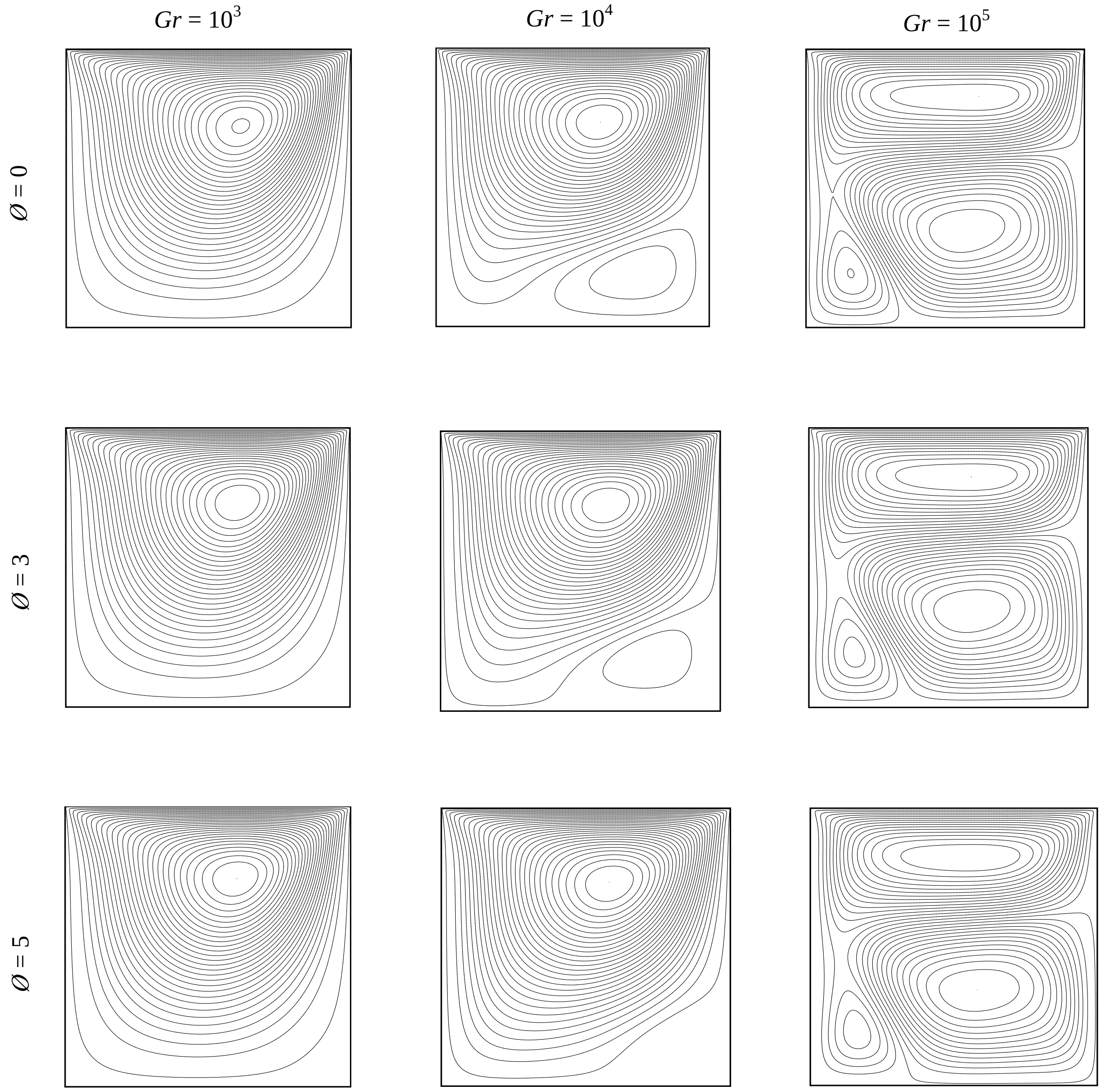

Figure 6. Plots of stream function contours obtained at the Re number of 100 and the Gr numbers of 10^3, 10^4, and 10^5 from Model 3 at different nanoparticle volumetric fractions.

In Figure 7, dimensionless temperature isotherms are observed at different *Gr* numbers and different nanoparticle volumetric fractions at the constant *Re* number for Model 3. In Figure 7, as the *Gr* number increases at the constant nanoparticle volumetric fraction in the dimensionless temperature isotherms of the Al_2O_3-water nanofluid in the square cavity geometry, the thermal boundary layer thickens and becomes frequent since the secondary vortex will also increase, and heat transfer occurs by natural convection, as can be clearly observed when the *Gr* number is 10^5.

In case when the *Gr* number is 10^3, the thermal boundary layer gets very close to the walls of the square cavity geometry, and this is an indication of forcedconvection heat transfer, and the medium in the main region of the geometry is almost isothermal. In case when the *Gr* number is 10^4, unlike the case that occurs in Model 2, it is clearly observed that the isothermal image in the main region of the geometry has not disappeared yet even at the moment when the nanoparticle volumetric fraction is 3%.

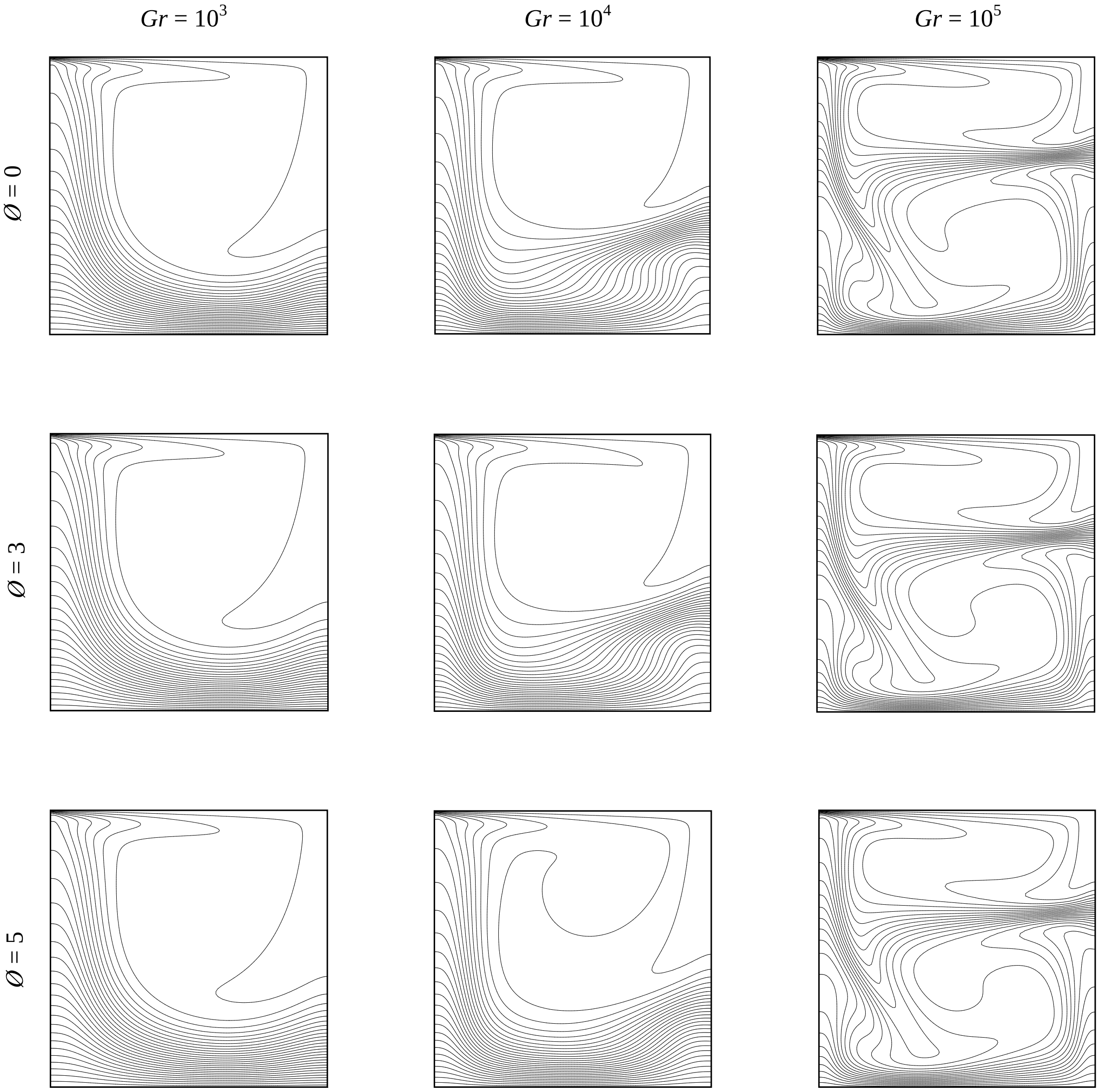

Figure 7. Plots of isotherms obtained at the *Re* number of 100 and the *Gr* numbers of 10^3, 10^4, and 10^5 from Model 3 at different nanoparticle volumetric fractions.

In Figure 8, both natural and forced convection heat transfer stream function in the square cavity geometry are demonstrated in cases when the *Re* numbers are 10, 100, and 1000 and the *Gr* numbers are 10^3, 10^4, and 10^5 and the Al_2O_3-water nanofluid concentrations are 0%, 3%, and 5% for Model 3. In case when the *Re* number is

10, the number of vortexes formed in the square cavity geometry increased with the increased *Gr* number. Here, it is observed that only one vortex is formed in the center when the *Re* number is 10 and the *Gr* number is 10^3, that a small increase occurs in the size and width of the vortex when the *Gr* number is 10^4, and that in the final case, a large secondary vortex occurs in the lower right corner under the effect of natural convection when the *Gr* number is 10^5. Furthermore, in the final case, when the *Re* number was 10 and the *Gr* number was 10^5, the effect of the nanoparticle volumetric fraction emerged. It is noteworthy that in the case when the *Re* number is 1000, the size and width of the stream function are almost the same at all *Gr* numbers. Here, since forced convection heat transfer is more dominant, no secondary vortex occurs anywise, while a shift in the vortex towards the upper right corner is observed due to the movement of the upper plate.

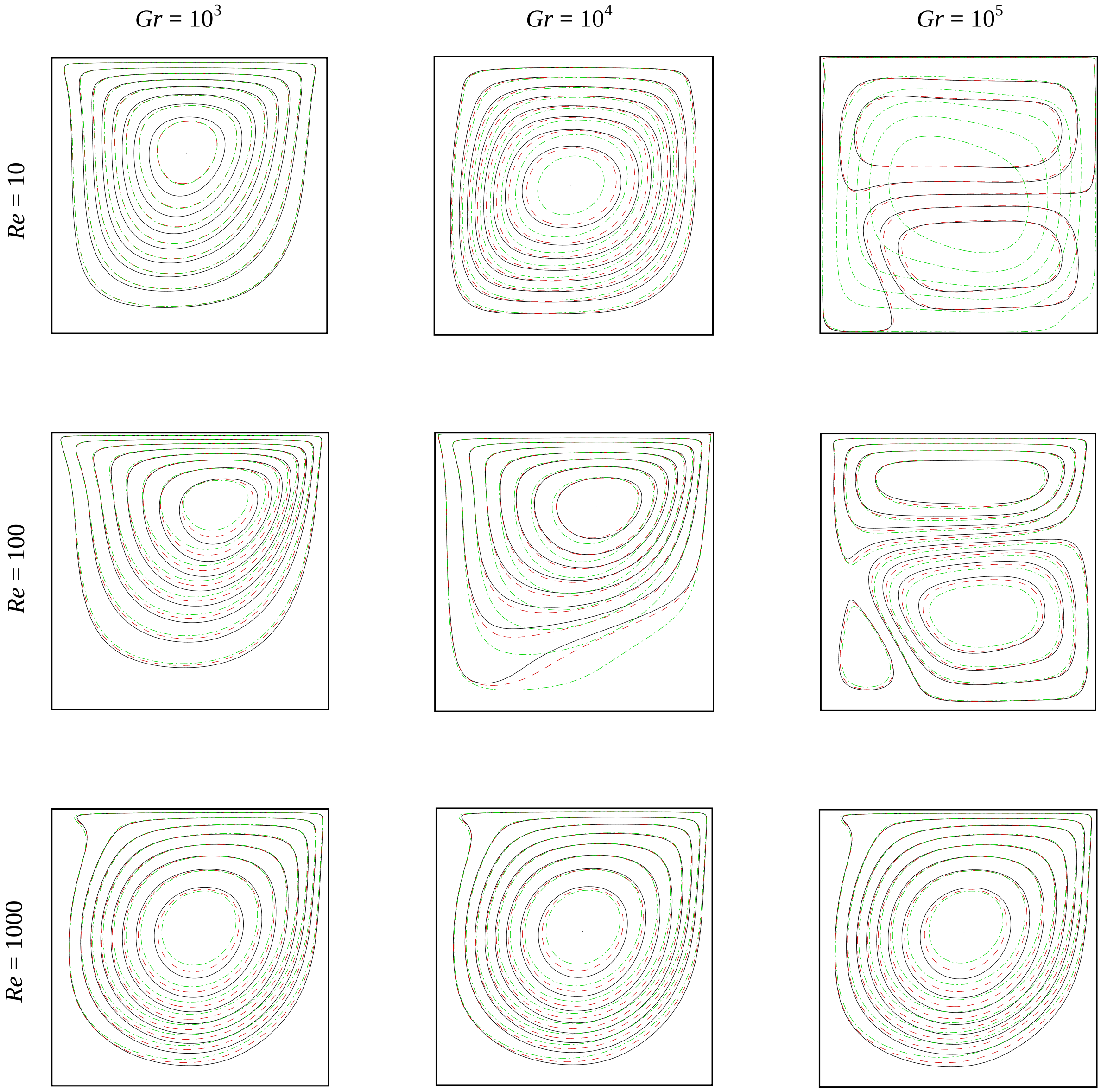

Figure 8. Plots of stream function contours obtained at the *Re* numbers of 10, 100, and 1000 and the *Gr* numbers of 10^3, 10^4, and 10^5 from Model 3 at different nanoparticle volumetric fractions. Straight line: Base fluid pure water; Dashed line: volumetric fraction $\emptyset$ = 3%, Dot-dashed line: volumetric fraction $\emptyset$ = 5%.

In Figure 9, both natural and forced convection heat transfer dimensionless temperature isotherms in the square cavity geometry are demonstrated in cases when the *Re* number is 10, 100, and 1000 and the *Gr* number is 10^3, 10^4, and 10^5 and the Al_2O_3-water nanofluid concentration is 0%, 3%, and 5% for Model 3. In the square cavity geometry, since the secondary vortex will increase as the *Gr* number increases in case when the Re number is constant and 10 in the dimensionless temperature isotherms of the Al_2O_3-water nanofluid, the thermal boundary layer thickens and becomes frequent, and heat transfer is realized by natural convection as it is clearly observed when the *Gr* number is 10^5. At low *Gr* numbers, heat transfer takes place here by natural convection, and the isotherms progress almost parallel to the horizontal walls. In case when the *Re* number is 100 and the *Gr* number is 10^4, both natural and forced convection heat transfer occurs, and while the medium in the center of the geometry is isothermal, thermal boundary layers are observed to be formed on the walls. At the *Re* number of 1000 and at all values of the *Gr*number, forced convection heat transfer occurs, as can be clearly observed from the dimensionless temperature isotherms, and the thermal boundary layer gets very close to the walls of the square cavity geometry, and the medium in the main region of the geometry becomes almost isothermal.

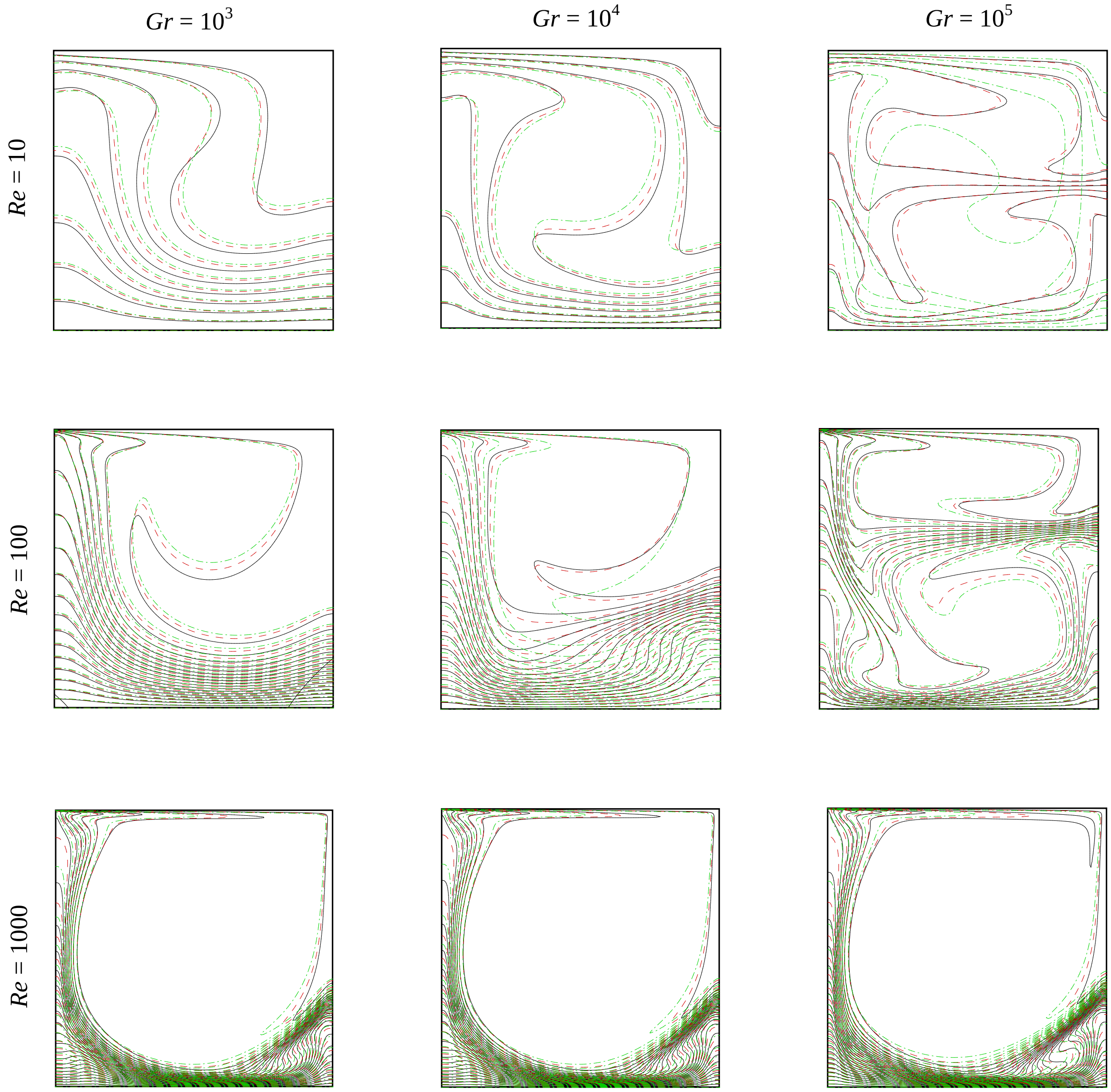

Figure 9. Plots of isotherms obtained at the *Re* numbers of 10, 100, and 1000 and the *Gr* numbers of 10^3, 10^4, and 10^5 from Model 3 at different nanoparticle volumetric fractions. Straight line: Base fluid pure water; Dashed line: volumetric fraction $\emptyset$ = 3%, Dot-dashed line: volumetric fraction $\emptyset$ = 5%.

The results obtained from the numerical solution are presented in Tables 3, 4 and 5 as the average *Nu* results obtained along the hot wall in Models 1, 2, and 3 for the *Gr* numbers in the range of 10^3 - 10^5, the *Re* numbers of 10 - 100 - 1000, and the nanoparticle volumetric fraction of 0-5%. The increase in heat transfer rate at

DOI: http://dx.doi.org/10.32571/ijct.697728 **E-ISSN:2602-277X**

high nanoparticle volumetric fractions and at constant *Gr* numbers indicates significant changes depending on the *Re* number. Furthermore, it is observed from the tables that the average *Nu* number increases significantly with the decreasing *Ri* number at constant nanoparticle volumetric fractions in all models. The results obtained are compatible with similar studies in the literature.[15–19]

Table 3. The average *Nu* results obtained along the hot wall for the Al_2O_3-water nanofluid as a result of both natural and forced convection for Model 1 in the square cavity geometry

MODEL 1									
Ø	***Gr* 10^3** ***Re***			***Gr* 10^4** ***Re***			***Gr* 10^5** ***Re***		
	10	100	1000	10	100	1000	10	100	1000
0	2.69424404	4.48216182	13.94232762	4.24429466	4.14744341	14.01411223	4.75732946	6.53374570	14.51737682
1	2.73408941	4.54370984	14.03291625	4.32616103	4.21598073	14.10101304	4.96577250	6.66038678	14.53190419
3	2.80761521	4.66156512	14.11548359	4.48450498	4.35206376	14.18134660	5.19772318	6.90535801	14.36249305
5	2.87274283	4.77296707	14.05252179	4.63587590	4.48875865	9.55710989	5.42329901	7.13869699	13.72670099

Table 4. The average *Nu* results obtained along the hot wall for the Al_2O_3-water nanofluid as a result of both natural and forced convection for Model 2 in the square cavity geometry

MODEL 2									
Ø	***Gr* 10^3** ***Re***			***Gr* 10^4** ***Re***			**Gr 10^5** ***Re***		
	10	100	1000	10	100	1000	10	100	1000
0	2.69424404	4.48216182	13.94232762	4.24429466	4.14744341	14.01411223	4.75732946	6.53374570	14.51737682
1	2.74035660	4.54778487	14.06456215	4.33511274	4.20498721	14.13614101	4.87869860	6.67723320	14.56513756
3	2.68805410	4.59871794	13.46401055	4.32049297	4.76506117	13.53830100	4.89155483	6.59627443	13.77169901
5	2.43470817	4.59902274	11.70808334	4.02832936	5.34386604	11.79175418	6.24078071	6.01816599	12.00956067

Table 5. The average *Nu* results obtained along the hot wall for the Al_2O_3-water nanofluid as a result of both natural and forced convection for Model 3 in the square cavity geometry

MODEL 3									
Ø	***Gr* 10^3** ***Re***			***Gr* 10^4** ***Re***			***Gr* 10^5** ***Re***		
	10	100	1000	10	100	1000	10	100	1000
0	2.69424404	4.48216182	13.94232762	4.24429466	4.14744341	14.01411223	4.75732946	6.53374570	14.51737682
1	2.72827432	4.54002029	13.99495980	4.31779231	4.22755615	14.06804469	4.85857939	6.64466637	14.50105043
3	2.75616969	4.63292033	13.83614958	4.41330144	4.47238444	13.90617540	5.00065179	6.77172960	14.10992917
5	2.84253633	4.70846295	13.36343161	4.45543648	5.10934326	13.42201614	6.98341032	6.80042011	13.22567790

DOI: http://dx.doi.org/10.32571/ijct.697728 **E-ISSN:2602-277X**

4. CONCLUSIONS

In this study, both natural and forced convection heat transfer of the Al_2O_3 - water nanofluid were examined in the square cavity geometry where the upper wall moved at a certain constant velocity, the other walls were immobile, the lower wall was heated, the upper wall was cooled, and the side walls were insulated. As a result of the numerical solution, the maximum, minimum *Re* and *Gr* numbers and average *Nu* number, and stream function and dimensionless temperature isotherms were examined in Models 1, 2, and 3 for the Gr number in the range of 10^3 - 10^5, the *Re* number of 10 - 100 – 1000, and the nanoparticle volumetric fraction 0%, 3%, and 5%, and the following conclusions were reached:

- An investigation of the mixed convection heat transfer of an Al_2O_3-water nanofluid was carried out at the constant Grashof number and altering Reynolds number, and with the order reversed. It was determined that enhancement occured in heat transfer at the constant Grashof number of 10^4 with nanoparticle concentration for the Reynolds numbers as low as 100. Nevertheless, enhancement occurred in heat transfer at the Reynolds number of 1000 with nanoparticle volume fractions reaching 0.01. Increasing the nanoparticle concentration even further causes a decrease in heat transfer.
- An increase in heat transfer took place with nanoparticle concentration at the constant Reynolds number of 100 and the low Grashof number of 10^3. Nevertheless, at the constant Reynolds number of 1000 and the high Grashof number of 10^5, the highest heat transfer was determined at the concentration of 0.01, and following the mentioned concentration, the performance of heat transfer got worse in comparison with the base fluid not containing nanoparticles.
- The average *Nu* number, which represents a measure of heat transfer in Models 1, 2, and 3 at constant *Re* numbers and calculated from the heated wall, was determined to increase with the increasing *Re* number.
- A decrease in heat transfer was revealed with the increasing *Gr* number at low *Gr* number values and at constant *Re* numbers. It was revealed that the reason for this was the realization of heat transfer by the natural convection mechanism as a result of the increase in the *Ri* number as the *Gr* number increases at constant *Re* numbers.
- In Models 1, 2, and 3, the average *Nu* number was found to increase significantly with the decrease in the *Ri* number at constant nanoparticle volumetric fractions.
- As a result, both natural and forced convection heat transfer of nanofluids in the square cavity geometry were demonstrated to change depending on the nanoparticle volumetric fraction, *Re* and *Gr* numbers.

ACKNOWLEDGEMENTS

The Scientific Research Project Fund of Sivas Cumhuriyet University provided its support for the present research under the project number M-489.

Conflict of interests

Authors declare that there is no a conflict of interest with any person, institute, company, etc.

REFERENCES

1. Esfe, M. H.; Saedodin, S.; Malekshah, E. H.; Babaie, A.; Rostamian, H. *J. Therm. Anal. and Calorim.* **2019**, *135* (1), 813-859.

2. Tiwari, R. K.; Das, M. K. *Int. J. Heat Mass Transf.* **2007**, 50, 2002-2018.

3. Talebi, F.; Mahmoudi, A. H.; Shahi, M. *Int. Commun. Heat Mass Tran.* **2010**, 37 (1), 79-90.

4. Arefmanesh, A.; Mahmoodi, M. *Int. J. Therm. Sci*. **2011**, 50 (9), 1706-1719.

5. Brinkman, H. C. *J. Chem. Phys.* **1952**, *20* (4), 571-582.

6. Maiga, S. E. B.; Nguyen, C. T.; Galanis, N.; Roy, G. *Heat transfer enhancement in forced convection laminar tube flow by using nanofluids*, Proceedings of the International Symposium on Advances in Computational Heat Transfer III, Paper CHT-040101, p. 24, Begell House Publishers, 2004.

7. Chamkha, A. J.; Rashad, A. M.; Armaghani, T.; Mansour, M. A. *J. Therm. Anal. Calorim.* **2018**, 132 (2), 1291-1306.

8. Kapil, M.; Roy, D., Sharma, B., Rana, S. C., Pramanik, S., Barman, R. N. *Mater. Today-Proc.* **2019**, 11, 700-707.

9. Abu-Nada, E.; Masoud, Z.; Hijazi, A. *Int. Commun. Heat Mass Tran*. **2008,** 35 (5), 657-665.

10. Kim, C. S.; Okuyama, K.; Fernández de la Mora, J. *Aerosol Sci. Tech*. **2003**, 37 (10), 791-803.

11. Yapici, K.; Obut, S. *Int. J. Numer. Method H*. **2015**, 25 (5), 998-1029.

12. Einstein, A. *Investigations on the theory of the Brownian movement*, Dover Books, 1956.

DOI: http://dx.doi.org/10.32571/ijct.697728 **E-ISSN:2602-277X**

13. Maxwell, J.C. *A Treatise on Electricity and Magnetism*. Third ed Clarendon Press, Oxford, 1904.

14. Chandrasekar, M.; Suresh, S.; Chandra Bose, A. *Exp. Therm. Fluid Sci.* **2010,** 34 (2), 210-216.

15. Öğüt, E. B.; Kahveci, K. *J. Mol. Liq.* **2016**, 224, 338-345.

16. Yapici, K.; Obut, S. *Heat Transfer Eng.* **2015**, 36 (3), 303-314.

17. Heydari, M. R.; Esfe, M. H.; Hajmohammad, M. H.; Akbari, M.; Esforjani, S. S. M. *Heat Transf. Res.* **2014**, 45 (1), 75-95.

18. Taamneh, Y.; Bataineh, K., *Stroj. Vestn-J. Mech. E.* **2017**, 63 (6), 383-393.

19. Lauriat, G. *Appl. Therm. Eng.* **2018**, 129, 1039-1057.

ORCID

ID https://orcid.org/0000-0002-8634-9232 (N. Keklikcioğlu Çakmak)

ID https://orcid.org/0000-0003-2454-7003 (H. H. Durmazuçar)

ID https://orcid.org/0000-0002-3902-9375 (K. Yapıcı)

DOI: http://dx.doi.org/10.32571/ijct.704871 **E-ISSN:2602-277X**

International Journal of Chemistry and Technology

http://dergipark.org.tr/ijct

Research Article

Investigation of structural and optical properties of ZnO thin films deposited on glass substrates by wet chemical sol-gel technique

Seydi DOĞAN

ID on the last page

Department of Electrical-Electronics Engineering, Faculty of Engineering, Balikesir University, Balikesir, 10145, Turkey

Received: 16 March 2020; Revised: 23 March 2020; Accepted: 26 March 2020

*****Corresponding author e-mail: dogans@balikesir.edu.tr

Citation: Doğan, S. *Int. J. Chem. Technol.* **2020**, 4 (1), 38-42.

ABSTRACT

Nickel doped ZnO (NZO) and undoped ZnO thin films were deposited by wet chemical sol-gel spin coating method and their optical and structural properties have in detail been investigated by X-ray diffraction and optical absorption measurements to observe the effect of doping with different values of Ni molarity. The NZO and undoped ZnO thin films showed a growing trend along the c-axis perpendicular to the substrate surface. The strong (002) diffraction peaks at 2θ = 35.743°, 35.836°, 35.840° and 36.041° were observed to belong to samples undoped ZnO, NZO (0.25%), NZO (0.50%) and NZO (0.75%) films, respectively. The band gap values have been calculated from the dependencies (α^2 *vs* hν) by extrapolating the straight lines to $\alpha^2 = 0$ and found as 3.2630 eV and 3.2820 eV for 0.75% NZO and undoped ZnO thin films, respectively.

Keywords: Nickel doped ZnO, sol-gel growth, thin film.

Islak kimyasal sol-jel tekniği ile cam alt tabanlar üzerine büyütülen ZnO ince filmlerin yapısal ve optik özelliklerinin incelenmesi

ÖZ

Nikel katkılı ZnO (NZO) ve katkısız ZnO ince filmler ıslak kimyasal sol-jel spin kaplama tekniği ile büyütüldü ve onların optik ve yapısal özellikleri farklı molaritedeki Ni katkılamasının etkisini gözlemlemek için X-ışını kırınımı ve optik soğurma ölçümleri ile ayrıntılı olarak incelendi. NZO ve katkılanmamış ZnO ince filmler, taban malzeme yüzeyine dik olan c-ekseni boyunca bir büyüme eğilimi gösterdi. 2θ = 35.743°, 35.836°, 35.840° ve 36.041° deki baskın (002) kırınım piklerin sırasıyla katkılanmamış ZnO, NZO (%0.25), NZO (%0.50) and NZO (%0.75) filmlerine ait olduğu gözlendi. Yasak enerji aralığı değerleri, (α^2 *vs* hν) grafiğinden $\alpha^2 = 0$ olduğu noktaya ekstrapolasyon yapılarak hesaplandı ve %0.75 NZO ve katkılanmamış ZnO filmler için sırasıyla 3.2630 eV ve 3.2820 eV olarak bulundu.

Anahtar Kelimeler: Nikel katkılı ZnO, sol-jel büyütme, ince film.

1. INTRODUCTION

Zinc oxide (ZnO) and its alloys have managed to capture the attention of many researchers because of their wide applications in optoelectronics and technology. Being a binary transparent conducting oxide and synthesized as thin film, ZnO is most suitable semiconductor for use in optoelectronic devices, and it has gained a great interest due to its usage in basic scientific studies and its potential technological applications such as light emitting diodes,[1] varistors, thin film solar cells[2,3] and transistor,[4-6] surface acoustic-wave devices, touch panels, gas detecting, solar cells, flat panel displays, piezoelectric devices etc. Some of its numerous advantages include the tuning of its physical properties, the low cost, availability in bulk material for homoepitaxial growth (by hydrothermal, melt and Seed Vapor Phase methods), non-toxicity, compatibility with large-scale processes, possibility of wet chemical etching, resistance to radiation damage, high quantum efficiency and its relative easy fabrication. It has a direct energy band gap values (3.3 eV at RT; and 3.43e V at

2K), large excitation binding energy (60 meV) enabling exciton recombination lasing mode and optical properties which are quite similar to GaN.[7-9]

Since undoped ZnO is an n-type intrinsic semiconductor due to both the presence of oxygen vacancies and the presence of zinc intersititals atoms, it is difficult to control some properties required by many optoelectronic applications. Therefore, in order to improve the quality of grown ZnO, many researchers have carried out experimental studies related to doping of ZnO with fluorine, erbium, tin, indium, nickel, antimony, manganese, iron etc.[10-15] There are much effort on ZnO to study optical and structural properties being associated with Ni doping. Of the elements available for doping, Ni is the most important element of the cation and anion dopants.

The sol-gel growth technique which is among the many chemical growth methods given in the literature such as chemical bath deposition, spray pyrolysis,[16] electrochemical deposition,[17] successive ionic layer adsorption and reaction[18] and sol-gel,[19-20] is the most preferred method due to its low equipment cost, simplicity, accurate control of stoichiometry, large area coating at low temperatures, high homogeneity, relatively low process, safety and easy control of chemical ingredients.

Undoped ZnO and Ni doped ZnO (NZO) thin films have recently emerged as the leading semiconductors because of their unique properties mentioned above. Kim and co-workers have carried out a study on the structural, electrical and optical properties of ZnO thin films having different Ni doping ratio grown by Sol-gel technique.[21] They have reported that although thin films (002) with dopant ratio of 0.2 mol% and 0.4 mol% had the preferred orientation direction, they have showed non-textured polycrystalline structure with increased Ni content. The smallest resistance and average optical transmittance values for 0.2 mol% Ni-doped ZnO thin film have been obtained as 4.8×10^{-4} Ω cm and 91.2% in the visible range, respecitively.

In another study, Khan and co-workers[22] have characterized the sol-gel grown ZnO thin films using X-ray diffraction (XRD), Fourier-transform infrared (FTIR) spectroscopy, Ultraviolet-visible (UV-vis), Photoluminescence (PL), Scanning electron microscopy (SEM) measurements. In this work, the band gap energy value of the films has been calculated as ~3.24 eV.

On the other hand, the optical and structurel properties of ZnO films grown by Spray Mist-CVD technique have also been study by Derbali and co-workers[23] to observe the effect of depoisiton time by means of XRD, SEM, Atomic force microscopy (AFM), PL spectroscopies. They have reported that the grown films had a hexagonal wurtzite crystal structure with lattice constants a = b = 3.260 Å, c = 5.214 Å and a high degree of crystallinity with [001] preferential orientation from XRD measurements.

In our study, undoped and Ni doped ZnO films (NZO) at variable concentrations (0.25%, 0.50% and 0.75%) were prepared by sol-gel technique and effect of Ni on optical and structural properties of ZnO was investigated by XRD, UV-Vis spectrometry and optical absorption measurements. According to the literature survey, no studies on Ni doped ZnO thin films have been conducted at these doping rates, and therefore this study demonstrates originality.

2. EXPERIMENTAL

Ni doped ZnO (NZO) and undoped ZnO thin films were grown by spin coating sol-gel technique on glass substrates. In order to prepare undoped and Ni doped ZnO: Nickel (II) nitrate-hexahydrate ($Ni(NO_3)_2.6H_2O$), Zinc acetate dehydrate ($Zn(CH_3COO)_2.2H_2O$), monoethanolamine (C_2H_7NO, MEA) and 2-methoxyethanol ($C_3H_8O_2$, 2-MTE) were utilized to be Ni additive source, ZnO precursor source, stabilizer and solvent, respectively. Solution was stirred at 60°C for 2h by magnetic stirrer till uniform and a clear sol was obtained. After cleaning glass substrates in acetone and methanol in the ultrasonic bath, immersing them in diluted 10% hydrofluoric acid for 20 s, rinsing them with de-ionized water and drying gently them with nitrogen gas, the obtained precursor solution was dropped on a substrate and coated at a speed of 3.000 rpm for 25 s. The flowchat for the growth of undoped ZnO and NZO thin films is given in Figure 1.

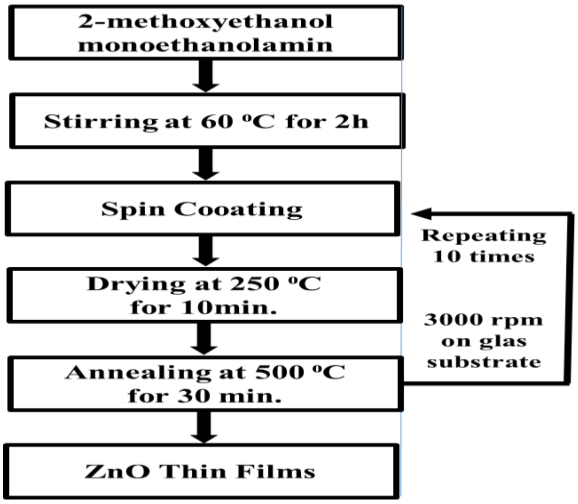

Figure 1. Flowchart for the growth of undoped ZnO and NZO films.

The coated film was sintered at 250℃ for 10 min to evaporate the remaining solvent. The same process was repeated 10 times to achieve the desired thickness value, and the undoped ZnO and NZO thin films were annealed in air at 500℃ for 30 min.

The optical absorbance of the undoped ZnO and NZO films were recorded in spectral region of 350-600 nm at room temperature (300 K) by a Perkin-Elmer Lambda-35 UV-Vis spectrophotometer working in the range of 200-1100 nm and having a wavelength accuracy of 0.3 nm. The crystalline behaviours of ZnO films were determined by a Rigaku/SmartLab XRD (CuKα radiation, k = 0.154059 nm) operated under 30 mA and 40 kV. The XRD measurements were carried out at room temperature (300K) and the values of 2θ were set between 20^o and 80^o.

3. RESULTS AND DISCUSSION

Figure 2 shows the XRD images of undoped ZnO and NZO thin films having different Ni concentrations.

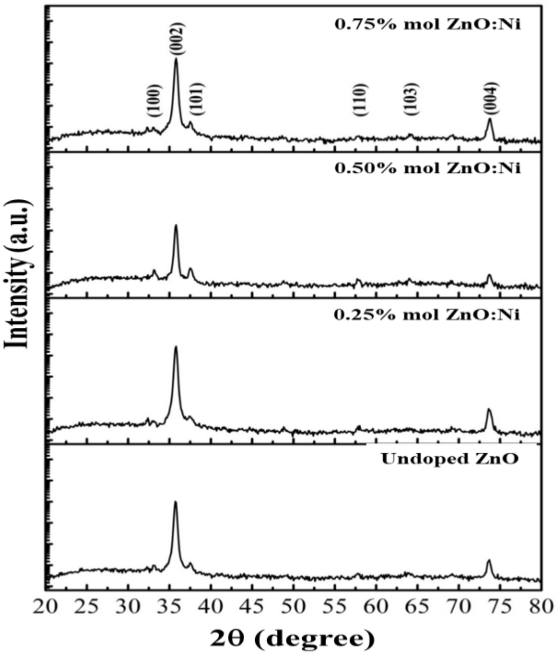

Figure 2. XRD patterns of undoped ZnO and NZO films.

The (002) diffraction peak around the 35.743 degrees shows a preferred growth direction along with the c-axis which is perpendicular to the substrate.[24] While the same dominant (002) diffraction peak have been observed for a dopant ratio of 0.2 mol% and 0.4 mol%, the structure of the film has changed to the non-textured polycrystalline structure with the Ni content exceeding of 0.6 mol%.[21] The strong (002) diffraction peaks observed at 2θ = 35.836°, 35.840° and 36.041° belong to samples NZO (0.25%), NZO (0.50%) and NZO (0.75%), respectively. As can be seen from these values, although the values of 2θ and Full width at half maxium (FWHM) vary slightly with the increase of the Ni ratio, the hexagonal wurtzite crystal structure of the deposited thin films remains unchanged. In addition to (002) dominant diffraction peak, some other peaks having lower intensities such as (004), (103) and (110) were also observed for the films.[25-26] The *a* and *c* lattice constant values of the grown ZnO films can be easily calculated from following equation;[18]

$$\frac{1}{d^2} = \frac{4}{3}\left(\frac{h^2 + k^2 + hk}{a^2}\right) + \left(\frac{l^2}{c^2}\right)$$

Where (*hkl*) and *d* indicate the miller indicies and interplaner distance, respectively. The mean values of the *a* and *b* latis parameters given in Table 1 were calculated to be *a* = *b* = 3.125 Å and c = 5.009 Å. The calculated *a* and *c* values match the ones given in JPCDS card no: 36-1451 and are almost agree with the findings of Derbali and co-workers.[23]

Table 1. The calculated lattice constant values of the films

Sample	2θ	FWHM	a (Å)	c (Å)
Undoped ZnO	35.743	0.33	3.131	5.019
NZO (0.25%)	35.836	0.38	3.126	5.012
NZO (0.50%)	35.840	0.41	3.122	5.005
NZO (0.75%)	36.041	0.43	3.119	5.000

Optical absorption spectra of undoped ZnO and NZO thin films were obtained in the wavelength range 350-600 nm (see Figure 3). The band gap values were calculated using the relation given below;[27]

$$(\alpha h\nu) = A(h\nu - E_g)^n$$

Where *A* is the absorbance, *α* is the absorption coefficient in cm^{-1}, *n* is a constant indicating the type of optical transition, and the *n* = 2 and *n* = 1/2 values are used for the allowed indirect and direct transitions, respectively. As could be seen in Figure 3, the band gap values were calculated from the dependencies (α^2 *vs* hν) by extrapolation to $\alpha^2 = 0$ and found as 3.2820 eV and 3.2630 eV for undoped ZnO and NZO (0.75%), respectively. The optical band gap values obtained are in agreement with those of Khan and co-workers.[22]

DOI: http://dx.doi.org/10.32571/ijct.704871 **E-ISSN:2602-277X**

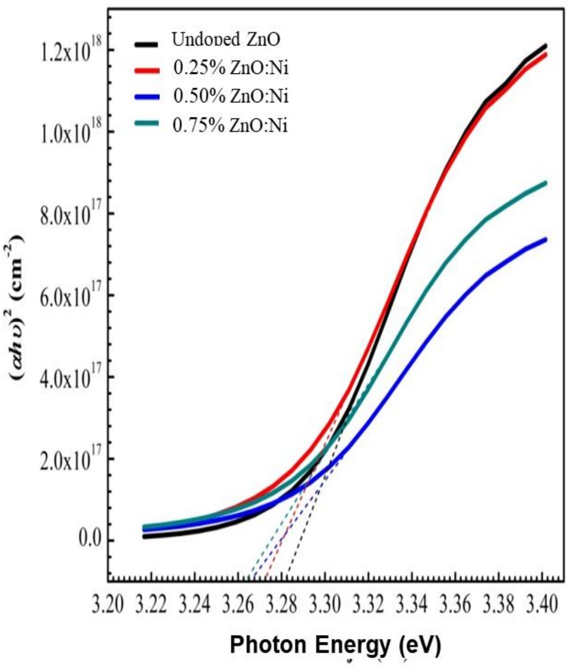

Figure 3. Optical absorption spectra of undoped ZnO and NZO films.

4. CONCLUSIONS

In this work, nickel doped ZnO (NZO) and undoped ZnO thin films were grown by wet chemical sol-gel spin coating method. The NZO and undoped ZnO thin films had a (002) diffraction peak around the 35.85 degrees which is an indication of high quality ZnO thin film growth. The strong (002) diffraction peaks at $2\theta = 35.836°$, 35.840° and 36.041° were observed for NZO (0.25%), NZO (0.50%) and NZO (0.75%), respectively. The band gap values calculated from the dependencies (α^2 vs hν) by extrapolation of the straight lines to $\alpha^2 = 0$ and were found as 3.2630 eV and 3.2820 eV for NZO (0.75%) and undoped ZnO thin films, respectively. As a conclusion, ZnO thin films can be considered a promising material for solar cell applications by adding nickel into them at different doping ratios due to their transparent properties.

Conflict of interests

I declares that there is no a conflict of interest with any person, institute, company, etc.

REFERENCES

1. Yan, Z.; Lei, G.; Meng, Li.; Mei, Y.; Shenguang, G.; Jinghua, Yu.; Xianrang, S.; Bingqiang, C. *Chem. Commun.* **2014**, 50, 1417–1419.

2. Pawar, B. N.; Ham, D.-H.; Mane, R. S.; Ganesh, T.; Cho, B. W.; Han, S. H.; *Appl. Surf. Sci.* **2008**, 254, 6294-6297.

3. Sanchez-Juarez, A.; Tiburcio-Silver, A.; Ortiz, A.; Zironi, E.P.; Rickards, J.; *Thin Solid Films* **1998**, 333, 196-202.

4. Huang, C.; Wang, M.; Deng, Z.; Cao, Y.; Liu, Q.; Huang, Z.; Liu, Y.; Guo, W.; Huang, Q.; *J Mater. Sci: Mater. El.* **2010**, 21, 1221–1227.

5. Maldonado, A.; Olvera, M. de la L.; Guerra, S. T.; Asomoza, R.; *Sol. Energ. Mat. Sol. C.* **2004**, 82, 75–84.

6. Huang, C.; Wang, M., Liu, Q., Cao, Y.; Deng, Z.; Huang, Z.; Liu, Y., Huang Q.; Guo, W., *Semicond. Sci. Tech*. **2009**, 24, 095019.

7. Zhu, J.; Zhang, H.; Zhu, Z.; Li, Q., Jin, G.; *Opt. Commun*. **2014**, 322, 66–72.

8. Duman, S.; Doğan, S.; Gürbulak, B., Türüt, M.; *Appl. Phys. A- Mater.* **2008**, 91, 337–340.

9. Chen, K.J.; Hung, F.Y.; Chang, S.J.; Hu, Z.S.; *Appl. Surf. Sci.* **2009**, 255, 6308–6312.

10. Sofiani, Z.; and Sahraoui, B.; *J. Appl. Phys*. **2007**, 101, 063104.

11. Choi, B.G.; Kim, I.H.; Kim, D.H.; Lee, K.S.; Lee, T.S.; Cheong, B.; Baik, Y.-J.; Kim, W.M.; *J. Eur. Ceram. Soc.* **2005**, 25, 2161–2165.

12. Maldonado, A.; Tirado-Guerra, S.; Cázares, J.M.; Olvera, M. de la L.; *Thin Solid Films* **2010**, 518, 1815–1820.

13. Zhang, K.; Zhu, F.; Huan, C. H. A.; Wee, A.T.S.; Osipowicz, T.; *Surf. Interface Anal*. **1999**, 28, 271–274.

14. Wen, Z. Z.; Zhong, H. L.; Qiu, Z. H.; Chang, S. J.; Ming, B. J.; Tong, S. K.; Xi, C.; Ze, Z. J.; Xue, L., Xia Z. J.; *Chinese Phys. Lett.* **2010**, 27, 017301.

15. Paraguay, F.D., Morales, J.; Estrada, W.L.; Andrade, E.; Yoshida, M. M.; *Thin Solid Films* **2000**, 366, 6-27.

16. Kumar, P. M. R.; Kartha, C.S.; Vijayakumar, K.P.; Abe, T.; Kashiwaba, Y.; Singh F.; Avasthi, D. K.; *Semicond. Sci. Tech*. **2005,** 20, 120–126.

17. Machado, G.; Guerra, D.N.; Leinen, D.; Barrado, J.R.; Marotti, R.E.; Dalchiele, E.A.; *Thin Solid Films* 2005, 490, 124–131.

DOI: http://dx.doi.org/10.32571/ijct.704871 **E-ISSN:2602-277X**

18. Sakthivelu, A.; Saravanan, V.; Anusuya, M.; Prince, J. J.; *J. Ovonic Res.* **2011**, 7 1-7.

19. Arredondo, E. J. L.; Maldonado, A.; Asomoza, R.; Acosta, D. R.; Lira, M.A. M.; Olvera, M. de la L.; *Thin Solid Film* **2005**, 490, 132 –136.

20. Ilican, S.; Caglar, Y.; Caglar, M.; Yakuphanoglu, F.; *Appl. Surf. Sci.* **2008**, 255, 2353–2359.

21. Kim, K.T.; Kim, G. H.; Woo, J. C.; Kim, C.; *Surf. Coat. Tech.* **2008**, 202, 5650-5653.

22. Khan Z. ; Khan, M.; Zulfequar, M.; Khan, M. S.; *Mater. Sci. Appl.* **2011**, 2(5), 340-345.

23. Derbali, S.; Nouneh, K.; Galca, A. C.; Touhami, M. E.; Secu, M.; Matei, E.; Leonat, L. N.; Pintilie, L.; Harfaoui, N.; Fahoume, M.; *Opt. Quant. Electron*. **2019**, 51, 210.

24. Cao, L.; Zhu, L.; Jiang, J.; Zhao, R.; Ye, Z.; Zhao, B., *Sol. Energ. Mat. Sol. C*. **2011**, 95, 894-898.

25. Yakuphanoglu, F.; Caglar, Y.; Ilican, S.; Caglar, M.; Physica B. **2007**, 394, 86–92.

26. Hernandez, R. G.; Martinez, A. I.; Falcony, C.; Lopez, A. A.; Pech-Canul, M.I.; Hdz-Garcia, H. M.; *Mater. Lett.* **2010**, 64, 1493–1495.

27. Tauc, J. *Amorphous and Liquid Semiconductors*, Plenum Press, New York, 1974.

ORCID

https://orcid.org/0000-0001-9875-4990 (S. Doğan)

DOI: http://dx.doi.org/10.32571/ijct.694558 **E-ISSN:2602-277X**

International Journal of Chemistry and Technology

http://dergipark.org.tr/ijct

Research Article

Dynamic mechanical properties of epoxy resin matrix reinforced with sugarcane bagasse

Mustapha ABDULLAHİ*

ID on the last page

Department of Chemistry, Ahmadu Bello University, Zaria, Kaduna state, Nigeria

Received: 25 February 2020; Final revised: 13 April 2020; Accepted: 17 April 2020

*****Corresponding author e-mail: mustychem19@gmail.com

Citation: Abdullahi, M. *Int. J. Chem. Technol.* **2020**, 4 (1), 43-48.

ABSTRACT

The dynamic mechanical analysis was performed on five different formulations of a reinforced epoxy resin matrix with sugarcane bagasse (SCB) using hand lay-up technique. The viscoelastic behaviours of the composites were studied by analyzing the thermal parameters such as storage modulus E'(MPa), loss modulus E''(MPa), and $\tan\delta$ as the temperature increases at periodic stress frequencies of 2.5, 5, and 10 Hz using Dynamic Mechanical Analyzer (DMA). The results revealed that E'(MPa) and E''(MPa) decreased with increasing temperature for all composites, while the $\tan\delta$ increased with increasing temperatures. As the frequency of oscillation is increased, the viscoelastic parameters was seen to increase as well. However, the $\tan\delta$ (damping coefficient) was found to decrease with increase in SCB fibre loading due to the good load-bearing capacity of the composites. The $\tan\delta$ peak temperature of the composites was found to be higher than the onset temperature of E'(MPa) and peak temperature of E''(MPa) which depict higher accuracy. Futhermore, it was seen that the increase in SCB fibre content in the epoxy resin increased the glass transition temperature (T_g).

Keywords: Viscoelastic parameters, storage modulus, loss modulus, epoxy resin; dynamic mechanical properties.

Şeker kamışı küspesi ile güçlendirilmiş epoksi reçine matriksinin dinamik mekaniksel özellikleri

ÖZ

Dinamik mekanik analiz, el yatırma tekniği kullanılarak şeker kamışı küspesi (SCB) ile güçlendirilmiş epoksi reçine matrisinin beş farklı formülasyonu üzerinde gerçekleştirildi. Kompozitlerin viskoelastik davranışları, dinamik mekanik analiz cihazı (DMA) kullanılarak sıcaklık 2,5, 5 ve 10 Hz lik periyodik stres frekanslarında arttıkça depolama modülü E'(MPa), kayıp modülü E''(MPa) ve $\tan\delta$ gibi termal parametrelerin analiz edilmesiyle incelendi. Sonuçlar, E'(MPa) ve E''(MPa)' nın tüm kompozitler için artan sıcaklıkla azaldığını gösterdi, halbuki $\tan\delta$ ise artan sıcaklıkla artmıştır. Salınım frekansı arttıkça viskoelastik parametrelerin de arttığı görüldü. Bununla birlikte, $\tan\delta'$ ın (sönümleme katsayısı) kompozitlerin iyi yük taşıma kapasitesi nedeniyle SCB fiber yükündeki artışla azaldığı bulundu. Kompozitlerin $\tan\delta$ pik sıcaklığının, daha yüksek doğruluğu gösteren E'(MPa) başlangıç sıcaklığından ve E''(MPa) pik sıcaklığından daha yüksek olduğu bulundu. Ayrıca epoksi reçinesindeki SCB içeriğindeki artışın ise camsı geçiş sıcaklığını (T_g) arttırdığı görüldü.

Anahtar Kelimeler: Viskoeleastik parametreler, depolama modülü, kayıp modül, epoksi reçine, dinamik mekanik özellikler.

1. INTRODUCTION

Nowadays, the natural-fibre reinforced polymeric materials have been utilized in many applications in a view of their easy availability, low cost, lightweight, high specific modulus, non-toxic and pollution-free production.[1] Due to the recent increase of environmental alertness, several studies were done on natural fibres as reinforcement or filler in composite so as to replace synthetic fibre.[2] Fundamentally, the use of natural fibre in polymers to form composite has numerous environmental benefits such as low pollutant, toxic chemical emissions, and increases dependence on non-renewable nergy ratio to material sources,

DOI: http://dx.doi.org/10.32571/ijct.694558 **E-ISSN:2602-277X**

enhanced energy recovery, low greenhouse gas emissions, and the end of life biodegradability of components. Such superior environmental performances are important driver of increased future use of natural fibre composites.[3] Advanced polymer composites are a relatively new set of materials that exhibit superior properties in comparison to traditional ones like steel and aluminum alloys in engineering applications.[3,4] In addition, natural fibres as reinforcement alternative in polymers have gained the attention of numerous material scientists because of their superior advantages over conventional carbon fibres and glass.[5,6] Dynamic thermomechanical analyzer (DTMA) is an instrument used for thermal analysis which measures the viscoelastic responses as the material deforms with temperature.[6] The viscoelastic response or parameter includes storage modulus (E'), loss modulus (E''), and modulus ratio (tan δ).[6] E' is defined as the stored energy per oscillating cycle which determines the elastic nature of the composite.[6] E'' is defined as the energy released per oscillating cycle which determines the viscous nature of the composite.[5,6] tan δ is the ratio between loss modulus to storage modulus which gives information about the viscoelastic nature or viscoelasticity of the composite material.[6] The oscillating frequency effects on the viscoelastic parameters of polymers were reported in many literatures, which gave information about the molecular motion on the polymer backbone.[6,7] Sugarcane bagasse fibres are environmental wastes that litter our environment. As such, utilizing the fibres as reinforcement or fillers in polymers could convert waste to wealth.[8] In our previous paper, we have reported the influence of the sugarcane bagasse powder addition on the viscoelastic parameters and activation energy of epoxy resin matrix at 10 Hz frequency only. However, glass transition temperature (T_g) and variation in frequencies on the viscoelastic parameters of the composites has not been reported.[9] Therefore, the ultimate goal of the present findings is to determine T_g, the effect of oscillation frequency on the viscoelastic parameters namely, E', E'', and tan δ as a function of the temperature of the SCB/Epoxy resin composite using dynamic mechanical analyzer (DMA).

2. EXPERIMENTAL

2.1. Methodology

The sample preparation method employed in this paper was adopted from our previous report.[9] Fresh sugarcane bagasse waste was sourced from a sugarcane juice center in Samaru Zaria of Kaduna State, Nigeria. The fresh bagasse was thoroughly washed with distilled water to remove sugar and dirt particles, then allowed to dried for two weeks. The dried sample was pulverized using a Lab milling equipment, and then sieved to 75 µm particle size using digital high-frequency sieve shaker. In addition, chemical pretreatment or fibre modification was not carried out in the present study. A bisphenol class of epoxy resin (3554A), and hardener (3554B) were supplied by a local supplier in Nigeria. In formulating the polymer composite, the hand lay-up method was adopted by manual stirring of the mixture with a rod, and the formulation of the SCB and epoxy resin were varied. The percent weight of reinforcement was weighed for the ratios of 0% wt (control), 10% wt, 20% wt, 30% wt, 40% wt and 50% wt of SCB/Epoxy while the epoxy matrix was formulated in the ratio of 2:1 (weight of epoxy resin to weight of hardener) as shown in Table 1.[9] The weighted matrix was mixed thoroughly with the SCB weight percentage at low speed for 15 min until the mixture became distributed evenly. Before demolding, petroleum jelly was applied to the surface of the mould with dimension (120 × 100 × 5 mm) before pouring the mixture into the mould. Thus, it prevents the composite from sticking to the mould and also aids the removal of the composite after curing. The composite was allowed to cure for 24 hours at temperature of 28°C before demoulding, then cut into suitable dimensions for further tests according to the ASTM standards.

Table 1. Nomenclature of the SCB/Epoxy resin composite materials.

Sample	Ratio	Matrix (g) 2:1		SCB (g)
		Epoxy resin	Hardener	
Pure Epoxy	100:0	66.60	33.30	0
10% wt SCB/Epoxy	10:90	60.00	30.00	10
20% wt SCB/Epoxy	20:80	53.24	26.76	20
30% wt SCB/Epoxy	30:70	46.60	23.40	30
40% wt SCB/Epoxy	40:60	40.00	20.00	40
50% wt SCB/Epoxy	50:50	33.30	16.70	50

2.2. Dynamic mechanical analyzer (DMA)

The DMA test was carried out using DMA 242E Artemis analyzer in the strength of materials laboratory, Mechanical Engineering Department, ABU Zaria in accordance with ASTM D7028 standard method.[10] The viscoelastic test parameters were initially configured via Proteus software using a personal computer. The viscoelastic response encompasses both elastic and viscous behavior of the composite. As such, the phase lag between applied oscillatory stress and the measured strain is between 0-90°. The applied stress (α), resultant strain (β), E', E'', and tan δ are given by the following equations.

DOI: http://dx.doi.org/10.32571/ijct.694558 **E-ISSN:2602-277X**

$$\alpha = \alpha_0 \sin(t\omega + \delta) \tag{1}$$

$$\beta = \beta_0 \sin(t\omega) \tag{2}$$

$$E' = \left(\frac{\alpha_0}{\beta_0}\right)\cos\delta \tag{3}$$

$$E'' = \left(\frac{\alpha_0}{\beta_0}\right)\sin\delta \tag{4}$$

$$\tan\delta = \left(\frac{E''}{E'}\right) \tag{5}$$

Where δ is the phase lag between stress and strain in MPa, ω is frequency of strain oscillation, α_0 is the stress amplitude, and β_0 is the strain amplitude.

However, the instrument was configured at furnace temperature range (30 to 120 degree Celsius), dynamic load/force (2.18 N), test frequencies (2.5, 5, and 10 Hz), and heating rate (5K/min) respectively. The sample with 40 x 12 x 5 mm dimension was loaded on to the machine using the three-point bending sample holder, then locked into the furnace to start the analysis. The rationale behind using the furnace temperatures of 30-120°C is to fully monitor the temperature scan as the materials deforms from glassy region at room temperature (lower temperature) to a rubbery region (higher temperature) where the material completely deforms. In addition, the T_g is expected to fall within this temperature range.

3. RESULTS AND DISCUSSION

3.1. DMA test curves and glass transition temperature (T_g)

DMA describes the stiffness stability of the composite material as a function of temperature when subjected to dynamic loading, and the modulus of materials is a measure of its stiffness property.[9,10] Figure 1 illustrates viscoelastic parameters such as E', E'', and tan δ of neat epoxy resin (control) with increasing temperature at oscillation frequencies of 2.5, 5, and 10 Hz respectively. The E' (MPa) curve shows the stability of the neat matrix under dynamic loading with an onset temperature of 35.6°C and inflection point of 38.8°C at 10 Hz. The E''(MPa) curve depicts peak maximum at 31.2°C (193 MPa) while tan δ curve describes the viscoelasticity of a neat epoxy resin matrix with a peak temperature of 63.2°C (1.056) at 10 Hz.

In **Figure 2**, the E'(MPa) curve displays an increased onset temperature of 38.0°C and inflection temperature of 41.7°C due to the incorporation of 10% wt of SCB into the matrix. The E''(MPa) curve also shows an increased onset temperature of 36.0°C (57 MPa), while tan δ curve indicates a decrease in peak temperature of 59.9°C (1.018).

Figure 3 shows better thermal stability of the 20% wt SCB/Epoxy composite under dynamic loading with an onset temperature of 45.60°C on E' curve at 10 Hz when compared to the neat epoxy resin and 10% wt SCB reinforcements respectively. The E'' curve depicts an increase in energy dissipation at peak maximum of 41.0°C (118 MPa), while the tan δ curve reveals an increased peak temperature of 66.5°C (0.716) compared to neat epoxy.

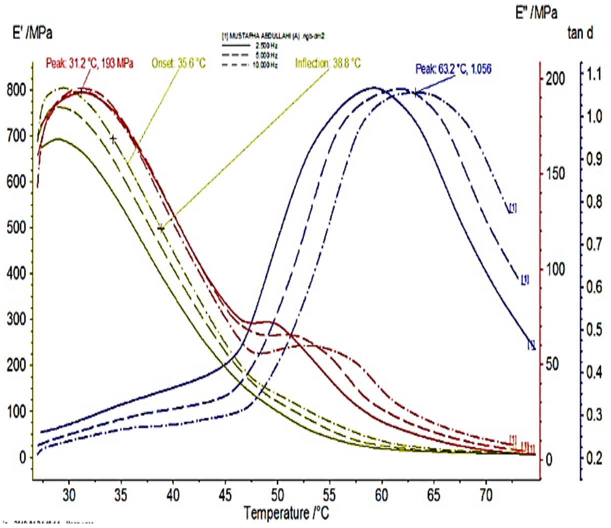

Figure 1. DMA test curves for 0% wt SCB/Epoxy resin composite at oscillation frequencies of 2.5, 5, and 10 Hz (neat epoxy).

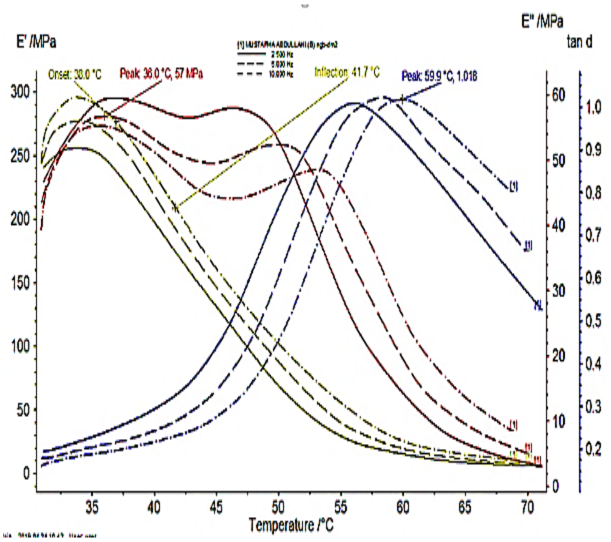

Figure 2. DMA test curves for 10% wt SCB/Epoxy resin composite at oscillation frequencies of 2.5, 5, and 10 Hz.

DOI: http://dx.doi.org/10.32571/ijct.694558 **E-ISSN:2602-277X**

The *E'* curve of 30% wt SCB/Epoxy resin composite reveals similar thermal stability compared to 20% wt SCB reinforcement with an onset temperature of 44.0°C. Also, the peak maximum at 40.6°C and 158 MPa of loss modulus was observed, while the viscoelastic nature is eminent at tan δ value of 0.689 and peak temperature of 66.7°C as shown in Figure 4.

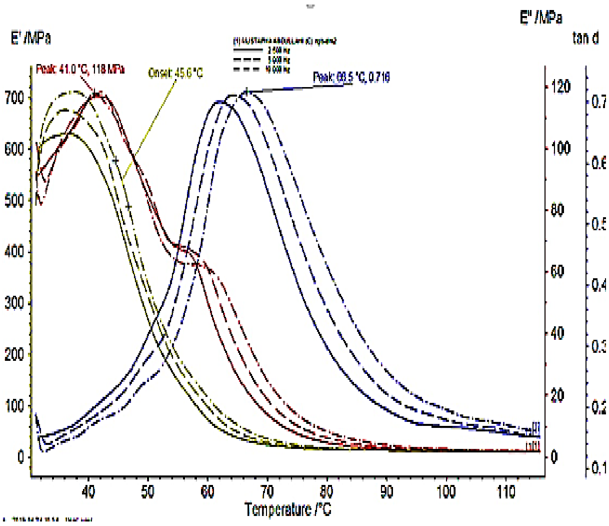

Figure 3. DMA test curves for 20% wt SCB/Epoxy resin composite at oscillation frequencies of 2.5, 5, and 10 Hz.

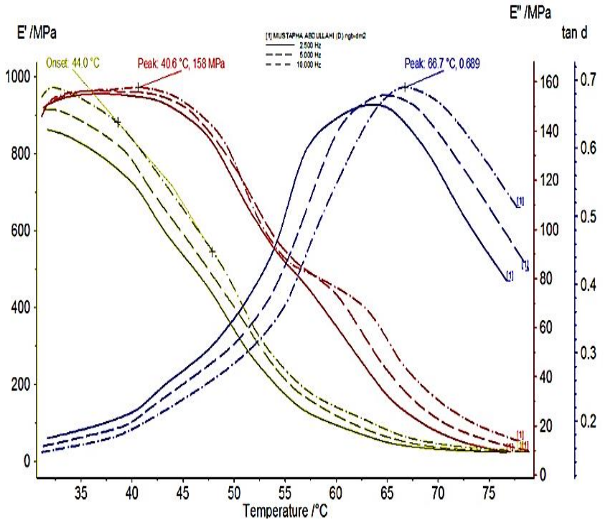

Figure 4. DMA test curves for 30% wt SCB/Epoxy resin composite at oscillation frequencies of 2.,5, 5, and 10 Hz.

Similar improvement in thermal stability is observed in *E'* curve for 40% wt SCB under dynamic loading at an onset temperature of 43.0°C and inflection point of 46.0°C respectively. The peak maximum of *E''* was observed at 36.3°C (169 MPa) and the viscoelastic nature of the composite is imminent with a loss factor of 0.683 and peak temperature (67.8°C) as shown in Figure 5.

In Figure 6, the *E'* curve shows that the 50% wt SCB/Epoxy composite under dynamic loading before the onset temperature (54.1°C) and inflection point (60.3°C) at 10 Hz.

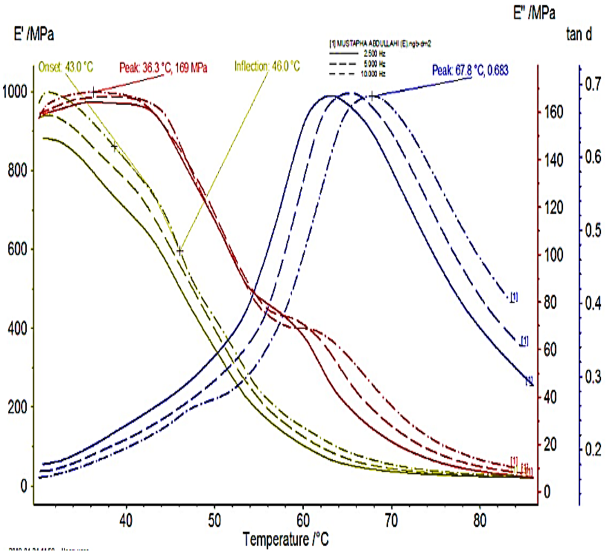

Figure 5. DMA test curves for 40% wt SCB/Epoxy resin composite at oscillation frequencies of 2.5, 5, and 10 Hz.

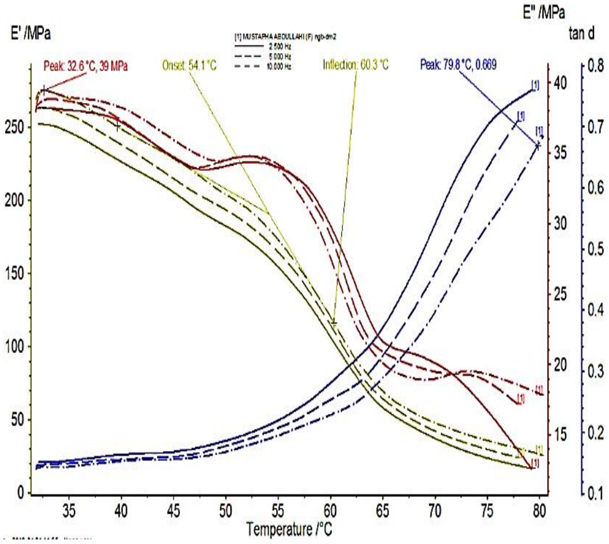

Figure 6. DMA test curves for 50% wt SCB/Epoxy resin composite at oscillation frequencies of 2.5, 5, and 10 Hz.

The *E*" curve depicts a peak maximum at 32.6°C and 39 MPa. However, the viscoelastic nature of the composite is eminent at the tan δ value of 0.669 and peak temperature of 79.8°C.

From the above DMA curves (Figures 1-6), it can be observed that E'(MPa) and $E"$(MPa) curves decrease with an increase in temperature for all composites, while the $\tan\delta$ curve increases with an increase in temperatures up to a particular peak height before decreasing. The steep decrease in E'(MPa) and $E"$(MPa) curves depict the glass transition region which is attributed to the enhancement of molecular motion with gain of energy.[11] Also, it can be seen that the viscoelastic parameters increase with an increase in the oscillation frequencies. The T_g is defined as the temperature region at which composite material changes from a glassy, "rigid" to a rubbery state.[13,14] In physical chemistry of polymers, the T_q region is the region where the polymer chains gains sufficient energy to increase the molecular mobility or motion in the matrix which resulted a sudden change in its physical and mechanical properties.[15] The T_g computed by storage modulus (E'), loss modulus (E'') and tan δ curves for the SCB reinforced epoxy composites are not alike. The tan δ peak temperatures in this study are found to be higher than the peak temperatures obtained from E'(MPa) and $E"$(MPa) respectively. In essence, the T_g is recorded as the onset temperature for E'(MPa) curve, peak temperature for $E"(MPa)$ and $\tan\delta$ curve accordingly. The summary of the recorded glass transition temperatures for the SCB reinforced epoxy resin composites obtained from the DMA test curves at 10 Hz is shown in Table 2. It is deduced that increase in the SCB fibre content increases the glass transition temperatures. In addition, the higher values of the T_g obtained from the tan δ curve depicts higher accuracy.[16] The results show the increase in E'(MPa) and $E"$(MPa) values with an increase in SCB fibre content in the epoxy matrix due to good interfacial adhesion between the fibre and the matrix which increased its thermal stability.[6,9]

3.2. Viscoelastic parameters at different oscillating frequencies

The viscoelastic parameters of composites are the E', E'', and tan δ. The storage modulus of a polymer composite material describes how materials are stiffer.[12] The loss modulus of a polymer composite material is defined as the highest energy dissipated by the composite material during deformation, and it is the viscous response which depends upon the motion of polymeric molecules in the composite.[12] tan δ coefficient or loss factor of a polymer composite gives balance information between the elastic and viscous phases in a polymeric structure.[10,12] The variation in oscillation frequencies (2.5, 5, and 10 Hz) of the viscoelastic parameters in the glass transition region is reported in Table 3. From the results, it is deduced that the viscoelastic parameters increase with an increase in the frequency of oscillation. This may be attributed to the increase in number of dynamic cycles which resulted more rapid or faster molecular motion of the polymer chain thereby increasing the viscoelastic parameters.[10]

Table 2. Peak temperatures for SCB/Epoxy resin composites

Composites	T_g (°C) from E' Onset peak (10 Hz)	T_g (°C) from E'' peak (10 Hz)	T_g (°C) from tan δ peak (10 Hz)
0% wt SCB/Epoxy	35.6	31.2	63.2
10% wt SCB/Epoxy	38.0	36.0	59.9
20% wt SCB/Epoxy	45.6	41.6	66.5
30% wt SCB/Epoxy	44.0	40.6	66.7
40% wt SCB/Epoxy	43.0	36.3	67.8
50% wt SCB/Epoxy	54.1	32.6	79.8

Table 3. Viscoelastic parameters at glass transition peak heights

Composites	Frequency (Hz)	E'(MPa)	E''(MPa)	tan δ
0% wt SCB/Epoxy	2.5	547.876	192.624	0.9949
	5	617.238	193.031	1.05731
	10	663.154	193.660	1.0560
10% wt SCB/Epoxy	2.5	226.263	55.3441	0.92433
	5	250.042	56.8887	0.99475
	10	265.18	57.0000	1.0180
20% wt SCB/Epoxy	2.5	456.291	117.160	0.65640
	5	487.146	117.818	0.70335
	10	550.016	118.000	0.7180
30% wt SCB/Epoxy	2.5	564.515	154.170	0.64665
	5	620.71	155.800	0.67454
	10	687.712	158.000	0.68900
40% wt SCB/Epoxy	2.5	626.772	164.133	0.63127
	5	690.128	166.409	0.66776
	10	744.173	169.000	0.6830
50% wt SCB/Epoxy	2.5	155.751	38.2076	0.62111
	5	165.982	38.8292	0.65721
	10	174.522	39.0000	0.6690

4. CONCLUSIONS

The dynamic mechanical analysis is carried out successfully on five different formulations of SCB/Epoxy resin composites at different oscillation frequencies (2.5, 5, and 10 Hz) and the following conclusions are attained.

- The viscoelastic parameters (E', E'' and $\tan\delta$) increase with an increase in oscillation frequencies.
- The storage modulus E'(MPa) and loss modulus E''(MPa) decrease with an increase in temperature for all composites, while the $\tan\delta$ increases with the increases in temperatures up to the highest peak before decreased.
- The peak temperature of $\tan\delta$ of the composites are higher than the onset temperature from E'(MPa) and peak temperature of E''(MPa). However, an increase in SCB fibre content increases the T_g of the composites.

- The acceptable dynamic mechanical properties of these optimum composites reveals that they can have end-use application in making the laminated circuit board and electronic component encapsulation.

Conflict of interests

Author declares that there is no a conflict of interest with any person, institute, company, etc.

REFERENCES

1. Raghavendra, S.; Sivaram, N. M.; Sadik, T.; Prabhakara, S. *Adv. Mater.* **2018**, 7 (3), 78-86.

2. Kalagi, G. R.; Patil, R.; Nayak, N. *Proceed.* **2018**, 5 (1), 2588-2596.

3. Neves Monteiro, S.; Salgado de Assis, F.; Ferreira, C.; Tonini Simonassi, N.; Pondé Weber, R.; Souza Oliveira, M.; Pereira, A. *Polym.* **2018**, 10 (3), 246-257.

4. Kumar, T. V.; Chandrasekaran, M.; Santhanam, V.; C. *ARPN J. Eng. Appl. Sci.* **2017,** 12 (8), 2401-2406.

5. Gheith, M. H.; Aziz, M. A.; Ghori, W.; Saba, N.; Asim, M.; Jawaid, M.; Alothman, O. Y. *J. Mater. Res. Tech.* **2019**, 8 (1), 853-860.

6. Obada, D. O.; Kuburi, L. S.; Dauda, M.; Umaru, S.; Dodoo-Arhin, D.; Balogun, M. B.; Iorpenda, M. J. *J. King Saud Uni-Eng. Sci.* **2018**.

7. Kumar, D.; Abhishek, N.; Vandana, P.; Ray, B. C. *Int. J. Curr. Eng. Sci. Res.* **2017**, 40 (7), 32-36.

8. Dan-asabe, B. *J. King Saud Uni-Eng. Sci.* **2016**, 30 (4), 296-304.

9. Abdullahi, M.; Mamza, P. A.; Shallangwa. G. A. *Amer. J. Polym. Sci. Tech*. **2018**. 4 (3), 53-60.

10. ASTM D7028-07, ASTM Int. 2015.

11. Danasabe, B.; Yaro, A. S.; Yawas, D. S.; Aku, S. Y. *Pak. J. Eng. Appl. Sci.* **2018**, 23 (2), 8-16.

12. Devangamath, S. S.; Lobo, B.; Masti, S. P.; Narasagoudr, S. *Polym. Fib.* **2018**, 19 (7), 1490-1499.

13. Jacob, J.; Mamza, P. A.; Ahmed, A. S.; Yaro, S. *Bayero J. P. Appl. Sci.* **2018**, 11 (1), 139-144.

14. Atiqah, A.; Jawaid, M.; Sapuan, S. M.; Ishak, M. R. *Polym. Comp.* **2019**, 40 (4), 1329-1334.

15. Luz, F. *Mater. Res.* **2018**, 21, 2-6.

16. Gupta, M. K. *J. Mater. Environ. Sci.* **2018**, 9 (1), 100-106.

ORCID

https://orcid.org/0000-0002-8533-6245 (M. Abdullahi)

DOI: http://dx.doi.org/10.32571/ijct.695754 **E-ISSN:2602-277X**

International Journal of Chemistry and Technology

http://dergipark.org.tr/ijct

Research Article

Molecular structure, frontier molecular orbitals, NBO, MESP and thermodynamic properties of 5,12-dibromo perylene with DFT calculation methods

Murat AKMAN[1], Ahmet Cagri ATA[1,*], Ümit YİLDİKO[2], İsmail CAKMAK[1]

ID on the last page

[1]*Faculty of Arts and Sciences. Department of Chemistry, Kafkas University, Kars, 36100, Turkey*

[2]*Architecture and Engineering Faculty, Department of Bioengineering, Kafkas University, Kars, 36100, Turkey*

Received: 27 February 2020; Final revised: 03 May 2020; Accepted: 05 May 2020

*****Corresponding author e-mail: *ahmetata1024@gmail.com*

Citation: Akman, M.; Ata, A. C.; Yildiko, Ü.; Cakmak, İ. *Int. J. Chem. Technol.* **2020**, 4 (1), 49-59.

ABSTRACT

Perylene-3,4,9,10-tetracarboxylic dianhydride (PTCDA) has been used as industrial pigments for many years. This perspective makes it important to determine the synthesis and physical properties of PTCDA derivatives and their functional properties for application as electron acceptors in organic transistors. In the gas phase, the quantum chemical study of the 5,12-dibromoperylene compound was performed using the basic set of LanL2DZ and 6-311G of the density function theory (DFT)-B3LYP method. Because basic set of LanL2DZ and 6-311G of the density function theory (DFT)-B3LYP method are predicted to yield more efficient and verifiable results than others. ^{1}H-NMR, ^{13}C-NMR, HOMO-LUMO analysis, dipole moment, molecular electrostatic surface potential (MESP) and natural orbital bond (NBO) analysis of the molecule were carried out. The results were shown with graphs, tables and figures. In the comparison of ^{1}H-NMR, ^{13}C-NMR results with the experimental values, B3LYP 6-311G gave more successful results. The nonlinear optical properties of the compound were determined.

Keywords: PTCDA derivatives, DBP, DFT, LanL2DZ.

5,12-dibromo perilenin DFT hesaplama yöntemleri ile moleküler yapısı, sınır moleküler orbitalleri, NBO, MESP ve termodinamik özellikleri

ÖZ

Perylene-3,4,9,10-tetrakarboksilik dianhidrit (PTCDA) birçok yıldan beri endüstriyel pigmentler olarak kullanılmaktadır. Bu bakış açısı, PTCDA türevlerinin sentez ve fiziksel özelliklerinin ve bunların organik transistörlerde elektron alıcısı olarak uygulanacak fonksiyonel özelliklerinin belirlenmesini önemli kılmaktadır. Gaz fazında, 5,12-Dibromoperyilen bileşiğinin kuantum kimyasal incelemesi, yoğunluk fonksiyonu teorisi (DFT) -B3LYP yönteminin temel LanL2DZ ve 6-311G seti kullanılarak gerçekleştirildi. Çünkü, yoğunluk fonksiyon teorisinin temel LanL2DZ ve 6-311G (DFT)-B3LYP yönteminin diğerlerinden daha verimli ve doğrulanabilir sonuçlar vereceği tahmin edilmektedir. ^{1}H-NMR, ^{13}C-NMR, HOMO-LUMO analizi, dipol momenti, moleküler elektrostatik yüzey potansiyeli (MESP) ve molekülün doğal orbital bağı (NBO) analizi yapıldı. Sonuçlar grafikler, tablolar ve şekillerle gösterildi. ^{1}H-NMR, ^{13}C-NMR sonuçlarının deneysel değerlerle karşılaştırılmasında B3LYP 6-311G daha başarılı sonuçlar verdi. Bileşiğin doğrusal olmayan opik özellikleri belirlendi.

Anahtar Kelimeler: PTCDA türevleri, DBP, DFT, LanL2DZ.

1. INTRODUCTION

Organic semiconductors and aromatic compounds are used in the production of many electronic devices.[1] thermal,[2-3] electrical, optical,[4-5] and properties of these materials can be improved by using new functional organic groups. Thus, it will provide the opportunity to design low-cost material for device applications.[6] The subject of our study may be perilen-3,4,9,10-tetracarboxylic dianhydride (PTCDA), organic type semiconductor based batteries and candidate materials for organic batteries.[7-8] Battery systems, one of the most important needs of today's electronic technology, are important in providing effective results.

However, in addition to its use as an important industrial pigment, PTCDAs exhibit many interesting properties such as near-unit products that enable them to be used in many new advanced applications, high photochemical stability and high electron uptake.[9-10] To date, PTCDAs have been utilized in a variety of electronic and optical applications, such as fluorescent solar collectors, electro-photographic devices, dye lasers, organic photovoltaic cells,[10] and optical energy limiters, due to their special physical, optical and electronic properties, in addition to being associated with their derivatives. In many of these applications, it plays a key role in the relatively pure and reversible reduction of PTCDAs. These pure reductions have led to their widespread use in basic research on photo-induced energy and electron transfer processes, the combination of easily identifiable excited state, anion and dianion absorption spectra. PTCDA derivatives,[10] an important monomer in the preparation of polymer materials, are indispensable. Density functional theory (DFT) is one of the most popular and versatile methods available in quantum chemistry and is used in many studies.[11-16]

In this study, the ab-initio calculations of the 5,12-dibromoperylene (DBP) molecule, which was synthesized by our group, were made in Gaussian 09 program. For DBP molecule, it was first plotted in ChemBioDraw program and minimized by SYBL2 (mol2) method with Chem3D program. DBP was optimized by using DFT/LanL2DZ and 6-311G basis set. The ^{1}H NMR and ^{13}C NMR spectra of the molecule were compared with the experimental results.

2. MATERIALS AND METHODS

3.1. Computer calculations

The DBP molecule synthesized by our group was first drawn in ChemBioDraw for each molecule for ab-initio calculations in Gaussian 09 program[17] and minimized by SYBL2 (mol2) method with Chem3D program. Minimized molecules were given to Gaussian 09 program and ab-initio calculations were made for each structure.

3. RESULTS AND DISCUSSION

3.1. Geometry optimization

In both research and industrial settings, the primary starting material for synthesizing PCTDA was optimized using powerful computational software of Gaussian 09 and by DFT / B3LYP and DBP methods with 6-311 ++ G (d, 2p) and LanL2DZ basis sets. Then the value of bond lengths amounts and angles between its constituent atoms were compared with each other from optimized structure and using two mentioned methods.[18] Calculations were made using the Density Function Theory / Becke-3- LeeYang-Parr (DFT / B3LYP)[19,20] method, which is a quantum mechanical method. The main idea that DFT is based on is to determine the energy of the molecule by using electron density instead of the wave function. The superiority of DFT methods is that the electron correlations are included in the calculations and the results obtained are in better agreement with the experimental results. It also requires less calculation. DFT is a variational method. The most used method in the DFT method is BLYP (Becke, Lee, Yang and Parr) and the B3LYP method formed by the modification of BLYP. Therefore, LanL2DZ (Hay and Wadt's effective core potential) basic set of DFT / B3LYP method was used in our calculations. In very large nuclei, near-nucleus electrons are treated as approximately effective nucleus potential (ECPs).[21] This behavior includes some relative effects that are important for these atoms. Since the LanL2DZ basic set is the best known, this set was used in our calculations. DBP optimized baseline structure and total energy conversion are given in Figure 1. Optimized bond length parameters of the molecule calculated with the basis set of 6-311G (d, p) and LanL2DZ of DFT-B3LPY are listed in Table 1. Comparison of two optimized methods of DBP compound was performed. With this optimization, it gives the molecule the minimum energy. A method is presented for generating a good initial guess of a transition path between given initial and final states of a system without evaluation of the energy. The bond lengths and bond angles in the aromatic phenyl rings are of normal value.

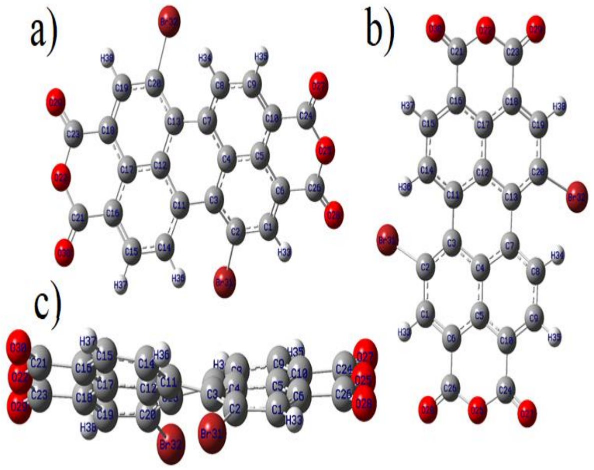

Figure 1. Optimized structures of the DBP compound from a different perspective.

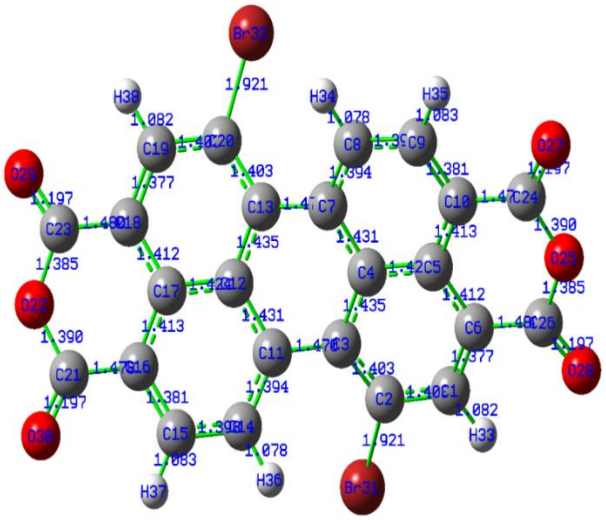

Figure 2. Optimized bond lengths of the DBP compound

C-C bond lenghts is 1.37-1.48 Å for DFT and 1.39 to 1.48 Å for LanL2DZ, and 1.19 to 1.38 Å for these values for C-O belong to the oxygen atom between the two phenyl rings. The C-H lengths in the aromatic ring are 1.07-1.08 Å and the C-Br length is 1.93 Å. All C-C-C angles range from 118° to 126°. The C-C-H angle in the compound is 119°-121°, C-C-O 117°-124°, Br- C-C 114°-124° and O-C-O 119°. In our study, the theoretically calculated molecule shows that the bond lengths and bond angles are compatible with the literature data and the results are consistent.[22,23] Some of the dihedral angles show negative results in the degree of angle in the Gaussian 09 program when atoms are selected as dihedral bonds. These calculated numbers depend on the state of the atoms in the bonds and in their place were valuable. There are very small differences between the DFT and LanL2DZ values.

Table 1. Theoretically obtained BL (A^o) and BA (^{o}) of the molecule

BL(A^o)	**6-311G**	**LanL2DZ**	**BA** (^{o})	**6-311G**	**LanL2DZ**
C2-C1	1.40276	1.41287	C3-C2-C1	121.87902	121.79513
C6-C1	1.37715	1.39016	C1-C2-Br31	113.47705	113.18623
C1-H33	1.08169	1.08493	C1-C6-C5	119.96614	119.95634
C2-C3	1.40269	1.41388	C1-C6-C26	119.49842	119.00333
C2-Br31	1.92060	1.97217	C2-C1-C6	120.46872	120.50160
C4-C5	1.42377	1.43324	C2-C1-H33	120.33833	120.63480
C4-C7	1.43137	1.44185	C3-C2-C1	121.87902	121.79513
C8-H34	1.07783	1.07995	C3-C2-Br31	124.54819	124.86472
C9-C10	1.38099	1.39355	C6-C26-O25	116.71404	116.39006
C14-H36	1.07783	1.07997	C6-C26-O28	124.90317	125.31475
C15-C16	1.38098	1.39357	C10-C9-H35	119.34112	119.20788
C15-H37	1.08274	1.08543	C10-C24-O25	116.90499	116.55425
O22-C23	1.38496	1.41655	O22-C21-O30	118.04399	117.94383
C23-O29	1.19732	1.23084	O22-C23-O29	118.38186	118.29606
C24-O25	1.38960	1.42158	C24-O25-C26	125.53681	125.11154
O25-C26	1.38494	1.41657	O25-C24-O27	118.04343	117.94444
C26-O28	1.19732	1.23084	O25-C26-O28	118.38271	118.29512

Theoretically calculated values of some perylene compounds can give an idea about the geometry of molecular changes.[24]

Table 1 shows optimized bond lengths and bond angles based on DFT-B3LPY / 6-311G (d, p) and LanL2DZ. The difference is very small and shows a good fit between the two systems. Table 2 shows theoretically obtained dihedral bond angles of the molecule.

3.2. ^{13}C NMR ve ^{1}H NMR spectral analysis

NMR spectroscopy is used to determine the content and purity of a sample. Also, molecular structure, conformation, solubility etc. parameters can be used to estimate. ^{13}C NMR and ^{1}H NMR chemical shifts were calculated by DFT-B3LPY / 6-311G (d, p) and LanL2DZ methods in the gas phase of the conformers of DBP.[25]

DOI: http://dx.doi.org/10.32571/ijct.695754 **E-ISSN:2602-277X**

Table 2. Theoretically obtained dihedral bond angles of the molecule (^{o}).

Dihedral Angles	6-311G	LanL2DZ
C1-C2-C3-C4	9.29497	9.27679
C1-C2-C3-C11	-168.94056	-168.52963
C1-C6-C5-C4	1.20436	1.70608
C1-C6-C26-025	-179.70499	179.39721
C1-C6-C26-O28	0.18758	-0.69970
C1-C6-C5-C10	-178.94833	-178.48016
C3-C2-C1-H33	178.57447	178.37931
C3-C4-C5-C10	-171.73565	-172.50192
C3-C4-C7-C8	169.25017	169.88180
C3-C4-C7-C13	-8.90052	-8.51608
C3-C11-C14-H36	3.77654	4.32008
C4-C3-C2-Br31	-166.91181	-165.90146
C5-C6-C1-H33	175.96350	175.90540
C5-C6-C26-O25	2.11829	1.29264
C5-C6-C26-O28	-177.98914	-178.80428
C5-C10-C24-O25	2.22711	1.35794
C4-C3-C2-Br31	-166.91181	-165.90146
C6-C1-C2-Br31	176.34344	175.16669
H33-C1-C2-Br31	-4.83131	-5.92354
H38-C19-C20-Br32	-4.83676	-5.89966
H34-C8-C9-H35	0.21872	-0.42258
H37-C15-C14-H36	0.21484	-0.42420

In this study, NMR chemical shifts were calculated using GIAO-B3LYP method and 6-311G + (d, p) basis set. The theoretical spectra obtained from the calculation results are shown in Figures 3-6.

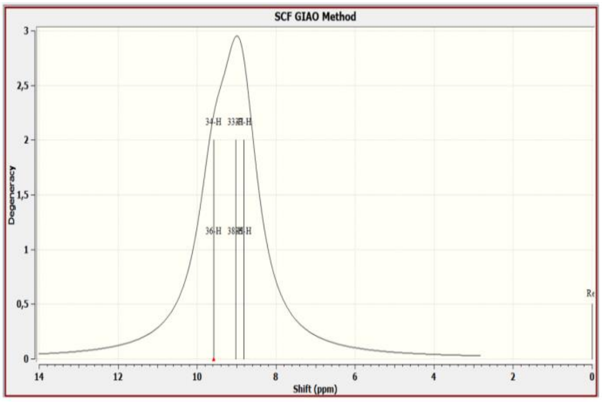

Figure 3. DBP DFT ^{1}H NMR spectra**.**

Experimentally obtained ^{1}H NMR and ^{13}C NMR spectra are presented in Figures 7 and 8. The experimental and theoretical ^{1}H NMR and ^{13}C NMR chemical shifts (ppm) in Tables 3 and 4 are listed and compared. ^{13}C NMR chemical shift graph of the comparison results is given in Figure 9. The DBP molecule has 6 H in the phenyl ring.

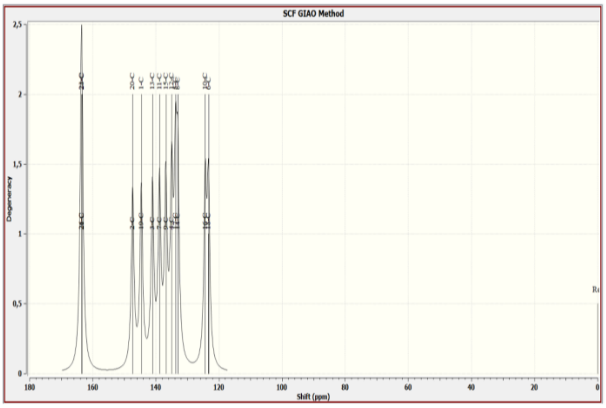

Figure 4. DBP DFT ^{13}C NMR spectra.

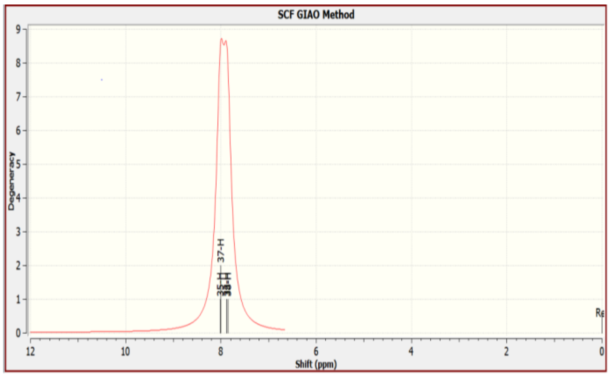

Figure 5. DBP LanL2DZ ^{1}H NMR spectra.

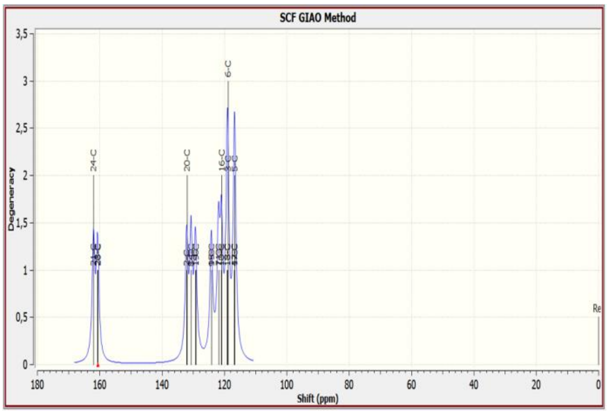

Figure 6. DBP LanL2DZ ^{13}C NMR spectra.

The chemical shift of these hydrogens was observed in the range of 8.89-9.56 ppm. Calculation for 6-311 G was found (H37-H35), (H33-H38) and (H34-H36) 8.92-8.10, 9.03-7.84 and 9.56-13.3 ppm. Since the calculation is in the gas phase, there may be deviations from the actual value. The chemical shift (ppm) of the hydrogens bonded to C-H groups was 8.91-8.00 ppm.

DOI: http://dx.doi.org/10.32571/ijct.695754 **E-ISSN:2602-277X**

The electronic environment of the proton can have a major impact on the chemical shift.[26] NMR results are consistent with the results obtained in previous studies. The regression graph shown in Figure 10 was found to be a good match for ^{13}C-NMR. Correlation was calculated as R = 0.97 (6-311G) and R = 0.92 (LanL2DZ).

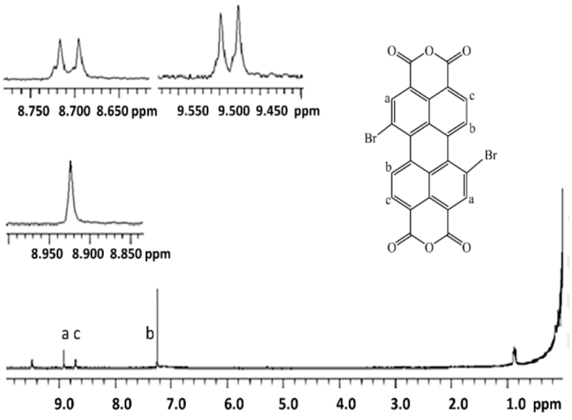

Figure 7. DBP experimental ^{1}H NMR spectra.

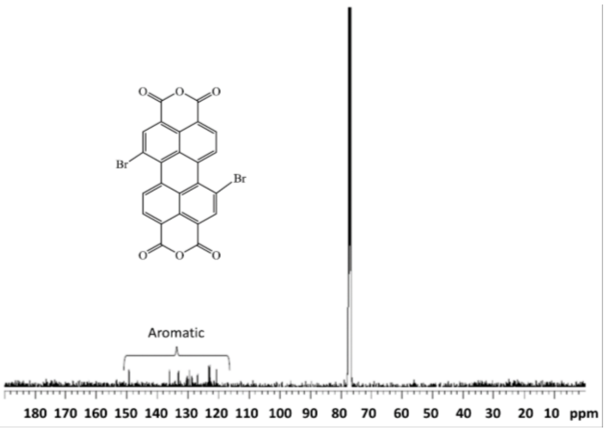

Figure 8. DBP ^{13}C NMR spectra.

3.3. Frontier molecular orbitals

The basic electronic parameters of the molecule can be calculated by predicting the highest occupied molecular orbital (HOMO) and the lowest unoccupied molecular orbital (LUMO) and bandgap. HOMO which can function as an electron donor, and LUMO which have enough space to accept electrons and can act as an electron acceptor are border orbitals.[27-29] Figures 11 and 12 show the densities of the orbital representation of HOMO and LUMO for the DBP molecule. LUMO$_{+1}$ and HOMO$_{-1}$ graphs of the compound were also obtained. HOMO -6.97 eV - LUMO -4.42 eV for the

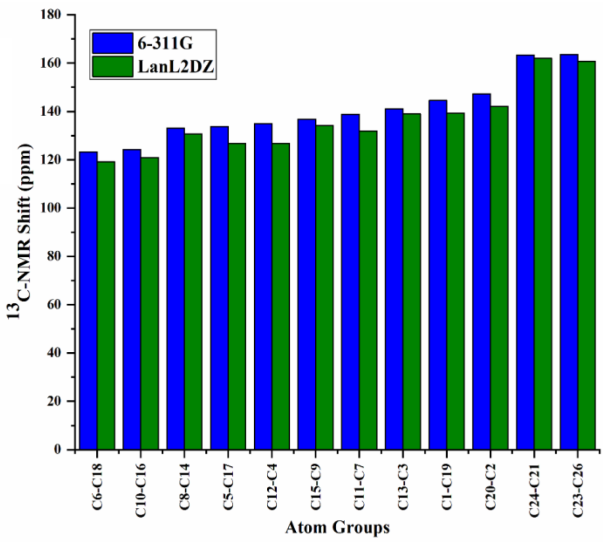

Figure 9. ^{13}C NMR chemical shift graph of DBP compound.

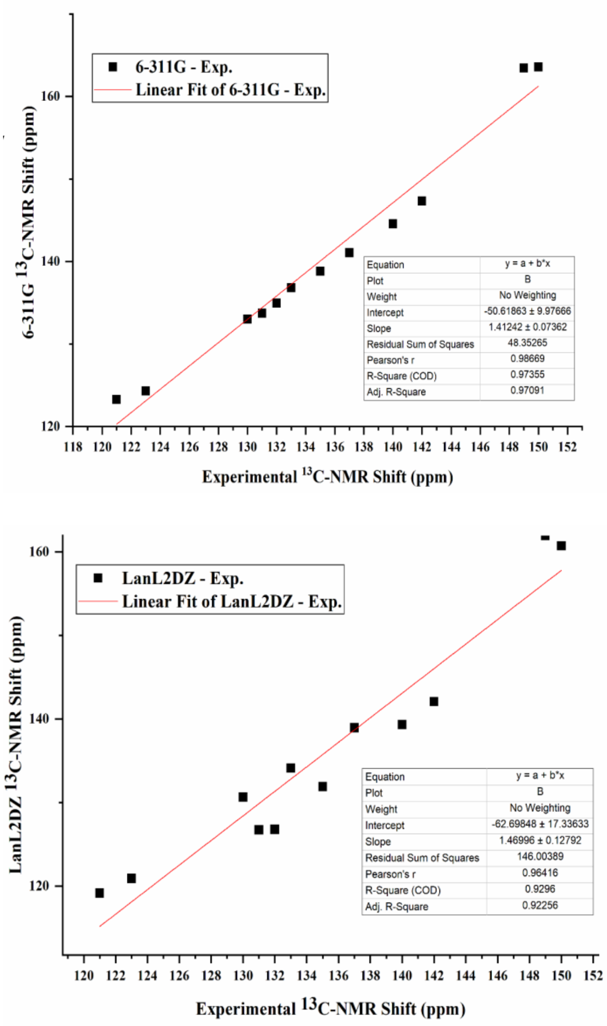

Equation	y = a + b*x
Plot	B
Weight	No Weighting
Intercept	-50.61863 ± 9.97666
Slope	1.41242 ± 0.07362
Residual Sum of Squares	48.35265
Pearson's r	0.98669
R-Square (COD)	0.97355
Adj. R-Square	0.97091

Equation	y = a + b*x
Plot	B
Weight	No Weighting
Intercept	-62.69848 ± 17.33633
Slope	1.46996 ± 0.12792
Residual Sum of Squares	146.00389
Pearson's r	0.96416
R-Square (COD)	0.9296
Adj. R-Square	0.92256

Figure 10. Correlation graph of ^{13}C-NMR experimental and theoretical results of DBP compound.

DOI: http://dx.doi.org/10.32571/ijct.695754 **E-ISSN:2602-277X**

Table 3. DFT-B3LPY / 6-311G (d, p) and LanL2DZ ^{13}C- NMR theoretical results for DBP molecule.

	Experi mental	**6-311G**	**LanL2DZ**
Atoms	**Shift (ppm)**	**Shift (ppm)**	**Shift (ppm)**
C6-C18	121	123.29	119.15
C10-C16	123	124.32	120.91
C8-C14	130	133.02	130.65
C5-C17	131	133.73	126.73
C12-C4	132	134.96	126.80
C15-C9	133	136.83	134.14
C11-C7	135	138.82	131.90
C13-C3	137	141.05	138.95
C1-C19	140	144.59	139.33
C20-C2	142	147.33	142.10
C24-C21	149	163.43	161.97
C23-C26	150	163.57	160.73

Table 4. For DBP molecule, DFT-B3LPY / 6-311G (d, p) and LanL2DZ ^{1}H-NMR theoretical results are given.

	Experimental	**6-311G**	**LanL2DZ**
Atom Groups	**Shift-(ppm)**	**Shift-(ppm)**	**Shift-(ppm)**
37-35	8.71-8.91	8.91	8.00
38-33	7.03	9.02	7.85
36-34	9.51	9.57	7.98

DFT method and HOMO -7.10 eV - LUMO -4.60 eV for the LanL2DZ method were calculated from thefigure. For other orbitals; HOMO$_{-1}$ -8.06 eV-LUMO$_{+1}$ 3.02 eV for the DFT method and HOMO$_{-1}$ -8.19 eV - LUMO$_{+1}$ 3.19 eV for the LanL2DZ method were calculated. Because, properties such as molecular orbitals (HOMO-LUMO) and energy are very useful for physicists and chemists and are very important for quantum chemistry. Analyzes of boundary molecular orbitals define an electron impulse from the HOMO to the LUMO. The energy of HOMO is directly related to its ionization potential, and the energy of LUMO is directly related to the electron affinity. The HOMO and LUMO energy gap explains the possible charge transfer in the interaction with molecules. A boundary orbital space with a molecule is often linked to high chemical reactivity, low kinetic stability, and softly expressed molecules**.** HOMO and LUMO orbitals determine how the molecule interacts with other compounds. It also helps to characterize band gap, chemical reactivity and kinetic stability. A small boundary shows the polarization, stiffness, electronegativity and other reactivity indices of a molecule with an orbital space. Table 5 shows the chemical reactivity indices.

Table 5. Comparison of HOMO-LUMO, band gaps (HOMO - LUMO) and related DBP (eV) chemical properties.

Molecular Energy	**6-311G**	**LanL2DZ**
LUMO	-4.42	-4.60
HOMO	-6.97	-7.09
(ΔE) Band Gaps	-2.55	-2.49
$(I = -E_{HOMO})$	6.97	7.09
$(A = -E_{LUMO})$	4.42	4.60
$(\eta = (A - I)/2)$	1.27	1.25
$(s = 1/2 \ \eta)$	0.64	0.62
$(\mu = -\chi)$	-5.69	-5.85
$(\chi = (I + A)/2)$	5.69	5.85
$(\omega = \mu^2 / 2\eta)$	12.75	13.69

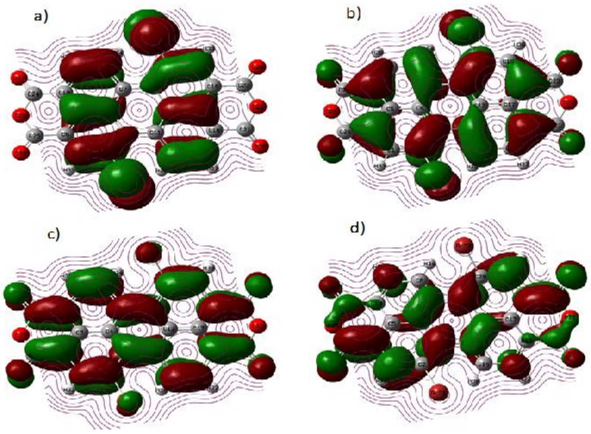

Figure 11. For the DBP molecule a) DFTHOMO$_{-1,}$ b) DFT$_{HOMO,}$ c) DFT$_{LUMO}$, d) DFT$_{LUMO+1}$

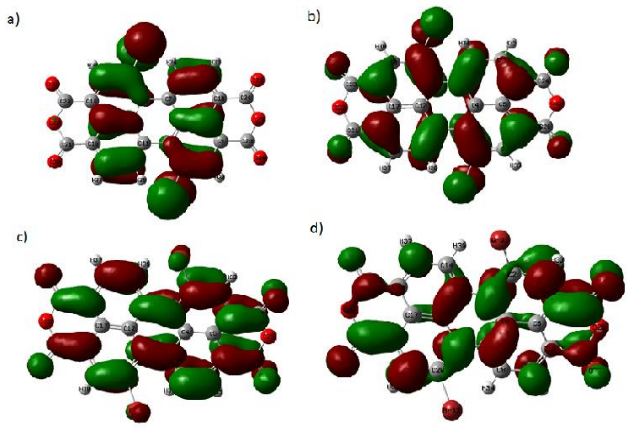

Figure 12. For the DBP molecule: a) LanL2DZ HOMO$_{-1}$, LanL2DZ HOMO, c) LanL2DZ LUMO, d) LanL2DZ LUMO$_{+1}$

DOI: http://dx.doi.org/10.32571/ijct.695754 **E-ISSN:2602-277X**

.

Table 6. The basic set of LanL2DZ with DFT is B3LYP / 6-31G (d, p), dipole moments, polarizability, β components of dibromide perylene value.

Parameters	**6-311G**	**LanL2DZ**	**Parameters**	**6-311G**	**LanL2DZ**
μ_x	0.0001	-0.0001	β_{XXX}	-0.0111	-0.0699
μ_y	0.0005	0.0005	β_{XXY}	0.0126	0.0198
μ_z	-0.0796	-0.0619	β_{XYY}	0.0214	-0.0165
$\mu_{(D)}$	0.0796	0.0619	β_{YYY}	0.0170	0.0313
α_{xx}	-297.1694	-307.3846	β_{XXZ}	-65.4351	-84.3452
α_{yy}	-202.1148	-197.0362	β_{XYZ}	-31.3278	-31.7962
α_{zz}	-202.4589	-196.8185	β_{YYZ}	-32.0949	-36.3150
α_{XY}	-14.8213	-0.0016	β_{XZZ}	-0.0200	0.0010
α_{XZ}	-0.0003	0.0016	β_{YZZ}	-0.0111	-0,0002
α_{YZ}	-0.0054	-0.0016	β_{ZZZ}	-55.9040	-75.1277
α(au)	-233.9143	-233.7464	β(esu)	153.43×10^{-29}	195.78×10^{-29}

Dipole moment is an important feature of the energy related to the electric field applied in the molecule.[30] Basically, the dipole moment consists of intermolecular interactions involving the Van der Waals type dipole-dipole forces and generates strong intermolecular attraction. Table 6 shows the calculated parameters, the electronic dipole moment and the total dipole moment. Dipole moment, molecular polarization and hyper polarizability values are important in determining the properties of nonlinear optics (NLR).

3.4. Molecular electrostatic potential surface (MESP)

The molecular electrostatic potential surface, MESP shows the shape, size and electrostatic potential values of the molecule and is plotted for the dibromide perylene molecule. MESP mapping is very useful in investigating the physicochemical properties of molecular structure.[31] A portion of the molecule with negative electrostatic potential is sensitive to electrophilic attack.

The red and blue regions on the MESP map correspond to the negative and positive potential regions and refer to electron rich and electron deficient regions respectively. The green color indicates neutral electrostatic potential.

In this study, MESP were mapped for the DBP molecule as shown in Figure 13. In the case of dibromide perylene, the MESP map shows that there are negative potential zones characterized by red color around the oxygen atoms. A relatively larger region around the oxygen atoms of the dibromide perylene molecule represents the most negative potential region (dark red) and is permissible for electrophilic interaction. The hydrogen atom carries the maximum force of the positive charge (dark blue). It shows an almost neutral potential as most of the aromatic ring region is represented by green.

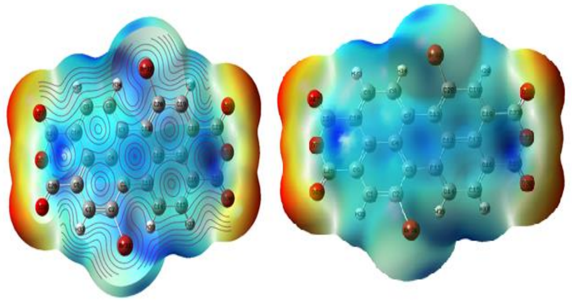

Figure 13. Molecular electrostatic potential and contour maps for the DBP molecule.

3.5. Mulliken atomic charges

Determination of mulliken atomic charge is an important parameter in quantum chemical calculations. Because, it affects many features such as atomic charges, dipole moment, molecular polarization and electronic structure in the molecule. It also shows the formation of electron donor and receiver pairs along with charge distribution and intra-molecular charge transfer. Mulliken atom was calculated in the B3LYP / 6-311G (d, p) basis set of DFT and LanL2DZ methods. The data are presented in Figures 14 and 15, and Table 7. The distribution of the mulliken atomic charge is that the oxygen atom attached to the aromatic ring is O27 (-0.22) - (-0.19), O25 (-0.20) - (-0.25), O29 (-0.22) - (-0.19), O28 (-0.23) - (-0.19), and O30 (-0.22) - (-0.19) have a negative charge. The charge value of the H atom attached to the aromatic ring has a positive charge. Some C atoms were observed to be negative and others positive.

DOI: http://dx.doi.org/10.32571/ijct.695754 **E-ISSN:2602-277X**

Table 7. Mulliken atomic charges were calculated with DFT and LanL2DZ B3LYP / 6-31G (d, p)

	6-311G	LanL2DZ		6-311G	LanL2DZ
C1	-0.45	-0.32	C20	-0.3	-0.56
C2	-0.35	-0.56	C21	0.20	0.13
C3	0.85	0.50	O22	-0.20	-0.25
C4	-0.02	-0.12	C23	0.19	0.13
C5	0.01	0.23	C24	0.21	0.13
C6	0.16	0.12	O25	-0.20	-0.25
C7	0.75	0.34	C26	0.19	0.13
C8	-0.67	-0.41	O27	-0.22	-0.19
C9	-0.75	-0.41	O28	-0.22	-0.19
C10	0.32	0.12	O29	-0.22	-0.19
C11	0.75	0.34	O30	-0.22	-0.19
C12	-0.02	-0.12	Br31	-0.10	0.04
C13	0.84	0.50	Br32	-0.10	0.04
C14	-0.67	-0.41	H33	0.18	0.29
C15	-0.75	-0.40	H34	0.15	0.27
C16	0.32	0.11	H35	0.16	0.28
C17	0.016	0.23	H36	0.15	0.27
C19	-0.45	0.11	H38	0.18	0.28

3.6. Natural orbital bond (NBO) analysis

The natural orbital bond **(**NBO) analysis provides research on the most accurate lewis structure of the molecule, detailed electron density of all orbitals. The NBO method is an evaluation of full and empty orbital interactions that provide information about both intra- and intermolecular interactions. In order to evaluate the donor-acceptor interactions in the NBO analysis of our compound, a second order Fock matrix was performed.

NBO calculation is used to understand the other second order interactions between the filled orbits of one subsystem and the empty orbitals of another subsystem. These results are delocalization and hyperconjugation measurements. The analyzed results are given in Table 8.

Intramolecular interactions are observed as an increase in electron density (ED) in antibody orbitals that weaken the relevant bonds (C-O). The electron density of the conjugated substituted bond (1.9734 au) clearly shows a strong delocalization. The occupancy rate of σ bonds is higher than σ* bonds, which provides more localization.

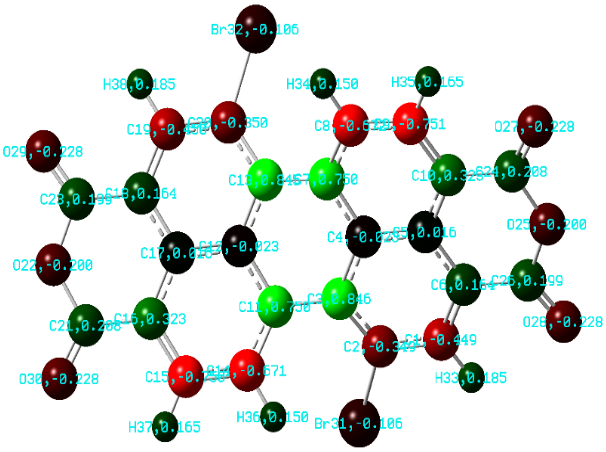

Figure 14. Mulliken atomic charges for the DBP molecule.

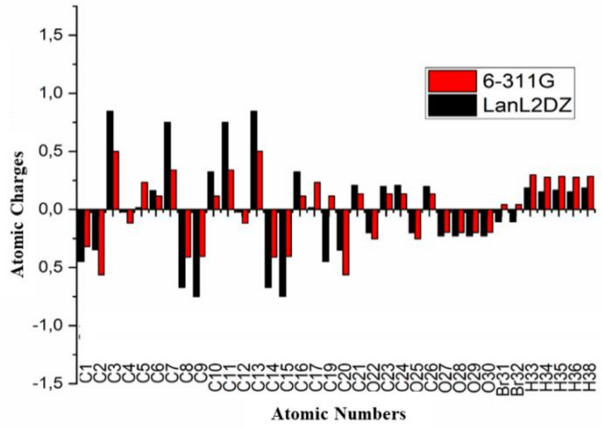

Figure 15. Comparison of Mulliken atomic charges for DBP molecule.

The intramolecular hyperconjugative interaction of the distribution to π (C2-C3) electrons in the ring leads to a stabilization of a portion of the ring as is evident from Table 8. Intramolecular hyperconjugative interaction of π* (C1-C6) and anti π* (C4-C5) in the ring leads to stabilization of 18.95 kcal mol^{-1}. These values increased conjugation leading to strong localization.

4. CONCLUSION

In this study, the spectroscopic characterization of 5, 12 Dibromo perylene (DBP) was performed. Detailed investigations were made theoretically using quantum chemical calculations for DBP molecule. The structural, electronic, vibration frequencies of the compound were calculated with the basic set of DFT-B3LPY / 6-311G (d, p) and LanL2DZ. The structural parameters (bond lengths, bond angles and dihedral angles) were determined.

Tablo 8. Selected NBO results show the formation of Lewis and non-Lewis orbitals for the DBP molecule using the DFT B3LYP / 6-311 G ++ (d, p) theory level

NBO(i)	**Type**	**ED/e**	**NBO(j)**	**Type**	**ED//e**	**E(2)^a (Kcal/mol)**	**E (j)-E(i)^b (a.u.)**	**F (i, j)^c (a.u)**
C1-C2	σ	1.97742	C6-C1	σ*	0.02248	3.69	1.30	0.062
			H33-C1	σ*	0.01530	1.26	1.13	0.034
			C3-C2	σ*	0.03455	4.53	1.28	0.068
			C11-C3	σ*	0.03468	3.95	1.20	0.062
			C26-C2	σ*	0.07304	3.47	1.10	0.056
C1-C6	σ	1.96536	C2-C1	σ*	0.02445	3.66	1.24	0.060
			H33- C1	σ*	0.01530	1.43	1.14	0.036
			Br31 - C2	σ*	0.03589	4.48	0.81	0.054
			C6 - C5	σ*	0.03200	4.95	1.25	0.070
			C5-C10	σ*	0.03287	2.89	1.25	0.054
			C6-C26	σ*	0.07304	2.21	1.10	0.044
			C26- O25	σ*	0.12693	1.32	0.98	0.033
			O28- C26	σ*	0.01934	0,72	0,83	0,024
	π	1.69323	C3- C2	π *	0.38644	16.07	0.28	0.061
			C5- C4	π*	0.43123	18.95	0.30	0.069
			C26- O25	π *	0.12693	1.02	0.52	0.022
			O28- C26	π*	0.17789	16.51	0.25	0.060
C1-H33	σ	1.97542	C2 -C1	σ*	0.02445	0.66	1.02	0.023
			C6-C1	σ*	0.02248	1.03	1.09	0.030
			C3-C2	σ*	0.03455	4.88	1.07	0.065
			C6-C5	σ*	0.03200	5.15	1.04	0.065
C2-Br31	σ	1.98238	C6-C1	σ*	0.02248	2.80	1.27	0.053
			C4-C3	σ*	0.03314	4.15	1.21	0.063
C19-H38	σ	1.97541	C20- C13	σ*	0.03453	4.88	1.07	0.065
			C18- C17	σ*	0.03203	5.16	1.03	0.065
			C19- C18	σ*	0.02249	1.03	1.09	0.030
			C19-C20	σ*	0.02444	0.66	1.02	0.023
C21-O22	σ	1.97328	C16- C15	σ*	0.02261	1.50	1.42	0.041
			O22- C21	σ*	0.12895	0.56	1.09	0.023
			O29-C23	σ*	0.01947	1.45	1.40	0.040
			O29-C23	σ*	0.17658	2.91	0.82	0.045
C21-O30	σ	1.99496	C17- C16	σ*	0.037	1.01	1.64	0.037
			C21-C16	σ*	0.049	1.93	1.48	0.049
			C23-O22	σ*	0.030	0.76	1.36	0.030
	π	1.98104	C16-C15	π *	0.28027	3.75	0.42	0.038
			O22-C23	π *	0.12708	0.90	0.64	0.022
C24-O25	σ	1.97345	C10- C9	σ*	0.02261	1.50	1.42	0.041
			O25-C24	σ*	0.12890	0.56	1.09	0.023
			O28- C26	σ*	0.01934	1.47	1.40	0.040
			O28- C26	σ*	0.17789	2.88	0.82	0.045
C24-O27	σ	1.99494	C10-C5	σ*	0.03287	1.01	1.63	0.037
			C24-C10	σ*	0.07329	1.94	1.48	0.049
			C26- O25	σ*	0.12693	0.76	1.36	0.030
	π	1.98101	C10- C9	π *	0.28011	3.76	0.42	0.038
			C26- O25	π *	0.12693	0.90	0.64	0.022
O25-C26	σ	1.97337	C6-C1	σ*	0.02248	1.55	1.42	0.042
			O27-C24	σ*	0.01949	1.45	1.40	0.040
			O27-C24	σ*	0.17666	2.90	0.82	0.045
			C26-O25	σ*	0.12693	0.54	1.09	0.022

Nonlinear optical properties were investigated. Finally, it was concluded that the compound examined could be used as a nonlinear optical (NLO) material. Because polarity (α = -233.9143 au and α = -233.7464 au) and static high-order polarity (β = 153.43 x 10^{-29} esu and β = 195.78 x 10^{-29} esu) parameters were determined from the calculations for the DBP molecule. The theoretically high degree of polarity values from the data obtained for the DBP molecule were considered to be a good candidate for nonlinear optical materials. In addition, MESP, HOMO-LUMO maps and Mulliken loads were visualized. It is available as a good intermediate material for syntheses. That is, the fact that the material is formed in the reaction and can be used in the next step means that the material is a good intermediate product in the reactions with mechanisms. Thus, by

DOI: http://dx.doi.org/10.32571/ijct.695754 E-ISSN:2602-277X

taking these data into consideration for future synthesis studies, this study will provide important facilities for the synthesis of molecules by minimizing the chemical consumption of the molecules to be synthesized in the future and making necessary predictions.

Conflict of interests

Authors declare that there is no a conflict of interest with any person, institute, company, etc.

REFERENCES

1. Paredes-Gil, K.; Mendizabal, F.; Páez-Hernández, D.; Arratia-Pérez, R. *Comput. Mater. Sci.* **2017,** 126, 514-527.

2. Kolcu, F.; Çulhaoğlu, S.; Kaya, İ. *Prog. Org. Coat.* **2019,** 137, 105284.

3. Kucinska, M.; Frac, I.; Ulanski, J.; Makowski, T.; Nosal, A.; Gazicki-Lipman, M. *Synth. Met.* **2019,** *250*, 12-19.

4. Dong, D.; Li, Q.; Hou, W.; Zhang, H. *J. Mol. Struct.* **2020,** 1199, 127002.

5. Cao, L.; Xu, L.; Zhang, D.; Zhou, Y.; Zheng, Y.; Fu, Q.; Jiang, X.-F.; Lu, F. *Chem. Phys. Lett.* **2017,** 682, 133-139.

6. Otero, R.; Vázquez De Parga, A. L.; Gallego, J. M. *Surf. Sci. Rep.* **2017,** 72 (3), 105-145.

7. Dere, A. *Physica B Condens. Matter.* **2018,** 547, 127-133.

8. Veerababu, M.; Kothandaraman, R. *Electrochim. Acta.* **2017,** *232*, 244-253.

9. Djurišić, A. B.; Fritz, T.; Leo, K. *Opt. Commun.* **2000,** 183 (1), 123-132.

10. Farag, A. A. M.; Osiris, W. G.; Yahia, I. S. *Synth. Met.* **2011,** 161 (17), 1805-1812.

11. Büyükekşi, S. I; Orman, E. B.; Acar, N.; Altındal, A.; Özkaya, A. R.; Şengül, A. *Dyes Pigments* **2019,** 161, 66-78.

12. Ozser, M. E.; Mohiuddin, O. *J. Mol. Struct.* **2018,** 1158, 145-155.

13. Lathiotakis, N. N.; Kerkines, I. S. K.; Theodorakopoulos, G.; Petsalakis, I. D. *Chem. Phys. Lett.* **2018,** 691, 388-393.

14. Cabir, B.; Yildiko, U.; Ağirtaş, M. S. *J. Coord. Chem.* **2019,** 72 (17), 2997-3011.

15. Basma, A.-K.; Dinleyici, M.; Abourajab, A.; Kök, C.; Bodapati, J. B.; Uzun, D.; Koyuncu, S.; Icil, H. *J Photoch Photobio A.* **2020,** 393, 112432..

16. Solğun, D. G.; Keskin, M. S.; Yıldıko, Ü.; Ağırtaş, M. S. *Chem .Pap.* **2020,** 74, 2389-2401.

17. M. J. Frisch, G. W. T., H. B. Schlegel, G. E. Scuseria, M. A. Robb, J. R. Cheeseman, G. Scalmani, V. Barone, G. A. Petersson, H. Nakatsuji, X. Li, M. Caricato, A. Marenich, J. Bloino, B. G. Janesko, R. Gomperts, B. Mennucci, H. P. Hratchian, J. V. Ortiz, A. F. Izmaylov, J. L. Sonnenberg, D. Williams-Young, F. Ding, F. Lipparini, F. Egidi, J. Goings, B. Peng, A. Petrone, T. Henderson, D. Ranasinghe, V. G. Zakrzewski, J. Gao, N. Rega, G. Zheng, W. Liang, M. Hada, M. Ehara, K. Toyota, R. Fukuda, J. Hasegawa, M. Ishida, T. Nakajima, Y. Honda, O. Kitao, H. Nakai, T. Vreven, K. Throssell, J. A. Montgomery, Jr., J. E. Peralta, F. Ogliaro, M. Bearpark, J. J. Heyd, E. Brothers, K. N. Kudin, V. N. Staroverov, T. Keith, R. Kobayashi, J. Normand, K. Raghavachari, A. Rendell, J. C. Burant, S. S. Iyengar, J. Tomasi, M. Cossi, J. M. Millam, M. Klene, C. Adamo, R. Cammi, J. W. Ochterski, R. L. Martin, K. Morokuma, O. Farkas, J. B. Foresman, And D. J. Fox, *Gaussian 09, Revision A.02, Gaussian, Inc., Wallingford Ct,* 2016.

18. Khajehzadeh, M.; Moghadam, M. *Spectrochim. Acta A:* **2017,** 180, 51-66.

19. Miehlich, B.; Savin, A.; Stoll, H.; Preuss, H. *Chem. Phys. Lett.* **1989,** 157 (3), 200-206.

20. Hertwig, R. H.; Koch, W. *Chem. Phys. Lett.* **1997,** 268 (5-6), 345-351.

21. Hay, P. J.; Wadt, W. R. *J. Chem. Phys.* **1985,** 82 (1), 270-283.

22. Ülküseven, B.; Bal-Demirci, T.; Akkurt, M.; Yalçın, Ş. P.; Büyükgüngör, O. *Polyhedron* **2008,** *27* (18), 3646-3652.

23. Akkurt, M.; Yalçın, Ş.; Gürsoy, E.; Ulusoy Güzeldemirci, N.; Büyükgüngör, O. *Acta Crystallogr. E.* **2007,** 63, O3103.

24. Matussek, M.; Filapek, M.; Gancarz, P.; Krompiec, S.; Grzegorz Małecki, J.; Kotowicz, S.; Siwy, M.; Maćkowski, S.; Chrobok, A.; Schab-Balcerzak, E.; Słodek, A. *Dyes Pigments* **2018,** 159, 590-599.

25. Li, H.; Meng, J.; Sun, X. *Inorg. Chem. Commun.* **2019,** 105, 194-198.

DOI: http://dx.doi.org/10.32571/ijct.695754 **E-ISSN:2602-277X**

26. Huang, C.; Barlow, S.; Marder, S. R. *J. Org. Chem.* **2011,** 76 (8), 2386-2407.

27. Pakseresht, M.; Bodapati, J. B.; Icil, H. *J. Photochem. Photobiol. A.* **2018,** 360, 270-277.

28. Wu, S.; Cheng, C.; Hou, W.; Li, Q.; Dong, D.; Gao, Y.; Liu, L.; Liang, B.; Zhang, H. *Tetrahedron* **2019,** 75 (41), 130577.

29. Yuen, J. D.; Pozdin, V. A.; Young, A. T.; Turner, B. L.; Giles, I. D.; Naciri, J.; Trammell, S. A.; Charles, P. T.; Stenger, D. A.; Daniele, M. A. *Dyes Pigments* **2019**, 108014.

30. Piosik, E.; Synak, A.; Martyński, T. *Spectrochim. Acta A: Mol. Biomol. Spectrosc.* **2018,** 189, 374-380.

31. Pekdemir, F.; Orman, E. B.; Selçuki, N. A.; Özkaya, A. R.; Salih, B.; Şengül, A. *J. Photochem. Photobiol. A* **2019,** *379*, 54-6.

ORCID

ID https://orcid.org/0000-0003-3345-6445 (M. Akman)

ID https://orcid.org/0000-0002-2296-2265 (A. Ç. Ata)

ID https://orcid.org/0000-0001-8627-9038 (Ü. Yıldıko)

ID https://orcid.org/0000-0002-3191-7570 (İ. Çakmak)

DOI: http://dx.doi.org/10.32571/ijct.712499 **E-ISSN:2602-277X**

International Journal of Chemistry and Technology

http://dergipark.org.tr/ijct

Research Article

Theoretical B3LYP study of contrast agent metrizoate

S. Giray KANDEMIRLI[1], M. Izzettin YILMAZER[2,*], Murat SARACOGLU[2], Fatma KANDEMIRLI[3]

on the last page

[1]*Department of Radiology, Roy Carver College of Medicine, University of Iowa, United States*

[2]*Faculty of Education, Erciyes University, 38039, Kayseri, Turkey*

[3]*Biomedical Engineering Department, Faculty of Engineering and Architecture, Kastamonu University, 37150, Kastamonu, Turkey*

Received: 01 April 2020; Revised: 12 May 2020; Accepted: 15 May 2020

*****Corresponding author e-mail: izzettin@erciyes.edu.tr

Citation: Kandemirli, S.G.; Yılmazer, M. I.; Saraçoğlu, M.; Kandemirli, F. *Int. J. Chem. Technol.* **2020**, 4 (1), 60-70.

ABSTRACT

Metrizoic acid is a molecule used as meglumine metrizoate, sodium metrizoate contrast agent. 6 Isopak 44o* is a contrast medium containing a mixture of sodium, calcium, magnesium and N-methylglucamine salts of metrizoic acid. In order to determine the reactivity properties of metrizoic acid, melagnomie, anionic form of metrizoate, Metrisoate K, metrizoate-melagnomie salt, and Na-metrizoate, DFT calculations were made in gas and water phses at the level of B3LYP/LANL2DZ with the help of Gaussian 09 software. Some global chemical reactivity descriptors such as highest occupied molecular orbital energy, lowest empty molecular orbital energy, absolute hardness, chemical potential, softness, electronegativity, chemical potential, global electrophilicity and electrofugality were calculated. Moreover, nonlinear optical properties of the title compound were calculated too. In addition, thermodynamic properties of the molecules examined at different temperatures were calculated in gas and water phases. The findings of this study, obtained from extensive and time-consuming calculations and analyses, will be an important source of information for the preparation of the drug combination in the future.

Keywords: Metrizoate, DFT, B3LYP, quantum chemical calculations.

Kontrast maddesi metrizoatın teorik B3LYP incelemsi

ÖZ

Metrizoik asit, meglumin metrizoat, sodyum metrizoat kontrast maddesi olarak kullanılan bir moleküldür. 6 izopak 44o*, metrizoik asidin sodyum, kalsiyum, magnezyum ve N-metilglukamin tuzlarının bir karışımını içeren bir kontrast ortamıdır. Metrizoik asit, melagnomi, anyonik metrizoat formu, metrisoate K, metrizoate-melagnomie tuzu ve Na-metrizoate formunun reaktivite özelliklerini belirlemek için gaz ve su fazında B3LYP / LANL2DZ seviyesinde Gaussian 09 yazılımı yardımıyla DFT hesaplamaları yapıldı. En yüksek işgal edilen moleküler orbital enerji, en düşük boş moleküler orbital enerji, mutlak sertlik, kimyasal potansiyel, yumuşaklık, elektronegatiflik, kimyasal potansiyel, küresel elektrofiliklik, nükleojenite ve elektrofugalite gibi bazı küresel kimyasal reaktivite tanımlayıcıları hesaplandı. Ayrıca, bileşiğin lineer olmayan optik özellikleri de hesaplandı. Bunun yanında farklı sıcaklıklarda incelenen moleküllerin termodinamik özellikleri gaz ve su fazlarında hesaplandı. Kapsamlı ve zaman alan hesaplama ve analizlerden elde edilen bu çalışmanın bulguları, gelecekte ilaç kombinasyonunun hazırlanması için önemli bir bilgi kaynağı olacaktır.

Anahtar Kelimeler: Metrizoate, DFT, B3LYP, kuantum kimyasal hesaplamalar.

1. INTRODUCTION

The basic principle is the application of contrast agents in a way that changes the absorption of specific anatomical structures relative to the x-ray environment. Positive contrast agents are iodine or barium compounds, and negative contrast agents are gases. Positive contrast agents absorb more x-rays than tissues because of their higher density and higher atomic number, but gaseous contrast agents absorb fewer X-ray than tissues because of their low density, even though the effective atomic number may be higher.

The basic building block of iodized contrast agents is a benzene ring, which has three iodine molecules attached to positions 2, 4 and 6. Side chains at positions 3 and 5

DOI: http://dx.doi.org/10.32571/ijct.712499 E-ISSN:2602-277X

are modified with hydroxyl groups or other molecules that further define the properties of an agent. They can be classified into two groups as ionic and non-ionic contrast agents depending on whether they are dissociated in solution. Contrast agents can be classified according to osmality values. Those with ≥ 1400 mOsm/kg are classified as high osmolar, those with 780-800 mOsm/kg as low osmases and those with approximately 300 mOsm/kg are classified as iso-osmolar agents.

Three properties that define the physical properties of iodinated contrast agents-ionicity, osmolality and viscosity play a separate role in tolerance and adverse reaction profiles.[1]

Pattinson and co-workers[2] reported that sodium amidotrizoate showed certain advantages over the contrast media which they had previously used for angiocardiography. And also they found that high flow rates had been achieved with triosil 75% resulting in a great improvement in the quality of the angiocardiograms when small catheters had been used.

Emergency urography has been performed using either low osniolar nonionic (iohexol) or high osmolar ionic (metrizoat) contrast agent. In 56 percent of all children, the pain has increased after injection of contrast medium. The increase in pain occurs without any difference between the contrast agent and the degree of pain and the number of patients who experience an increasing pain.[3]

Ten radiographic contrast agents containing iodine have been tested to assess whether there are a rapid, continuous and reversible inhibition of thyroxine (T4) secretion from perfused canine thyroid lobes. All of four agents used for cholecystography (iocetamate, iodipamide, oglycamate and iotroxate) cause rapid inhibition of T4 secretion from TSH-induced perfused canine thyroid lobes, while amidotrizoate, metrizamide, metrizoate, iodamide, diodone and iodamide, significantly impressed. All cholecystographic agents have been reported to inhibit T4 deiodinases from canine thyroid and liver.[4]

In a double-blind, randomized, two-group study with 99 “high-risk” patients with essentially coronary artery disease, the nonionic contrast agent, amipak (metrizamide), have been compared to the ionic medium isopaque coronar (meglumine-Na-Ca-metrizoate) in inecardioangiography and they reported that the patients with a basal LVEDP above 15 mmHg, no significant change has occurred in LVEDP after left ventriculography with any of the 2 contrast media. It has been reported that no serious complications occurred.[5]

Cerebral computed tomography has been performed in 60 patients who applied for screening before and after contrast. Non-ionic contrast agent, iohexol, and an ionic contrast agent sodium metrizoate have been randomly administered to the patients as a contrast agent. Very minor side effects have been recorded with both iohexol and metrizoate, but iohexol causes much less discomfort than metrizoate. It has been reported that there is no difference in the development of normal intracranial structures.[6] Isopaque 44o* is a contrast medium which contains a mixture of the sodium, calcium, magnesium, and N-methylglucamine salts of metrizoic acid. Theoretical studies on the constructional features of metrizoate are seldom found in literature. In order to interpret molecular properties of metrizoic acid (MetA), melagnomie (Melag), anionic form of metrizoate (an-Met), metrisoate K (K-Met), metrizoate-melagnomie salt (Melag-Met), Na-metrizoate (Na-Met), theoretical studies are needed on the electronic and thermodynamic properties of molecules. B3LYP functional of quantum chemical calculation methods is widely used in studying both physical and chemical properties of molecules.[7]

In this study, thermodynamic properties and frontier molecular orbitals were theoretically calculated for the MetA, Melag, an-Met, K-Met, Melag-Met, Na-Met. Polarizability, hyperpolarizability and some parameters related to HOMO and LUMO energies were investigated using B3LYP/LANLZDZ basis set.

2. CALCULATION METHODS

Structural parameters for each molecule were optimized for at the B3LYP method of Gaussian Program,[8] Becke’s three parameter hybrid functional combined with the gradient correlation functional of Lee, Yang and Parr (LYP), denoted B3LYP, in the computations using DFT/LANL2DZ level of theory, and the harmonic vibrational frequencies and zero-point vibrational energies (ZPVE) were computed at the same level. Throughout this paper, all calculations for B3LYP optimization of molecular geometry were carried out with B3LYP/LANL2DZ Opt. Freq. “Opt Freq” means that the frequency was calculated after optimization.

The values of the absolute electron negativity (χ), the chemical potential (μ_i), the absolute hardness (η), and the softness (σ, the inverse of the hardness), global electrophilicity (ω), nucleofugality (ΔE_n) and electrofugality (ΔE_e) related with the HOMO and LUMO energies can be determined by Equations (1-10).

$$\mu = -\chi \cong \left(\frac{E_{HOMO}+E_{LUMO}}{2}\right) \quad (1)$$

$$\eta = \frac{E_{LUMO}-E_{HOMO}}{2} \quad (2)$$

$$\sigma = \frac{\eta}{2} \tag{3}$$

$$\omega = \frac{\mu^2}{2\eta} \tag{4}$$

$$\Delta E_n = \frac{(\mu+\eta)^2}{2\eta} \tag{5}$$

$$\Delta E_e = \frac{(\mu-\eta)^2}{2\eta} \tag{6}$$

The complete equations (Equations (7)-(10)) for calculating the magnitude of total static dipole moment (μ), the mean polarizability ($<\alpha>$), the anisotropy of the polarizability ($\Delta\alpha$), the mean first hyperpolarizability (β) are defined as follows.

The total static dipole moment is

$$\mu = \left(\mu_x^2 + \mu_y^2 + \mu_z^2\right)^{1/2} \tag{7}$$

Mean polarizability is

$$\alpha = \frac{1}{3}(\alpha_{xx} + \alpha_{yy} + \alpha_{zz}) \tag{8}$$

The anisotropy of the polarizability $<\Delta\alpha>$:

$$\Delta\alpha = \left[\frac{(\alpha_{xx}-\alpha_{yy})^2+(\alpha_{yy}-\alpha_{zz})^2+(\alpha_{zz}-\alpha_{xx})^2+6(\alpha_{xz}^2+\alpha_{xy}^2+\alpha_{yz}^2)}{2}\right]^{1/2} \tag{9}$$

And the average hyperpolarizability is:

$$\beta = \left[(\beta_{xxx} + \beta_{xyy} + \beta_{xzz})^2 + (\beta_{yyy} + \beta_{yzz} + \beta_{yxx})^2 + (\beta_{zzz} + \beta_{zxx} + \beta_{zyy})^2\right]^{\frac{1}{2}} \tag{10}$$

3. RESULT AND DISCUSSION

3.1. Frontier orbital

The optimized form, HOMO and LUMO contour plots for MetA, Melag, an-Met, K-Met, Melag-Met, Na-Met molecules are shown in Figure 1. LUMO of MetA, an-Met, K-Met, Melag-Met, Na-Met consists of benzene ring and all the iodine atoms attached to benzene ring. HOMO of MetA consists of mainly spread benzene ring and N-methylacetamide group, HOMO of an-Met consists of mainly carboxylate group, HOMO of K-Met consists of benzoate group and iodine atoms, HOMO of Melag-Met consists of benzene ring and all the iodine atoms attached to benzene ring and N-methylacetamide group, and HOMO of Na-Met consist of two iodine atoms and N-methylacetamide group. The variation in the contribution to the HOMO was influenced by the neutral anionic and salt form.

The most widely used theory by chemists is the molecular orbital (MO) theory. From the Koopman's theorem, the ionization potential (*I*) and electron affinity (*EA*) are the Eigen value of the HOMO and LUMO with change of sign.[9]

It is important to reveal HOMO energy, LUMO energy, the electrophilicity index, chemical potential, electronegativity, hardness and softness in the Molecular Orbital framework. Based on density functional descriptors global chemical reactivity descriptors of compounds such as hardness, chemical potential, softness, electro negativity and electrophilicity index local reactivity has been calculated.[10]

The HOMO-LUMO energy gap (ΔE) along with computed global descriptors namely, absolute electron negativity (χ), the chemical potential (μ), the absolute hardness (η), and the softness (S), global electrophilicity nucleofugality (ΔE_n) and electrofugality (ΔE_e) of MetA, Melag, an-Met, K-Met, Melag-Met and Na-Met are reported in Table 1.

The molecule with the highest HOMO-LUMO energy gap will be the least prone to any external disruption and these orbital energies help to characterize the chemical reactivity and kinetic stability of the molecule. A small frontier orbital gap means that the molecule is more polarizable and is generally associated with a high chemical reactivity, low kinetic stability and it is also termed as soft molecule. The HOMO acts as an electron donor, and the LUMO acts as the electron acceptor. As presented in Table 1, the compound which have the lowest energetic gap is the anionic form of metrizoate (ΔE = 3.004 eV). This lower gap makes it the softest molecule. The compound that have the highest energy gap is the metrizoate-melagnomie (ΔE = 4.466 eV). The compound that has the highest HOMO energy is the anionic form of metrizoate (E_{HOMO} = -2.428 eV).

Which electrons are polarized or resists to deformation is measured with the magnitude of hardness (η). The values of η for MetA, Melag, an-Met, K-Met, Melag Met, Na-Met are 2.202, 3.399, 1.502, 2.170, 2.300, 2.233 in gas phase and 2.391, 3.633, 2.081, 2.214, 2.413

DOI: http://dx.doi.org/10.32571/ijct.712499 **E-ISSN:2602-277X**

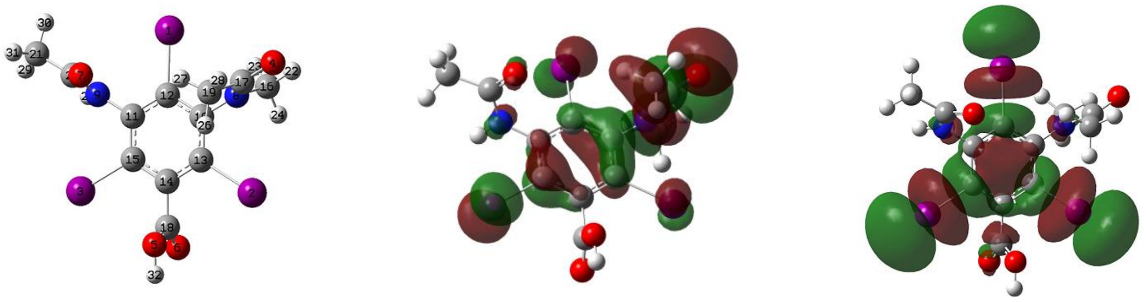

MetA-opt MetA-HOMO MetA-LUMO

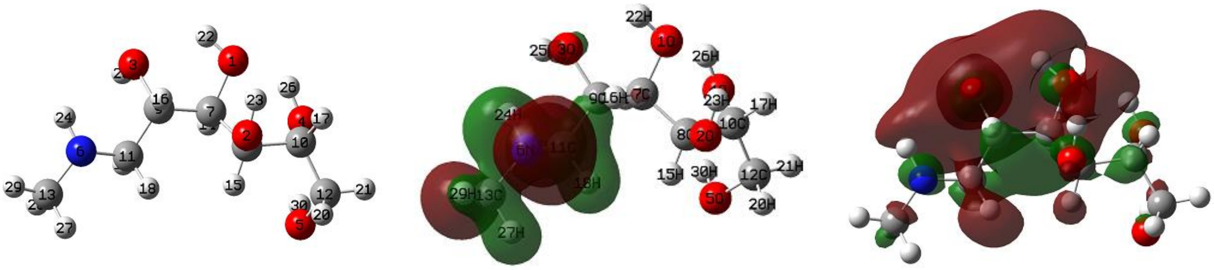

Melag-opt Melag-HOMO Melag-LUMO

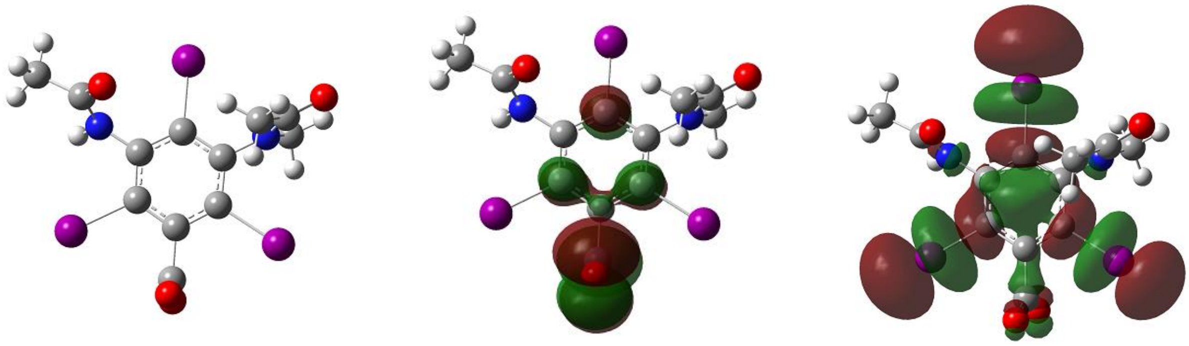

an-Met-opt an-Met-opt an-Met-LUMO

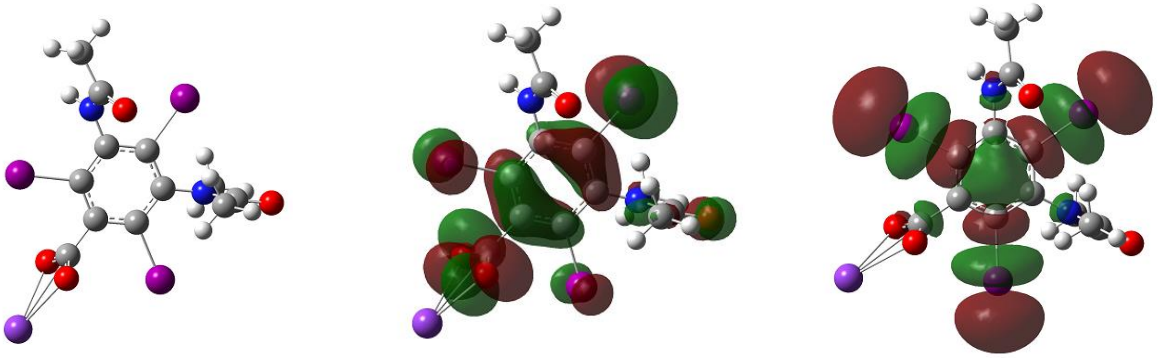

K-Met-opt K-Met-HOMO K-Met-LUMO

Figure 1. The optimized and HOMOs, LUMOs of molecules by using DFT/B3LYP/LANL2DZ basic set.

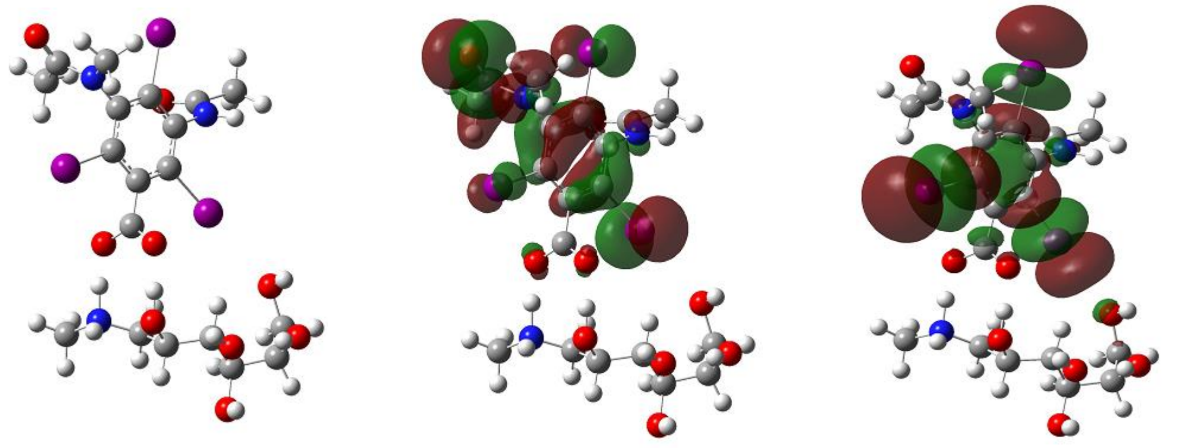

Melag-Met-opt Melag-Met-HOMO Melag-Met-LUMO

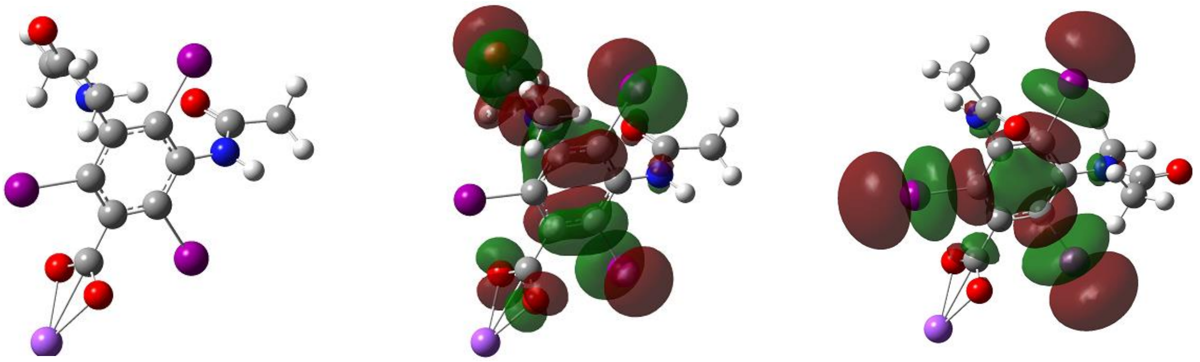

Na-Met-opt Na-Met-HOMO Na-Met-LUMO

Figure 1. (continuous)

and 2.264 in solvent phase, respectively. The results indicate that an-Met is relatively soft in gas phase and water phase. Increases in the hardness values of MetA, Melag, an-Met, K-Met, Melag-Met, Na-Met going from the gas phase to the aqueous medium are 8.54%, 6.86%, 38.57%, 2.00%, 4.90% and 1.39%, respectively.

Physically, the escaping tendency of electrons from an equilibrium system is defined as chemical potential. The greater the electronic chemical potential means that the compound is the less stable or more reactive. The values of μ for MetA, Melag, an-Met, K-Met, Melag-Met, Na-Met are -4.669, -2.492, -0.926, -3.989, -4.253 and -4.214 in gas phase, -4.725, -2.343, -4.141, -4.345, -4.517, -4.414 in solvent phase, respectively. The results indicates that chemical potential of the molecules under study in gas phase are less than in water phase except Melag. Decreases in the chemical potential values of MetA, an-Met, K-Met, Melag-Met, Na-Met going from the gas phase to the aqueous medium are 1.20%, 347.24%, 8.92%, 6.23% and 4.75%. In a study related with the electronic chemical potential of some of the reagents involved in Diels-Alder reactions, authors reported that the tetracyanoethylene molecule with a chemical potential of 7.04 eV acted as strong electron accepting molecules and the dimethylvinyl amine molecule with chemical potential of 1.85 eV acted as strong electron donating molecules.[10]

The electrophilicity index is a powerful tool to investigate the reactivity of organic molecules in polar reactions.[11] Molecules with an electrophilic index > 1.5 eV are classified as strong electrophiles, those with an electrophilic index between 0.8 and 1.5 are classified as medium electrophiles, and those less than 0.8 are marginal electrophiles.[12]

The values of ω for MetA, Melag, an-Met, K-Met, Melag-Met, Na-Met, is 4.949, 0.913, 0.285, 3.666, 3.931, 3.976 in gas phase, 4.67, 0.755, 4.119, 4.264, 4.229, 4.303 in water phase, respectively. The results indicate that electrophilicity index of the molecules under study are higher in gas phase compared to water phase.

Table 1. The calculated quantum chemical parameter values for gas and water phases

Molecule	**E_{HOMO} (eV)**	**E_{LUMO} (eV)**	**ΔE (eV)**	**μ (D)**	**MV (cm^3/mol)**	**TNC (e)**	**η (eV)**
MetA	-6.871	-2.467	4.405	5.7534	229.451	-3.530	2.202
Melag	-5.891	0.907	6.799	3.6635	151.934	-0.738	3.399
an-Met	-2.428	0.576	3.004	11.6898	261.558	-4.006	1.502
K-Met	-6.159	-1.819	4.341	13.6385	282.419	-4.181	2.170
Melag-Met	-6.553	-1.952	4.600	8.3651	359.370	-4.869	2.300
Na-Met	-6.447	-1.981	4.466	11.4035	257.500	-4.200	2.233
MetA*	-7.116	-2.334	4.781	7.2749	212.329	-3.646	2.391
Melag*	-5.975	1.290	7.265	4.8106	140.316	-0.814	3.633
an-Met*	-6.222	-2.060	4.163	17.4443	208.520	-4.258	2.081
K-Met*	-6.559	-2.131	4.427	15.7723	211.834	-4.272	2.214
Melag-Met*	-6.930	-2.105	4.826	10.1261	382.705	-5.039	2.413
Na-Met*	-6.678	-2.150	4.528	13.7972	278.837	-4.298	2.264

	σ (eV^{-1})	**χ (eV)**	**μ_i (eV)**	**Ω (eV)**	**ΔE_n (eV)**	**ΔE_e (eV)**	**SEZPE (eV)**
MetA	0.227	4.669	-4.669	4.949	1.381	10.720	-908.095
Melag	0.147	2.492	-2.492	0.913	0.121	5.105	-707.475
an-Met	0.333	0.926	-0.926	0.285	0.110	1.962	-907.585
K-Met	0.230	3.989	-3.989	3.666	0.762	8.740	-935.729
Melag-Met	0.217	4.253	-4.253	3.931	0.829	9.334	-1615.620
Na-Met	0.224	4.214	-4.214	3.976	0.879	9.307	-907.786
MetA*	0.209	4.725	-4.725	4.670	1.140	10.590	-908.125
Melag*	0.138	2.343	-2.343	0.755	0.229	4.914	-707.498
an-Met*	0.240	4.141	-4.141	4.119	1.019	9.301	-907.688
K-Met*	0.226	4.345	-4.345	4.264	1.026	9.716	-935.798
Melag-Met*	0.207	4.517	-4.517	4.229	0.918	9.953	-1615.475
Na-Met*	0.221	4.414	-4.414	4.303	1.021	9.850	-907.862

*Water Phase, ΔE: Energy gap, μ: Dipole moment, MV: Volume, TNC: Total negative charge, η: Hardness, σ: Softness, χ: Electronegativity, μ_i: Chemical potential, ω: Global electrophilicity, ΔE_n: Nucleofugality, ΔE_e: Electrofugality, SEZPE: Sum of electronic and zero point energy.

DOI: http://dx.doi.org/10.32571/ijct.712499 **E-ISSN:2602-277X**

The electrophilicity index of MetA, Melag, an-Met, K-Met, Melag-Met, Na-Met is greater than 1.5 eV, so they can be said to be strong electrophiles.

The electrophilicity index includes the tendency of an electrophile to obtain an extra electron density given around it, that is, the resistance to change the electron density with the given electron. Thus, a good electrophile is characterized by high electrophilicity index and low hardness parameter.

Another parameters proposed by Ayers and co-workers[13,14] are nucleofugality, ΔE_n and electrofugality, ΔE_e defining the quantify nucleophilic and electrophilic capabilities of a leaving group. As seen from Table 1, the values of nucleofugality and electrofugality of MetA, Melag, an-Met, K-Met, Melag-Met, Na-Met are bigger in gas phase than that in water phase. The other properties such as molar volume, total negative charge, sum of zero point and electronic energy for gas and solvent phase are given in Table 1.

3.2. Thermodynamic analysis

The thermodynamic parameters were calculated using B3LYP method with the LANL2DZ basis set at the temperatures between 200 and 1000 K in gas phase and water phase for MetA, Melag, an-Met, K-Met, Melag-Met, Na-Met.

The standard statistical thermodynamic functions such as heat capacity, entropy and enthalpy changes for Metrizoic acid (MetA), melagnomie (Melag), anionic form of metrisoate (an-Met), K-Metrizoate (K-Met), metrizoate-melagnomie salt (Melag-Met), Na-Metrizoate (Na-Met), in gas phase and water phase were obtained from the theoretical harmonic frequencies on the basis of vibrational analysis at B3LYP/LANL2DZ level. In order to determine the estimated precise value of thermodynamic functions, 0.96 rating factor was used. Figure 2 demonstrates the correlation graphs between various temperatures versus heat capacity, entropy, enthalpy for the methods of DFT level in gas and water phase. Figure 2 reveals that the heat capacities, entropy, and enthalpy changes increase with temperatures between 200 and 1000 K since the intramolecular vibrational intensities increase with temperature. [15]

The correlation equations between heat capacity, entropy, enthalpy and temperatures were fitted by parabolic formula. These thermodynamic data can provide useful information in determining the direction of chemical reactions in future studies.[16] Fitting equations for heat capacity, entropy and enthalpy and correlation coefficient in water medum are given in Table 2. For the title molecule, the equations are used to predict approximately the values of heat capacity at constant pressure, entropy and enthalpy for other range of temperature. The regression coefficient is also given in the parabolic equation.

3.3. Non-linear optical properties

Under the applied electric field, first order hyperpolarizability (third order tensor) can be defined by the 3 × 3 × 3 matrix. The Kleinman symmetry reduces the components of the 3D matrix to 10 components.[17] β components are defined as the coefficients in the Taylor series expansion of energy in the external electric field. The components of β are defined as the coefficients in the Taylor series expansion of the energy in the external electric field. When the external electric field is weak and homogeneous, this expansion is as in Equation (11).

$$E = E^{o} - \mu_{\alpha} F_{\alpha} - \frac{1}{2} \alpha_{\alpha\beta} F_{\alpha} F_{\beta} - \frac{1}{6} \beta_{\alpha\beta\gamma} F_{\alpha} F_{\beta} F_{\gamma} + \ldots \tag{11}$$

where E^o is the energy of the unperturbed molecules, F_a is the field at the origin, and m_a, a_{ab} and b_{abg} are the components of dipole moment, polarizability and the first order hyperpolarizabilities, respectively.

.

The dipole moment is expected to be larger in solution than in the gas phase. Table 3 presents the dipole moments computed in the gas phase and in water at the level of B3LYP theory with LANL2DZ basis set. The values of the electric dipole moment (Debye) and dipole moment components are listed in Table 3. The total dipole moment of MetA, Melag, an-Met, K-Met, Melag-Met, Na-Met is found to be 2.862, 1.893, 6.863, 3.703, 5.428 D for gas phase, and 2.862, 1.893, 6.863, 3.703, 5.428 D for water phase, respectively. As expected, the dipole moment is larger in water than in the gas phase.[18]

The first hyperpolarizability values calculated with Equations 11 and 12 for MetA, Melag, an-Met, K-Met, Melag-Met, Na-Met are presented in Figure 3. The first hyperpolarizability and the polarizability values calculated in atomic unit from Gaussian 09[8] output have been converted into electrostatic units (esu) (for hyperpolarizability 1 a.u. = 8.639 x 10^{-33} esu, for polarizability 1 a.u. = 0.1482 x 10^{-24} esu).

The first hyperpolarizability of MetA, Melag, an-Met, Melag-Met, Na-Met molecules are 3.25 10^{-30} esu, 0.46 10^{-30} esu, 17.28 10^{-30} esu, 2.91 10^{-30} esu, 10. 91 10^{-30} esu in gas phase, and they are 4.35 10^{-30} esu, 0.93 10^{-30} esu, 16.62 10^{-30} esu, 6.73 10^{-30} esu, 2. 13 10^{-30} esu in water phase.

DOI: http://dx.doi.org/10.32571/ijct.712499 **E-ISSN:2602-277X**

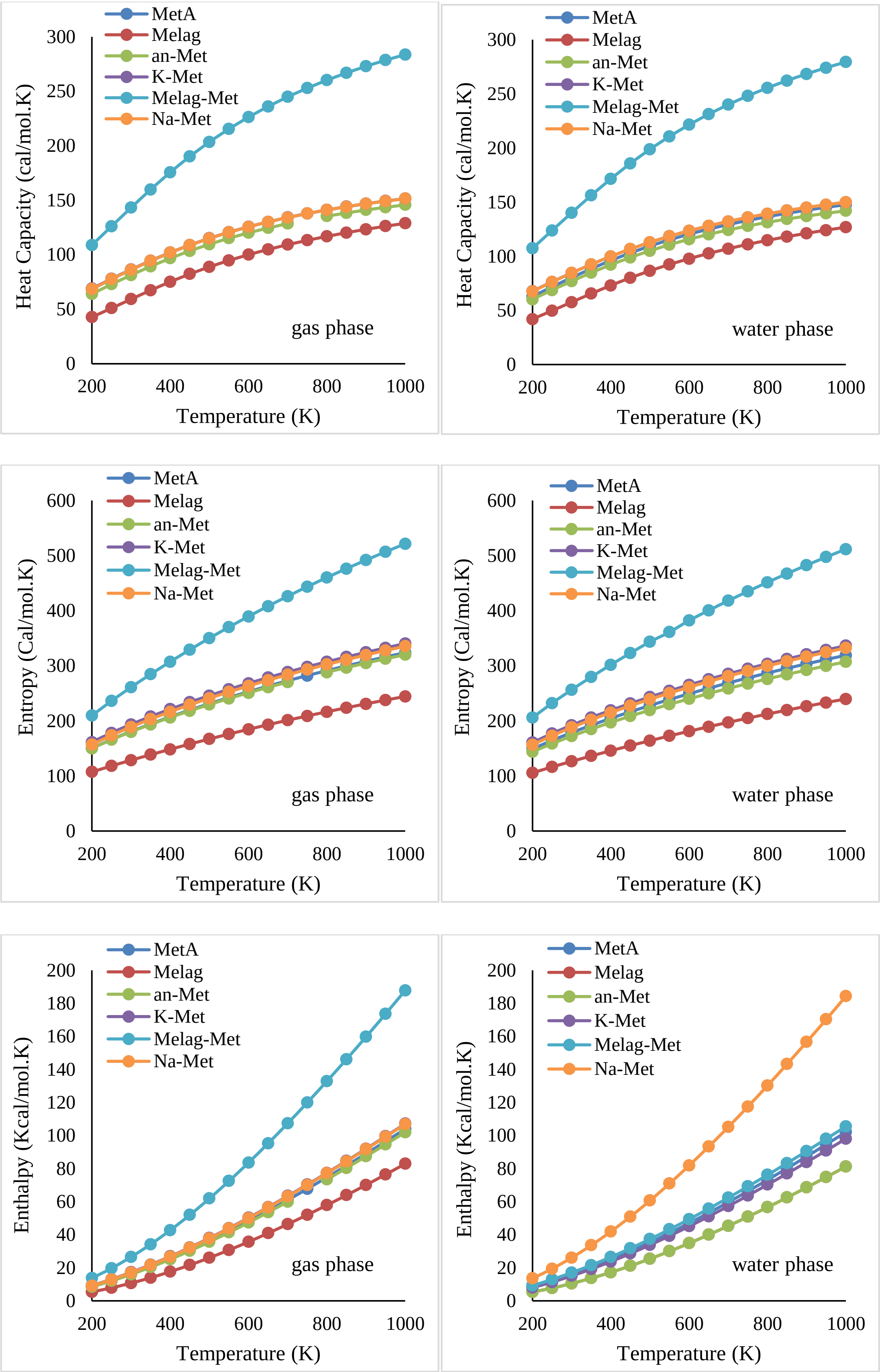

Figure 2. Thermodynamic properties at different temperatures at the B3LYP/LANL2DZ level of metrizoate.

DOI: http://dx.doi.org/10.32571/ijct.712499 **E-ISSN:2602-277X**

Table 2. Equation and correlation coefficient between temperatures and heat capacities, entropies, enthalpies for gas and water phases

	Gas Phase	**Water Phase**
Molecule	**Heat Capacity**	
MetA	$C = -0.0001T^2 + 0. 2228T + 24.592$ $R^2 = 0.9995$	$C = -0.0001T^2 + 0.2184T + 23.456$ $R^2 = 0.9997$
Melag	$C = -0.00009T^2 + 0. 215T + 3. 2548$ $R^2 = 0.9997$	$C = -0.00008T^2 + 0.2073T + 3.5785$ $R^2 = 0.9998$
an-Met	$C = -0.0001T^2 + 0. 2156T + 25.27$ $R^2 = 0.9996$	$C = -0.00009T^2 + 0.2107T + 22.153$ $R^2 = 0.9997$
K-Met	$C = -0.0001T^2 + 0. 2175T + 29.941$ $R^2 = 0.9995$	$C = -0.00009T^2 + 0.2119T + 29.506$ $R^2 = 0.9997$
Melag-Met	$C = -0.0002T^2 + 0. 4438T + 27.769$ $R^2 = 0.9997$	$C = -0.0002T^2 + 0.4264T + 28.981$ $R^2 = 0.9998$
Na-Met	$C = -0.0001T^2 + 0.219T + 29.295$ $R^2 = 0.9995$	$C = -0.00009T^2 + 0.2126T + 29.218$ $R^2 = 0.9997$
	Entropy	
MetA	$S = -0.0001T^2 + 0. 3318T + 89.462$ $R^2 = 0.9998$	$S = -0.00009T^2 + 0.3225T + 89.82$ $R^2 = 0.9998$
Melag	$S = -0.00005T^2 + 0. 2367T + 62.366$ $R^2 = 1.0000$	$S = -0.00005T^2 + 0.2299T + 62.068$ $R^2 = 1.0000$
an-Met	$S = -0.0001T^2 + 0. 3281T + 89.861$ $R^2 = 0.9998$	$S = -0.00009T^2 + 0.3093T + 87$ $R^2 = 0.9998$
K-Met	$S = -0.0001T^2 + 0. 3481T + 97.98$ $R^2 = 0.9998$	$S = -0.0001T^2 + 0.3403T + 98.568$ $R^2 = 0.9998$
Melag-Met	$S = -0.0001T^2 + 0.5655T + 104.08$ $R^2 = 0.9999$	$S = -0.0001T^2 + 0.5496T + 103.62$ $R^2 = 0.9999$
Na-Met	$S = -0.0001T^2 + 0.347T + 93.61$ $R^2 = 0.9998$	$S = -0.0001T^2 + 0.3398T + 94.637$ $R^2 = 0.9998$
	Enthalpy	
MetA	$H = 0.00005T^2 + 0.0596T - 9.0876$ $R^2 = 0.9998$	$H = 0.00005T^2 + 0.0571T - 5.7795$ $R^2 = 0.9998$
Melag	$H = 0.00005T^2 + 0. 035T - 4. 3754$ $R^2 = 0.9998$	$H = 0.00005T^2 + 0.0334T - 4.073$ $R^2 = 0.9998$
an-Met	$H = 0.00005T^2 + 0. 0588T – 5.9065$ $R^2 = 0.9998$	$H = 0.00005T^2 + 0.0545T - 5.5691$ $R^2 = 0.9998$
K-Met	$H = 0.00005T^2 + 0. 0643T – 6.2947$ $R^2 = 0.9998$	$H = 0.00005T^2 + 0.0622T - 5.8723$ $R^2 = 0.9999$
Melag-Met	$H = 0.0001T^2 + 0.0924T - 10.466$ $R^2 = 0.9998$	$H = 0.0001T^2 + 0.0893T - 9.8837$ $R^2 = 0.9998$
Na-Met	$H = 0.00005T^2 + 0.0639T – 6.4095$ $R^2 = 0.9998$	$H = 0.00005T^2 + 0.062T - 5.9832$ $R^2 = 0.9999$

Table 3. Dipole moment components and dipole moment of MetA, Melag, an-Met, K-Met, Melag-Met and Na-Met.

	Gas Phase				**Water Phase**			
Molecules	μ_x	μ_y	μ_z	μ	μ_x	μ_y	μ_z	μ
MetA	-1.981	-0.481	-0.984	2.264	-2.328	-0.349	-1.628	2.862
Melag	-0.890	0.794	-0.809	1.441	-1.103	1.124	-1.049	1.893
an-Met	-1.839	3.977	-1.398	4.599	-2.008	6.101	-2.418	6.863
Melag-Met	3.226	-0.038	0.650	3.291	2.532	2.127	-1.669	3.703
Na-Met	-3.881	1.715	-1.457	4.487	-4.661	1.664	-2.230	5.428

DOI: http://dx.doi.org/10.32571/ijct.712499 **E-ISSN:2602-277X**

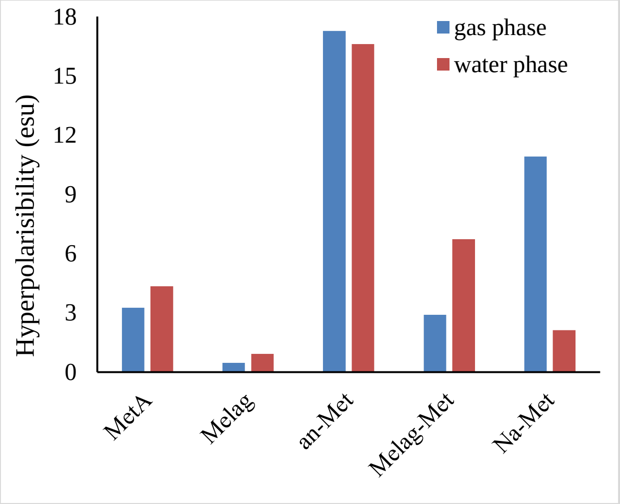

Figure 3. First hyperpolarizability *β* of MetA, Melag, an-Met, K-Met, Melag-Met and Na-Met (as values × 10^{-30} esu).

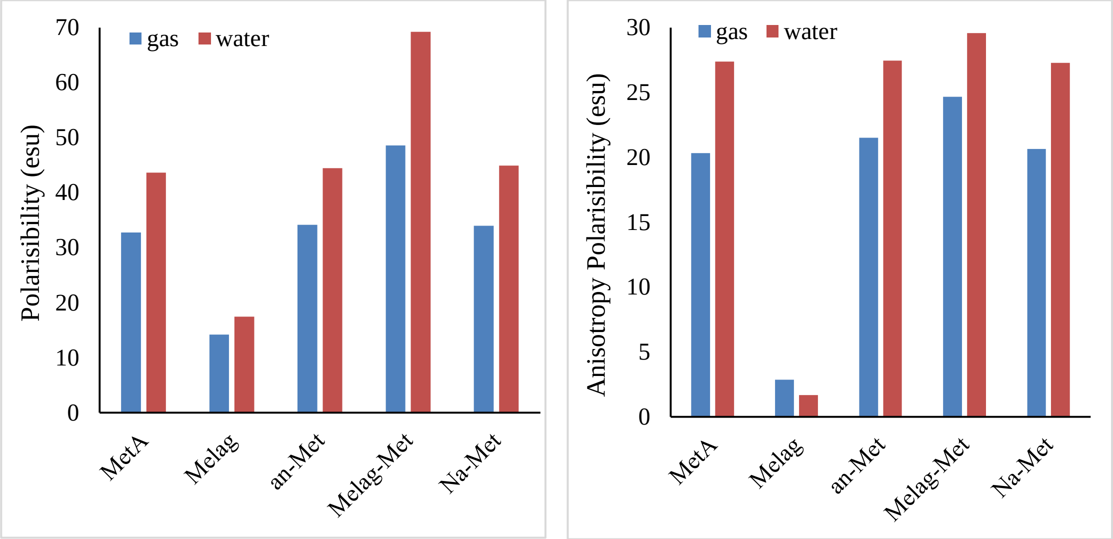

Figure 4. The average polarizability *α* (esu), the anisotropy of the polarizability *Δα* (esu), of MetA, Melag, an-Met, K-Met, Melag-Met and Na-Met calculated by B3LYP/LANL2DZ method (as values × 10^{-24} esu).

4. CONCLUSION

In the present work, the effect of the medium on the descriptors such as dipole moment and global reactivity was determined by B3LYP functional and LANL2DZ basis set. The HOMO-LUMO energy gap has been calculated to get the global reactivity descriptors such as η, μ, ω, electronic charge ΔN max, nucleofugality ΔE_n, electrofugality ΔE_e of the titled molecule. The value of the energy gap between the HOMO and LUMO of anionic form of metrisoate is very small 3.004 eV compared to other studied compounds, and this energy gap gives significant information about the reactivity of anionic form of metrizoate.

Conflict of interests

Authors declare that there is no a conflict of interest with any person, institute, company, etc.

REFERENCES

1. Widmark, J. M. *Bayl. Univ. Med. Cent.* **2007**, 20 (4), 408–417.

2. Pattinson, J. *British J. Radiol.* **1962**, 35, 824-830.

3. Billström, Å.; Hietala, S. O.; Sunnegårdh, O.; Sjödin, J. G.; Wirell, S. *Acta Radiol.* **1990,** 31(5), 509-520.

4. Laurberg, P.; Boye, N. *J. Endocr*. **1987,** 112, 387–390.

5. Levorstad, K,; Vatne, K,; Simonsen, S,; Nitter-Hauge, S.; Andrew, E. *Acta Radiol. Diagn. (Stockh)*. **1985**, 26 (4), 463-469.

6. Ingar, O.; Skalpe, H.; Markus, H. *ARRS* **1983**, 4, 326-328.

7. Saracoglu, M.; Kokbudak, Z.; Cimen, Z.; Kandemirli, F. *J. Chem. Soc. Pakistan* **2019**, 41, 479-488.

8. Frisch, M. J.; Trucks, G. W.; Schlegel, H. B.; Scuseria, G. E.; Robb, M. A.; Cheeseman, J. R.; Scalmani, G.; Barone, V.; Mennucci, B.; Petersson, G. A.; Nakatsuji, H.; Caricato, M.; Li, X.; Hratchian, H. P.; Izmaylov, A. F.; Bloino, J.; Zheng, G.; Sonnenberg, J. L.; Hada, M.; Ehara, M.; Toyota, K.; Fukuda, R.; Hasegawa, J.; Ishida, M.; Nakajima, T.; Honda, Y.; Kitao, O.; Nakai, H.; Vreven, T.; Montgomery, J. A. Jr.; Peralta, J. E.; Ogliaro, F.; Bearpark, M.; Heyd, J. J.; Brothers, E.; Kudin, K. N.; Staroverov, V. N.; Kobayashi, R.; Normand, J.; Raghavachari, K.; Rendell, A.; Burant, J. C.; Iyengar, S. S.; Tomasi, J.; Cossi, M.; Rega, N.; Millam, J. M.; Klene, M.; Knox, J. E.; Cross, J. B.; Bakken, V.; Adamo, C.; Jaramillo, J.; Gomperts, R.; Stratmann, R. E.; Yazyev, O.; Austin, A. J.; Cammi, R.; Pomelli, C.; Ochterski, J. W.; Martin, R. L.; Morokuma, K.; Zakrzewski, V. G.; Voth, G. A.; Salvador, P.; Dannenberg, J. J.; Dapprich, S.; Daniels, A. D.; Farkas, Ö.; Foresman, J. B.; Ortiz, J. V.; Cioslowski, J.; Fox, D. J. *Gaussian Inc.*, 2009.

9. Khaled, K. F. *Electrochim. Acta*, **2010**, 55, 6523-6532.

10. Domingo, L.R.; Chamorro, E.; Pérez, P. *Org. Biomol. Chem.* **2010**, 8, 5495–5504.

11. Pérez, P.; Domingo, L.R.; Aizman, A.; Contreras, R. The Electrophilicity Index in Organic Chemistry, *In: Theoretical Aspects of Chemical Reactivity*; Elsevier: New York, 2007; pp. 139-201.

12. Domingo, L.R.; Aurell, M.J.; Pérez, P.; Contreras, R. *J. Phys. Chem. A* **2002**, 106(29), 6871-6875.

13. Ayers, P. W.; Anderson, J. S. M.; Bartolotti, L. J. *Int. J. Quantum Chem.* **2005,** 101, 520-534.

14. Roos, G.; Loverix, S.; Brosens, E.; Belle, K.; Wyns, Van, L. *ChemBioChem* **2006**, 7, 981-990.

15. Bellamy L. J. *The infra-red spectra of complex molecules*. Methuen & Co: London, 1964; pp. 203-233.

16. Christiansen, O.; Gauss, J.; Stanton, J.F.; *Chem. Phys. Lett.* **1999**, 305, 147-155.

17. Kleinman, D. A. *Phys. Rev.* **1962**, 126(6), 1977-1979.

18. Mohammad, F. K.; Ridwan B. R. *J. Theor. Comput. Sci.* **2015**, 2(4), 134-137.

ORCID

https://orcid.org/0000-0002-3976-4062 (S. G. Kandemirli)

https://orcid.org/0000-0001-8790-902X (M. İ. Yımazer)

https://orcid.org/0000-0003-4027-9643 (M. Saraçoğlu)

https://orcid.org/0000-0001-6097-2184 (F. Kandemirli)

DOI: http://dx.doi.org/10.32571/ijct.724056 **E-ISSN:2602-277X**

International Journal of Chemistry and Technology

http://dergipark.org.tr/ijct

Research Article

Eco-friendly synthesis of nano copper and its use in fenton-like reactions for methylene blue degradation

Demet DEMİRCİ GÜLTEKİN [1,*], Azize ALAYLI [2], Hayrunnisa NADAROĞLU [3,4]

ID on the last page

[1]*Department of Metallurgical Program, Askale Vocational Training School, Ataturk University, Askale, Erzurum, Turkey*

[2]*Nursing Department, Faculty of Health Sciences, Sakarya University of Applied Sciences, Akyazı, Sakarya, Turkey*

[3]*Department of Food Technology, Vocational School of Technical Science, Ataturk University, Erzurum, Turkey*

[4]*Department of Nano-Science and Nano-Engineering, Faculty of Engineering, Ataturk University, Erzurum, Turkey*

Received: 20 April 2020; Revised: 16 May 2020; Accepted: 20 May 2020

*****Corresponding author e-mail: demet.gultekin@atauni.edu.tr

Citation: Demirci Gültekin, D.; Alaylı, A.; Nadaroğlu, H. *Int. J. Chem. Technol.* **2020**, 4 (1), 71-78.

ABSTRACT

Copper oxide nanoparticles (CuO NPs) were produced using green synthesis method with Cimin grape extract (*Vitis vinifera cv.*). The produced CuO NPs were used to remove methylene blue (MB) from water by degradation with Fenton-like reactions. The surface properties of the CuO NPs were determined by FT-IR, SEM and XRD techniques. Experimental parameters for MB removal were selected as: pH: 3 – 11; Temp: 20 - 80°C; initial MB concentration (15 - 50 ml^{-1}), and CuO NPs concentrations (25 - 800 mg ml^{-1}). The best reaction conditions were found to be pH: 7 - 11, temperature: 40 - 45°C, interaction time: 120 min, initial MB concentration: 3.125 mg ml^{-1} and CuO NPs concentration: 25 mg ml^{-1}. Under these conditions, CuO NPs showed a 97.80% efficacy for the removal of MB from wastewater with Fenton-like process. Moreover, this study showed that reagents were reusable, inexpensive, biocompatible, easy to prepare, harmless (CuO NPs, H_2O_2), and Fenton-like reaction conditions were created.

Keywords: Copper oxide nanoparticles, fenton-like, methylene blue, degradation, removal.

Nano bakırın çevre dostu sentezi ve metilen mavisinin bozunması için fenton benzeri reaksiyonlarda kullanımı

ÖZ

Bakır oksit nanopartiküller (CuO NP'ler), Cimin üzüm ekstresi (*Vitis vinifera cv.*) ile yeşil sentez metodu kullanılarak üretildi. Üretilen CuO NP'ler, Fenton benzeri reaksiyonlarla metilen mavisinin (MB) degradasyonla sudan uzaklaştırılması için kullanıldı. CuO NP'lerin yüzey özelikleri FT-IR, SEM ve XRD teknikleri ile belirlendi. MB uzaklaştırılması için deneysel parametreler pH: 3 - 11, sıcaklık: 20 - 80°C, başlangıç MB konsantrasyonu (15 - 50 mg ml^{-1}) ve CuO NP'lerin konsantrasyonu (25 - 800 mg ml^{-1}) olarak seçildi. En iyi reaksiyon şartlarının pH: 7-11, sıcaklık: 40 - 45°C, etkileşim süresi: 120 dak., başlangıç MB konsantrasyonu: 3,125 mg ml^{-1} ve CuO NP'lerin konsantrasyonu: 25 mg ml^{-1} olduğu bulundu. Bu koşullar altında CuO NP'ler, Fenton benzeri işlemle atık sudan MB'nin ortadan kaldırılması için% 97,80'lik bir etkinlik gösterdi. Ayrıca bu çalışma, reaktiflerin tekrar kullanılabilir, ucuz, biyouyumlu, kolay hazırlanabilir, zararsız (CuO NPs, H_2O_2) ve Fenton benzeri reaksiyon şartlarının oluşturulduğunu göstermiştir.

Anahtar Kelimeler: Bakır oksit nanopartiküller, Fenton benzeri, metilen mavisi, bozulma, uzaklaştırma.

1. INTRODUCTION

Methylene blue (MB) is a cationic dye. It consists of dark green powder crystals and is odorless. MB is a stain material widely used in the textile industry due to its adsorbable feature. MB is frequently used in paper, hair and cotton fabric dyeing. MB is a substance with a molecular mass of 319.86 g mol^{-1} and its formula is $C_{16}H_{18}ClN_3S.H_2O$. Its structure and some general characteristics are shown in Table 1.[1]

It has various harmful effects. In case of inhalation, it may cause difficulty in breathing in short periods. It creates a flammable sensation in the mouth, and also may cause nausea, stomach, vomiting, gastritis, cyanosis, jaundice, quadriplegia, human cell necrosis and an increment in heart beats.

Table 1. General characteristics of MB dye

Synonyms	Blue N, methylene blue, Swiss chromosmon methylene blue, methylene blue N, methylthionine chloride, methylthioninium chloride, swiss blue, urolene blue
Molecular formula	$C_{16}H_{18}ClN_3S$
Molecular weight	319.851 g/mol
Safety and Hazard	-Damaging if swallowed serious toxicity. -Bases skin irritation -Effects severe eye irritation -Might reason breathing irritation -Reasons injury to tissues through lengthy or recurrent contact
3D conformer	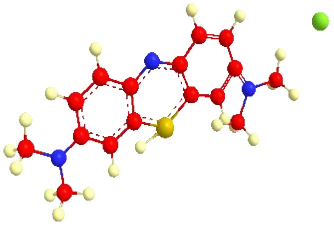

On the other hand, some information about *Vitis vinifera L.* used in this study where green nanoparticle production is aimed is given. *Vitis vinifera* L. (common grape) belonging to Vitaceae family has been presented for their therapeutic and dietary worth for thousands of years. Egyptians had consumed grapes for more than 6,000 years in the past, and the first Greek philosophers had praised the medicinal strength of grapes. Phenolic compounds present in nearly all parts of grape are increasingly believed to exhibit antioxidants and antimicrobial efficiency. Grape leaves contain many compounds such as polyphenols, anthocyanins, flavonoids and organic acids (malic, fumaric, oxalic, tartaric, citric and succinic acid).[2,3]

Metal nanoparticles have been considered widely since of their exclusive physicochemical features with optical, electronic, magnetic properties, and catalytic and antimicrobial activities.[4-6] Today, many synthesis methods are being investigated due to these properties of nanoparticles.[7] In general, metal nanoparticles are produced by some chemical means, such as chemical reduction[8] and photochemical reactions[9], and recently by green chemistry.

Usage of fungi, bacteria and plant extracts[10-11] for the green chemistry which offers benefits to chemical and physical techniques is more economical and ecological. Roy and co-workers have defined the Green synthesis of silver nanoparticles using fruit extract of grapes, and also their antibacterial activity.[12]

Disposed dyes create a real danger to health and ecosystems and cause cancer formation. Nowadays, removal of dyes in wastewater by degradation is extremely important and create a striking work due to their dangerous effects.[13,14] In sectors such as fabric production, water containing large amounts of waste dye used for coloring is discharged into the sewage system without being cleaned. Since they are structurally aromatic and complex, it is difficult to remove such dyes by microbial, chemical and biological methods.[15-16] It is not possible to maintain a biological and biodegradation based wastewater management against azo dyes, which are widely used in numerous productions of artificial dyes and is one of the main classes with its wide variety of colors. Widespread wastewater management by chemical and physical methods (adsorption, chemical conversion, firing, photo catalyst or ozonation) used to remove dyes is effective but relatively expensive.[17,18]

As a result, great attention has been paid to the development of water cleaning methods that will completely remove the dye molecules. Due to the high oxidative power of the hydroxyl radical, a large number of processes based on this type of removal have been called oxidation processes. Oxidation processes have shown moderate processes in reducing organic and inorganic pollutants in water or wastewater. Hydrogen peroxide (H_2O_2), ultraviolet (UV) light, or combined both are amoung the most commonly used oxidation processes. The heterogeneous photocatalytic oxidation combined with Fenton (H_2O_2) and photo-Fenton (H_2O_2/UV) are also effective oxidation processes.[19-24] The removal of organic pollutants and dyes that cannot be biodegradable can be removed successfully with Fenton reactions.[25] In recent years, Fenton and Fenton-like reactions have attracted great attention. In various Fenton reactions, the iron species attach to the surface of the catalysts in a suitable aqueous medium, and the redox reactions between Fe (II)/(III) occur in the presence of hydrogen peroxide, which enables the formation of reactive mechanisms such as (•OH) and hydroperoxyl (•OOH) radicals.[26-28] In Fenton-like reactions, the metal ions that resemble iron and hydrogen peroxide are separated. The metal ions play an important role in a series of consecutive chemical and biological events. Many applications of Fenton chemistry are used in wastewater management. Iron or iron-like copper ions also separate hydrogen peroxide in the Fenton reaction. Therefore, such recreations have technical and biological importance. However, the optimization of this reaction is difficult. Copper

DOI: http://dx.doi.org/10.32571/ijct.724056 **E-ISSN:2602-277X**

concentration, ligand and/or organic substrate formation, pH of the solution and buffer composition significantly affect the dissociation kinetics and mechanism of hydrogen peroxide.[29]

Current research aims to develop an inexpensive method for the removal of MB in solution medium. Therefore, green CuO NPs was produced using Vitis vinifera L. The produced CuO NPs were used for the removal of MB by degradation. The effects of CuO NPs concentration, pH, contact time, temperature on the degradation were investigated.

2. MATERIALS AND METHODS

2.1. Chemicals and reagents

$CuCl_2.2H_2O$, Na_2HPO_4, CH_3COONa, methylene blue (MB) and hydrogen peroxide (H_2O_2) (w/w, 30 %) were provided from Sigma-Aldrich. All of the compounds were used without further purification, as they are of analytical purity.

2.2. Preparation of methylene blue and H_2O_2 solutions

1000 mg l^{-1} standard solution of MB was first prepared. Then, the solutions with lower concentration were prepared from this standard solution using distilled water. A 10.0% H_2O_2 solution (v/v) was prepared from a standard 30.0 % H_2O_2 solution with distilled water.

2.3. Preparation of CuO NPs

The production of gold nanoparticles using cimin grape extracts has been reported previously.[30] In this work, the cimin grape extracts was prepared by mixing 60.0 g l^{-1} cimin grape with distilled water. Subsequently settle down for 1.0 h, the extract was vacuum-filtered. Individually, a solution of 0.10 M $CuCl_2·2H_2O$ was prepared by addition 19.9 g of solid $CuCl_2·2H_2O$ in 1.0 l of deionized water. As a result, 0.10 $CuCl_2·2H_2O$ solution was added to the grape extract of 60.0 g l^{-1} cimin in a 2:3 volume ratio. Subsequently, when the pH of the medium was adjusted to 6.0, the formation of dark blue mullet showed the formation of CuO NPs. Then, the copper nanoparticles were washed with pure water and alcohol and then dried in an oven for 24 hours.

2.4. Characterization of CuO NPs surface

The chemical structure of CuO NPs was analyzed by scanning electron microscopy (SEM) and other spectral studies. A scanning electron microscope (SEM; Metek, Apollo prime, Active field 10 mm^2, Microscope examination S50, SE detector R580) was used to examine the surface of the metal material covered with metal, which magnifies 5000 times. SEM analysis is done by coating the sample surfaces with a thin layer of gold (20 nm) to obtain a conductive surface and prevent electrostatic charge throughout the investigation. Energy dispersive EDX analysis was used to determine the chemical composition of the synthesized CuO NPs. Fourier Transform Infrared (FT-IR) analysis was used for the analysis of functional groups in the structure. The FT-IR spectrum was recorded in the range of 4000 - 400 cm^{-1} wavelength by a Mattson 1000 FT-IR. The XRD pattern of CuO NPs was analyzed using XRD (Rigaku D-Max 2000 and CuKα (λ = 0.154 nm) with 2θ, 5° - 100°) radiation.

2.5. Degradation study

All the degradation experiments were performed in a 50 ml bottle having 50 mg l^{-1} MB and 0.1 g CuO NPs with 5 ml distilled water in temperature controlled shaking water bath under atmospheric pressure at 25°C. The desired pH values were adjusted using 0.1 M NaOH or 0.1 M HCl. The degradation reaction was started by adding 3% H_2O_2 solution (w/w) to the previously prepared medium. The reaction medium was placed on a shaker (300 rpm) at room temperature. The reaction mixture samples were centrifuged at 6000 x g for 15 min. Samples were taken from the reaction medium at regular intervals using a micropipette. The supernatant was was passed through a filter. The concentration of MB was determined spectrometrically. The UV–Vis absorbance was measured at λ_{max} = 660 nm for MB by a spectrophotometer. The final concentrations were obtained using the standardization curves. In addition, similar blank tests were performed with H_2O_2 solution under only equal conditions and the ability of H_2O_2 alone to degrade without CuO NPs was measured. Percentage values of MB removed by degradation were calculated from Eq. (1).

$$\% \text{ MB removal} = \frac{Ci - Ce}{Ci}\, x\, 100 \qquad (1)$$

Where C_i is initial concentrations of dye (mg l^{-1}), C_e is final (equilibrium) concentrations of dye (mg l^{-1}).

2.6. Effects of contact time, pH, temperature, H_2O_2 and adsorbent concentrations

The influence of the amount of CuO NPs was studied by changing metal amount between 0.0125 - 0.20 mg/50 ml, and also the experimental conditions were between pH: 3 - 11, T: 20 - 80°C, and MB concentration: 3.25 - 50 mg l^{-1}. It is detected that MB degradation increases at first 20 min of interaction with CuO NPs. Essentially, MB degradation is fast at the beginning but it regularly decreases with time until it reaches the equilibrium.

This shows that the concentration of MB in the solution is reduced quickly in 20 min and was nearly finished at 120 min of interaction time.

2.7. Statistical analysis

All of the experiments were repeated three times. Statistics were shown as mean ± standard error. Statistical analysis were achieved by SPSS version 10.0 software (SPSS Inc., Chicago, IL., USA), and the important action changes were founded with a 95% confidence (P □□0.05) by Tukey's test.

3. RESULTS AND DISCUSSIONS

3.1. SEM study

The SEM analysis is important to determine the surface structure of CuO NPs. The SEM image of CuO NPs produced with means of grape fruit water extract concentrations with 0.1 M $CuCl_2.2H_2O$ at room temperature is shown in Figure 1.

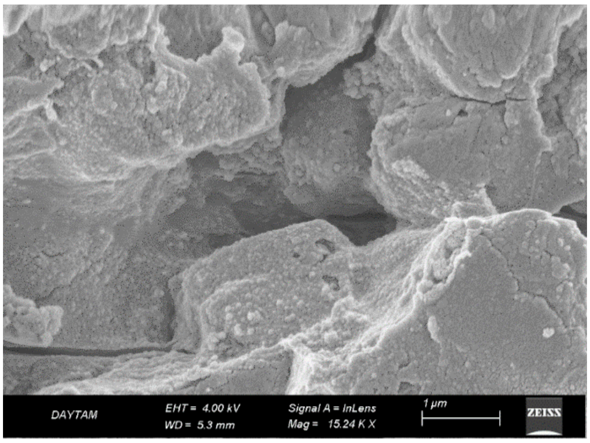

Figure 1. SEM image of CuO NPs.

As seen from Figure 1, the shape of the nanoparticles is spherical on the accumulated extract concentration.[31-33] CuO NPs have been determined to have a particle size ranging from about 35 nm to 50 nm.

EDX spectrum on the elemental configuration of the CuO NPs is shown in Figure 2. From the EDX results, it is seen that there are present 35.10% Cu and 15.40% O in CuO NPs nanoparticular structure.

3.2. XRD analysis

The stage configuration of crystal buildings of the formed products, taken from dark blue suspensions of CuO NPs, was explored by XRD.[34] The XRD spectrum of CuO NPs is shown in Fgure 3.

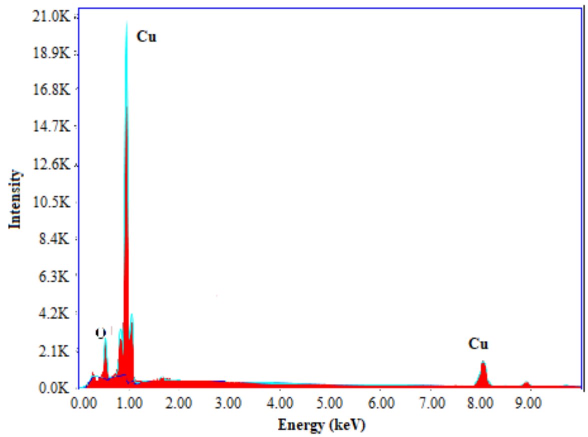

Element	Weight %	Atomic %
O K	6.2	15.4
Na K	18.2	31.8
Au M	5.1	1
Cl K	14.7	16.7
Cu K	55.7	35.1

Figure 2. EDX spectrum of CuO NPs.

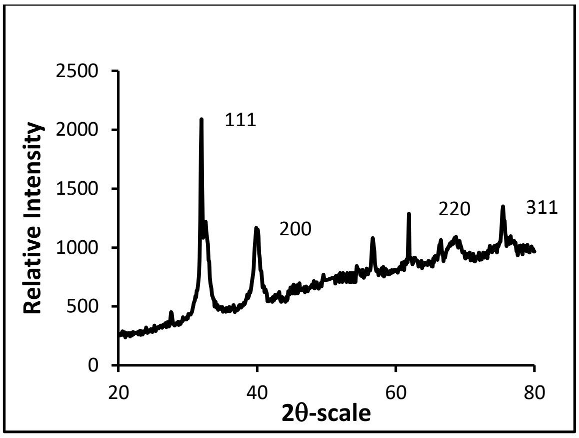

Figure 3. XRD spectrum of CuO NPs.

As seen from Figure 3, XRD peaks obtained for dark blue compound found after two weeks of the synthesis are indexed to CuO with characteristic diffraction indices (111), (200), (220) and (311) at 2 theta value of 32°, 39.8°, 61.6° and 75.3° respectively.

3.3. FT-IR analysis

Fourier transform infrared (FT-IR) spectroscopy was used to describe the functional groups of the synthesized CuO NPs. The FT-IR spectrum of CuO NPs is presented in Figure 4. From Figure 4, the characteristics peaks were observed at 612, 1056, 1111, 1309 and 1669 cm^{-1}. The weak peak at 631cm^{-1} indicates Cu–O vibration in CuO NPs.[35]

DOI: http://dx.doi.org/10.32571/ijct.724056 **E-ISSN:2602-277X**

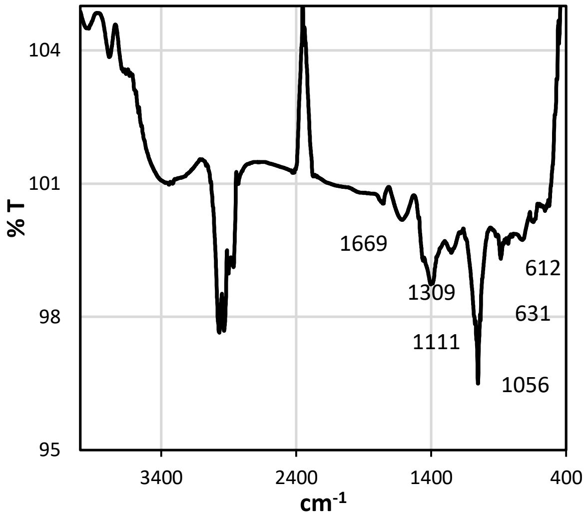

Figure 4. FT-IR spectrum of CuO NPs.

3.4. Degradation studies

The degradation of MB by CuO NPs was investigated under conditions changed such as pH (3 - 11), temperature (20 - 80°C), initial MB concentration (15 - 50 mg l^{-1}), and nanoparticles concentration (25 - 800 mg ml^{-1}). Dye degradation was determined by a UV-Vis spectrophotometer. Absorption spectrum of MB is shown in Figure 5. As seen from this spectrum, MB has maximum peak at 660 nm.

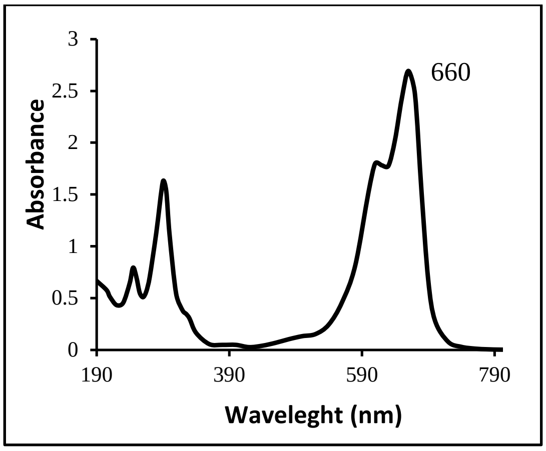

Figure 5. Absorption spectrum of MB (Initial dye concentration: 25 mg l^{-1}, pH: 10, Temperature: 40 ^{o}C).

Figure 6 shows the effect of contact time on MB degradation by CuO NPs. As seen this figure, the percent degradation of MB increases with increasing contact time. It is seen that maximum dye degradation occurs at 120 min. Therefore, this time has been accepted an equilibrium time.

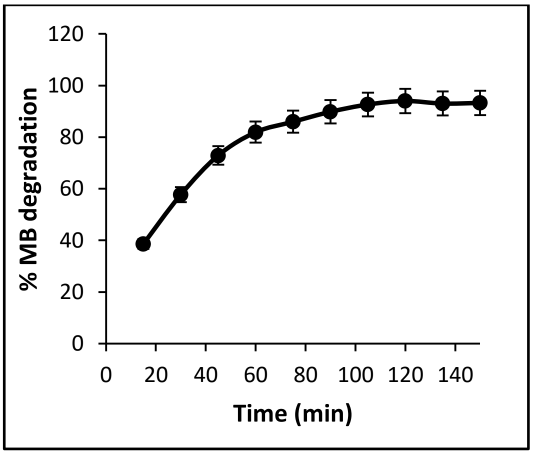

Figure 6. Effect of contact time on MB degradation by CuO NPs (Initial dye concentration: 25 mg l^{-1}, Temperature: 40 °C, pH: 10, CuO NPs concdentration: 25 mg l^{-1}).

Figure 7 shows the effect of pH on MB degradation by CuO NPs. pH value of solution has a significant effect in the fenton-like reaction because it affects both the solubility of MB and the degree of ionization of CuO NPs. As seen from Figure 7, it is determined that MB degradation significantly increases with increasing pH of the solution. Generally, fenton reactions are more effective at low pH, but our research has shown that pH values higher than 6 are more suitable for dye removal.[36-40]

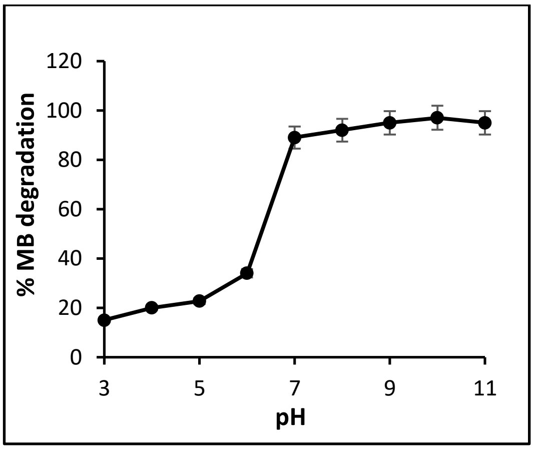

Figure 7. Effect of pH on MB degradation by CuO NPs (Initial dye concentration: 25 mg l^{-1}, Temperature: 40^{o}C, CuO NPs concentration: 25 mg ml^{-1}).

Figure 8 illustrates the effect of temperature on MB degradation by CuO NPs. From this figure, it is seen that the percent degradation of MB increase similarly withincreasing temperature. It is found that the maximum percent degradation of MB occurs at 40 - 45°C.

The degradation efficacy of MB with fenton-like process is found to be more advantageous for industrial discharge at more temperatures.

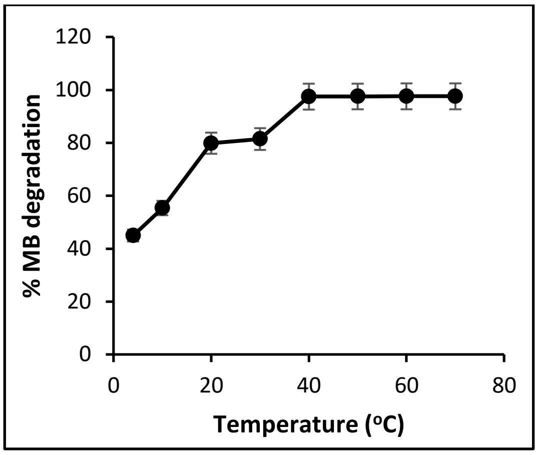

Figure 8. Effect of temperature on MB degradation by CuO NPs (Initial dye concentration: 25 mg l^{-1}, pH: 10, CuO NPs concentration: 25 mg ml^{-1}).

Figure 9 shows the effect of CuO NPs concentration on MB degradation. As seen from this figure, MB degradation increases with increasing CuO NPs concentration. It is seen that the maximum percet degradation occurs at 0.4 mg l^{-1} CuO NPs concentration.

Figure 10 demonstrates the percent degradation of MB for various initial MB concentration. As seen from Figure 10, the maximum degradation of 97.80% is obtained for initial MB concentration of 3.125 mg ml^{-1}.

Figure 11 illustrates the effect of H_2O_2 concentration on MB degradation. As seen from Figure 11, the percent degradation of MB significantly increases with increasing H_2O_2 concentration. It is seen that the maximum percent degradation occurs for 0.8 μg ml^{-1} H_2O_2.

4. CONCLUSION

Metal nanoparticles are widely used commercially to remove dyes in many areas. In this research, firstly, copper nanoparticles (CuO NPs) were manufactured using green synthesis technique. For this aim, Cimin grape seeds water extract was employed as green synthesis intermediate. The synthesized CuO NPs were analyzed by means of different spectroscopy techniques (UV-Vis spectrophotometer, SEM, EDX, XRD and FT-IR). Then CuO NPs were used in the Fenton-like reaction, to eliminate the methylene blue dye from water. It was determined that green CuO NPs could be easily used in removing of MB by degradation method.

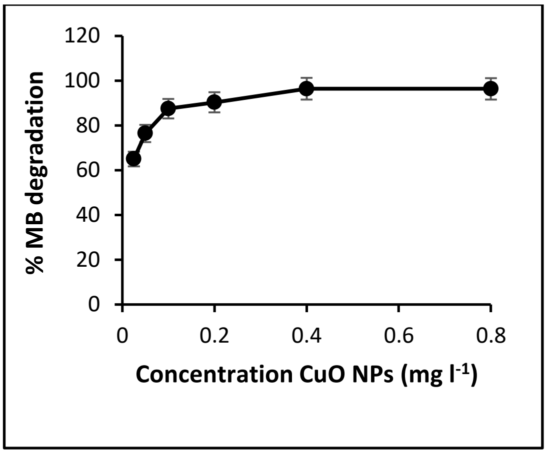

Figure 9. Effect of CuO NPs concentration on MB degradation (Initial dye concentration: 25 mg l^{-1}, pH: 10, Temperature: 40°C).

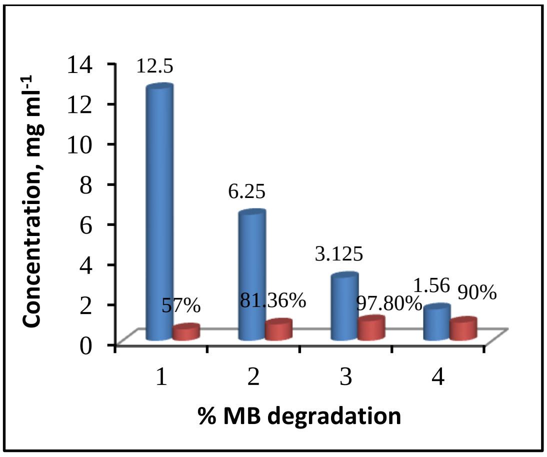

Figure 10. Percent of MB degradation (Blue: Initial dye concentration, Red: Percent of dye removal) (Temperature: 40 °C, pH: 10, CuO NPs concentration: 25 mg ml^{-1}).

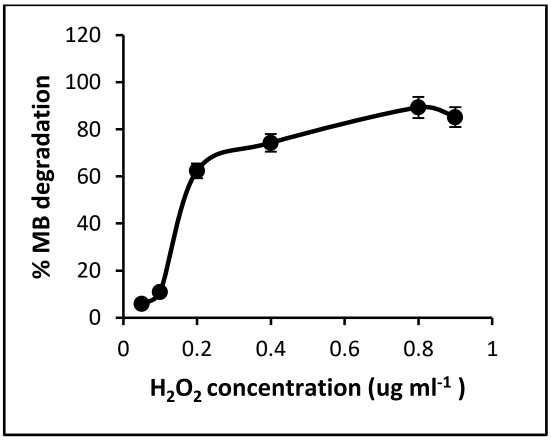

Figure 11. Effect of H_2O_2 concentration on MB degradation (Initial dye concentration: 25 mg l^{-1}, Temperature: 40°C, pH: 10, CuO NPs concentration: 25 mg ml^{-1}).

DOI: http://dx.doi.org/10.32571/ijct.724056 **E-ISSN:2602-277X**

ACKNOWLEDGEMENT

The SEM, EDX, XRD and FTIR analyses were performed in the DAYTAM (East Anatolia High Technology Application and Research Centre) in Ataturk University.

Conflict of interests

Authors declare that there is no a conflict of interest with any person, institute, company, etc.

REFERENCES

1. Sen, T. *Int. J. Environ. Pollut. Control Manage*. **2011**, 3 (1), 1-10.

2. Bombardelli, E.; Morazzoni, P. *Fitoterapia (Milano).* **1995**, 66 (4), 291-317.

3. Fan, P.; Lou, H.; Yu, W.; Ren, D.; Ma, B.; Ji, M. *Tetrahedron Lett.* **2004,** 45 (15), 3163-3166.

4. Królikowska, A.; Kudelski, A.; Michota, A.; Bukowska. J. *Surf. Sci*. **2003**, 532, 227-232.

5. Catauro, M.; Raucci, M. G.; De Gaetano, F.; Marotta, A. *J. Mater. Sci-Mater. M.* **2004**, 15 (7), 831-837.

6. Crabtree, J. H.; Burchette, R. J.; Siddiqi, R. A.; Huen I. T.; Hadnott, L. L.; Fishman, A. *Periton. Dialysis Int.* **2003,** 23 (4), 368-374.

7. Sharma, V. K.; Yngard, R. A.; Lin, Y. *Adv. Colloid Interfac*. **2009**, 145 (1-2), 83-96.

8. Balantrapu, K.; Goia, D. V. *J. Mater. Res*. **2009**, 24 (9), 2828-2836.

9. Taleb, A.; Petit, C.; Pileni, M. P. *Chem. Mater*. **1997,** 9 (4), 950-959.

10. Begum, N. A.; Mondal, S.; Basu, S.; Laskar, R. A.; Mandal, D. *Colloid Surface B*. **2009**, 71 (1), 113-118.

11. He, S.; Guo, Z.; Zhang, Y.; Zhang, S.; Wang, J.; Gu, N. *Mater. Lett*. **2007**, 61 (18), 3984-3987.

12. Roy, K. Green'Synthesis of Silver Nanoparticles by using Grape (Vitis Vinifera) Fruit Extract: Characterization of the Particles and Study of Antibacterial Activity. PhD Dissertation, Indian Institute of Technology, Kharagpur, 2012.

13. Robinson, T.; Chandran, B.; Nigam, P. *Enzyme Microb. Tech*. **2001**, 29 (8-9), 575-579.

14. de Campos Ventura-Camargo B.; Marin-Morales, M. A. *Text. Light Ind. Sci. Technol*. **2013**, 2 (2), 85-103.

15. Correia, V. M.; Stephenson, T.; Judd, S. J. *Environ. Technol*. **1994**, 15 (10), 917-929.

16. Wesenberg, D.; Kyriakides I.; Agathos, S. N. *Biotechnol. Adv.* **2003**, 22 (1-2), 161-187.

17. De Moraes, S. G.; Freire, R. S.; Duran, N. *Chemosphere* **2000**, 40 (4), 369-373.

18. Celebi, N.; Nadaroglu, H.; Kalkan, E.; Kotan *R. Arch. Environ. Prot*. **2016,** 42 (4), 58-69.

19. Hoffmann, M. R.; Martin, S. T.; Choi, W.; Bahnemann DW. *Chem. Rev*. **1995**, 95 (1), 69-96.

20. Pérez, M.; Torrades, F.; García-Hortal, J. A.; Domènech, X.; Peral, J. *Appl. Catal. B- Environ.* **2002**, 36 (1), 63-74.

21. Nadaroglu, H.; Kalkan, E.; Celik, H. *Inter. J. Environ. Sci. Technol*. **2015,** 12 (6), 2079-2090.

22. Alaton, I. A.; Balcioglu, I. A.; Bahnemann, D. W. *Water Res*. **2002,** 36 (5), 1143-1154.

23. Neamtu, M.; Siminiceanu, I.; Yediler, A.; Kettrup, A. *Dyes Pigments* **2002**, 53 (2), 93-99.

24. Solmaz, S. K.; Birgül, A.; Üstün, G. E.; Yonar, T. *Color. Technol*. **2006**, 122 (2), 102-109.

25. Deng, J.; Jiang, J.; Zhang, Y.; Lin, X.; Du, C.; Xiong, Y. *Appl. Catal. B- Environ.* **2008,** 84 (3-4), 468-473.

26. Neyens, E.; Baeyens, J. *J. Hazard. Mater*. **2003**, 98 (1-3), 33-50.

27. Sun, J. H.; Sun, S. P.; Wang, G. L.; Qiao, L. P. *Dyes Pigments* **2007**, 74 (3), 647-652.

28. Gürtekin, E.; Şekerdağ, N. *Sigma Mühendislik ve Fen Bilimleri Dergisi*. **2008**, 26 (3), 216-226 (in Turkish).

29. Naqvi, K. R.; Marsh, J.; Chechik, V. *Dalton T.* 2014, 43 (12), 4745-4751.

30. Ismail, E. H.; Khalil, M. M.; Al Seif, F. A.; El-Magdoub, F.; Bent, A. N.; Rahman, A. *Prog. Nanotechnol. Nanomater*. **2014**, 3, 1-12.

31. Rai, A.; Singh, A.; Ahmad, A. *Langmuir* **2006**, 22 (2), 736-741.

DOI: http://dx.doi.org/10.32571/ijct.724056 **E-ISSN:2602-277X**

32. Ogale, S. B.; Ahmad, A.; Pasricha, R.; Dhas, V. V.; Syed, A. *Appl. Phys. Lett*. **2006**, 89 (26), 263105.

33. Nadaroglu, H.; Kalkan, E. *Indıan J. Chem. Techn.* **2014**, 21, 249-256.

34. Tian K.; Liu C.; Yang H.; Ren X. *Colloids and Surfaces A.* **2012**, 397, 12-15.

35. Joseph, A.; Sumalatha, D.; Shubha, L. N. *IJMTER* **2016**, 03 (11), 186-190.

36. Benhammou, A.; Yaacoubi, A.; Nibou, L.; Tanouti, B. *J. Colloid Interf. Sci*. **2005**, 282 (2), 320-326.

37. Nadaroglu, H.; Kalkan, E.; Demir, N. *Desalination* **2010,** 251 (1-3), 90-95.

38. Onundi, Y. B.; Mamun, A. A.; Al Khatib, M. F.; Ahmed, Y. M. *Int. J. Environ. Sci. Te*. **2010**, 7 (4), 751-758.

39. Nadaroğlu, H.; Kalkan, E.; Celebi, N. *Carpath. J. Earth Env. Sci*. **2014**, 9 (1), 69-80.

40. Gultekin, D. D.; Gungor, A. A.; Onem, H.; Babagil, A.; Nadaroglu H. *J. Turkish Chem. Soc. A.* **2016**, 3 (3), 623-636.

ORCID

https://orcid.org/0000-0003-0773-6048 (D. Demirci Gültekin)

https://orcid.org/0000-0002-7568-6970 (A. Alaylı)

https://orcid.org/0000-0002-7015-5169 (H. Nadaroğlu)

DOI: http://dx.doi.org/10.32571/ijct.725783 **E-ISSN:2602-277X**

International Journal of Chemistry and Technology

http://dergipark.org.tr/ijct

Research Article

Use of peanut shell-based polyurethane type rigid foam in removing remazol orange RGB dye from aqueous solution

Bilal ACEMIOĞLU *

ID on the last page

Department of Chemistry, Faculty of Science and Arts, Kilis 7 Aralık University, 79000, Turkey

Received: 23 April 2020; Revised: 07 June 2020; Accepted: 09 June 2020

*****Corresponding author e-mail: acemioglu@kilis.edu.tr

Citation: Acemioğlu, B. *Int. J. Chem. Technol.* **2020**, 4 (1), 79-89.

ABSTRACT

This study reflects the adsorption ability and usable of peanut shell-polyurethane type rigid foam for the removal of remazol orange RGB (RO-RGB) dye, a reactive dye, from aqueous solution. RO-RGB removal was studied for initial dye concentrations (10-150 mg l^{-1}), pH values (3-9), and temperatures (20-60°C) at various contact times. Dye removal increased with the increases in initial dye concentration and temperature while it was decreasing with an increase in pH. Maximum dye removal was determined to be about 98% under all the experimental conditions. Equilibrium data obtained were adapted to the Langmuir, Freundlich, and Temkin isotherm models, and it was seen that the adsorption obeyed the Freundlich isotherm model with determination of coefficient of r^2 = 0.966. Kinetics data was found to be harmony with the pseudo-second kinetic order model (higher than r^2 = 0.9908). As a result, it was determined that the polyurethane-type rigid foam produced from peanut shell could be used as an alternative to activated carbon and could easily be used as an adsorptive material to remove RO-RGB dye.

Keywords: Peanut shell, polyurethane type rigid foam, remazol orange RGB, removal, adsorption.

Remazol turuncu RGB boyasının sulu çözeltiden uzaklaştırılmasında fıstık kabuğu bazlı poliüretan tipi sert köpük kullanımı

ÖZ

Bu çalışma reaktif bir boyar madde olan remazol turuncu RGB (RO-RGB)' nin sulu çözeltiden uzaklaştırılması için yerfıstığı kabuğu esaslı poliüratan tipi sert köpüğün adsorpsiyon kabiliyetini ve kullanılabilirliğini yansıtmaktadır. RO-RGB uzaklaştırılması, çeşitli temas sürelerinde farklı konsantrasolar (10-150 mg l^{-1}), pH değerleri (3-9), ve sıcaklılar (20-60°C) için incelenmiştir. Boya uzaklaştırlması pH daki bir artışla azalırken başlangıç boyar madde konsantrasyonu ve sıcaklıktaki artışlarla artmıştır. Maksimum boya uzaklaştırılmasnın tüm deneysel şartlar altında yaklaşık % 98 civarında olduğu belirlenmiştir. Elde edilen denge dataları Langmuir, Freundlich, and Temkin isotherm modellerine uyarlanmıştır ve adsorpsiyonun r^2 = 0.966' lık bir belirlenme katsayısı ile Freundlich isotherm modeline uyduğu görülmüştür. Kinetik dataların yalancı ikinci dereceden kinetik model ile uyumlu olduğu bulunmuştur (r^2 = 0.9908' den daha büyük). Sonuç olarak, yer fıstığı kabuğundan üretilen poliüretan tipi sert köpüğün aktif karbona alternatif olarak kullanılabileceği ve RO-RGB boyasının uzaklaştırılması için adsorptif bir malzeme olarak kolayca kullanılabileceği belirlenmiştir.

Anahtar Kelimeler: Yerfıstığı kabuğu, poliüretan tipi sert köpük, remazol turuncu RGB, uzaklaştırma, adsorpsiyon.

1. INTRODUCTION

In today's world, where industrialization is increasing, environmental problems affect negatively human health. Especially the wastes of factories such as dyeing, ink, textile, automotive, paper, leather industries etc. cause to many diseases such as allergy, dermatitis, cancer, mutation and skin irritation.[1] Therefore, it is extremely important to remove such undesired substances from the environment.[2] For this purpose the adsorption method, which is a cheap and effective method, has been commonly used recently. The adsorption method can

DOI: http://dx.doi.org/10.32571/ijct.725783 **E-ISSN:2602-277X**

be described generally as the removal of dyes or metal ions from an aqueous medium using an adsorbent material. Activated carbon is used generally in adsorption method. However, since activated carbon is expensive, many scientists have used cheaper adsorbents recently.[3] According to the literature search, some inexpensive adsorbents such as organic, inorganic, biological, and lignocellulosic materials which are used to effectively remove environmental pollutants are listed below. For example, poly(N-isopropylmethacrylamide-acrylic acid) microgels[4] and polydopamine microspheres[5] as organic adsorbents; zinc oxide,[6] perlite,[7] clay[8] as inorganic adsorbents; fungus,[9,10] alge[11] and yeast[12] as biological materials; coconut sawdust,[3] shells,[13] watermelon rind,[14] tree barks,[15,16] wheat straw,[17] orange peel,[18] and peanut shell,[19] as lignocellulosic materials have been used.

Of these, the adsorbents with lignocellulosic content are natural agricultural wastes with no economic value. Such materials have been used directly in the literature for dye and metal adsorption, but they usually do not show very high adsorption capacity. In order to increase the adsorption capacity, lignocellulosic adsorbents have been used either by modifying or by producing new adsorbent materials. According to the literature survey, new adsorbents produced from lignocellulosic materials can be listened as: phenolated wood resin,[20] Polyurethane cross-linked pine cone biomass,[21] lignin-based hydrogels,[22] the polyurethane type rigid foam produced from peanut shell. Our previously some studies can be expressed as follows, respectively.

Removal of remazol orange RGB (RO-RGB) using biochar produced from peanut shell has been studied.[23] Adsorption of safranin-O dye[24] using peanut shell-based polyurethane type foam (PSPUF) pretreated with HCl has been investigated. Also, PSPUF obtained by chemically modification with HCl has been used for the adsorption of remazol brilliant blue R.[25] However, no study has been reported for RO-RGB removal by this foam in the literature. Therefore, in this study, the use of PSPUF for RO-RGB removal from aqueous solution is aimed. Thus, the present paper reflects an original study. Effects of contact time, initial dye concentration, temperature, and pH on dye removal are investigated. Moreover, isotherm, kinetics and thermodynamic studies for dye removal are also performed.

2. EXPERIMENTAL

2.1. The supply of raw material peanut shell for the production of polyurethane type rigid foam

In order to obtain the polyurethane-type rigid foam from peanut shell, the peanut shell wastes were received from Osmaniye province of Turkey. Firstly the samples were cleaned well and then then dried in an oven until a constant weight. Dried samples were powdered by a grinding mill, and stored after sieving over 100-mesh molecular sieve to produce polyurethane-type rigid foam.

2.2. Preparation of peanut shell-based polyurethane type rigid foam for dye removal

PSPUF was produced from a reaction between the peanut shell and methylene diphenyl diisocyanate (MDI) via polyaddition polymerization as described in our previous study. The formation of PSPUF using the foam and MDI is shown in Scheme 1.[24]

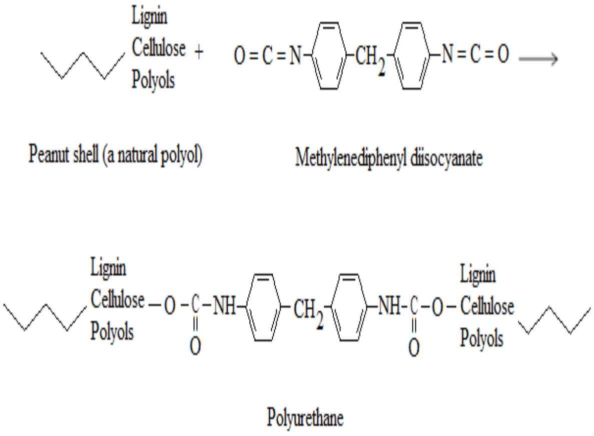

Scheme 1. The formation of polyurethane-type rigid foam using peanut shell and methylenediphenyl diisocyanate (MDI).

PSPUF was modified for dye removal experiments because the resulting foam did not adsorb RO-RGB dye. Modification was carried out by chemically reacting the foam with HCl at 140°C for 6 h. This reaction was performed using 10 g foam and 10 ml 0.5 N HCl. After the reaction time of 6 h, the reaction mixture was filtered and then the modified PSPUF was washed well with distilled water to clear impurities.[25]

2.3. Characterization of the foam

Specific BET surface area and porosity, elemental analysis, density measurement, FT-IR and SEM analyses were performed for characterization of the foam. Specific BET surface area and porosity was determined using Micromeritics ASAP ® 2420 device. Elemental analysis was carried out by a LECO CHNS-932 analyzer. Density measurement was peformed using a graduated tape measure. FT-IR measurements were recorded between 4000 and 650 cm^{-1} wavenumbers by a ATR spectrophotometer. SEM analysis was recorded by a LEO 435 VP SEM brand device.

DOI: http://dx.doi.org/10.32571/ijct.725783 **E-ISSN:2602-277X**

2.4. Supply of the dye

RO-RGB was provided from Dystar. Since this dye is a new generation of reactive dyes for medium to deep shades, its structure has been protected by manufacturer firm. This dye was analyzed using a spectrophotometer by us and its absorption spectra for various concentrations are illustrated in Figure 1.[23] The maximum wavelength of this dye was determined to be 478 nm.

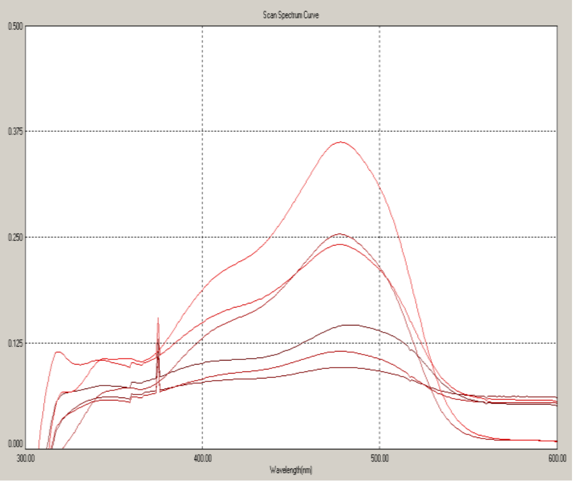

Figure 1. UV-Vis spectra of RO-RGB for different initial concentrations (top to bottom concentrations: 150, 100, 75, 50, 20 and 10 mg l^{-1}).

2.5. Preparation of dye solutions

The RO-RGB was used as taken. Firstly the stock solution of 500 mg l^{-1} of RO-RGB dye was obtained using pure water. Then the working concentrations were prepared diluting the stock solution. pH values of solutions were regulated using diluted NaOH and HCl solutions.by a pH meter (Elmetron pH Meter)

2.6. Removal experiments

Batch experiments were performed with 0.10 g foam and 50 ml dye solution using a temperature-controlled shaking water bath under all the experimental conditions. After shaking at 130 rpm for various times, the samples were centrifuged at 5000 rpm for 5 min by taking from shaking bath. The concentration of dye unadsorbed in the supernatant was determined by a T80 UV/Vis spectrometer at λ_{max} = 478 nm. The percent removal and the dye amount removed (q_t) were estimated using Equations (1) and (2), respectively:

$$Removal\ \% = (C_o - C_e / C_o)\cdot 100 \qquad (1)$$

$$q_t = (C_0 - C_t)\ V / m \qquad (2)$$

Where, C_0 (mg l^{-1}) indicates the initial dye concentration. C_e and C_t (mg l^{-1}) refer the dye concentrations at equilibrium and any time, respectively. q_t (mg g^{-1}) shows the amount of RO-RGB removed by unit mass of adsorbent at any time. V (l) refers to the volume of the RO-RGB solution. m (g) shows the mass of the foam. At the equilibrium time, q_t is equal to q_e, and C_t is equal to C_e (mg l^{-1}).

3. RESULTS AND DISCUSSION

3.1. Characterization of PSPUF

Some physical properties of the foam have been given in our previous study.[25] As seen in this study, the values we obtain are as follows: Specific BET surface area and porosity of the peanut shell-based-polyurethane type rigid foam are 2.824 m^2 g^{-1} and 0.00215 cm^3 g^{-1}, respectively. The color of the foam is brownish, and its density is 0.0341 g cm^{-3}. According to elemental analysis results, the percent components of the modified foam are 61.20% C, 5.848% H, 6.975% N, and 0.274% S.

Figure 2 shows SEM image of the modified PSPUF. From this figure, it is seen that the surface of the foam has a porous, rough and heterogeneous structure which will adsorb dye molecules. It is determined from the isotherm studies that the adsorption on heterogeneous surface best fits the Freundlich model. This indicates a randomn adsorption (i.e. local adsorption) on the heterogeneous surface of the foam.

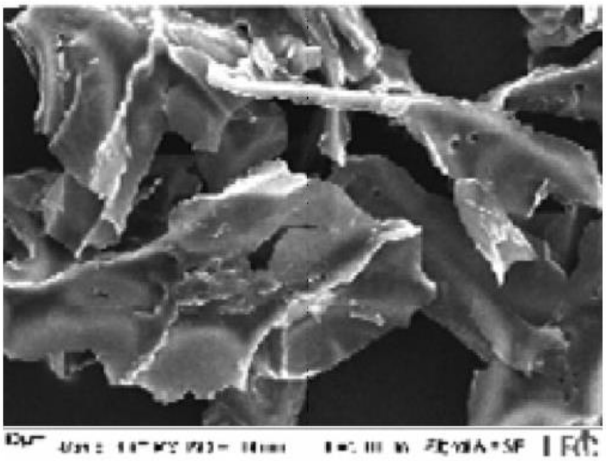

Figure 2. SEM image of the modified PSPUF.

FT-IR spectra for the determination of functional groups of the foam, modified foam and dye-adsorbed foam are shown in Figure 3.

DOI: http://dx.doi.org/10.32571/ijct.725783 **E-ISSN:2602-277X**

Carefully looking at Figure 3, it is seen that some peaks shift or disappear after modification and adsorption, and the intensities of some peaks are also decreased. All these changes are summarized in Table 1.

It may be concluded from Table 1 that the decrease or disappear or shift of intensity of some peaks points to a physical adsorption between the dye molecules and the foam.[2]

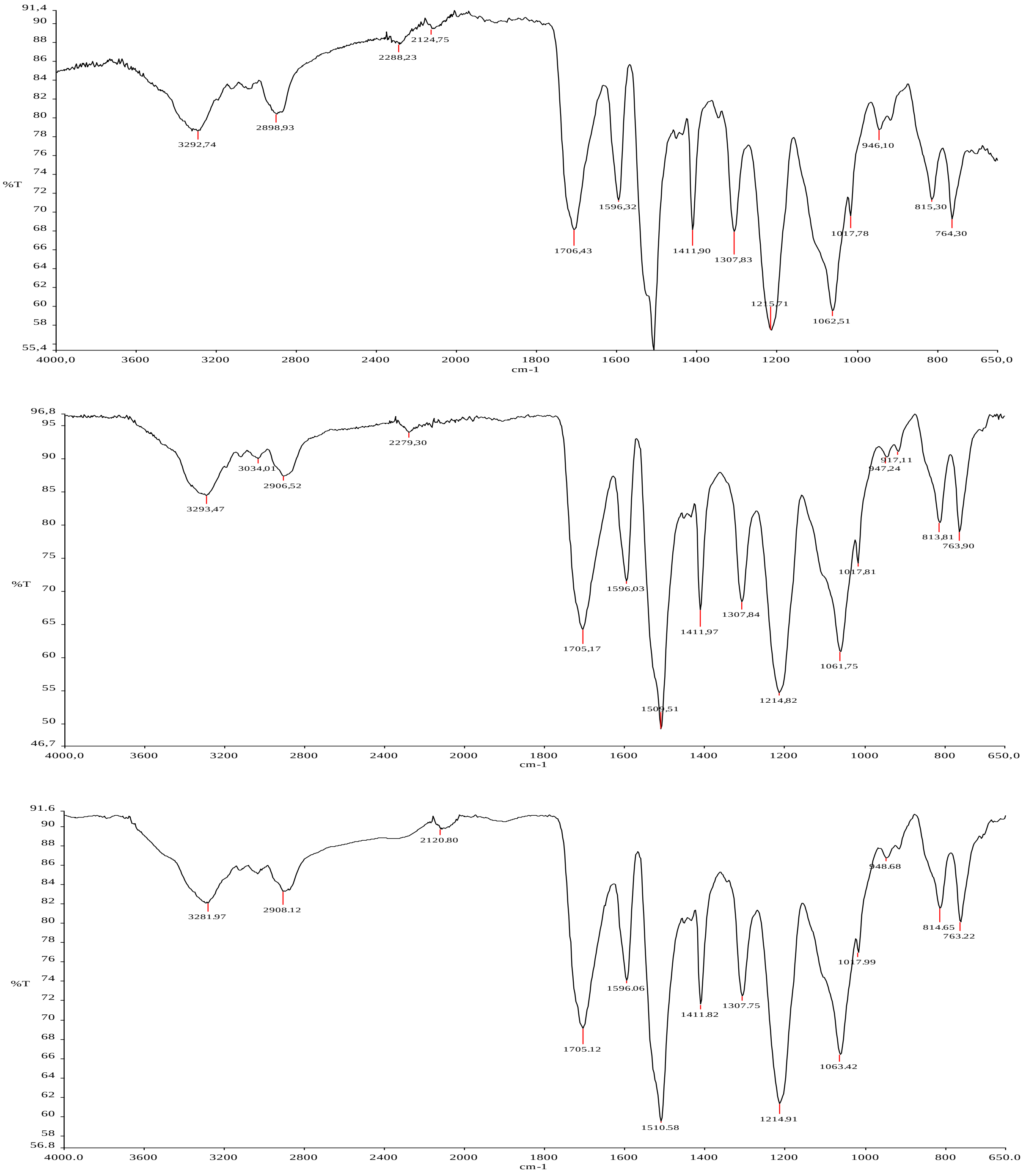

Figure 3. FT-IR spectra of: a) the foam, b) the foam modified with HCl, c) adsorbed dye on modified foam.

Table 1. FT-IR results

Functional groups	Before adsorption*	After modification with HCl	After adsorption
-OH in cellulose and NH and NH_2 groups	3292.74 cm^{-1} (broad band)	3293.47 cm^{-1} (slightly shifted)	3281.97 cm^{-1}, Band shifted and intensity slightly decreased.
-CH stretching of carboxyl group	2898.93 cm^{-1}	2906.52 cm^{-1} (very slightly shifted)	2908.12 cm^{-1} (very slightly shift)
C=C stretching groups	2124.75 cm^{-1}	Diminished	2120.80 cm^{-1} (reappeared)
Amide I and amide II groups	1706.43 cm^{-1}, 1596.32 cm^{-1}	Unchanged	Unchanged
Phenyl fragment	1411.90 cm^{-1}	Unchanged	Unchanged
-CH_2 (methylene group)	1307.83 cm^{-1}	Intensity decreased.	1307.75 cm^{-1} (very slightly shifted)
-C-O and –C-O-C stretching groups	1062.51 and 1017.78 cm^{-1} (very strong peaks)	1061.75 cm^{-1} (Peak at 1062.51 very slightly decreased and shifted)	1063.41 cm^{-1} (very slightly shifted)
-C=O stretching of carboxylic group	1215.71 cm^{-1} (strong band)	1214.82 (very slightly shifted)	1214.91 (very slightly shifted)
-O-H bending	946.30 cm^{-1}	947.20 cm^{-1} (very slightly shifted and intensity decreased)	948.68 cm^{-1} (very slightly shifted)
C-H out-of-plane bending	764.30 cm^{-1}	763.90 cm^{-1} (very slightly shifted)	763.22 cm^{-1} (very slightly shifted)

3.2. Contact time effect and equilibrium time determination

Contact time effect on RO-RGB removal by the foam was studied for the conditions of various initial dye concentration, temperature and pH, respectively. In the case of initial dye concentration effect, the equilibrium time was attained at shorter times for lower concentrations and at longer time for higher concentrations. For instance, the equilibrium time was estimated to be 30 min for the initial dye concentrations of 10 and 20 mg l^{-1}, and 60 min for 50 mg l^{-1}. The equilibrium times were estimated to be 100, 150, and 300 minutes for 75, 100 and 150 mg l^{-1}, respectively. In the case of pH effect, the equilibrium time was determined as 60 min for all pH values for 50 mg l^{-1}. In the case of temperature effect, for 50 mg l^{-1} at pH 3, the equilibrium times were determined to be 150 min for the temperatures of 20 and 30°C, 100 min for the temperatures of 40 and 50°C, and 60 min for the temperature of 60°C. A similar result has also been found for RO-RGB adsorption on peanut shell.[26]

3.3. Initial dye concentration effect

Initial dye concentration effect on RO-RGB removal by the foam was studied for the concentrations of 10, 20, 50, 75, 100 and 150 mg l^{-1} at pH 3, 60°C and 130 rpm. The results are graphed in Figure 4.

Herein, it is seen that the maximum dye removal (i.e. dye removal at equilibrium time) occurs at shorter time for lower initial dye concentration and at longer time for higher initial dye concentration. A similar trend has also been found for the removal of light green dye by cationic surfactant-modified peanut husk.[27] Herein, the maximum dye removals were determined as 0.98 mg g^{-1} (98.60%) and 1.88 mg g^{-1} (94.05%) for 10 and 20 mg l^{-1} at the equilibrium time of 30 min. On the other hand, the maximum dye removals were estimated to be 4.56 mg g^{-1} (91.24%), 5.56 mg g^{-1} (74.20%), 7.294 mg g^{-1} (% 72.94%) and 10.62 mg g^{-1} (70.77%) for 50, 75, 100 and 150 mg l^{-1} at the related equilibrium times, respectively.

DOI: http://dx.doi.org/10.32571/ijct.725783 **E-ISSN:2602-277X**

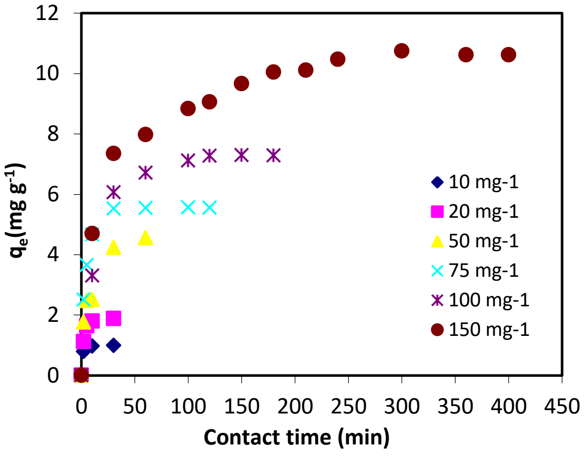

Figure 4. Initial dye concentration effect on RO-RGB removal by the foam.

From these results, it is seen that the dye removal is highly dependent on contact time and initial dye concentration. These values show that the percent dye removal is higher at lower initial concentration. This situation indicates that the dye will initially be adsorbed by more sites on the adsorbent surface. A similar result has also found for methylene blue removal using activated carbon obtained from *Cucumis sativa fruit* peel.[28]

3.4. pH effect

pH effect on RO-RGB removal by the foam was studied at pH values of 3, 5, 7 and 9 for 50 mg l^{-1} at 60°C and 130 rpm. The results are graphed in Figure 5.

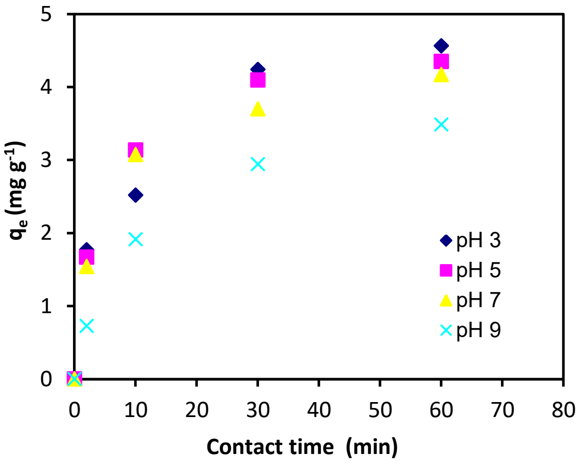

Figure 5. pH effect on RO-RGB removal by the foam.

Herein, t is seen that the dye removal increases with decreasing pH values (namely, with acidic pH). For example, the maximum dye removals were determined as 4.52 mg g^{-1} (91.24%), 4.35 mg g^{-1} (86.98%), 4.17 mg g^{-1} (83.36%) and 3.48 mg g^{-1} (69.76%) for pH values of 3, 5, 7 and 9, respectively.

The dye removal of 91% to 69% between pH 3 and pH 9 indicates that pH has an important effect on dye removal. The fact that the dye removal is higher at lower pH value refers that a more electrostatic interaction occurs between more positively charged foam and negatively charged RO-RGB in acidic medium. A similar result has also been obtained for the removal of remazol brillant blue R from aqueous solution using peanut shell pretreated with HCl.[19]

3.5. Temperature effect

Temperature effect on RO-RGB removal by the foam was worked at the temperatures of 20, 30, 40, 50 and 60°C for 50 mg l^{-1} at pH 3 and 130 rpm. The results are graphed in Figure 6. Herein, dye removal increases with an increase in temperature, indicating an endothermic process. For instance, the maximum dye removals were determined as 1.30 mg g^{-1} (26%), 2.78 mg g^{-1} (55.66%), 2.82 mg g^{-1} (56.56%), 3.17 mg g^{-1} (63.34%), and 4.56 mg g^{-1} (91.24%) for 20, 30, 40, 50, and 60°C. The fact that the dye removal is greater at higher temperature indicates both the enlarged of the foam particles and the increase in the mobility of the large dye ion with an increase in temperature. A similar result has been obtained for remazol brillant blue R adsorption onto peanut shell-based polyurethane type foam.[25]

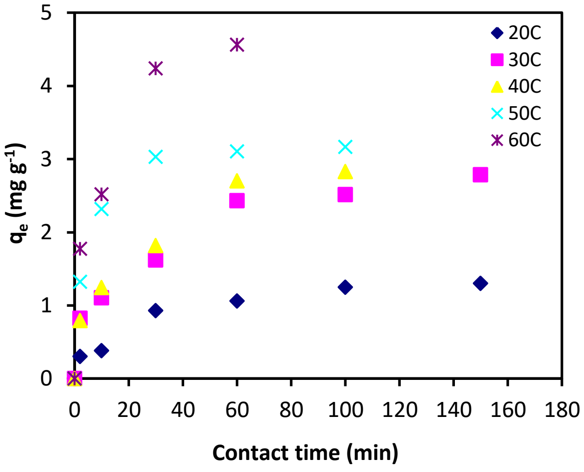

Figure 6. Temperature effect on RO-RGB removal by the foam.

3.6. Isotherm study

The adsorption equilibrium data were adapted to the Langmuir, Freundlich and Temkin isotherm models.

The linearized equations for these isotherms are expressed as follows.[29]

$C_e/q_e = 1/Q_o.b + C_e/Q_o$ Langmuir (3)

$\ln q_e = \ln k + 1/n \ln C_e$ Freundlich (4)

$q_e = B \ln A + B \ln C_e$ Temkin (5)

Where, q_e (mg g^{-1}) shows the amount of dye removed by unit gram of the foam at the equilibrium time. C_e (mg l^{-1}) indicates the equilibrium concentration of dye remained in solution. Q_o (mg g^{-1}) and b (l mg^{-1}) indicate Langmuir constants indicating adsorption capacity and energy, respectively. k (mg g^{-1}) and n (g l^{-1}) refer Freundlich isotherm constants indicating adsorption capacity and intensity, respectively. B (J mol^{-1}) is equal to RT/b_T, and it denotes the heat of the adsorption. b_T refers Temkin constant, A_T (l g^{-1}) indicates equilibrium binding constant.

The Q_0 and b values were estimated from the slope and intercept of the plot of C_e/q_e *vs* C_e, respectively. The k and n values were determined from the intercept and slope of the plot of $\ln q_e$ *vs* $\ln C_e$, respectively. The B and A_T values were calculated from the slope and intercept of the plot of q_e *vs* $\ln C_e$, respectively. All of the isotherm plots drawn are shown in Figure 7. The isotherm parameters were determined from the regression analyses of the plots in the figure. All parameters are presented in Table 2. The values of the determination of coefficient (r^2) were determined as 0.864, 0.966, and 0.824 for the Langmuir, Freundlich, and Temkin models, respectively. The isotherm results indicate that dye adsorption is the best consistent with Freundlich model with r^2 = 0.966. The compliance of the adsorption to the Freundlich model indicates the heterogeneous surface of the foam and a random adsorption on the surface. A similar result has also been found for remazol brillant blue R adsorption onto peanut shell.[19]

Table 2. Isotherm parameters

Langmuir	Freundlich	Temkin
Qo (mg g^{-1}) = 10.46	k (mg g^{-1}) = 2.05	B (J mol^{-1}) = 1.483
b (l mg^{-1}) = 0.147	n (g l^{-1}) = 2.50	A_T (l g^{-1}) = 6.481
r^2 = 0.864	r^2 = 0.966	r^2 = 0.824

3.7. Kinetic study

Kinetic studies of dye removal were performed according to three kinetic models used commonly. The linear equations of these kinetic models are given in the following. The linear equation of the pseudo-first order kinetic model of Lagergren[30] is

$$\log (q_e - q_t) = \log q_e - \frac{k_1}{2.303} t \tag{6}$$

The linear equation of the pseudo-second order kinetic model of Ho[31] is

$$\frac{t}{q_t} = \frac{1}{h} + \frac{1}{q_e} t \tag{7}$$

The linear equation of the intra-particle diffusion model of Weber and Morris[32] is

$$q_t = k_i \cdot t^{1/2} \tag{8}$$

Where, k_1, k_2 and k_i indicate the rate constants for the pseudo-first order (PFO), pseudo-second order (PSO) and the intra-particle diffusion models, respectively. q_e and q_t show the amounts of dye adsorbed per unit gram of the foam at the equilibrium and any time, respectively. h is the initial adsorption rate, it is equal to $k_2 q_e^2$. Herein, the plots of $\log (q_e - q_t)$ against t for the PFO model; the plots of t/q_t against t for the PSO model; the plots of q_t *vs* $t^{1/2}$ for intra-particle diffusion model are drawn. The all plots obtained are illustrated in Figure 8.

All of isotherm parameters obtained from regression analyses of these plots are submitted in Table 3. From linear regression analyses of the PFO plots, the r^2 values were determined as 0.8625, 0.9768, 0.9723, 0.881, 0.9618 and 0.9544 for 10, 20, 50, 75, 100 and 150 mg l^{-1}, respectively. For the PSO plots, the r^2 values were found as 0.9999, 0.9995, 0.9908, 0.9997, 0.999 and 0.9996 for 10, 20, 50, 75, 100 and 150 mg l^{-1}, respectively. For the intra-particle diffusion plots, the r^2 values were estimated to be 0.5789, 0.6604, 0.9377, 0.7086, 0.791 and 0.9177 for 10, 20, 50, 75, 100 and 150 mg l^{-1}, respectively.

The values from the PSO model were the most, and they were found to be higher than 0.999. On the other hand, because the values of q_1 from the PFO kinetics model do not obey the experimental data, $q_e(exp)$, even though the r_1^2 for some initial concentrations have high values (see Table 3), the adsorption does not obey this model.

The q_2 values from the PSO kinetic model are harmony with the $q_e(exp)$, and thus the adsorption follows the PSO kinetics. A similar result has also been found for reactive blue 19 adsorption onto grafted chitosan.[33] This situation may be attributed to a chemical activation between RO-RGB molecules and the functional groups of the foam.

Moreover, because of the low values of the r_i^2, it may be also said that the adsorption process does not follow the intra-particle diffusion kinetics.

3.8. Thermodynamic study

Thermodynamic parameters for RO-RGB adsorption were determined in the range of 20 and 60°C. The change in standard free energy *(ΔG°)*, enthalpy (*ΔH°*), and entropy(*ΔS°*) of adsorption were estimated from Equations (9-11).[29]

$$K_c = C_{Ae} \,/\, C_{Se} \tag{9}$$

$$\Delta G° = RT \ln K_c \tag{10}$$

$$\ln Kc = -\Delta H° / RT + \Delta S° / R \tag{11}$$

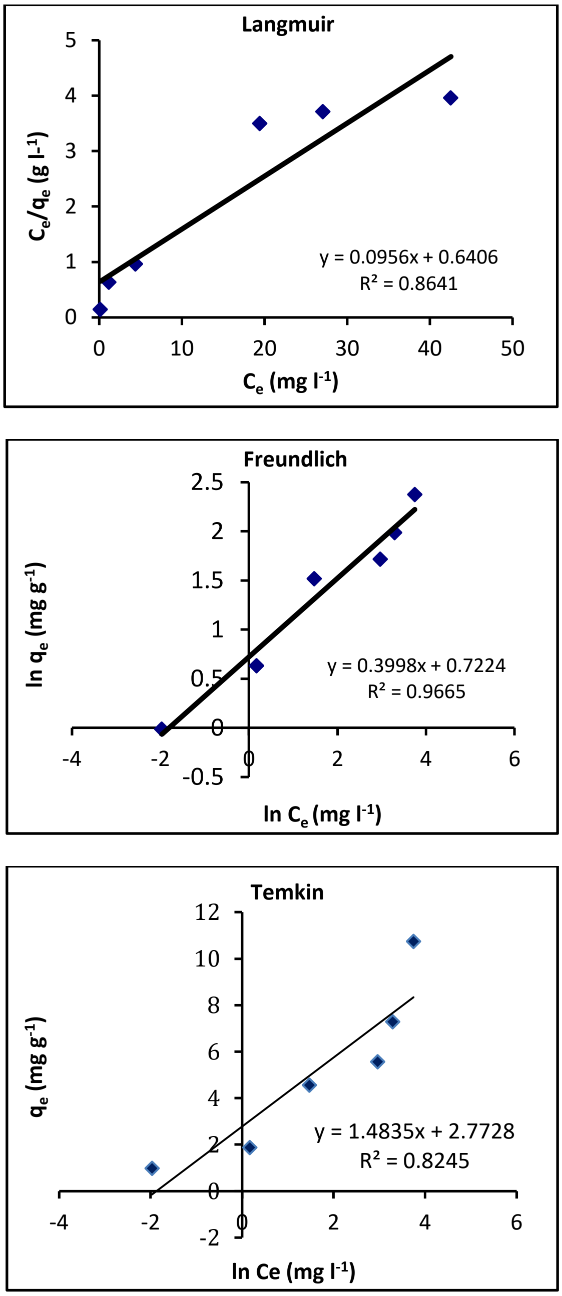

Figure 7. Isotherm plots.

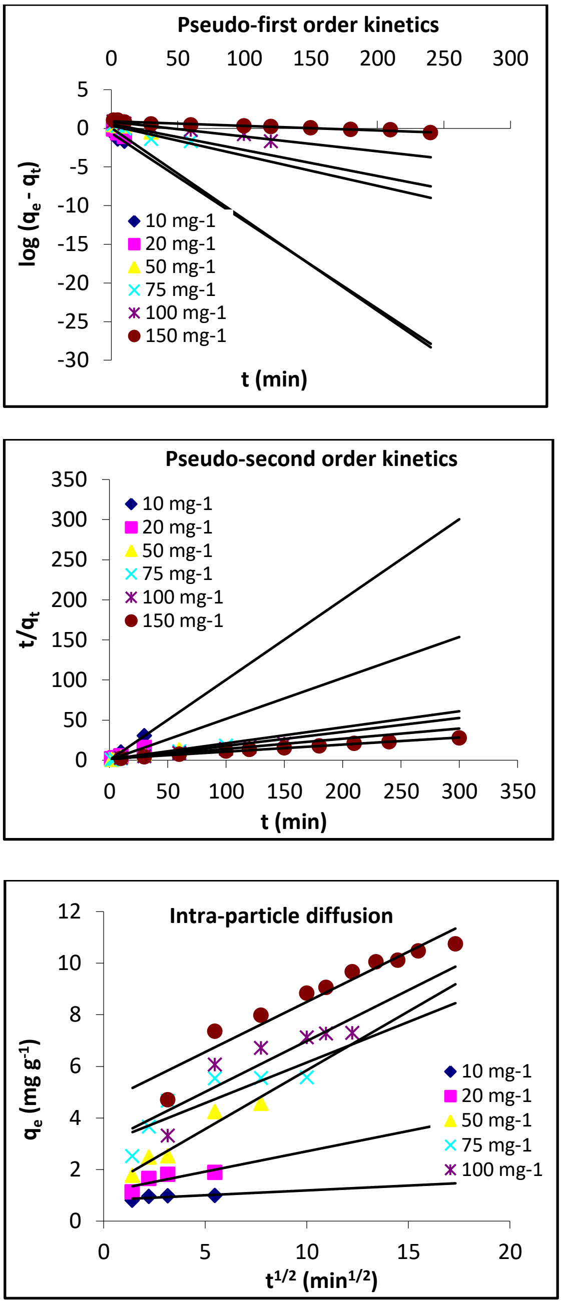

Figure 8. Kinetic plots at different concentrations.

Table 3. Kinetic parameters

	PSO				PFO			Intra-particle Difussion		
C_0[a]	q_2[b]	k_2[c]	h[d]	r_2^2[e]	q_1[f]	k_1[g]	r_1^2[h]	k_i[i]	r_i^2[j]	q_e[k]
10	0.997	2.396	0.3941	0.9999	0.233	0.261	0.8625	0.0378	0.5789	0.98
20	1.159	0.440	0.5923	0.9995	0.414	0.272	0.9768	0.1579	0.6684	1.88
50	4.997	0.047	1.1881	0.9908	0.292	0.077	0.9723	0.4563	0.9377	4.56
75	5.717	0.012	0.3867	0.9997	0.128	0.089	0.881	0.3151	0.7086	5.56
100	7.911	0.022	1.4346	0.999	0.743	0.044	0.9618	0.3590	0.7910	7.29
150	11.363	0.015	1.9529	0.9996	0.810	0.133	0.9544	0.3888	0.9177	10.62

[a] Initial dye concentration (mg l^{-1}).
[b] Equilibrium adsorption capacity from the PSO equation (mg g^{-1}).
[c] The rate constant from the PSO model (g/mg min).
[d] The initial adsorption rate from the PSO kinetics (mg/g min).
[e] Determination of coefficient from the PSO kinetics (mg/g min).
[f] Equilibrium adsorption capacity of the PFO model (mg g^{-1}).
[g] The rate constant from the PFO model (min^{-1}).
[h] Determination of coefficient from the PFO kinetics.
[i] Intra-particle diffusion rate (mg/g $min^{1/2}$).
[j] Determination of coefficient from the intra-particle diffusion.
[k] Experimental adsorption capacity at equilibrium time (mg g^{-1}).

Where, K_c shows adsorption equilibrium constant. C_{Ae} (mg l^{-1}) is the equilibrium concentration of dye adsorbed on the foam. C_{Se} (mg l^{-1}) is the concentration of RO-RGB remained in solution at the equilibrium time. R refers to the gas constant. T shows the absolute temperature. Eq. (11) refers Van't Hoff equation. Van’t Hoff plot of $\ln K_c$ vs $1/T$ is shown in Figure 9.

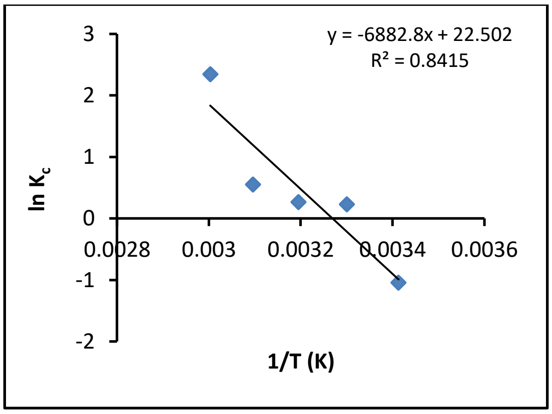

Figure 9. Van't Hoff plot.

The ΔH° and ΔS° values were determined from the slope and intercept of Van't Hoff plot, respectively. All of the thermodynamic parameters are presented in Table 4. Herein, the ΔH° and ΔS° values were determined as 55.56 kJ mol^{-1} and 187 J $mol^{-1}K^{-1}$, respectively.

The positive ΔH° value refers an endothermic adsorption. Since the ΔH° value is lower than 80 kJ mol^{-1}, the adsorption indicates a physical-chemical adsorption.[34] The positive ΔS° value indicates a random adsorption.

Table 4. Thermodynamic parameters

Temperature (in K)	K_c	ΔG° (J mol^{-1})	ΔH° (kJ mol^{-1})	ΔS°(k J $mol^{-1}K^{-1}$)
20	0.351	2547	55.56	0.187
30	1.255	-573		
40	1.302	-687		
50	1.727	-1468		
60	10.415	-6488		

The negative ΔG° values for temperatures (except for 20°C) refer spontaneous adsorption of RO-RGB on the foam. The ΔG° values regularly decrease with an

DOI: http://dx.doi.org/10.32571/ijct.725783 E-ISSN:2602-277X

increase in the temperature. This situation shows the increase of spontaneous trend with an increase in the temperature. Similar results have also been obtained for methylene blue adsorption on $ZnCl_2$ activated carbon prepared from wood apple outer shell.[35]

4. CONCLUSIONS

The following conclusions were concluded from this study.

- Polyurethane type rigid foam prepared from the peanut shell was used as a low-cost adsorbent for RO-RGB removal from aqueous solution.
- RO-RGB removal was studied for various initial dye concentrations, temperatures, and pH values as function of contact time. The dye removal increased with the increases in initial dye concentrations and temperature, and with a decrease in pH. Under all the experimental conditions, the maximum dye removal was determined to be about 98%.
- Adsorption obeyed best the Freundlich isotherm model with the determination of coefficient of 0.966.
- The kinetics data was in harmony with the PSO model with the determination of coefficients higher than 0.9908.

As a result, it was concluded that the polyurethane-type hard foam produced from peanut shell will be used as a potential adsorbent as an alternative to activated carbon to remove other dye contamination besides RO-RGB removal from the environment.

ACKNOWLEDGEMENTS

This study was supported by The Scientific and Technical Research Council of Turkey (TUBITAK), project number: 107Y043.

Conflict of interests

Author declare that there is no a conflict of interest with any person, institute, company, etc.

REFERENCES

1. Acemioğlu, B. *J. Colloid Interf. Sci.* **2004**, 274, 371-379.

2. Aljeboree, A. M.; Alshirifi, A. N.; Alkaim, A. F. *Arab. J. Chem.* **2017**, 10, S3381-S3393.

3. El-Aila, H. J.; Elsousy, K. M.; Hartany, K. A. *Arab. J. Chem.* **2016**, 9, S198-S203.

4. Naseem, K.; Farooqi, Z. H.; Begum, R.; Ghufran, M.; UrRehman, M. Z.; Najeeb, J.; Irfan, A.; .Al-Sehemi, A.G. *J. Mol. Liq.* **2018**, 268, 229-238.

5. Fu, J.; Xin, Q.; Wu, X.; Chen, Z.; Yan, Y.; Liu, S.; Wang, M.; Xu, Q. *J. Colloid Interf. Sci.* **2016**, 461, 292-304.

6. Zhang, F.; Lan, J.; Yang, Y.; Wei, T.; Tan, R.; Song. W. *J. Nanopart. Res*. **2013**, 15, Article number: 2034.

7. Acemioğlu, B. *Chem. Eng. J.* **2005**, 106, 73-81.

8. Adeyemo, A. A.; Adeoye, I. O.; Bello, O. S. *Appl. Water Sci.* **2017**, 7, 543-568.

9. Acemioğlu, B.; Kertmen, M.; Digrak, M.; Alma, M.H.; Temiz, F. *Asian J. Chem.* **2010**, 22 (2), 1394-1402.

10. Bankole, P.O.; Adekunle, A.A.; Govindwar, S.P. *J. Environ. Chem. Eng*. **2018**, 6(2), 1589-1600.

11. Errgene, A.; Ada, K.; Tan, S.; Katırcıoğlu, H. *Desalination* **2009**, 249, 1308-1314.

12. Martorell, M. M.; Pajot, H. F.; de Figueroa, L. I. C. *J. Environ. Chem. Eng.* **2017**, 5987-5993.

13. Jóźwiak, T. C.; Filipkowska, U.; Bugajska, P.; Kalkowski, T. *J. Ecol. Eng.* **2018**, 19 (4), 129-135.

14. Husein, D. Z.; Aazam, E.; Battia, M. *Arab. J. Sci. Eng.* **2017**, 42, 2403-2415.

15. Acemioğlu, B.; Alma, M. H.; Demirkıran, A. R. *J. Chem. Soc. Pak.* **2004**, 26 (1), 82-89.

16. Rajamohan, N.; Rajasimman, M.; Rajeshkannan, R. R.; Saravanan, V. *Alexandria Eng. J.* **2014**, 53, 409-415.

17. Guo, Y.; Zhu, W.; Li, G.; Wang, X.; Zhu, L. *J Chem-NY*, **2016**, Article ID 6326372.

18. Kule, L.; Acemioğlu, B.; Baran, E. *Int. J. Chem. Technol.* **2017,** 1, 58-66.

19. Acemioglu, B.; Sakalar, N. *Fresen. Environ. Bull.* **2017,** 26 (8), 5305-5313.

20. Kara, A.; Acemioğlu, B.; Alma, M.H.; Cebe, M. *J. Appl. Polym.* **2006**, 101, 2838-2846.

21. Kupeta, A. J. K.; Naidoo, E. B.; Ofomaja, A. E. *J. Clean. Prod.* **2018**, 179, 191-209.

DOI: http://dx.doi.org/10.32571/ijct.725783 **E-ISSN:2602-277X**

22. Domínguez-Robles, J.; Peresin, M.S.; Tamminen, T.; Rodríguez, A.; Jääskeläinen, A.S. *Int. J. Biol. Macromol.* **2018**, 115, 1249-1259.

23. Acemioğlu, B. *Int. J. Coal Prep. Util.* DOI: 10.1080/19392699.2019.1644326

24. Acemioğlu, B.; Bilir, M. H.; Alma, M. H. *Int. J. Chem. Technol.* **2018**, 2 (2), 95-104.

25. Bilir, M. H.; Sakalar, N.; Acemioğlu, B.; Baran, E.; Alma, M. H. *J. Appl. Polym. Sci.* **2013,** 6, 4340-4350.

26. Samil, A.; Acemioğlu, B.; Gültekin, G.; Alma, M. H. *Asian J. Chem.* **2011**, 23 (7) 3224-3230.

27. Zhao, B.; Xiao, W.; Shang, Y.; Zhu, H.; Han, R. *Arab. J. Chem.* **2017**, 10, S3595-S3602.

28. Thirumalisamy, S.; Subbian, M. *BioResources* **2010**, 5 (1), 419-437.

29. Koçer, O.; Acemioğlu, B. *Desalin. Water Treat.* **2015**, 1–17.

30. Lagergren, S. *Kung. Sven. Veten. Hand.* **1898**, 24, 1-39.

31. Ho, Y. S.; Mckay, G. *Chem. Eng. J.* **1998**, 70 (2), 115-124.

32. Weber, W.J.; Morris, J.C. *J. Sanit Eng. Div.* **1963**, 89, 31-59.

33. Jiang, X.; Sun, Y.; Liu, L.; Wang, S.; Tian, X. *Chem. Eng. J.* **2014**, 235, 151-157.

34. Mihăilescu, M.; Negrea, A.; Ciopec, M.; Davidescu, C. M.; Negrea, P.; Narcis Duţeanu, N.; Rusu, G. *Sci. Rep-UK* **2019**, 9:8757.

35. Bhadusha, N.; Ananthabaskaran, T. *E-J. Chem.* **2011**, 8 (4), 1696-1707.

ORCID

https://orcid.org/0000-0002-0728-2747 (B. Acemioğlu)

DOI: http://dx.doi.org/10.32571/ijct.725601 **E-ISSN:2602-277X**

International Journal of Chemistry and Technology

http://dergipark.org.tr/ijct

Research Article

Phase transition of GeO_2 crystal at high pressure: An ab initio molecular dynamics study

Sebahaddin ALPTEKİN*

on the last page

Department of Physics, Çankırı Karatekin University, Çankırı, 18100, Turkey

Received: 22 April 2020; Final revised: 16 June 2020; Accepted: 17 June 2020

***Corresponding author e-mail: salptekin@karatekin.edu.tr**

Citation: Alptekin, S. *Int. J. Chem. Technol.* **2020**, 4 (1), 90-96.

ABSTRACT

The phase transition of GeO_2 structure was studied under constant pressure by using ab initio calculation and the generalized gradient approximation (GGA). A structural phase transition was observed at 30 GPa for the first time under the constant hydrostatic pressure, and $P4_2/mnm$ structure was transformated into a $CaCl_2$ (Pnnm) structure. This phase transition was also investigated using total energy, enthalpy, and the phase shift calculations. It was determined that the obtained transformation parameters and bulk modulus properties were compatible with the previous experimental and theoretical first principle calculations.

Keywords: High pressure, molecular dynamic, enthalpy.

GeO_2 kristalinin yüksek basınçta faz geçişi: Bir ab initio moleküler dinamik çalışması

ÖZ

GeO_2 yapısının faz geçişi, sabit basınçta ab initio hesaplaması ve genelleştirilmiş gradyan yaklaşımı (GGA) kullanılarak incelenmiştir. Yapısal faz dönüşümü sabit hidrostatik basınç altında ilk kez 30 GPa'da gözlendi ve $P4_2/mnm$ yapısı $CaCl_2$ (Pnnm) yapısına dönüştü. Bu faz geçişi, toplam enerji, entalpi ve faz kayması hesaplamaları kullanılarak da araştırılmıştır. Elde edilen dönüşüm parametrelerinin ve yığın modül özelliklerinin, önceki deneysel ve teorik birinci prensip hesaplamalarıyla uyumlu olduğu belirlenmiştir.

Anahtar Kelimeler: Yüksek basınç, moleküler dinamik, entalpi.

1. INTRODUCTION

It is important to understand atomic structures of nano-dimensional materials, and behavior of the material under high pressure in material science and application of geological, physical and chemical materials. Empirical research in the literature has played an important role in understanding the phase change caused by the pressures of many materials. However, it has been difficult to interpret the experimental results of some materials over the last two decades. The structural and electronic structure of GeO_2 in tetragonal rutil type structure with space group $P4_2/mnm$ have been studied in the past extensively.[1-5] The structural, electronic and optical properties of GeO_2 under high pressure and temperature have been investigated using different experimental techniques and theoretical calculations.[1-7] Under ambient conditions, GeO_2 which is a crystalline compound has two crystalline forms: α-GeO_2 quartz-type phase $P3_221$[8] and r-GeO_2 $P4_2/mnm$ phase with rutile structure.[9] In the r-GeO_2 rutile phase, GeO_4 is characterized by a tetrahedral structure with four oxygen atoms surrounding a germanium atom. The α-GeO_2 phase is characterized by a GeO_6 octahedral structure containing six oxygen atoms surrounding a germanium atom. The crystalline sample also has showed complex behavior at high pressures and temperatures where several additional structural transformations have been observed.[10] In addition, molecular-dynamic calculations have been made to investigate the behavior of GeO_2 under high pressure. Lodziana and co-workers have performed ab initio calculations of GeO_2 and observed phase transition from rutile-type structure to $CaCl_2$-type structure at around 19 GPa.[2] Using angle-dispersive X-ray pover-diffraction data, a transition has been observed from rutile to $CaCl_2$ type GeO_2 structure at 36 GPa.[3] Second-order phase

DOI: http://dx.doi.org/10.32571/ijct.725601 **E-ISSN:2602-277X**

transition from rutile-type to $CaCl_2$-type has also been observed in GeO_2 at 26.7 GPa by raman spectroscopy.[5] High pressure studies have been performed using extended X-ray absorption fine structure (EXAFS) spectroscopy,[6,7,11] X-ray diffraction and neutron diffraction experiments.[12-14] All experimental studies agree that the number of coordination between Ge-O changes at a pressure range of 3-15 GPa. EXAFS studies have shown that the bond length of Ge-O ranges from 1.74 (0 GPa) to 1.8 (13 GPa).[11] In the first study to address this issue, Itie and co-workers have measured X-ray radiation absorption up to 23.2 GPa and found that the Ge coordination has passed from four-fold to six-fold under the pressure of 7 to 9 GPa.[7] Vaccari has not found evidence of a six-fold structure despite the high pressures being raised to around 13 GPa.[11] The latest X-ray absorption fine structure (XAFS) and EXAFS studies[6,15] have also been extended to 53 and 44 GPa, respectively, in the working interval, and it has been estimated that only 25-30 GPa was reached for six-fold coordination of Ge ions. The application of high pressure is a powerful tool for examining the structural and electronic properties of crystal materials.

Here, a new contribution of this article is to examine the change in the physical Phase transition properties of the GeO_2 crystal under high pressure with an ab initio molecular dynamic study. This study is an original study since it has not been studied in the literature before.

2. METHOD

The Parrinello-Rahman method has been used to investigate phase-based transitions in various materials, mostly to investigate crystal-to-crystal phase transitions in small-sized cells. In these simulations; the transformation mechanism, the formation and the structural and electronic properties of the phases under pressure can be easily explained. In this study, hydrostatic pressure was applied to the simulation cell, and calculations were made using SIESTA code[16] and the program density functional theory (DFT) based on the ab initio (first-principle) pseudopotential method. For Khon Sham Hamiltonian, Troullier-Martin was chosen as the "norm-conserving pseudopotential" along with the GGA using the exchange-correlation function of Ernzerhof and Perdew-Burke.[17,18] The double-zeta plus polarization numerical base set was selected with a kinetic energy cut-off of 600 meV. The simulation cell in which periodic boundary conditions are used consists of 96 atoms. We used a regular mesh with the plane-wave cut-off of 150 Ry to express the numerical base set and the electron density, the local part of the pseudopotentials, the Hartree and the exchange correlation potential, and the Γ point shape for the 96 atomic simulation cell. It is used for Broullin region integration and because of the energy difference of 0.03 eV/atom between the 96 atomic simulation cell and the 256-k point, 2 atomic primitive cell. The reason for choosing this community is to remove the thermal surge so that the structure is more easily inspected during the phase transition. Pressure was applied via the Parrinello-Rahman method.[19] The system is initially balanced at zero pressure and then the pressure is gradually increased by increments of 10 GPa. The balancing period consists of 1000 steps with each step being 1 fs. In addition, 'Power Extinguishing Technique' has been used throughout MD simulations. Energy volume calculations were carried out in unit cells of rutile and $CaCl_2$. The Brillouin region integration was calculated with 8 x 8 x 8 and 10 x 10 x 10 k-point squares automatically generated by Monkhorst and Pack approach for rutile and $CaCl_2$ phases respectively.[20] We have used the KPLOT program that provides detailed information about the cell parameters, the space group and the atomic position of a given structure.[21] The tolerances of 0.2 Å, 4° and 0.7 Å are used for bond lengths, bond angles, interplanar spacing.

3. RESULTS AND DISCUSSION

Pressure-volume graph in Figure 1 was drawn to classify the phase transition of GeO_2 by pressure effect in the thermodynamic category. As seen from this graph, the volume of GeO_2 varies suddenly when the simulation pressure is increased from 20 to 30 GPa. The pressure-volume curve shows a discontinuity at this point.

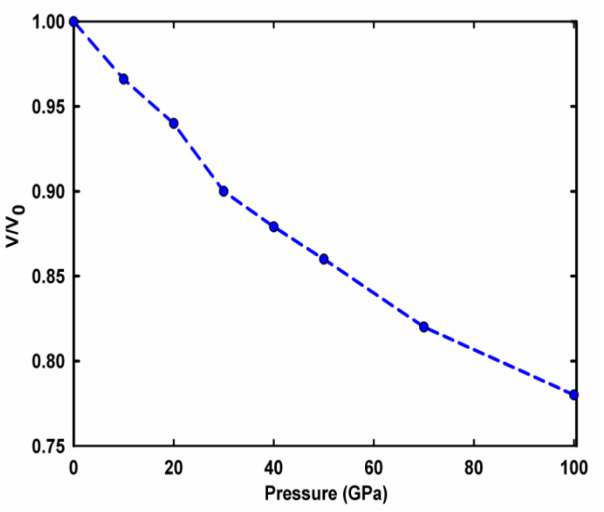

Figure 1. The volume-pressure plot (y axis shows normalized values).

DOI: http://dx.doi.org/10.32571/ijct.725601 **E-ISSN:2602-277X**

Because the Gibbs free energy is equal to the derivative volume in relation to the pressure at constant temperature, the pressure-based phase transition unit exhibits a sudden change from one phase to another in the volume of the cell. Since there is a second degree phase transition, there is no sharp decrease on the volume- pressure plot in Figure 1, we can observe the sharp decrease in the first degree phase transition. The symmetry change in the phase transition was determined by the group theory method. The structure obtained for each pressure value applied in the simulation program was analyzed symmetrically using the KPLOT program.[21]

At 30 GPa simulation pressure, it was observed that the crystal lattice structure passes from the rutile structure ($P4_2/mnm$) to the $CaCl_2$ structure (Pnnm), and it is shown in Figure 2a-d. The structural parameters and atomic positions of the initial structure and the structure at 30 GPa are given in Table 1. In a detailed analysis of 30 GPa, the rutile symmetry continued to 969 time step and in step 970 it was converted to the $CaCl_2$ structure. We obtained the lattice constants as a = 4.420 Å, b = 4.420 Å and c = 2.914 Å for rutile structure ($P4_2/mnm$) and a = 4.374 Å, b = 4.134 Å and c = 2.844 Å for $CaCl_2$ structure (Pnnm). This result is a definite proof that GeO_2 returns to the $CaCl_2$ structure under high pressure.

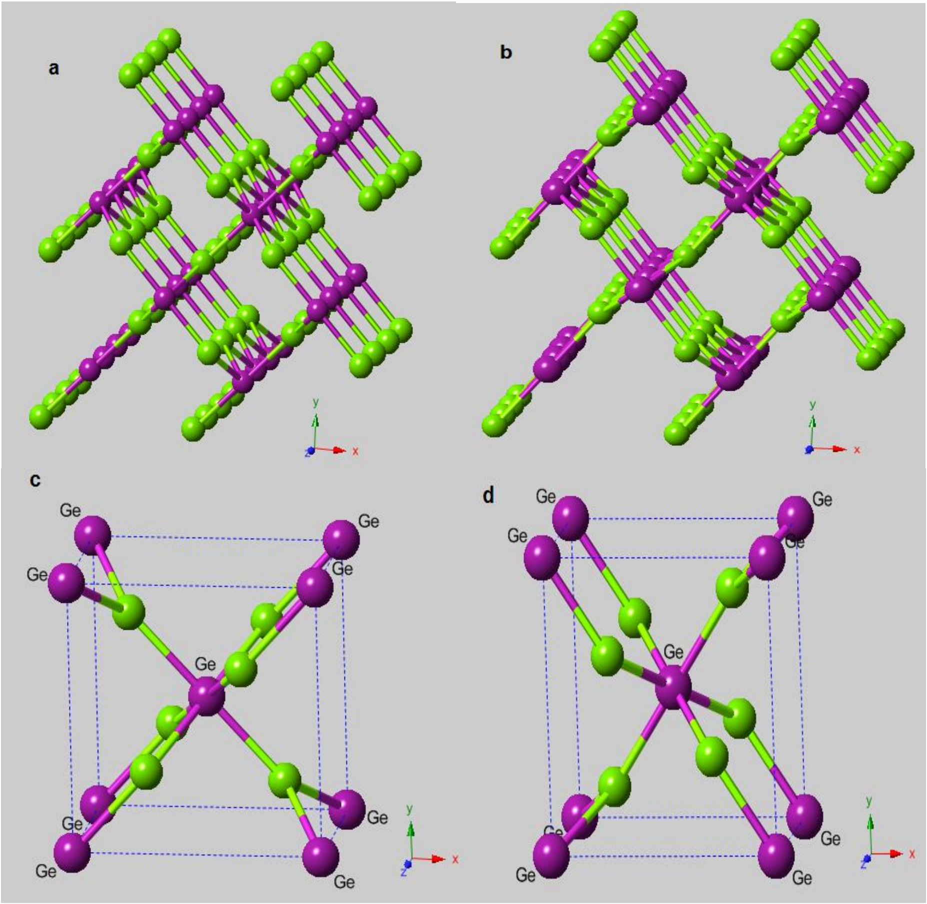

Figure 2. Crystal structures of GeO_2 $P4_2/mnm$ at zero pressure and Pnnm at 30 GPa (a: $P4_2/mnm$ simulation-cell, b: Pnnm simulation-cell, c: $P4_2/mnm$ unit-cell and d: Pnnm unit-cell, respectively).

Table 1. The fractional coordinates and lattice parameters of GeO_2 at 0 and 30 GPa.

Structure	a (Å)	b (Å)	c (Å)	x	y	z	Angles
Rutile	4.420	4.420	2.914	Ge:0.000	0.000	0.000	90, 90, 90
				O: 0.306	0.306	0.000	
$CaCl_2$	4.375	4.134	2.844	Ge:0.000	0.000	0.000	90, 90, 90
				O: 0.2745	0.6687	0.000	

Table 2. Lattice parameters (a, b, c), B_0, c/a and *u* for $P4_2/mnm$ and Pnnm phases of GeO_2

Structure	a (Å)	b (Å)	c (Å)	B_0(GPa)	c/a	u	Ref.
Rutile	4.420	4.420	2.914	269	0.643	0.306	This study
	4.407	4.407	2.862		0.649	0.306	(1)
	4.384	4.384	2.864		0.653	0.306	(2)
	4.397	4.397	2.863	250			(3)
	4.492	4.492	2.923		0.660		(4)
$CaCl_2$	4.375	4.134	2.844	259			This study
	4.258	4.203	2.805				(1)
	4.281	4.143	2.798				(2)
	4.263	4.263	2.815	262			(3)
	4.364	4.422	2.854				(4)

As can be clearly seen in Figure 3, the system has undergone specific rearrangement after the 970th simulation step. Separate volume–energy calculations for the rutile and $CaCl_2$ phases of GeO_2 were performed.

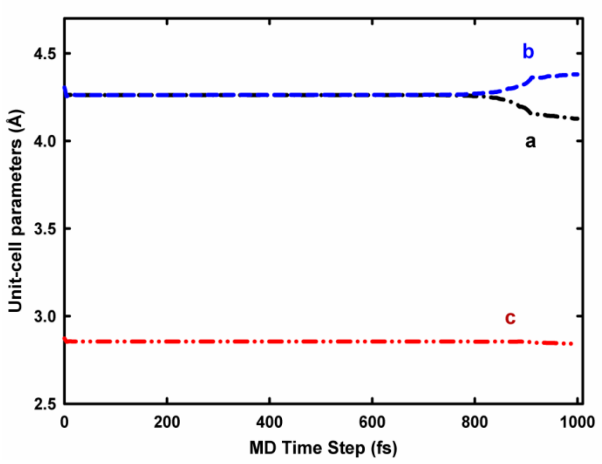

Figure 3. The time evulation of the unit- cell parameters at 30 GPa.

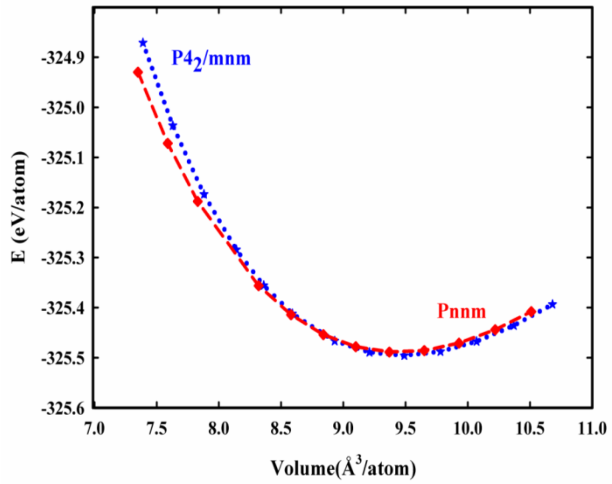

Figure 4. The energy-volume plot as a function of the volume of the unit atom for GeO_2.

The graph of the data obtained from the total energy calculations is shown in Figure 4. The volume-energy curves obtained for each phase were fitted to the Birch-Murnaghan state equation. The cell parameters calculated for the high pressure phase together with B_0 values are given in Table 2. Finally, enthalpy calculations were performed to determine exactly at which pressure GeO_2 passed from the rutile crystal structure to the $CaCl_2$ crystal structure. Structural phase transformations in simulations occur in all simulation cells. Systems must pass an important energy barrier to transform from one phase to another. This means that simulated structures must be under extreme pressure to achieve a phase transition. In addition, the absence of thermal movement in our simulations shifts the transitions to a higher pressure. On the other hand, free energy $G = E_{tot} + PV - TS$ should be used to determine the most stable structure at finite pressure and temperature. Density functional calculations are made at zero kelvin temperature and entropic additives can be neglected. Therefore, enthalpy values, including pressure-volume effects, $H = E + pV$ were calculated.

The enthalpy for both the rutile phase and the $CaCl_2$ phase of GeO_2 can be calculated using the calculated volume-energy data for each phase. As shown in Figure 5, the enthalpy of the crystal structure of the rutile formed by the stable atomic order of GeO_2 up to a certain pressure value is increased by the increase of the pressure. After a certain pressure value, there is a structure with a free energy atomic array ($CaCl_2$) that is smaller than the free energy of the system. At this pressure value, the atomic sequence of the rutile phase material is unstable relative to the new atomic sequence. The phase transition caused by the pressure can be obtained from the cross-over of enthalpy-pressure curves (Figure 5).

The 36.5 GPa value calculated for the phase transition from Rutile to $CaCl_2$ is compatible with the 36 GPa experimental value.[3] The values of the lattice parameters, bulk modulus, u value and c/a of GeO_2 in this study and in other theoretical and experimental studies are summarized in Table 2. The lattice parameters calculated for the phase of GeO_2 in ambient conditions and the phase at high pressure are in agreement with the bulk modulus of the theoretical and experimental studies. The rutile-$CaCl_2$ transition pressure has a new phase-transition pressure value which is different from the theoretical and experimental transition pressure values previously found. The electronic density of state (EDOS), the electronic property of GeO_2, is calculated for pressures of 0 and 30 GPa and is given in Figure 6. From this figure, it is seen that GGA band gap are found as 1.15 eV at zero pressure and 2.62 eV at 30 GPa. Despite increasing band gap energy, it shows semiconductor property. In Figure 7, the values of a, b and c of the simulation lattice parameters are given as a function of applied pressure. It was seen that there was a decrease in a, an increase in b, and no change of c at 30 GPa.

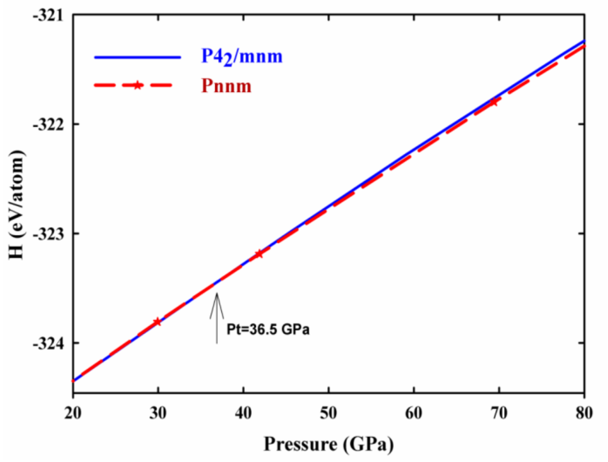

Figure 5. The enthalpy curves of $P4_2/mnm$ and Pnnm phases of GeO_2.

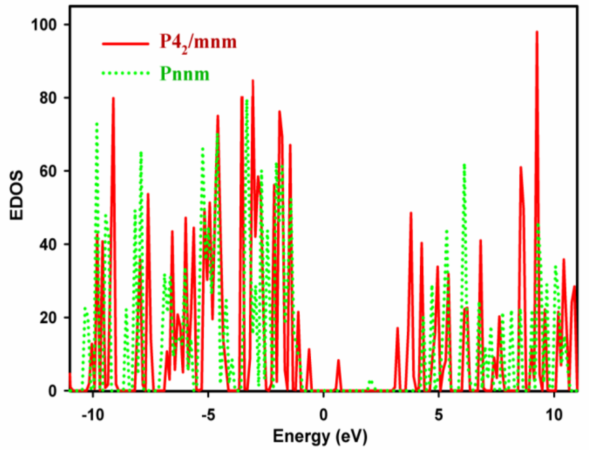

Figure 6. The electronic density of states (EDOS) for GeO_2 phases.

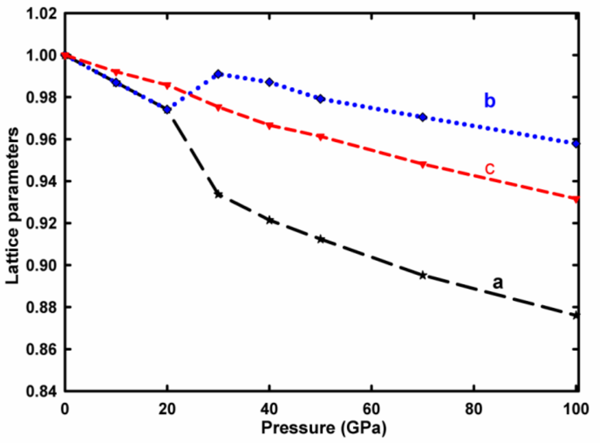

Figure 7. The lattice parameters-pressure plots for GeO_2.

DOI: http://dx.doi.org/10.32571/ijct.725601 **E-ISSN:2602-277X**

Using a constant pressure ab initio technique, GeO_2 has been studied on rutile-$CaCl_2$ phase transition and similar phase transitions for CrO_2 have been observed in previous study by Alptekin.[22] Similarly, ab initio molecular dynamic studies have been performed on ZrO_2 [23] and MgF_2 constructs.[24] In an experimental study, transitions from rutile to $CaCl_2$ phase have been observed by Prakapenka and co-workers[1] and in this experimental study lattice constants for rutile were found as a= 4.407 Å, c=2.862 Å and lattice constants for $CaCl_2$ have been found as a = 4.258 Å, b = 4.203 Å and c = 2.805 Å. At the same time, the c/a = 0.649 and u = 0.306 have been estimated by, Prakapenka and co-workers.[1] The values we obtained are c / a = 0.643 and u = 0.306 and are compatible with the results in the literature. In another experimental study, rutile lattice constants have been found as a = 4,397 Å, c = 2,863 Å and lattice constants for $CaCl_2$ have been found as a = 4,263 Å, b = 4.263 Å, c = 2.815 Å by Haines and co-workers.[3] and similarly, bulk modulus B_0 = 250 GPa and B_0 = 262 GPa.

In this study, we found these values for the rutile phase as a = 4.420 Å, c = 2.914 Å and B_0 = 269 GPa; and for $CaCl_2$ phase as a = 4.375 Å and B_0 = 259 GPa. In Table 2, our results were compared with other studies. In similar studies, wurtzite (WZ) and zinc-blend were studied using the constant pressure MD technique for CdSe and BeO.[25-27]

4. CONCLUSIONS

In this study, the rutile and $CaCl_2$ structure change of GeO_2 under high pressure was investigated. The phase transition was observed to pass from the tetragonal rutile structure to the orthorhombic $CaCl_2$ structure. The pressure was applied between 0 and 100 GPa with ab initio constant pressure technique and a phase transition was first observed at 30 GPa. Furthermore, the total energy and enthalpy calculations were based on the enthalpy-pressure graph of phase transition around 36.5 GPa. In theoretical and experimental studies on the GeO_2, crystal phase transitions were observed at 19 and 36 GPa. The electronic density of state (EDOS) for high pressure phases were calculated for GeO_2 and electronic calculations indicated that GeO_2 was still a semiconductor at 30 GPa. We obtained the the lattice parameters, bulk modulus and phase transition pressures which were in agreement with experimental and theoretical studies.

ACKNOWLEDGEMENTS

The author wants to thank the SIESTA group for allowing using their code.

Conflict of interests

Author declares that there is no a conflict of interest with any person, institute, company, etc.

REFERENCES

1. Prakapenka, V. P.; Shen, G.; Dubrovinsky, L. S.; Rivers, M L.; Sutton, S. R. *J. Phys. Chem. Solids* **2004**, 65, 1537-1545.

2. Łodziana, Z.; Parlinski, K.; Hafner , J. *Phys. Rev. B.* **2001**, 63, 134106.

3. Haines, J.; Léger, J.; Chateau, C.; Pereira, A. *Phys. Chem. Miner*. **2000,** 27, 575-582.

4. Ono, S.; Hirose, K.; Nishiyama, N.; Isshiki, M. *Am. Mineral*. **2002**, 87, 99-102.

5. Haines, J.; Léger, J.; Chateaub, C.; Bini, R.; Ulivi, L. *Phys. Rev. B.* **1998**, 58, R2909.

6. Baldini, M.; Aquilanti,G.; Mao, H.; Yang, W.; Shen, G.; Pascarelli, S.; Mao, W. L. *Phys. Rev. B.* **2010**, 81,024201.

7. Itie, J.; Polian, A.; Calas, G.; Petiau, J.; Fontaine, A.; Tolentino, H. *Phys. Rev. Lett*. **1989**, 63, 398-401.

8. Smith, G. S.; Isaacs, P. B. *Acta Crystallogr.* **1964**, 17, 842-846.

9. Baur, W. H.; Khan, A. A. *Acta Crystall. B Stru*. **1971**, 27, 2133-2139.

10. Haines, J.; Leger, J.; Chateau, C. *Phys. Rev. B.* **2000**, 61 (13), 8701-8706.

11. Vaccari, M.; Aquilanti, G.; Pascarelli, S.; Mathon, O. *J. Phys. Condens. Matter*. **2009**, 21, 145403.

12. Salmon, P. S.; Barnes, A. C.; Martin, R. A.; Cuello, G.J. *J. Phys. Condens. Matter.* **2007**, 19, 415110.

13. Guthrie, M.; Tulk, C.; Benmore, C.; Xu, J.; Yarger, J.; Klug, D.; Tse, J.; Mao, H.; Hemley, R. *Phys. Rev. Lett*. **2004**, 93, 115502.

14. Drewitt, J. W.; Salmon,P. S.; Barnes, A. C.; Klotz, S.; Fischer, H.E.; Crichton, W. A. *Phys. Rev. B.* **2010**, 81, 014202.

15. Hong, X.; Newville, M.; Prakapenka, V. B.; Rivers. M. L.; Sutton, S. R. *Rev. Sci. Instrum*. **2009**, 80, 073908.

DOI: http://dx.doi.org/10.32571/ijct.725601 **E-ISSN:2602-277X**

16. Ordejón, P.; Artacho, E.; Soler, J.M. *Phys. Rev. B.* **1996** , 53, R10441.

17. Perdew, J. P.; Burke, K.; Ernzerhof, M. *Phys. Rev. Lett*. **1996**, 77 (18), 3865-3868.

18. Troullier, N.; Martins, J. L. *Phys. Rev. B.* **1991**, 43 (3), 1993-2006.

19. Parrinello, M.; Rahman, A. *Phys. Rev. Lett*. **1980**, 45 (14), 1196-1197.

20. Monkhorst, H. J.; Pack, J. D. *Phys. Rev. B*. **1976**, 13, 5188-5192.

21. Hundt, R.; SchoÈn, J. C.; Hannemann, A.; Jansen, M. *J. Appl. Crystallogr*. **1999**, 32, 413-416.

22. Alptekin, S. *J. Mol. Model.* **2015**, 21 (12), 304-305.

23. Öztürk, H.; Durandurdu, M. *Phys. Rev. B*. **2009**, 79, 134111.

24. Öztürk, H.; Kürkçü, C.; Kürkçü, C. *J. Alloy. Compd*. **2014**, 597, 155-160.

25. Durandurdu, M. *Chem. Phys*. **2010**, 369, 55-58.

26. Alptekin, S.; Durandurdu, M. *Solid State Commun*. **2009**, 149, 345-348.

27. Özduran, M.; Duranduran, M. *Europhys. Lett*. **2008**, 84 (5), 56001.

ORCID

ID https://orcid.org/0000-0003-2903-4725 (S. Alptekin)

DOI: http://dx.doi.org/10.32571/ijct.735747 **E-ISSN:2602-277X**

International Journal of Chemistry and Technology

http://dergipark.org.tr/ijct

Research Article

Statistical analysis of the effect of melt flow index and weight changes on strength properties of polypropylene spunbond fabrics

İsmail TİYEK[1,*], Emrah KAÇMAZ[2], Mustafa YAZICI[3], Mahmut KILINÇKIRAN[4]

on the last page

[1]*Department of Textile Engineering, Faculty of Engineering and Architecture, Kahramanmaraş Sütçü İmam University, 46050, Kahramanmaraş, Turkey*
[2]*Department of Textile Engineering, Institute of Natural and Applied Sciences, Kahramanmaraş Sütçü İmam University, 46050, Kahramanmaraş, Turkey*
[3]*Department of Mathematics and Science Education, Faculty of Education, Kahramanmaraş Sütçü İmam University, 46050, Kahramanmaraş, Turkey*
[4]*Department of Textile, Clothing, Footwear and Leather, Vocational School of Technical Sciences, Kahramanmaraş Sütçü İmam University, 46050, Kahramanmaraş, Turkey*

Received: 11 May 2020; Revised: 11 June 2020; Accepted: 18 June 2020

*****Corresponding author e-mail: ismailtiyek@ksu.edu.tr

Citation: Tiyel, İ.; Kaçmaz, E.; Yazıcı, M. Kılınçkıran, M. *Int. J. Chem. Technol.* **2020**, 4 (1), 97-102.

ABSTRACT

Spunbond method is widely used in the production of nonwoven fabrics. Melt flow index (MFI) is one of the most important polymer processing parameters. In this paper, tensile strength and elongation values of spunbond fabrics with four different weights produced from polypropylene polymers with two different MFI values were measured. Tensile strength tests were analyzed by two-way multiple variance analysis (Two-Way Manova) in the SPSS statistical package program, and the effects of MFI and weight values on the strength properties of spunbond textile surfaces were examined. As a result of the statistical analysis, it was observed that statistically significant differences ($p < 0.05$) occurred in both tensile strength and elongation values with the change of weight value. In addition, significant differences ($p < 0.05$) occurred in tensile strengths with the change of MFI value, but the differences in elongation values were not statistically significant ($p > 0.05$).

Keywords: Spunbond, melt flow index (MFI), weight, tensile strength, elongation.

Polipropilen bükülmüş kumaşların mukavemet özellikleri üzerine erime akış indeksi ve ağırlık değişimlerinin etkisinin istatistiksel analizi

ÖZ

Spunbond yöntemi dokusuz yüzey kumaşların üretiminde yaygın olarak kullanılmaktadır. Erime akış indeksi (MFI), polimerlerin işlenmesinde en önemli parametrelerden bir tanesidir. Bu çalışmada, iki farklı MFI değerine sahip polipropilen polimerinden dört farklı gramajda üretilen spunbond dokusuz tekstil yüzeylerinin kopma mukavemeti ve uzama değerleri ölçüldü. Kopma mukavemeti testleri SPSS istatistik paket programında iki yönlü çoklu varyans analizi (Two-Way Manova) ile analiz edildi ve MFI ve gramaj değerlerinin spunbond tekstil yüzeylerin mukavemet özellikleri üzerindeki etkileri incelendi. İstatistik analiz sonucunda ağırlık değerinin değişimiyle hem kopma mukavemeti hem de uzama değerlerinde istatistiksel açıdan anlamlı farklar ($p < 0.05$) meydana geldiği gözlendi. Ayrıca, MFI değerinin değişmesi ile kopma mukavemetlerinde anlamlı farklılıklar ($p < 0.05$) oluştu, fakat uzama değerlerindeki farklılıklar istatistiksel olarak anlamlı değildi ($p > 0.05$).

Anahtar Kelimeler: Spunbond, eriyik akış indeksi (MFI), gramaj, kopma mukavemeti, uzama.

1. INTRODUCTION

Nowadays, with the emergence of various developments in the variety of fabric technology, it has become difficult for both manufacturers and consumers to choose and use them for different purposes. Conventional textile producers and consumers consider long lifespan as an important factor along with comfort.[1,2]

Spunbond nonwoven surfaces are used in a wide spectrum such as home textiles, special clothings, medical products, construction and geotextile applications, shoe and leather industry, automotive industry, industrial applications, advertisement and packaging industry.[3,4] Therefore, strength is the first and foremost quality parameter expected from spunbond surface used in all of these areas. Several differences may occur in the variance and strength qualities of non-woven polypropylene in terms of Melt Flow Index (MFI). Polypropylene (PP) is one of the widely used polymers in creating spunbond nonwoven surfaces.[5] PP is a thermoplastic polymer and a material the most widely used after polyethylene in the polymer industry. Melting temperature of polypropylene is about 160°C and it is usually processed at temperatures over 200°C. In the production of spunbond textile surfaces, PP polymer melted by heating in the extruder to ensure suitable viscosity is extruded to cold air zone from spinnerets under certain pressure and formed webs by laying on the collector.[2, 5-8]

PP has been first introduced to the industry by Montecatini in 1957. Studies aimed to increase its application areas and to decrease its cost have continued until 1968 when it has started to be used and produced more frequently.[8,9] MFI is directly related to the molecular weight of polypropylene.[10] MFI is a measure of the capacity of the molten polymeric materials to flow under the pressure and it is inversely proportional to their viscosities at the conditions of the test.[9, 11,12]

MFI values are the most important features of the flow used after density when determining the physical, chemical and thermomechanical properties of plastics and especially when creating catalogs by plastic raw material manufacturers.[13-15] MFI is one of the important elements in the production process because MFI value is directly proportional to molecular weight of polymer. it affects the definition of the processing properties of the polymer and the material to be produced.[10,12,14] MFI test measures the mass of plastic material passed through a capillary tube at a specific diameter and length under a suggested temperature and press conditions for 10 minutes in accordance with ASTM D1238 and TS EN ISO 1133. MFI test result is expressed as g 10 min^{-1}.[14, 16-18]

In this study, spunbond textile surfaces with four different weight were produced from polypropylene polymer with two different MFI value. Depending on MFI of polypropylene polymers and weight of spunbond fabrics, the change in the strength and elongation (%) values of spunbond fabrics were analyzed by statistical analysis. The originality of this article and its difference from other studies is the use of advanced statistical analysis methods. Statistical analyzes both scientifically strengthened the results of the study and provided mathematical models that can be used practically in the industry where strength properties can be predicted before production.

2. MATERIALS AND METHODS

2.1. Materials

In this study, spunbond fabrics produced by Teknomelt Teknik Mensucat San. Tic. A.Ş., polypropylene polymers (Exxon Mobil) of 25 MFI and 35 MFI values at weights of 10 g m^{-2}, 30 g m^{-2}, 50 g m^{-2} and 70 g m^{-2} were used.

2.2. Methods

2.2.1. Formation of spunbond nonwoven surfaces

In the spunbond method, which is known as one of the most common methods of forming texture, fiber formation takes place simultaneously with the texture formation. As shown in Figure 1, the thermoplastic polymer in the form of chips is melted and is extruded from the nozzle at a constant pressure similarly to the synthetic fiber production.[19,20]

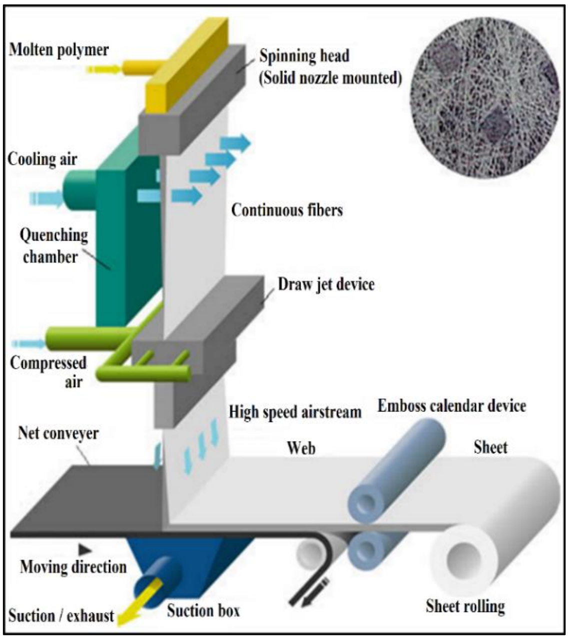

Figure 1. Spunbond surface production.[20]

Table 1. Test values of spunbond surfaces

Material Properties		**Tensile Strength (TS)** (N5 cm^{-1})				**Elongation (E)** (%)			
Weight (g m^{-2})	**MFI** (g 10 min^{-1})	**Machine Direction (MD.TS)**		**Cross Direction (CD.TS)**		**Machine Direction (MD.E)**		**Cross Direction (CD.E)**	
		Mean	**St.Dev.**	**Mean**	**St.Dev.**	**Mean**	**St.Dev.**	**Mean**	**St.Dev.**
10	25	18.70	1.93	10.89	1.60	69.25	11.44	44.68	10.43
	35	16.23	2.01	7.94	0.97	79.90	15.14	40.33	13.14
30	25	61.52	8.68	35.17	5.21	127.62	24.36	118.02	21.84
	35	51.87	5.08	28.82	3.70	110.27	20.07	103.08	19.46
50	25	124.47	8.43	83.21	9.41	129.61	15.96	125.15	13.10
	35	105.48	11.06	65.78	10.67	134.63	17.15	130.00	17.23
70	25	182.27	13.27	125.65	14.38	126.92	15.46	125.75	18.01
	35	164.60	9.16	101.91	7.97	150.03	14.10	149.25	10.54

Then, the filaments formed are cooled with cold air and the macromolecules within the fiber structure are drawn to ensure a proper orientation. The flow in the venturi tube causes the filaments to pass through the distributor ring and to distribute randomly because of ventilation. Afterwards, the formed fibers are laid on the conveyor belt with a porous structure. Following the formation of texture, nonwoven surface is produced by connecting the filaments to each other via thermal, mechanical or chemical methods.[19-21]

The formation of spunbond surfaces was performed via spunbond machine with slot system at nozzle (spinneret) pressure of 3.2 bar, nozzle temperature of 235°C, cooling air temperature of 22°C and calendar temperature of 150°C for 10 g m^{-2}, 30 g m^{-2}, 50 g m^{-2} and 70 g m^{-2}.

2.2.2. Tensile Strength

The tensile test stands out as one of the most common test methods used to determine the mechanical properties of materials. The tensile strength and elongation of spunbond surfaces with different weights and MFI values were measured by Zwick Roell tensile strength testing device in accordance with EDANA WSP 110.4 (05) standard. Tensile tests were carried out under the conditions of 5 N pretension, 10 mm/min jaw speed and 200 mm jaw distance.[22]

3. RESULTS AND DISCUSSION

Tensile strength (TS) and Elongation (E) tests were carried out in the machine direction (MD) and cross direction (CD). The average values of tensile strength and elongation test results of 10 g m^{-2}, 30 g m^{-2}, 50 g m^{-2} and 70 g m^{-2} spunbond fabrics produced from polypropylene polymers of 25 MFI and 35 MFI are given in Table 1.

Bar charts (Figures 2-5) were prepared to visually show the effect of weight and MFI on tensile strength and elongation values by Microsoft Excel. In addition, the line graphs showing the trend of weight–tensile strength and weight-elongation changes were drawn on bar charts, and trend equations and R^2 values of these graphs were also given.

The bar charts of the tensile strengths in the machine direction and in the cross direction of spunbond fabrics with different MFI and weight values are shown in Figures 2 and 3, respectively.

For all MFI values, it was observed that the tensile strength values in both the machine and cross direction increased regularly with the increase of the weight values and the highest R^2 values were found for linear trend equations. For all weight values, it was seen that

DOI: http://dx.doi.org/10.32571/ijct.735747 **E-ISSN:2602-277X**

the tensile strength decreased slightly with the increase of MFI values. However, since there were only two different MFI values, it was not appropriate to calculate any trend equation.

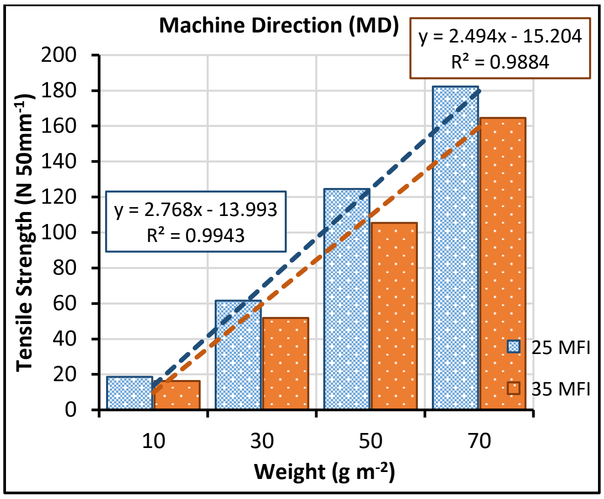

Figure 2. Tensile strengths of spunbond surfaces in the machine direction (Left equation is for 25 MIF, right equation is for 35 MFI).

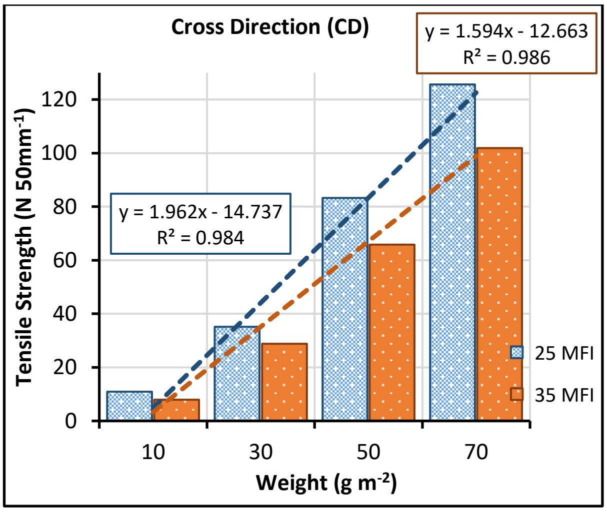

Figure 3. Tensile strengths of spunbond surfaces in the cross direction (Left equation is for 25 MIF, right equation is for 35 MFI).

The bar charts of the elongation values in the machine direction and in the cross direction of spunbond fabrics with different MFI and weight values are shown in Figures 4 and 5, respectively.

For all MFI values, it was observed that the elongation values in both the machine and cross direction increased with the increase of the weight values and the highest R^2 values were found for quadratic polynomial trend equations. Therefore, it was concluded that there was a quadratic relationship between weight and elongation values. For all weight values (except 30 g m^{-2}), it was seen that the elongation values in machine direction generally increased with the increase of MFI values. In the cross direction, it was observed that the elongation values decreased at low weights (10 g m^{-2} and 30 g m^{-2}) and increased at high weights (50 g m^{-2} and 70 g m^{-2}) with the increase of MFI value.

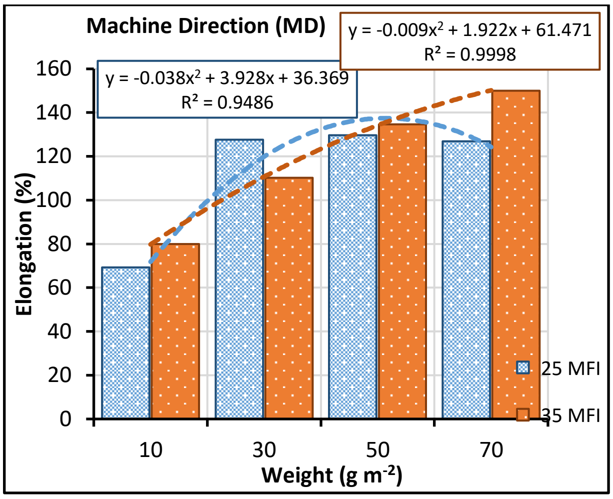

Figure 4. Elongation (%) of spunbond surfaces in the machine direction. (Left equation is for 25 MIF, right equation is for 35 MFI).

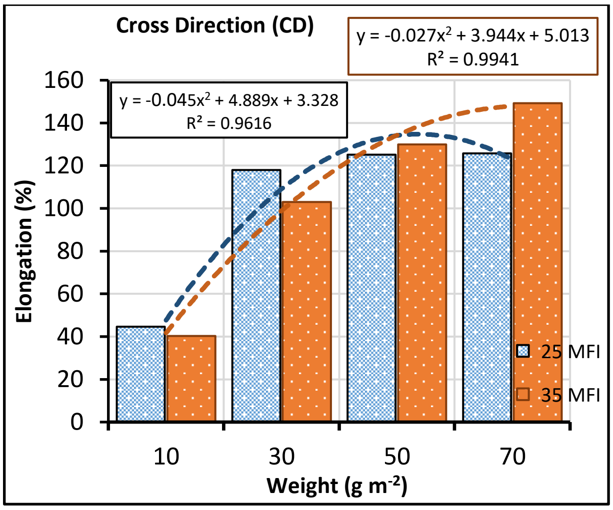

Figure 5. Elongation (%) of spunbond surfaces in the cross direction (Left equation is for 25 MIF, right equation is for 35 MFI).

In this study, it was also aimed to examine the effect of MFI*Weight interaction besides MFI and weight values on the tensile strength and elongation values of the spunbond fabric samples at the machine direction and cross direction by multiple comparison. For this purpose, Two-Way Manova test was carried out at a significance level of $\alpha = 0.05$, in other words, with

DOI: http://dx.doi.org/10.32571/ijct.735747 **E-ISSN:2602-277X**

95% confidence interval by statistical package program of SPSS. In the analysis of Two-Way Manova, while variables of the weight and MFI were selected as independent variables, the variables of the tensile strength and elongation in both machine and cross directions were also selected as dependent variables. The multivariate test results obtained from the Two-Way Manova analysis are summarized in Table 2.

Table 2. Multivariate test results

Effect	Wilks' Lambda	F	p	Partial Eta Squared
MFI	0.480	46.281	0.000	0.520
Weight	0.006	228.75	0.000	0.822
MFI*Weight	0.534	10.111	0.000	0.189

In Table 2, significance value indicates whether the effect of independent variables on dependent variables is statistically significant and is also expressed as p. It can be seen from Table 2 that significance (p) values of MFI, Weight and MFI*Weight interaction are 0.000, that is, all p values are less than 0.05 ($p < \alpha$). This situation shows that there are statistically significant differences in both tensile strength and elongation values with the change of MFI and Weight values. This means that MFI, weight and MFI*Weight interaction have an effect on the tensile strength and elongation in general.

In addition, Partial Eta Squared expresses the effect value of independent variables on dependent variables. It is observed that the effect of weight (0.822) on the tensile strength and elongation values is higher than the effect of MFI (0.520), and also the combined effect of the MFI and weight (MFI*Weight) is at a very low level compared to their individual effects.

However, the details of the effects of independent variables on dependent variables are given in Table 3. It can be seen in Table 3 that only the P values of MFI-MD.E (0.086), and MFI-CD.E (0.423) are greater than 0.05 ($p > \alpha$). This shows that there are no statistically significant differences in elongation values in both machine direction and cross direction with the change of MFI value. This means that the effect of MFI value on elongation values (MD.E and CD.E) is not statistically significant. However, all the other p values (0.000) are less than 0.05 ($p < \alpha$). Consequently, the effect of MFI values on tensile strengths (MD.TS and CD.TS), the effects of weight values and MFI*Weight interaction values on both tensile strengths (MD.TS and CD.TS) and elongation values (MD.E and CD.E) are statistically significant.

When the Partial Eta Squared values are examined; it is observed that the weight has the highest effect values on both tensile strength and elongation values. It is seen that MFI has almost no effect on elongation values while the effect values of MFI on tensile strength values is at medium levels. It is also seen that MFI*Weight interaction has a very weak effect on both tensile strength and elongation values.

Table 3. Tests of between-subject effects

Source	Dependent Variable	F	p	Partial Eta Squared
MFI	MD.TS	94.703	0.000	0.352
	CD.TS	133.893	0.000	0.435
	MD.E	2.986	0.086	0.017
	CD.E	0.646	0.423	0.004
Weight	MD.TS	2660.831	0.000	0.979
	CD.TS	1605.944	0.000	0.965
	MD.E	106.113	0.000	0.647
	CD.E	288.576	0.000	0.833
MFI*Weight	MD.TS	10.652	0.000	0.155
	CD.TS	18.174	0.000	0.239
	MD.E	9.354	0.000	0.139
	CD.E	7.598	0.000	0.116

4. CONCLUSIONS

In this study, it was aimed to investigate the effect of the change of MFI and weight values on the tensile strength properties of nonwoven textile surfaces with different weight values produced from polypropylene polymers with different MFI values by spunbond method. It was observed that the MFI value of the PP polymer had a negative effect on the strength properties on both the machine direction and the cross direction of the spunbond fabrics. When the elongation values were analyzed, it was observed that the elongation values decreased at low weights and increased at high weights with the increase of MFI value. It was observed that all strength and elongation values of PP spunbond fabrics increased with the increase in weight values. That is, the weight values of the spunbonded fabrics were found to have a greater effect on the strength properties of spunbonded fabrics. These results were also confirmed by Two-Way Manova statistical analysis. Consequently, the relationship of the strength properties of the spunbond R^2 values were found to be between weight and strength properties. Fabrics with the fabrics' weight and MFI values of PP polymer was revealed with advanced statistical analysis. Thanks to these mathematical models, it will be possible to estimate the strength of spunbond fabrics very close to reality before production.

ACKNOWLEDGEMENTS

The authors are grateful to the Teknomelt Teknik Mensucat San. Tic. A. Ş. for their supports in the experimental studies.

Conflict of interests

Authors declare that there is no a conflict of interest with any person, institute, company, etc.

REFERENCES

1. Kalebek, N. A.; Babaarslan, O. *Tekstil ve Konfeksiyon* **2009,** 19 (2), 145-150 (In Turkish).

2. Wang, X. Y.; Gong, R. H.; Dong, Z.; Porat, I. *Polym. Eng. Sci.* **2006,** 46 (7), 853-863.

3. Limem, S.; Warner, S. B. *Text. Res. J.* **2005,** 75 (1), 63-72.

4. Lim, H. *JTATM*. **2010,** 6 (3), 1-13.

5. Bledzki, A. K.; Faruk, O. *J. Appl. Polym. Sci.* **2005,** 97 (3), 1090-1096.

6. Karger-Kocsis, J.; Mouzakis, D. E.; Ehrenstein, G. W.; Varga, J. *J. Appl. Polym. Sci.* **1999,** 73 (7), 1205-1214.

7. Nanjundappa, R.; Bhat, G.S. *J. Appl. Polym. Sci.* **2005,** 98 (6), 2355-2364.

8. Durmuş, A. Investigation of Processed Poliolefins by DSC. Master Thesis, University of İstanbul, İstanbul, 2001.

9. Necipoğlu, A. Synthesis of Polypropylene-Clay Nanocomposites and Investigation of the Gas Permeability. Master Thesis, Yıldız Technical University, Istanbul, 2011.

10. Ferg, E. E.; Bolo, L. L. *Polym. Test.* **2013,** 32 (8), 1452-1459.

11. Ersu, D. Preparation and Characterization of Nanocomposites with a Thermoplastic Matrix and Spherical Reinforcement. Master Thesis, Middle East Technical University, Ankara, 2006.

12. Chui, Q. S. H.; Franciscone, C.; Baptista, J. A. F.; Rosa, D. S. *Polym. Test.* **2007,** 26 (5), 576-586.

13. Savaşçı, Ö. T.; Uyanık, N.; Akovalı, G. *Ana Hatları İle Plastikler ve Plastik Teknolojisi,* 3rd ed.; PAGEV Yayınları, İstanbul, 2008 (In Turkish).

14. Güldaş, A.; Çankaya, A.; Güllü, A.; Gürü, M. *Gazi Üniv. Müh. Mim. Fak. Der.* **2014,** 29 (2), 227-234 (In Turkish).

15. Yang, J.; Liang, J. Z.; Tang, C. Y. *Polym. Test.* **2009,** 28 (8), 907-911.

16. Das, A.; Kothari, V. K.; Vandana, N. *AUTEX Res. J.* **2005,** 5 (3), 133-140.

17. ASTM D 1238. Standart Test Method For Melt Flow Rates of Thermoplastics by Extrusion Plastomer, Annual Book of ASTM Standard, sayı 08.01, S 265-276, 2001.

18. TS EN ISO 1133. Plastics-Determination of The Melt Mass - Flow Rate (MFR) and The Melt Volume-Flow Rate (MVR) of Thermoplastics, TSE, Ankara, 2011.

19. Çinçik, E. Experimental and Statistical Analysis of The Propertıes of Polyester/Viscose Blended Nonwovens Produced by Needle Punching Method. PhD Thesis, Çukurova University, Adana, 2010.

20. Jeon, B. S. *Text. Res. J.* **2001,** 71 (6), 509-513.

21. Onan, M. Disposable Hydrophilic Antimicrobial Nonwoven Bed Sheet. Master Thesis, Istanbul Technical University, Istanbul, 2010.

22. EDANA WSP 110.4 (05). Breaking Force and Elongation of Nonwoven Materials (Strip Method). Nonwovens Standard Procedures, 2012.

ORCID

iD https://orcid.org/0000-0002-1643-8977 (İ. Tiyek)

iD https://orcid.org/0000-0001-5857-2077 (E. Kaçmaz)

iD https://orcid.org/0000-0003-1071-0316 (M. Yazıcı)

iD https://orcid.org/0000-0002-0550-4668 (M. Kılınçkıran)